
Third-Order Nonlinear Optical Properties of Ruthenium Alkynyl Complexes

Adam Barlow

A Thesis submitted for the degree of Doctor of Philosophy

The Australian National University



Australian
National
University

December 2014





Declaration

The work described in this Thesis is my own unless otherwise stated. I have not submitted this work for any other degree or qualification. Any contribution from others has been acknowledged appropriately.

A handwritten signature in black ink, appearing to read 'Adam Barlow', written in a cursive style.

Adam Barlow
December 2014

Acknowledgements

Foremost I'd like to thank Prof. Mark Humphrey and Dr Marie Cifuentes for their excellent supervision during my time here, and for the unique international liquor they supplied as incentive. Also Prof. Marek Samoc for guidance concerning the laser work presented in the Thesis. Prof. Rob Stranger for his role on my supervisory panel and Dr Tony Willis for tutelage in single crystal X-ray diffraction.

Thanks to Dr Graeme Moxey for running many X-ray diffraction analyses on the many crystals unsuitable for such purposes. To Dr Mahbod Morshedi for lessons in electrochemistry and coffee brewing. Dr Erandi Kulasekera for her patience in computational analysis of these very large compounds. Dr Guillaume Grelaud, Dr Torsten Schwich and Dr Bandar Babgi for being shining examples of experimentalists.

I'm also thankful for the opportunity to teaching in undergraduate labs offered by Dr Mark Ellison and Assoc. Prof. Geoff Salem.

Cheers to Paul Gugger for his assistance and extensive knowledge of the lab, Hendrik Maat for keeping the laser alive beyond expectations, Anitha Jeyasingham for her skills and perseverance in mass spectrometry, and Dr Genmiao Wang for general laser knowledge.

Shout out to 'Dungeonmaster' Dr Chris Corkery, 'Don't work weekends' Dr Mike Randles, 'Drink this, its good' Dr Lasse Nören, 'You twat' Dr Adam Berlie, Dr Katy Green, 'Only my fourth' Dr Pete Simpson, Dr Caterina Greunwaldt; you peeps are great!

I'd like to thank the students I've had the pleasure of working with throughout my candidature; Nicolas Ripoché, Richard Dexter, Alison Pert, Suzannah Streatfield, Vivek Gupta, Junhong (Nate) Fu, Mark 'Junior' Jennaway, Anthony Nolan, Aradana Dissanayake, Aisyah Shah, Huajin Zhao, Xinwei Yang, Fazira Ilyana, and all the Bramley's Crew.

Prudence Guest, thanks for the proofreading and fine formatting. Thanks for all the fish.

Finally, thanks for the support and encouragement from my Mum and Dad, my brothers Andrew, Campbell and Darcy, my lovely niece Chloe.

Abstract

The field of nonlinear optics has expanded rapidly over the last 50 years as these nonlinear optical (NLO) effects are increasingly utilised in devices. NLO involves the manipulation of light by as it travels through a material, which has the potential to be used in all optical data processing as well as intensity dependent imaging. These applications demand new materials with large nonlinear optical properties, of which organometallics and metal coordination complexes have a good reputation. Organometallics, especially ruthenium alkynyl complexes permit many different structural alterations which result in linear and nonlinear optical property tuning allowing for precise design of materials, however understanding of the structure-property relationships is imperative for such design.

In this work, complexes with a systematically varied structure have been had their third order nonlinear optical properties analysed utilising the Z-scan technique covering a broad wavelength range; the nonlinear absorptive properties being of particular interest. Comparison of these results allows for determination of structural moieties that give high NLO response.

Ruthenium alkynyl dendrimers have considerable nonlinear absorptive properties and the second part of this work covers the modification of the core structure to assess its potential for inclusion into larger systems. The level of core substitution (the number of arms branching from the core) and even the core symmetry influences the electronic properties of the molecule and therefore the nonlinear optical properties. The design limitations and synthesis of ruthenium alkynyl complexes with twelve different core substitutions is detailed and the optical and nonlinear optical properties discussed.

Table of Contents

Abstract	IV
Table of Contents	VI
Abbreviations	ix
Chapter 1 - An Introduction to the NLO Properties of Organometallic Complexes	1
1.1 Introduction	3
1.2 Nonlinear optics	4
1.3 Nonlinear optical (NLO) effects	6
1.3.1 Second-order NLO effects	6
1.3.2 Third-order NLO effects	8
1.4 Nonlinear optical measurement techniques	9
1.4.1 Second-order NLO techniques	9
1.4.2 Third-order NLO techniques	10
1.5 Structure property relationships in organometallic complexes	17
1.5.1 Modification of π -delocalisable systems	18
1.5.2 Changing metal and ligand set	25
1.5.3 The dendritic effect	28
Chapter 2 - Third-order NLO Properties of Organometallic Complexes	31
2.1 Introduction	32
2.2 Z-scan Measurements	32
2.2.1 Standardisation	32
2.2.2 Isocyanurate cored octupolar complexes	36
2.2.3 Fluorene containing complexes	39
2.2.4 Dendrimers	41
2.2.5 Metal content of dendrimers	45
2.2.6 Porphyrin Complexes	48
2.2.7 Protic Switching	51

52.2.8 Molybdenum and Niobium cluster complexes	53
2.2.8.1 Molybdenum cluster complexes	53
2.2.8.2 Niobium cluster complexes	57
2.3 Experimental	59
2.3.1.1 Materials	59
2.4.1.2 Methods and Instrumentation	60
Chapter 3 - Core Modification in Ruthenium Alkynyl Stars	63
3.1 Introduction	65
3.1.1 Core substitution level in NLO materials	66
3.1.2 Organometallic compounds	68
3.1.3 Previous work with alkynylruthenium compounds	69
3.1.2 Synthetic considerations	71
3.2 Synthesis	73
3.2.1 Synthetic design	73
3.2.2 Preparation of a tri(Phenyleneethynylene) containing arm	74
3.2.3 TMS-protected cores	75
3.2.4 Core synthesis and metallation	80
3.3 NMR analysis	85
3.3.1 Extending arm	85
3.3.2 TMS cores	86
3.3.3 Organic cores	88
3.3.4 Ruthenium alkynyl compounds	90
3.4 Linear optical properties	92
3.4.1 UV-Visible properties	92
3.5 Electrochemistry	101
3.5.1 Cyclic voltammetry and spectroelectrochemistry	101
3.6 Nonlinear optical properties	104
3.6.1 TIPS-protected cores	104
3.6.2 Ruthenium alkynyl complexes	107
3.7 Concluding remarks	112
3.8 Experimental section	114
3.8.1 Atom labeling	114
3.8.2 Materials	115

3.8.3 Instrumentation	115
3.8.4 Experimental data for compounds 1 - 61	116
References	148
Appendix	153
4.1 NMR Spectra	155
4.2 NLO data	229
4.2.1 Chapter 2 NLO data	229
4.2.2 Chapter 3 NLO data	250
4.3 Foldout figures	273

Abbreviations

α	Linear polarisability
β	First hyperpolarisability
γ	Second hyperpolarisability
γ_{imag}	Imaginary component of the second hyperpolarisability
γ_{real}	Real component of the second hyperpolarisability
λ	Wavelength
σ_0	Ground state absorption cross-section
σ_{eff}	Excited state absorption cross-section
σ_2	Two-photon absorption cross-section
appq	Apparent quartet
d	Doublet
dd	Doublet of doublets
DFWM	Denerate four-wave mixing
DMF	Dimethylformamide
dppe	Bis(diphenylphosphino)ethane
dppeO	Bis(diphenylphosphino)ethane Oxide
dppm	Bis(diphenylphosphino)methane
E_{loc}	Local electric field
EFISH	Electric field-induced second-harmonic generation
EI	Electron impact
ESI	Electrospray ionization
fs	Femtosecond
HMBC	Heteronuclear Multiple Bond Correlation
HSQC	Heteronuclear Single Quantum Coherence
LMCT	Ligand to metal charge transfer
m	Multiplet
MeOH	Methanol
MS	Mass spectrometry
Et	Ethyl
MLCT	Metal to ligand charge transfer
MW	Molecular weight
NLO	Nonlinear optical
NMR	Nuclear magnetic resonance
ppm	Parts per million
RT	Room temperature
s	Singlet
SHG	Second harmonic generation
SFG	Sum frequency generation
TBAF	Tetrabutylammonium fluoride
TIPS	triisopropylsilyl
TMS	Trimethylsilyl
TLC	Thin layer chromatography
nPA	n-photon absorption

Introduction	1
Chapter 1. The History of the Book	15
Chapter 2. The Book in the Middle Ages	35
Chapter 3. The Book in the Renaissance	55
Chapter 4. The Book in the 17th and 18th Centuries	75
Chapter 5. The Book in the 19th Century	95
Chapter 6. The Book in the 20th Century	115
Chapter 7. The Book in the 21st Century	135
Chapter 8. The Book in the Future	155
Appendix A. Bibliography	175
Appendix B. Glossary	195
Appendix C. Index	215
Appendix D. List of Figures	235
Appendix E. List of Tables	255
Appendix F. List of Appendices	275
Appendix G. List of References	295
Appendix H. List of Citations	315
Appendix I. List of Footnotes	335
Appendix J. List of Endnotes	355
Appendix K. List of Bibliographies	375
Appendix L. List of Bibliographies	395
Appendix M. List of Bibliographies	415
Appendix N. List of Bibliographies	435
Appendix O. List of Bibliographies	455
Appendix P. List of Bibliographies	475
Appendix Q. List of Bibliographies	495
Appendix R. List of Bibliographies	515
Appendix S. List of Bibliographies	535
Appendix T. List of Bibliographies	555
Appendix U. List of Bibliographies	575
Appendix V. List of Bibliographies	595
Appendix W. List of Bibliographies	615
Appendix X. List of Bibliographies	635
Appendix Y. List of Bibliographies	655
Appendix Z. List of Bibliographies	675

Chapter 1 - An Introduction to the NLO
Properties of Organometallic Complexes

1.1 Introduction

The field of nonlinear optics has been of great interest in recent years as light based information transmission becomes more widespread and the devices used in such applications become ever smaller.¹⁻⁴ The ability of materials to modulate light properties, such as frequency, intensity and phase, makes them ideal candidates for use in these devices. Materials with large nonlinear optical (NLO) properties and the processes this field encompasses have been suggested for use in a variety of roles such as optical data storage, optical switching and even optical computing. In modern computing these functions are carried out by silicon based semiconductors using electron flow for data processing and control, and the materials are rapidly reaching their limits of speed and size. One possibility to overcome this roadblock is to change to light based transmission and processing, which has a better signal to noise ratio and faster transmission speed. For this to eventuate, methods for detection of ultrashort light pulses and materials with fast response times and high efficiency will be needed. The development of novel NLO materials is required to advance the knowledge base with the aim of producing suitable materials for implementation into such optical devices.

The current applications of NLO materials are dominated by inorganic salts in crystalline form such as LiNbO_3 and KH_2PO_4 (KDP).⁴ Inorganic salts with large NLO responses are commonly used in frequency mixing for light generation and are found in most lasers. They typically have the downside of slow response times which makes them unsuitable for faster response applications needed for optical computing, as well as fragility and, for some materials, size limitations.⁵ Recently, research into organic dyes, polymers and organometallics for NLO applications has increased.⁵⁻¹⁰ Organic molecules tend to have better design flexibility than inorganic salts, as functional groups can be modified to a particular purpose or absorption maxima can be tuned to a particular wavelength. Investigations into organic compounds for NLO applications have led to structure-property directed development of NLO compounds, where the effect of changing a molecular structure can be ascertained, leading to the design of materials for precise applications.¹¹⁻¹³ The installation of donor - acceptor functional group pairs such as nitro and dialkylamino has been shown to increase nonlinear behavior in organic compounds, with precise selection of pairs allowing for design of effects at particular wavelengths.¹⁴⁻¹⁶ Most compounds having high NLO properties typically have large conjugated systems with electron donating and withdrawing groups.^{7,14,17}

Organometallic compounds have increased advantages compared to organic based materials as the compounds often have higher thermal stability, allowing use in high-powered lasers.^{18,19} A larger range of options for the tuning of NLO properties exist in organometallics as the metal centre donates electron density into the conjugated ligand.²⁰ This allows modification of the auxiliary ligand set, to increase or decrease electron density donated to the π -bridging ligand, which can also be affected by oxidation of the metal center allowing for switching between two states.^{21,22} The Humphrey research group has made a number of organometallic dendrimers utilizing ruthenium alkynyl groups connected by highly conjugated oligo(phenylenethynylene) ligands for NLO applications and this work seeks to increase the understanding of which structural modifications of these systems improve these effects.²³⁻²⁶

What follows in this introduction is a brief summary of nonlinear optics, the origin of the physical characteristics used to compare NLO materials and some methods used for this characterisation and lastly the structure-property links known for the cubic NLO responses of metal alkynyl complexes.

1.2 Nonlinear optics

Nonlinear optical materials can be used to modify light in a variety of advantageous ways, but these effects are only observed when intense light sources are used, which currently limits their use to lasers.^{1,4} The effects arise from the mixing of a number of intense oscillations from the electric field of light mediated by the material through which it is moving. The material can also have particular internal fields or resonances which influence this conversion of light properties, which means the effects are intrinsic to the properties of the material itself. When intense light is moving through a medium the electric fields in the material (or molecule) become polarised. When the polarisation of the medium is not linear with respect to the contributing electric field the interaction is said to be nonlinear.

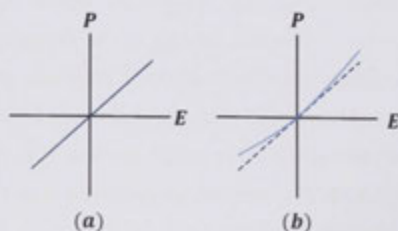


Figure 1.1- A representation of the polarisation of a linear medium (a) and a nonlinear medium (b)¹

Figure 1.1 shows the relationship between polarisation and electric field for a dielectric medium and a nonlinear medium. A nonlinear material in a focused laser beam with sufficient intensity will be 'hyperpolarised' by the light-derived electric fields. The departure of the polarisation (\mathbf{P}) from the linear norm in a nonlinear material in an applied electric field such as a laser beam is described in equation 1:

$$\bar{\mathbf{P}} = \epsilon_0(\chi^{(1)}\mathbf{E} + \chi^{(2)}\mathbf{E}^2 + \chi^{(3)}\mathbf{E}^3 + \dots) \quad (1)$$

where the term $\chi^{(1)}$ is the linear polarisation (related to dielectric constant) of the material by the applied electric field (\mathbf{E}) and $\chi^{(2)}$ and $\chi^{(3)}$ are the electric susceptibility of the medium in the second- and third-order. These values indicate the susceptibility of a material for second-order or third-order NLO effects, and can be used in material development as a comparison of bulk effectiveness. For detailed structure-property relationship determination, to assess the effect of structural change in molecules, it is better to measure the molecular hyperpolarisabilities, so as to eliminate contributions from elements other than those in the molecule only. Values of the macroscopic polarisability (in equation 1) are useful for comparing conjugates or crystals and even solutions of material when considering the effectiveness for a particular application.⁴ The following equation (2) shows the modification of the dipole moment of a NLO active compound under high light intensities:

$$\mu = \mu_0 + \alpha E_{loc} + \beta E_{loc}^2 + \gamma E_{loc}^3 + \dots \quad (2)$$

At low light levels (small values of E_{loc}) the response is linear and observed interactions can be described by $\mu_0 + \alpha E_{loc}$, where μ_0 is the molecules' intrinsic dipole and α is the linear hyperpolarisability. The quadratic and cubic hyperpolarisability terms (β and γ , respectively) make negligible contributions at low intensities and only at high light intensities is the dipole moment affected significantly by the hyperpolarisability terms describing nonlinear behaviour. The hyperpolarisability terms are tensors that describe the influence of the field on the molecular electron density in directions in space. Since the terms correspond to either the square (β) or the cube (γ) of the applied field the NLO effects that correspond to these terms differ, as do the molecular structural design needed to express large NLO effects. In this Thesis the focus is the third-order term γ , and the nonlinear optical properties of the compounds studied are reported as such, the effects usually being of the order of 10^{-36} electro static units (esu).

1.3 Nonlinear optical (NLO) effects

Equation 2 can be expanded by inserting E_{loc} terms originating from the electric field component of light emitted from the laser (equation 3):

$$E(t) = E_0 \cos(\omega t) = 1/2 E_0 [\exp(i\omega t) + \exp(-i\omega t)] \quad (3)$$

into equation 2 to gives:

$$\begin{aligned} \mu &= \mu_0 + \alpha E_0 \cos(\omega t) + 1/2 \beta E_0^2 + 1/2 \beta E_0^2 \cos(2\omega t) + \quad (4) \\ &\quad 3/4 \gamma E_0^3 \cos(\omega t) + 1/4 \gamma E_0^3 \cos(3\omega t) + \dots \\ &= \mu_0 + 1/2 \alpha E_0 \exp(i\omega t) + 1/2 \beta E_0^2 + 1/4 \beta E_0^2 \exp(2i\omega t) + \\ &\quad 3/8 \gamma E_0^3 \exp(i\omega t) + 1/8 \gamma E_0^3 \exp(3i\omega t) + \dots \end{aligned}$$

From equation 4 the component terms include frequency doubling (2ω) and DC for the first hyperpolarisability (β), and tripling (3ω) and the optical Kerr effect (ω) for the second (γ). The observed magnitudes of these effects are generally dwarfed by the linear optical effects of the material, and this intensity effect reduces further as order increases. To see these effects, a wavelength needs to be chosen to be outside of the intrinsic linear effects and absorptions of the molecule. For compounds at this wavelength with a permanent structural dipole the effects relating to β will be the most readily detectable. If the compound doesn't have a permanent dipole, or the dipole is opposed by the structural symmetry, the γ term will dominate.

1.3.1 Second-order NLO effects

The frequency dependent β term from equation 4 is the source of the second-harmonic generation (SHG) effect where an input frequency can be doubled to generate an output with double the frequency ($\omega + \omega \rightarrow 2\omega$). Second-order effects (in fact, all 'even' order effects) vanish in centrosymmetric media. SHG is commonly used in laser pointers where visible light is generated from a doubling of an infrared frequency. If the laser light applied is not monochromatic or if the material is polarized by two laser beams a multitude of frequency addition or subtraction effects can arise. A material influenced by

two laser wavelengths (ω_1 and ω_2) will generate oscillations at $2\omega_1$, $2\omega_2$, $\omega_1 + \omega_2$, $\omega_1 - \omega_2$, and 0ω (DC).⁴

This can be abbreviated to the Fourier components of the nonlinear polarisation, such as a frequency (ω_3) generated by the oscillation of two other frequencies (ω_1 and ω_2) at their respective field strengths (E_1 or E_2):

$$P^{(2)} = \epsilon_0 D^{(2)} \sum \chi^{(2)}(-\omega_3; \omega_1, \omega_2) E(\omega_1) E(\omega_2) \quad (5)$$

or for the molecular hyperpolarisability:

$$\Delta\mu^{(2)}(\omega_3) = \beta(-\omega_3; \omega_1, \omega_2) E(\omega_1) E(\omega_2) \quad (6)$$

This is a convenient abbreviation as it eliminates the need for the time dependent quantities in equation 4 and replaces them with Fourier amplitudes which are frequency dependent. These effects are heavily utilized in tunable laser light generation systems where multiple frequencies can be generated from the same source. These include sum or difference frequency generation ($[\omega_1 + \omega_2 \rightarrow \omega_3]$ or $[\omega_1 - \omega_2 \rightarrow \omega_3]$ in figure 1.2 (a)), optical parametric amplification (figure 1.2 (b)) or oscillation (figure 1.2 (c)) and parametric down-conversion. These effects are commonly called three-wave mixing (two incident waves plus a generated wave).

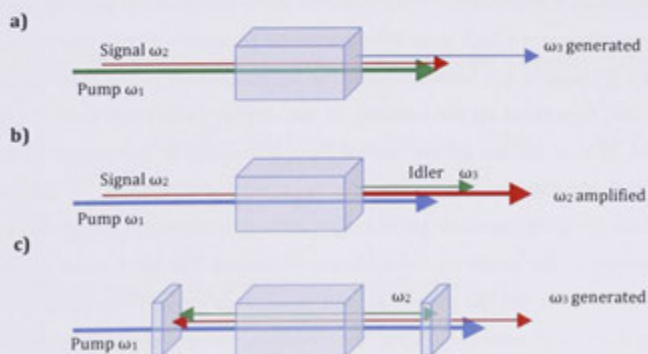


Figure 1.2- Forms of second-order three-wave mixing. a) Optical frequency conversion (SFG), b) optical parametric amplification (OPA) and c) optical parametric oscillation (OPO).¹

The laser system at the Research School of Chemistry (RSC) utilizes all of these processes to some extent for the generation of fs timed laser light for measurement of nonlinear materials.

The second-harmonic and sum and difference frequency generation are used in combination with optical parametric amplification to convert the 795 nm pump beam into wavelengths between 460 and 2400 nm. Optical parametric amplification is used in the pump laser itself for amplification of the weak femtosecond seed signal to a much higher intensity. A green nanosecond 30 W laser is used to amplify this signal to around 3 W with the original timing (femtosecond) and wavelength (795 nm).

The other term arising from expansion of the β coefficient in equation 2 is a direct current term which is independent of frequency. This results in the electro-optic effect, where the transmission of a light beam in the NLO material generates a voltage across the material. This tends to be a weak effect, but the process can be reversed in that a DC voltage put across the medium will create a change in the linear susceptibility, changing the material's refractive index. Second-order nonlinear optical effects have found many applications in current technology as they are orders of magnitude stronger than higher-order effects.

1.3.2 Third-order NLO effects

In centrosymmetric media the second-order terms reduce to zero and third-order effects become the dominant processes.^{1,4} The expansion above (equation 4) gives two terms: one with triple the frequency which gives third-harmonic generation (THG; $\gamma(-3\omega; \omega, \omega, \omega)$); and the other is a ($\gamma(-\omega; \omega, -\omega, \omega)$) term similar to the DC component in the quadratic example, but in this case dependent on the intensity of the applied field rather than the square of the DC field. This is known as the optical Kerr effect and is the source of nonlinear refraction and absorption. Most interest in third-order NLO is in the refractive components as the third-harmonic generation is difficult to observe (3ω generally appears in the UV region of the spectrum with IR source lasers). The third-order properties of interest to this Thesis are the refraction and absorption (mostly absorption) from the $3/8\gamma E_0^3 \exp(-i\omega t)$ (or $\gamma(-\omega; \omega, -\omega, \omega)$) term from the molecular polarisability expansion. This term has a negative frequency component of the same frequency as the original though out of phase. This causes refractive index change which is intensity dependent:

$$\Delta n = n_2 I \quad (7)$$

where n is the refractive index and n_2 is the nonlinear refractive index. This is related to the third-order susceptibility ($\chi^{(3)}$) by:

$$n_2 = \frac{0.039}{n^2} \chi^{(3)} \quad (8)$$

The high interest in the nonlinear refractive properties of third-order materials led to active minimisation of observed absorption at resonant light wavelengths through material design.^{1,4} This is especially the case for nonlinear waveguides, where high efficiency transmission is desired at high power.²⁷ These effects occur simultaneously and during characterisation, so nonlinear refractive measurements need to be corrected for the absorption interference. Recently nonlinear absorption has been an area of interest in its own right with materials designed to maximise this effect. Nonlinear absorption can proceed through many different processes where a NLO material absorbs intense light in a wavelength region it doesn't absorb in under low light conditions. One mechanism is two-photon or multi-photon absorption, giving rise to the nonlinear absorption effect. Alternatively the excited-state population distribution is altered by the propagation of the beam through the sample, leading to excited-state absorption. Applications of nonlinear absorption include two-photon spectroscopy, optical power limiting and optical data storage. In either case, the change of transmission through a cubic nonlinear material is modeled by:

$$\Delta T = -\alpha l - \beta I^2 \quad (9)$$

where β is the two-photon absorption coefficient related to the imaginary part of $\chi^{(3)}$ by:

$$\beta = \frac{3\pi}{\epsilon_0 n^2 c \lambda} \text{Im}[\chi^{(3)}(-\omega; \omega, -\omega, \omega)] \quad (10)$$

1.4 Nonlinear optical measurement techniques

1.4.1 Second-order NLO techniques

Several techniques exist for quantification of nonlinear optical properties (molecular hyperpolarisability terms). For quadratic hyperpolarisability terms two main techniques are used: hyper-Rayleigh scattering (HRS) and the electric field-induced second-harmonic

generation (EFISH) technique. The measurements and compounds presented in this Thesis are focused on the third-order NLO effects, so discussion of the technique to measure the second-order effects will be brief.

EFISH requires the polarization of a solution of molecule with an intrinsic dipole by an external electric field.²⁸ The molecules align with the field polarisation and are interrogated by a laser and the generation of a frequency doubled response is measured. Due to the alignment the molecular undertake, the value measured is a product of the molecules dipole and the hyperpolarisability term ($\mu\beta$). The dipole value (if known or calculated) can then be used to elucidate the true β term. The χ value obtained contains two terms (one β and one γ term) and requires correction for the purely electronic third-order hyperpolarisability (γ), but this is usually a couple of orders of magnitude lower than the second-order term.

HRS is now more commonly used for second-order NLO characterisation.²⁹ HRS measures the scattered second-harmonic generated from a solution of an NLO material. It can characterise a wider variety of materials in solution from salts to octupolar compounds (ie. without an overall dipole moment). The scattered light is weak so the setup uses a mirror to collect as much 2ω light generated and direct it to a highly sensitive detector. Different concentrations of a sample are measured and the β term is calculated from the linear dependency of the SHG intensity on the sample concentration. Compounds which show fluorescence at the probing measurement wavelength (typically a 532 nm second harmonic corresponding to a 1064 nm laser) require corrections to the β term as these effects increase the observed value. This technique is the most commonly used, due to its simplicity.

1.4.2 Third-order NLO techniques

Degenerate four-wave mixing

DFWM is a common technique used for determination of the magnitude of third-order NLO properties of materials.⁴ A sample material is pumped by two coherent beams of the same frequency and probed by a third beam of the same frequency to produce a fourth, which is measured. The generated beam is orthogonal and counter-propagating to the probe beam, which allows for the measurement of the intensity. Typically, all three beams are from the same source laser with a number of mirrors and beam-splitters to generate

and orient them. Samples are typically solutions (but don't have to be) and usually referenced to CS₂.

The generated intensity is measured over increasing input intensity, which can be fit to the equation:

$$I_c = b' I_{pump}^2 \quad (11)$$

which can then be used to calculate the $\chi^{(3)}$ value using:

$$\chi_{eff}^{(3)} = \frac{\epsilon_0 n_0^2 c \lambda}{3\pi L} \sqrt{\frac{b'}{\eta}} \quad (12)$$

The advantages of this technique are the conjugate beam (beam generated) is readily distinguished from the others and the time dependence of the nonlinearity can be obtained with a slight modification to the procedure. However, the real and imaginary parts of the third-order susceptibility can't be discerned from this technique, and strong nonlinear absorption can be problematic.

The Z-scan experiment

The most useful technique for measuring the nonlinear absorption and nonlinear refractive properties is the Z-scan technique.³⁰ As previously discussed these properties arise from the third-order nonlinear polarisability terms (γ) and are light intensity dependent. There are two components to the γ hyperpolarisability from the nonlinear refractive dependence (γ_{real}) and the absorptive properties (γ_{imag}) of the material as described by the following equation:

$$\gamma = \sqrt{(\gamma_{real}^2 + \gamma_{imag}^2)} \quad (13)$$

The setup involves moving a sample through a focused laser beam, thereby subjecting the sample to an increasing light intensity (beam profile - Figure 1.3) The resulting beam is then split between two detectors: an open aperture detector perpendicular to the beam direction and a closed aperture detector which is behind a pin-hole screen. The closed aperture detector is a measure of the refractive index change in the sample over the intensity change and has a transmission profile as the Z position changes described by trace a) or b) (Figure 1.3). The open aperture detector collects all the light split off from the beam splitter and thus measures the absorption change as the intensity increases

through the sample. The profile for the three possible observed traces for this detector is c), d), and e). The traces in figure 1.3 are ideal traces and the measurement actually takes an intensity reading at any value for z that should closely follow these model trends. A reference detector is used to normalise the traces to remove distortions from laser fluctuations. This is achieved by division of the closed and open aperture traces by the reference values. The intensity of the light used for the experiment has to be attenuated to get sensible traces, that is, a closed- aperture trace has to have a nonlinear phase shift below 1 rad (for assumptions related to the experiment to uphold). This is achieved by a neutral density filter before the reference detector. The beam is spatially cleaned (by aperture) before it is used in the experiment.

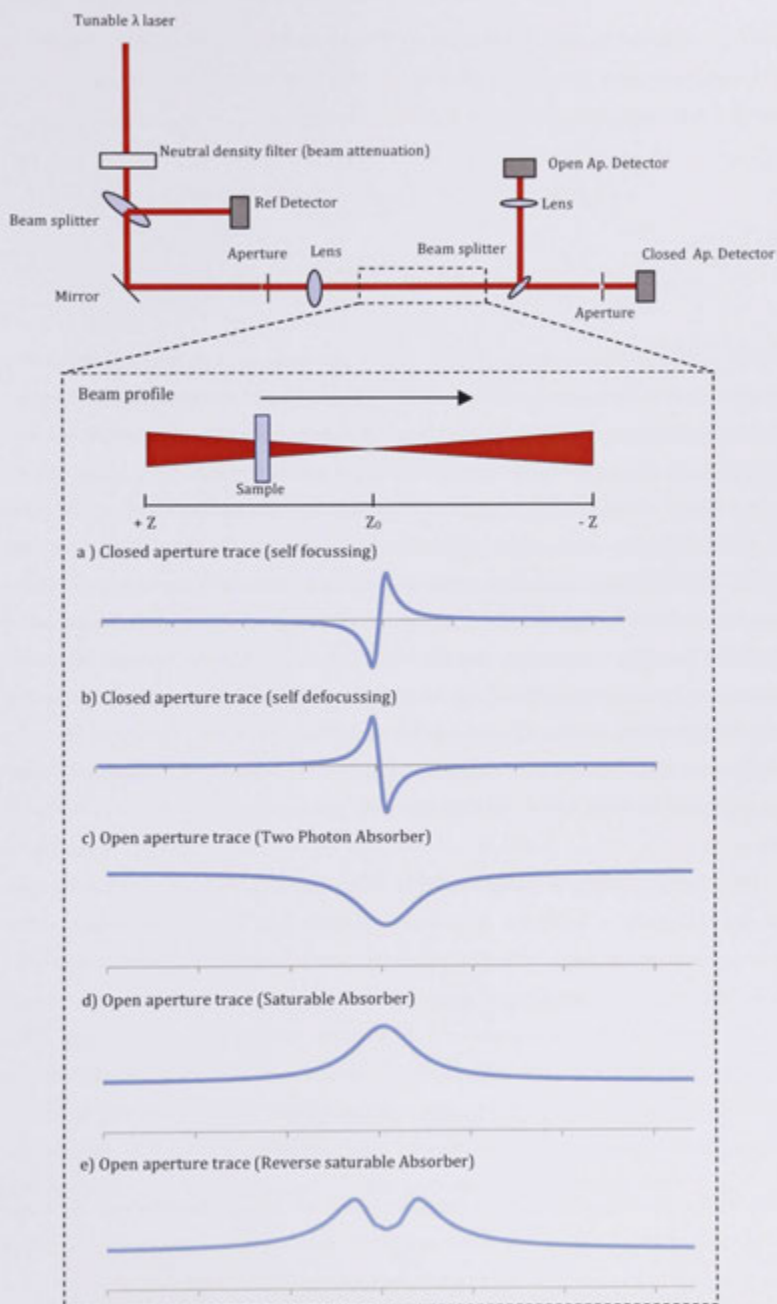


Figure 1.3 -Diagram of the z-scan setup. The dashed box shows the focused beam profile, which the samples moves through. The open and closed aperture traces are shown underneath which display light transmission at the corresponding value for Z .

Using the traces from the open aperture experiment (c-e (figure 1.3)), a theoretical fitting can be done to calculate the 2PA coefficient (β) which can then be used to calculate the imaginary component of $\chi^{(3)}$. The fitting uses the equation:

$$\Delta T(z) \approx -\frac{q_0}{2\sqrt{z}} \frac{1}{[1+z^2/z_0^2]} \quad (14)$$

where

$$q_0 = \beta I_0 L_{eff} \quad (15)$$

The closed aperture experiment detects the shift in the focal point as the sample position changes. Depending on the nature of the material the focal point will shift closer or further away from the aperture (self-defocussing or self-focussing respectively) allowing more or less light through the pin-hole. For a self-focussing material far from the pinhole ($z < 0$), the light intensity passing through the aperture will be less than normal as the focal point of the beam will have been moved away from the aperture. The materials nonlinear refraction is focussing the beam tighter than before, which increases the dispersion of the beam at the aperture. As the sample moves towards the original focal point (defined as $z = 0$), the light intensity transmitted through the aperture returns to normal. When the sample is close to the aperture ($z > 0$) the beam is then focused through the pin-hole and a increased transmission results. The resulting trace plotted against the z position gives the trace in figure 1.3 a); the nonlinear phase shift can be determined which can then be used to obtain n_2 (nonlinear refractive index) as follows:

$$\Delta T_{pv} \cong 0.406(1-S)^{0.27} |\Delta\phi_0| \quad (16)$$

where :

$$|\Delta\phi_0| = \frac{2\pi}{\lambda} n_2 I_0 L_{eff} \quad (17)$$

and :

$$L_{eff} = \frac{(1-e^{-\alpha L})}{\alpha} \quad (18)$$

where S is the transmittance of light through the aperture, ΔT_{pv} is the difference between peak and valley transmittance, $\Delta\phi_0$ is the nonlinear phase shift, I_0 is the irradiance at the focus, α is the absorption coefficient, and L is the sample length. The fitting of both curves in the present work was done using a program written by Marek Samoc, where $\Delta\phi$ and the T factor can be obtained quite easily using the input of the two detectors traces and λ .

ΔT_{pv} and I_0 are calculated by the program from the input values and require only an input of $\Delta\phi$ (and the beam waist extracted by fitting the closed aperture trace of fused silica) to model the closed-aperture trace or to obtain the T factor from the open aperture trace. From the values of n_2 derived from fitting the above equation (16) to the closed aperture trace and using equation (8), the $\chi^{(3)}$ value can then be calculated. For

$$\sigma_2 = \frac{0.039h\omega L^4}{\lambda n^2} 4\pi\gamma_{imag} \quad (19)$$

Several observable effects can arise from the open- and closed-aperture detectors in the Z-scan setup. The closed-aperture trace can have reduced or increased transmission at the $z < 0$ displacement, which as previously discussed, denote self-focusing or defocusing in the material (figure 1.3). The open-aperture experiment has three possible traces: the first is standard intensity-dependent absorption which can consist of several absorptive processes:- multi-photon absorption or excited state absorption (ESA), if the material has a non-zero absorption at the measurement wavelength, or intensity dependent scattering, where the input light is scattered off the line of beam propagation and isn't detected. The last of these effects is not desirable for characterisation of the absorptive properties of a material, and is generally avoided by regulating the irradiance into the experiment. The other two effects tend to give the plot (c) in figure 1.3. The gradient of the curve is dependent on the effect observed; ESA has the broadest plot and the higher the multiphoton absorption order the greater the gradient of the curve. Two-photon absorption (2PA) typically dominates as it relates to the third-order hyperpolarisability where higher orders are less abundant (e.g. 4PA, which is a seventh-order effect). Saturable absorption is a type of ESA that can occur at or near strong linear absorption wavelengths and gives what appears to be an inverted 2PA trace ((d) in figure 1.3).⁴ This leads to negative two-photon absorption cross-sections and an effect that finds applications in Q-switches where intensity dependent opacity can be utilised. An effect known as reverse saturable absorption gives a trace like that in (e) (figure 1.3) where the material acts as a saturable absorber until a threshold intensity is reached, where another absorptive process begins to occur, and the material starts absorbing again.

ESA covers several excitation processes that result in intensity dependent absorption. While not arising from the hyperpolarisability constant, its effects are still nonlinear. It generally occurs when the incident intensity is above the saturation intensity for the

material and the excited state becomes significantly populated, permitting excitation beyond the higher level state.⁴

The five level theorem (Jablonski diagram) which is used to explain a multitude of optical phenomena is displayed in figure 1.4. S_0 denotes the electronic ground state in a polyatomic molecule in which electrons can be excited to a higher energy state (S_1) by electromagnetic absorption. Due to vibrational distortion in the molecule there are a multitude of closely associated energy states at each level; the electron will thermally relax to the lowest lying level at this state (dark black lines).⁴

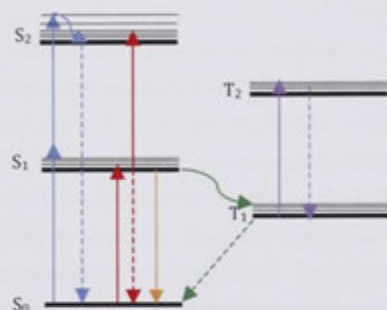


Figure 1.4 - Jablonski diagram showing four levels of excitation and the origin of several optical effects.

After this initial excitation three possible events can occur:

- Relaxation from this energy level by radiative (orange line) or nonradiative (red dotted line) processes back to the ground state. Radiative relaxation gives fluorescence.
- Excitation with a laser with a long pulse length (ns) allows for further excitation from S_1 to S_2 (red line). This is excited state absorption and is dependent on the population density at this energy level and the rate of relaxation from this level.
- Inter-system crossing and relaxation to a lower lying energy level, which is not the ground state (triplet state)(green line). Relaxation from this state is slow, requiring the spin to revert to the original orientation. This is the origin of molecular phosphorescence (green dotted line).

A two-photon absorption event is also possible as shown by figure 1.4 (blue line), and decay from the S_2 state can proceed in any of the events discussed above. Two-photon excited fluorescence is often observed in organic materials with the Z-scan experiment, and is exploited in the two-photon fluorescence technique, which allows for characterisation of the 2PA cross-section. Additional excitation from the triplet state is allowed giving four possible transition mechanisms for light intensity attenuation. Relaxation from the S_2 and T_2 states is very quick and therefore the population density at these is negligible compared to those of the S_1 and T_1 states. Under intense light the population density of the ground state (σ_0) becomes less than the excited state (σ_1), a process known as population inversion. Materials with a larger excited-state population are good optical limiters as the large number of excited state absorptive events possible can dissipate high light intensities.

The characterisation of ruthenium alkynyl compounds typically demands the reduction of other absorption processes so as to focus on two-photon or multiphoton processes. This is achieved by controlling the input intensity and ensuring the wavelength is outside of the linear absorptive range to reduce the excited state population. Short pulse lengths (fs) are also used to reduce excited-state effects. The input intensity is controlled by the use of neutral density filters applied to the beam before the experiment setup (figure 1.3). Characterisation of the 2PA properties is also usually conducted in a transparent region of the material (typically above 500 nm for ruthenium alkynyl complexes). Occasionally the linear absorption of the molecule makes this unavoidable (e.g. compounds **55-58** in part 2.4.4) and the excited state is populated due to linear absorption, and then excited further. This can be a useful effect in organometallics, as redox switching of the ruthenium alkynyl complexes generates a low-energy absorption band at a wavelength with significant 2PA in the neutral complex, demonstrating the modulation of 2PA via electronic switching.

1.5 Structure property relationships in organometallic complexes

The nonlinear optical properties of organometallic compounds are closely related to their molecular structures. By creating a large pool of NLO data of complexes with systematic structural changes the underlying effects which create large nonlinearities can be determined and ultimately exploited for purposes discussed previously. Considerably more structure-property determinations have been carried out on the first hyperpolarisability (β) effects as these are of a larger magnitude than the higher-order

effects. The most important structural feature for even-order terms is the permanent molecular dipole. Only structural features that affect the third-order nonlinearity will be discussed in this part, and the discussion will be focused on metal alkynyl, vinylidene and some alkenyl complexes. Due to the large errors inherent to the measurements used, precise comparison between values is difficult and observations are made to identify loose trends.

1.5.1 Modification of π -delocalisable systems

A benefit that organic and organometallic materials have is the wealth of modifications available to tune the underlying electronics which give rise to the NLO effects. Myers *et al.* have studied the third-order NLO effects of dialkenylbenzene-linked dizirconium compounds (figure 1.5).³¹ The change of the position of the alkenes on the benzene ring from meta- to para- substitution resulted in a threefold increase of the third-order hyperpolarisability. The ease of conjugation through the π -delocalised bridge is the root cause in this case, as the (1,4)- has easier charge transfer through the benzene ring than the (1,3)- (this is pertinent to the study in chapter 3). The reduced conjugation causes isolation of the two metals and a shorter conjugation length; this alters the energy of transition between ground and excited states. **1** has a lower transition energy and therefore a higher third-order response.

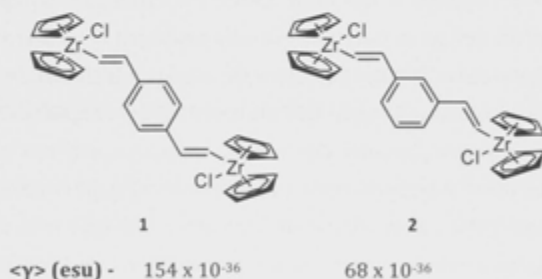


Figure 1.5 - Zirconium alkenyl complexes with meta- and para- disposed linker groups.

Transition energy differences also exist between linkages with different bond orders in π -delocalised compounds. Organic bridges between metals can be made entirely or as a mixture of phenyl groups, alkene or alkyne groups. Polyethenyl and polyethynyl structures will have the lowest transition energies but tend to lack the stability of poly(phenylethylenes) and poly(phenylethynylenes).³² In figure 1.6, the two ferrocene terminated compounds have a similar conjugative length (4 π bonds) with greatly different γ values.^{33,34} Presumably a complex with two alkene bonds in the place of the

phenyl ring will likely have a higher nonlinearity still, as shown by the very large values for β -carotene and a synthetic carotenoid derivative with donor and acceptor functionality (**5** and **6**).³⁵ Ruthenium compounds have been made with both phenylethynylene and phenylethylenylene bridge types and the ethenyl examples have larger γ values.^{36,37} In Table 1.1 complex **8** with the vinylidene/alkenyl linked phenyl groups has a γ value that is 20 times larger than the metal alkynyl analogue **7**, however the extended π -system of **9** gives a larger value than **8**. For the dpmm containing analogues the alkyne/alkynyl **10** < alkyne/vinylidene **11** < alkene/alkynyl **12**.

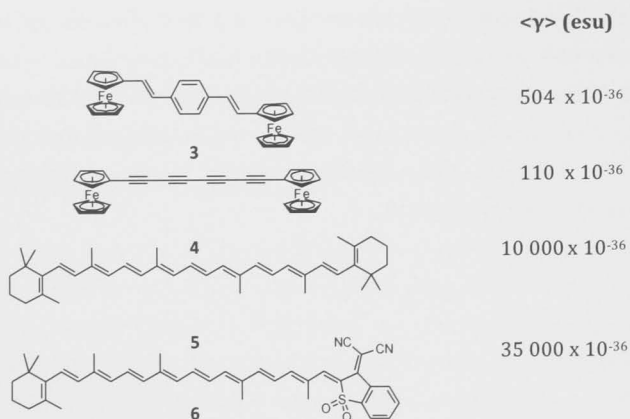


Figure 1.6 - Effect of C hybridisation on the third-order polarisability.

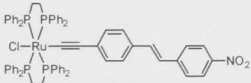
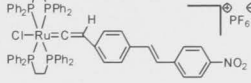
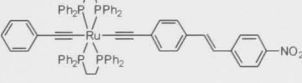
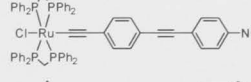
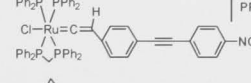
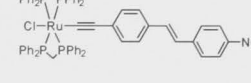
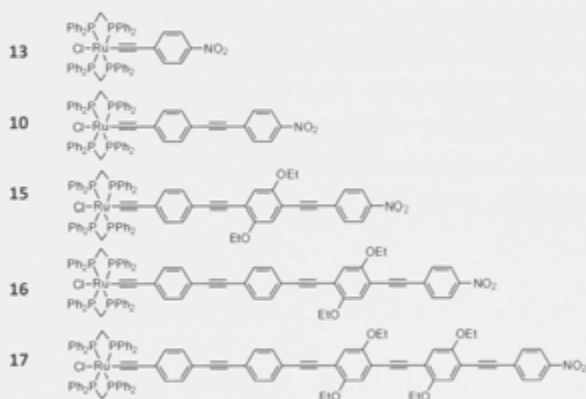
#	γ_{real} (10 ⁻³⁶ esu)	γ_{imag} (10 ⁻³⁶ esu)	$\langle \gamma \rangle$ (10 ⁻³⁶ esu)	Ref
	40 ± 200	< 100	40 ± 200	25
	650 ± 500	< 50	650 ± 500	25
	-830 ± 200	320 ± 100	900 ± 200	26
	-160 ± 80	160 ± 60	230 ± 100	25
	< 500	420 ± 60	420 ± 60	25
	200 ± 40	1000 ± 220	1100 ± 220	25

Table 1.1 - Comparison of γ values for ruthenium complexes with varying unsaturation in the π -bridge.

In addition to C hybridisation alteration, organic bridge length modification can also be used to increase the third-order NLO properties of organometallic compounds. Alkynyl ruthenium complexes with different bridge lengths have been synthesised and assessed by the Humphrey group.²³ The two-photon absorption behavior increases as the bridge length increases from 1 to 3 phenyleneethynylene units but decreases with further lengthening. The reason for this may be twofold; either bridge rotation breaks the conjugation upon lengthening, or the distance between the metal and the nitro group becomes so great that the donor-acceptor interaction reduces to no longer give benefit. This is also observed in the UV-visible spectrum, where there is a progressive increase in energy of the MLCT absorption band upon chain lengthening as the nitro is progressively further away from the metal.

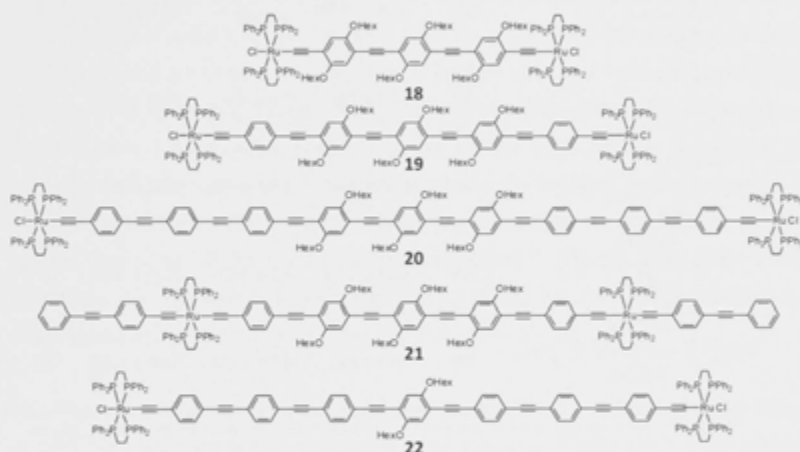


Compound #	λ_{max} (nm)	$\sigma_{2\text{PAmax}}$ (nm)	σ_2 (GM)
13	473	940	135 ± 13
10	464	890	567 ± 56
15	459	890	1160 ± 116
16	411	840	780 ± 78
17	423	840	850 ± 85

Table 1.2 - Data showing the effect of *n*-bridge lengthening on λ_{max} and 2PA cross section.²³

The effect of π -bridge length increases has been assessed further in diruthenium complexes with up to a nonaphenyleneethynylene bridge between two $\text{Ru}(\text{dppe})_2$ centres.³⁸ Hexyloxy groups were used to maintain the solubility of the molecule for characterisation of the third-order NLO properties; while simple to incorporate synthetically, these groups have some electronic influence as seen in the UV-Visible properties. There is a blue shift in λ_{max} values on increasing the distance that the hexyloxy groups are from the metal centres. On proceeding from **18-20**, the γ and σ_2 values increase slightly with chain lengthening. For such a large structural change (3-5-9 phenyleneethynylene units) the increases in TPA and γ values are low. The marginal impact of this structural change is thought to be caused by conjugation breaking due to out-of-plane phenyl rotation, which becomes more marked as π -bridge length is increased. Interestingly the bis-alkynyl complex (**21**) which still has a total of 9 phenyleneethynylene units has the largest TPA cross-section. Complex **22** has a larger TPA cross-section than the nona(phenyleneethynylene)-linked mono-alkynyl complex, **20**. It also has just a single solubilising phenylene unit and possibly reduced phenyl rotation in the chain. This is probably the source of the larger NLO properties than the analogues with three hexyl linkers which are in sequence, suggestive of some sterically induced rotation and consequential reduction of the effective π -delocalised chain. Studies are continuing into an appropriate solubilising bridge with some enforced planarity to investigate this possibility.

Complex	λ_{\max} (nm)	$\lambda_{\text{TPA,max}}$ (nm)	γ_{real} (10^{-36} esu)	γ_{imag} (10^{-36} esu)	$\langle\gamma\rangle$ (10^{-36} esu)	σ_2 (GM)*
18	450	880	-7 000	2 700	7 000	530
19	438	880	-9 800	3 000	10 200	580
20	425	880	-12 000	3 000	12 300	630
21	429	880	-9 400	5 200	10 700	1050
22	411	880	-	3 700	-	730

* errors are within $\pm 10\%$ Table 1.3 - Optical data for compounds with 3-9 phenyleneethynylene linkers between metals.³⁸

The nitro functional group influences the transition energy as well as the nonlinear properties of the compounds **13-17**. Functional group modification is a quick way to 'tune' molecules to have a particular optical behavior (linear or otherwise).^{36,37,39,40} Changing the low-energy maxima of molecules' linear absorption spectra also has the effect of changing the two-photon absorption maxima. Accordingly, the synthesis of organic molecules with differing electron donor or acceptor pairs has been pursued vigorously. In organometallics, the trends mimic those observed with organic compounds, but the donor units are generally the metal atoms which have large polarisable electron density and correspondingly larger NLO effects.

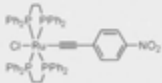
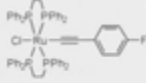
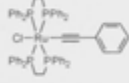
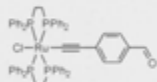
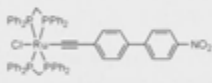
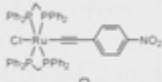
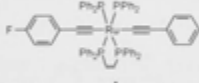
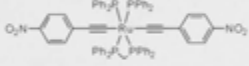
#	γ_{real} (10^{-36} esu)	γ_{imag} (10^{-36} esu)	$\langle \gamma \rangle$ (10^{-36} esu)	Ref.	
	23	320 ± 55	< 50	320 ± 55	40
	24	120 ± 200	66 ± 20	140 ± 200	37
	25	-170 ± 40	71 ± 20	200 ± 50	40
	26	-300 ± 500	< 210	300 ± 500	40
	27	140 ± 30	64 ± 10	153 ± 30	40
	13	170 ± 34	230 ± 46	290 ± 57	40
	29	350 ± 100	45 ± 20	350 ± 100	37
	30	300 ± 60	490 ± 98	534 ± 110	39

Table 1.4 - Nonlinear properties of complexes furnished with differing electron withdrawing groups.

γ values increase with the increasing electron withdrawing nature of the alkynyl ligand, from non-substituted (**25**) to fluoro- (**24**) substituted up to formyl- (**26**) and then nitro-substituted (**23**). Isolation of the metal centre from the withdrawing group (e.g. in the nitrobiphenyl example (**27**)) returns the γ value to non-substituted levels. Bis-alkynyl complexes have larger nonlinearity, especially when using an EWG as in **30** as electron density moves through the metal with ease.

1.5.2 Changing metal and ligand set

Alteration of the organic bridge for NLO tuning results in changing energy levels in the UV-Visible spectrum. For organometallics another electronic tuning is available: the metal centre itself. Many ruthenium alkynyl (indeed most organometallic) complexes have the metal to ligand charge transfer as the lowest energy transition. We've seen that changing the bridge can tune NLO properties but it is the same for the metal and it can be achieved through two methods. The metal itself can be changed with great effect as the larger the metal, the more dispersed the electron density and therefore the more polarisable the metal centre. Series of complexes have been synthesised incorporating metals from the same group to study this effect.^{36,40-42} A clear trend is evident in the second-order NLO properties (β) of metal alkynyl complexes ($\text{Fe} < \text{Ru} < \text{Os}$), but the trend is not so clear for third-order NLO properties, possibly due to limited data sets hindering a widespread assessment of the result of metal change, as well as minor discrepancies between laser setups (Table 1.5). Another problem is the limited measurement wavelength. NLO properties are strongly wavelength dependent and the maximal γ values may be at a different wavelength. The complexes shown are the best set for comparison, as they all possess the same alkynyl ligand (nitrophenylalkynyl) although they have different phosphine auxiliary ligands (which itself has an effect). For the cyclopentadienyl metal alkynyl complexes the γ values increase from $\text{Au} < \text{Ru} < \text{Ni} < \text{Fe}$.

The third-order properties of group 4 metal complexes have been investigated by Myers *et al.* showing a decrease of γ in proceeding down the group (Table 1.6).³¹ They concluded that the decrease is due to reduced metal d to alkynyl π -orbital mixing, as evidenced by the blue shifting of the λ_{max} values upon metal alternation. This is a surprising result as the larger metals should have better orbital overlap.

	#	γ_{real}	γ_{imag}	$\langle \gamma \rangle$	λ^*	Ref.
	31	-270 ± 100	70 ± 50	278 ± 110	800	41
	32	-230 ± 70	74 ± 30	240 ± 75	800	41
	33	-210 ± 50	< 10	210 ± 50	800	41
	34	120 ± 40	20 ± 15	121 ± 42	800	41
	35	-410 ± 200	580 ± 200	710 ± 280	800	42
	36	170 ± 34	230 ± 46	290 ± 60	800	38
	23	$-1\ 100 \pm 200$	800 ± 100	1360 ± 220	940	25**
	23	320 ± 55	< 50	320 ± 55	800	38

Compounds measured in THF * measurement wavelength **run in CH₂Cl₂

Table 1.5 - Cubic nonlinear optical properties of selected metal alkynyl complexes.

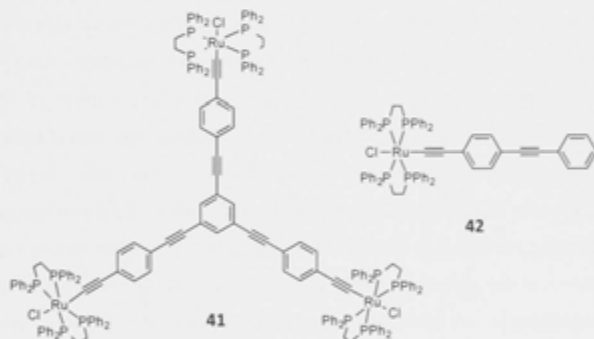
	γ (10^{-36} esu)*	λ_{max} (nm)	Ref.
38	92	416	31
39	58	370	31
40	51	358	31

- THG technique. Measured at 1907 nm tripled to 636 nm * Errors are \pm 15 %

Table 1.6 - Cubic nonlinear optical properties of selected metal alkynyl complexes.

The auxiliary ligands on organometallic complexes can be changed to modify NLO behavior. Similar to the functional group modification seen previously, an electron withdrawing ligand will increase the energy of the crucial MLCT transition, resulting in a blue shift of λ_{max} and $\sigma_{2\text{max}}$. In Table 1.5 compounds **32**, **33**, **36** and **23** all have a different ligand set, but the same metal and alkynyl ligand. γ values increase with increasing donor nature of the ligand: **32** has the more donating PMe_3 to **33**'s PPh_3 while removing the Cp group entirely to give a bis-dppe/dppm ligand set increases values further, **23**'s favorable bite angle presumably allowing better electron donation than the dpmm.

Using organometallics allows for modification of oxidation state of the metal and profound transformation of the optical properties of the material, a useful property for use in logic devices. Redox properties exist in organic materials also, but tend to be irreversible due to the reactivity of the oxidised/reduced state. Organometallic redox processes tend to be reversible with comparatively stable oxidised states, which frequently allows for multiple oxidation/reduction events per sample.⁴³



	γ_{real} (10^{-36} esu)	γ_{imag} (10^{-36} esu)	$\langle \gamma \rangle$ (10^{-36} esu)	σ_2^* (GM)
41	-330 ± 100	2200 ± 500	$2\,220 \pm 600$	530 ± 120
41³⁺	$13\,500 \pm 3\,000$	$-4\,700 \pm 500$	$14\,000 \pm 3\,000$	$-1\,200 \pm 100$
42	-100 ± 100	450 ± 200	460 ± 200	110 ± 50
42⁺	$2\,900 \pm 1\,000$	$-1\,200 \pm 600$	$3\,100 \pm 1\,000$	-300 ± 70

*Measurement wavelength - 800 nm

Table 1.7 - Nonlinear optical properties of metal alkynyl complexes **41** and **42** and their tri- and mono- cations **41³⁺** and **42⁺**.⁴³

As shown in table 1.7 the two compounds exhibit large changes in the $\langle\gamma\rangle$ and TPA properties upon oxidation to the Ru^{III} complex. The TPA process can therefore be controlled by redox stimulus, as the complexes become saturable absorbers upon oxidation, allowing more light through the sample with intensity increase. Oxidation creates an absorption band at ~ 800 nm in these alkynyl ruthenium complexes, coupled with a diminishing of the MLCT band. The new band has been computationally shown to have strong LMCT character. This new band is at the same energy as the Z-scan measurement, which saturates the absorptive elements in the sample causing increased transmission through the sample. Utilising multiple metal centres with different redox properties potentially permits access to many more states in the same molecule. This feature is under continuing examination with the synthesis in the Humphrey group of a compound comprising of iron and ruthenium (group 8) metals which allows 3 different accessible redox states.⁴⁴

1.5.3 The dendritic effect

Another recent structural modification of organometallics to be explored is hyper-branching in dendrimers. It is difficult to incorporate certain metals and metal-ligand sets into organic dendrimers without terminating the structure; ruthenium alkynyl complexes are easiest to incorporate as they are quite easily made unsymmetrical following the correct methodology (isolation of the vinylidene intermediate, removal of excess acetylene and then subsequent deprotonation).^{26,45} Dendrimers have been shown to possess significant third-order NLO properties, greater than the sum of the linear components, and even outperforming the building blocks when scaling for π -electron number or molecular weight. The cause of the enhancement is obscure, but is linked to dendrimer generation (number of branching points from the core). A summary of third-order polarisability data and TPA cross-section values is given in Table 1.8; there is more than a tenfold increase in σ_2 values in proceeding from G₀ to G₁ and to G₂.

#		χ_{real} (10 ⁻³⁶ esu)	χ_{imag} (10 ⁻³⁶ esu)	$\langle\gamma\rangle$ (10 ⁻³⁶ esu)	σ_2 (GM)	Ref
43	G ₀	-600 ± 200	2 900 ± 500	3 000 ± 600	700 ± 120	26
44	G ₁	-5050 ± 500	20 100 ± 2000	20 700 ± 2000	4 800 ± 500	26
45	G ₁	-29 000 ± 5 000	41 000 ± 10 000	50 000 ± 11000	11 800 ± 1 000	44
46	G ₂	-160 000 ± 30 000	120 000 ± 20 000	200 000 ± 36 000	29 000 ± 6000	44

Measurement wavelength - 800 nm in CH₂Cl₂ solutions

Table 1.8 - Nonlinear optical properties of ruthenium alkynyl dendrimer complexes 43 - 46.

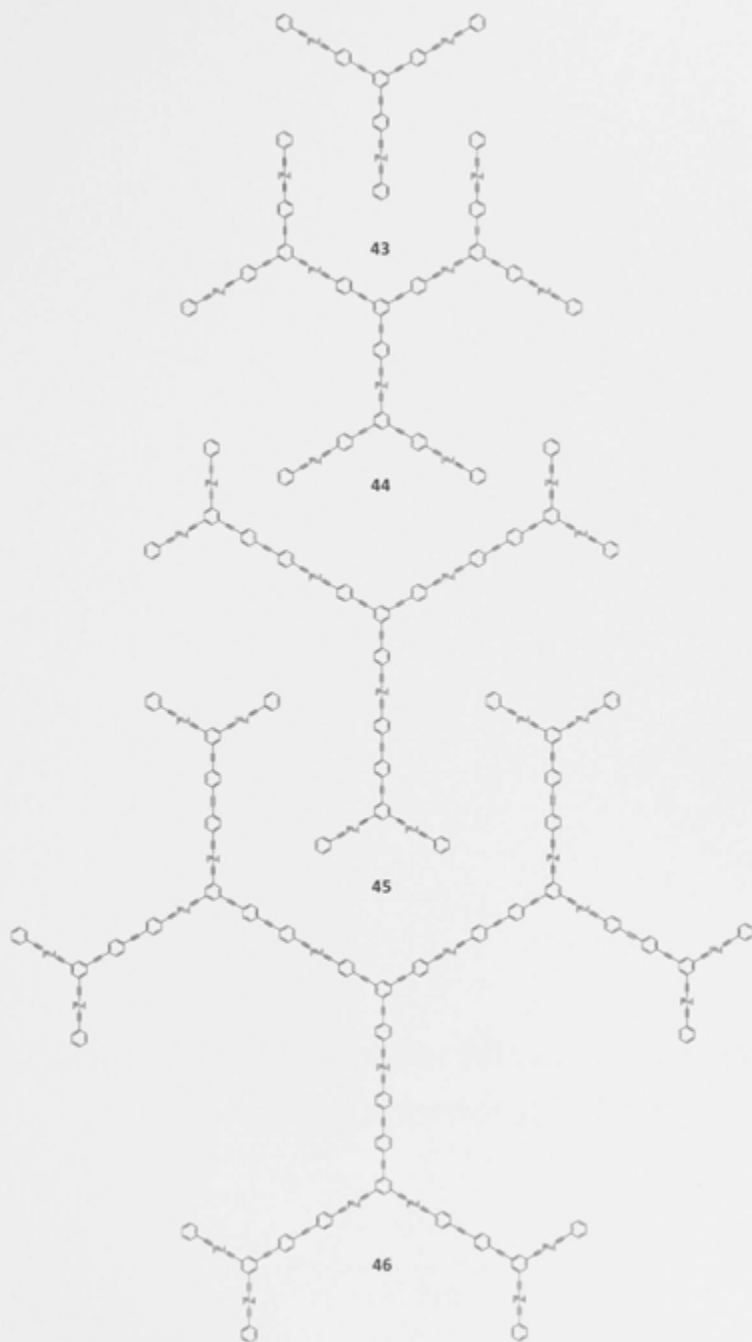


Figure 1.7 - Molecular structures of dendrimers 43-46.

Chapter 2 - Third-order NLO Properties of Organometallic Complexes

2.1 Introduction

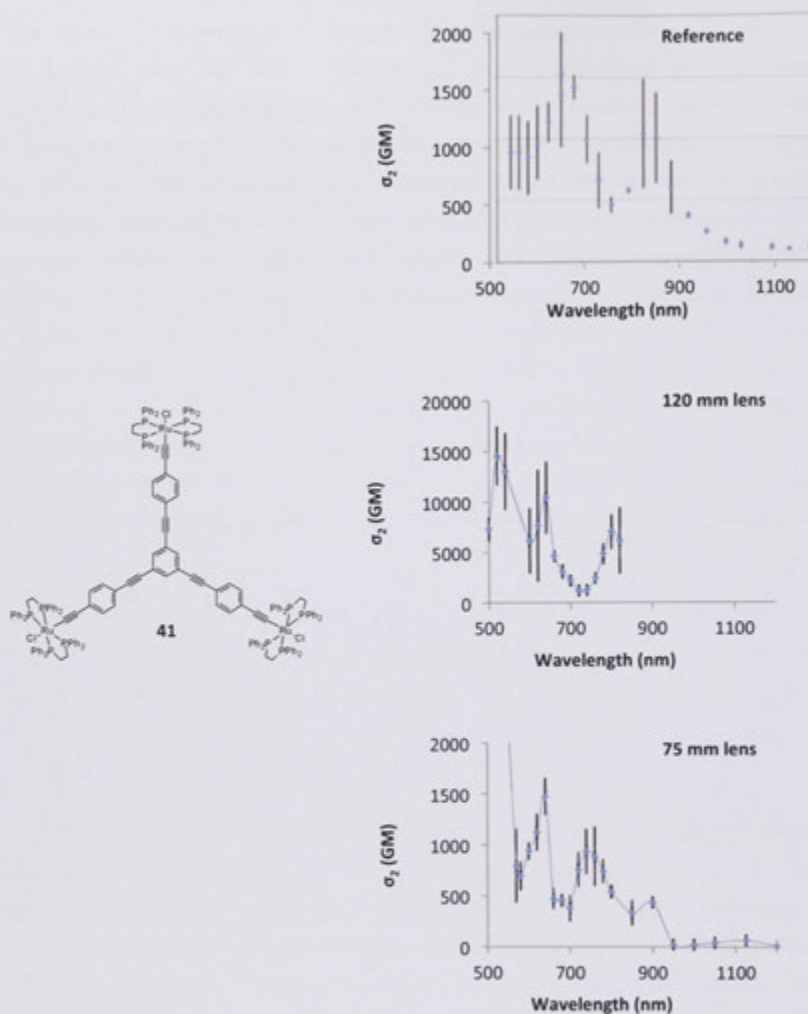
This Chapter details the third-order nonlinear optical property characterisation conducted on a number of materials prepared either by the Humphrey group or sent by other international material development groups. Parts 2.2.1 to 2.2.6 are spectral dependence Z-scan experiments, which assess the third-order merit of the compounds as the wavelength of the incident beam changes. Part 2.2.7 is a switching Z-scan experiment where the materials properties are changed by the application of acid and Z-scan experiments conducted on the starting and resulting material. In Part 2.2.8 the Z-scan experiment is used to survey the optical limiting merit of materials under high laser light inputs. Some graphs of interest from the Z-scan experiments are plotted in this discussion. This is focused on the absorptive component of the experiment and the two-photon absorption cross-section. Supplementary plots of NLO data can be found in the appendix.

2.2 Z-scan Measurements

2.2.1 Standardisation

Most ruthenium alkynyl complexes previously studied by the Z-scan technique have been examined either at the Research School of Physics and Engineering (RSPE) or in The Institute of Physical and Theoretical Chemistry at Wroclaw University of Technology, Poland. The laser set-ups used for characterisation have changed little over the years which means comparison of values of γ and TPA is more accurate as deviations due to subtle set-up differences are minimised. Care should be taken upon comparing results emanating from different laser systems as sources of inaccuracies can be as small as the environmental stability in the laser housing (temperature or particulate), distance between components such as detectors or aperture width. The recent setup of a femtosecond laser system at the Research School of Chemistry facilitated access to Z-scan measurements but the consistency of results needed to be assessed. A spectral dependence Z-scan measurement was conducted on a compound (**41**) previously characterised at RSPE and the respective magnitudes and absorption ranges compared to assess the discrepancies between the systems.⁴⁶ The two laser set-ups were kept as consistent as possible in experimental set-up and a similar power input was maintained

through the sample. However, due to a temporary limit in the wavelength generation capacity of our OPA the measurement was limited to a wavelength range that could be confirmed by spectrophotometric means (500 - 800 nm); this affected many measurements discussed in this Chapter. Two measurements were conducted with differing focal lengths of the lens leading into the experiment (75 mm and 120 mm). This was observed to result in a large change in the values obtained for similar samples at the same input power, as the dispersion of the beam at the closed aperture is much greater with the tighter focused beam. The results are shown in Figure 2.1 and Table 2.1. Traces of both the γ_{imag} and γ_{real} can be found in the Appendix.



Reference ⁴⁵		75 mm lens		120 mm lens	
λ	σ_2	λ	σ_2	λ	σ_2
				520	14 500 \pm 3000
650	1 500 \pm 400	640	1 470 \pm 200	640	10 000 \pm 4000
845	1 050 \pm 400	760	880 \pm 200	800	6 100 \pm 3000

Figure 2.1 - Spectral dependence Z-scan plots run on three different set-ups. At the Research School of Physics and Engineering (top)⁴⁶, RSC at 120 mm focal length (middle) and RSC at 75 mm focal length (bottom). σ_2 values compared at peak wavelengths. A trend line has been added to the σ_2 data as a visual aid.

The 2PA maxima at a wavelength of 640 nm are in very good agreement whereas it is difficult to compare the data at the 800-850 nm peak due to the large errors associated with the reference plot. The magnitude of the peaks for the 75 mm measurement are closer to the reference than are the 120 mm data, which are around 7 times larger. This might suggest the use of a correction or a scaling factor to allow comparison of the peak values between the RSP measured values or 75 mm focal length values (which are very similar) and the values obtained on the 120 mm set up.

λ	Property	Reference ⁴⁵	120 mm	Ratio	75 mm	Ratio
570	$\gamma_{real}(10^{-36} \text{ esu})$	$-3\,000 \pm 1\,000$	$-151\,000 \pm 4\,000$	50	$-2\,300 \pm 200$	0.7
	$\gamma_{imag}(10^{-36} \text{ esu})$	$1\,800 \pm 500$	$14\,000 \pm 5\,000$	7.1	$1\,600 \pm 750$	0.8
	$\sigma_{2,max}(\text{GM})$	850 ± 400	$6\,100 \pm 2\,200$	7.1	800 ± 350	0.9
650	$\gamma_{real}(10^{-36} \text{ esu})$	$-1\,600 \pm 600$	$-180\,000 \pm 4\,000$	115	$-1\,100 \pm 200$	0.7
	$\gamma_{imag}(10^{-36} \text{ esu})$	$4\,100 \pm 1\,000$	$27\,000 \pm 8\,000$	6.5	$3\,900 \pm 184$	0.95
	$\sigma_{2,max}(\text{GM})$	$1\,500 \pm 400$	$10\,000 \pm 3\,000$	6.6	$1\,470 \pm 200$	0.98
845	$\gamma_{real}(10^{-36} \text{ esu})$	$-2\,000 \pm 1\,000$	$-21\,000 \pm 7\,000$	10.5	$-3\,300 \pm 1500$	1.6
	$\gamma_{imag}(10^{-36} \text{ esu})$	$4\,700 \pm 2\,000$	$35\,000 \pm 7\,000$	7.4	$1\,500 \pm 500$	0.3
	$\sigma_{2,max}(\text{GM})$	$1\,050 \pm 400$	$6100 \pm 3\,000$	7.1	350 ± 120	0.3

Table 2.1 - Comparison of γ values and σ_2 values at selected wavelengths and deviation from the reference.

The maximal γ values from the reference have been tabulated and the values of the new measurements at corresponding wavelengths added for comparison. The difference between them has been displayed in the form of a ratio. There is a consistently larger γ_{real} value from the 120 mm measurements that may be due to a larger transmission of light through the experiment leading to large values of S (equation 16). There doesn't appear to be any regularity in the difference of the γ_{real} values, whereas the γ_{imag} ratio is a very regular 7 times the reference value. The values of the 75 mm focal length data are more consistent, with values for all γ_{real} and γ_{imag} data at or near equivalent data to the reference, with the exception of the 850 nm data. There is more than a 40 % error margin on these values in the reference, but the similarity in the 570 and 650 nm data is promising. For accurate scaling it would be advisable to run a standard compound with every 'batch' of compounds run for spectral dependence studies, as power levels at certain wavelengths can vary between runs despite the best efforts to use a constant input power. This is the

policy for current measurements, however the measurements in this chapter were all run on the 120 mm focal length set-up.

2.2.2 Isocyanurate cored octupolar complexes

As discussed in part 1.5.1, functional group modification can be used to tune linear optical and nonlinear optical properties of organometallic compounds. Addition of donor-acceptor pairs into a complex can favorably alter their properties. In octupolar compounds and (1,3,5)-substituted benzene compounds the effect of addition of electron-withdrawing groups has not been broadly explored and has usually been done by capping with a strong acceptor such as a nitro-functionalised phenylethynyl ligand. A novel approach is the addition of electron withdrawing groups to the core in a (1,3,5)-arrangement. This idea has been explored with many different electron-withdrawing functional groups such as cyanines and the isocyanurate trimers.

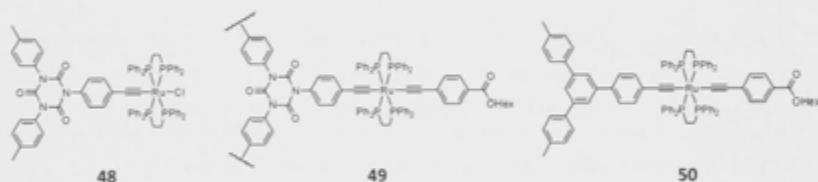


Figure 2.2 - Isocyanurate and triphenylbenzene cored complexes measured by Z-scan.

Organometallic and organic compounds containing the isocyanurate moiety have been synthesised and the second-order NLO properties measured by the HRS technique, but only organic analogues have been studied for their third-order NLO properties.^{47,48} The compounds were synthesised by Romain Veillard (**48**, **49** and **50**) and their two-photon absorption properties assessed by spectral dependence Z-scan, the results being summarised in Table 2.2 and a plot of the wavelength trace being shown in Figure 2.2. The TPA cross-sections were measured in the range 500 to 1000 nm and are displayed at twice the frequency to compare with the corresponding linear absorptions. The compounds are structurally similar, with slight differences in order to develop structure-property relationships. **48** is a mono-ruthenium complex with two tolyl- groups on the isocyanurate moiety, **49** is a triruthenium analogue of **48** and **50** is a mono-ruthenium complex with methyl groups at the other positions on the 1,3,5-triphenylbenzene core. **49** and **50** are

also bis-alkynyl complexes containing peripheral 4-hexylester- functionalised phenylethynyl ligands and, the ester helping to increase the solubility of the complex.

	λ_{\max} (nm)	$\lambda_{\text{TPA max}}$ (nm)	χ_{imag} (10^{-36} esu)	χ_{real} (10^{-36} esu)	σ_2 (GM)
48	342	680	1 110	-5 900	373 ± 70
49	379	720	9 330	-81 200	2794 ± 800
50	387	600	4 790	-3 540	2066 ± 890
23	477	800	<50	320	135 ± 30
41	413	640	2200	-330	530 ± 120

Table 2.2 - Third-order NLO maxima for compounds 48-50.

The 2PA maximises at twice the λ_{\max} for **48** but the correspondence is not so good for the other two complexes, where a peak at 760 nm is expected. The maximum presumably corresponds to the Ru- \rightarrow NCO charge-transfer transition (the band at 350 nm for the isocyanate compounds) in **48** and **49**. A charge transition between the metal centre and the ester solubilising group may be the origin of the principal linear absorption at 380 nm in the spectra of compounds **49** and **50**; these do not seem to correspond to any 2PA peaks in the σ_2 traces.

The 2PA data for similar compounds previously measured is provided for comparison. The 2PA cross-section for **49** is larger than other trimetallated alkynyl ruthenium compounds, such as **41**, consistent with the smaller π -delocalised system of that compound. **23** is of similar size to **48**; the nitrophenylethynyl containing **23** has the smaller TPA cross-section maximum, despite its functional group (NO_2) having a larger EWG capacity. **48** also has tolyl donor groups, with a greater π -delocalised system which may be the cause of the larger value. **50** has a sizeable σ_2 value, similar to the tri-metallated complex **49**. The 1,3,5-(triphenyl)phenyl core is effectively isolated from efficient conjugation to the metal centre due to phenyl-phenyl ortho-H repulsion (as seen in the 4-nitro-biphenylethynyl ruthenium complex (**27**, Section 1.5.1, Table 1.4)) and should have a lower TPA. The λ_{\max} of this compound is the lowest of the three, which suggests a stronger donor-acceptor interaction than with **49** in which the ester also acts as an acceptor, perhaps the cause of the reduction in TPA cross section. A more electronically innocent solubilising group would be better for these compounds. The trimetallated organometallics appear to have 2PA values three times those of the corresponding organic compounds measured by Argouarch *et al.* for however, their data were measured by two-photon excited fluorescence, making for an unfair/inaccurate comparison.⁴⁷

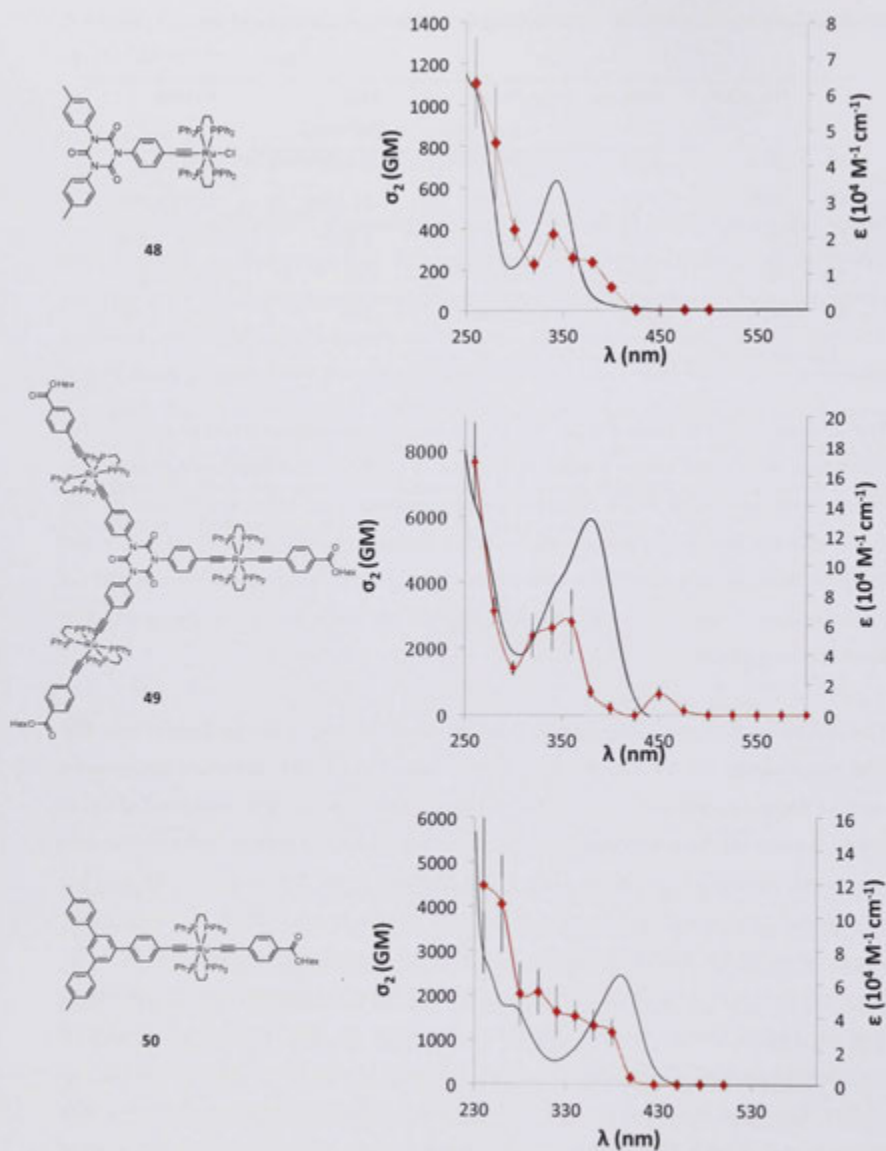


Figure 2.3 - TPA cross sections for 48, 49 and 50 plotted as $(1/2)\lambda_{TPA}$ and λ_{TPA} . A trend line has been added to σ_2 data as a visual aid.

Isocyanurate containing complexes have already been shown to have promising second order NLO properties and have been shown in these studies to possess good third-order NLO responses in comparison to comparably sized organic molecules. Properties observed in these small molecules suggest that extension to larger dendritic compounds should afford complexes with significant NLO properties.

2.2.3 Fluorene containing complexes

The fluorene functional group has been used in the design of many two-photon absorbing materials and other dyes.⁵⁰⁻⁵² These molecules have large molar extinction coefficients as well as considerable fluorescent properties which is the basis of such utilisation. These effects arise from the conformationally locked biphenyl and the highly strained 5-membered ring. Metal alkynyl complexes featuring fluorene groups have been made by Floriane Malvoti, and their 2PA properties assessed in the present work.

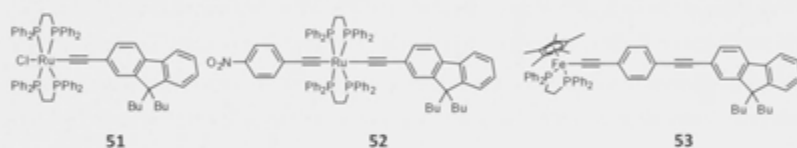


Figure 2.4 -Complexes with fluorenyl containing ethynyl ligands.

The three compounds comprise two alkynyl-ruthenium complexes, one of which is a bis-alkynyl complex with a nitrophenylalkynyl electron-withdrawing ligand, and another an alkynyl-iron complex with an extended π -bridge (Figure 2.4). Optical data are summarised in Table 2.3 and the 2PA cross section at half the wavelength is displayed in Figure 2.5.

Compound	λ_{\max} (nm)	σ_2^{\max} (nm)	Υ_{imag} (10^{-36} esu)	σ_2^{\max} (GM)
51	373	800	3750	908 ± 140
52	489	760	2810	756 ± 160
53	448	760	2890	969 ± 360

Table 2.3 - Optical and NLO data for fluorene complexes.

The plots for **51** and **52** closely follow the linear absorption traces for the respective compounds. **52** has a nitrophenylethynyl moiety which results in a broad MLCT transition at 489 nm, limiting the range of wavelength dependence scans to 600 nm and longer wavelengths.

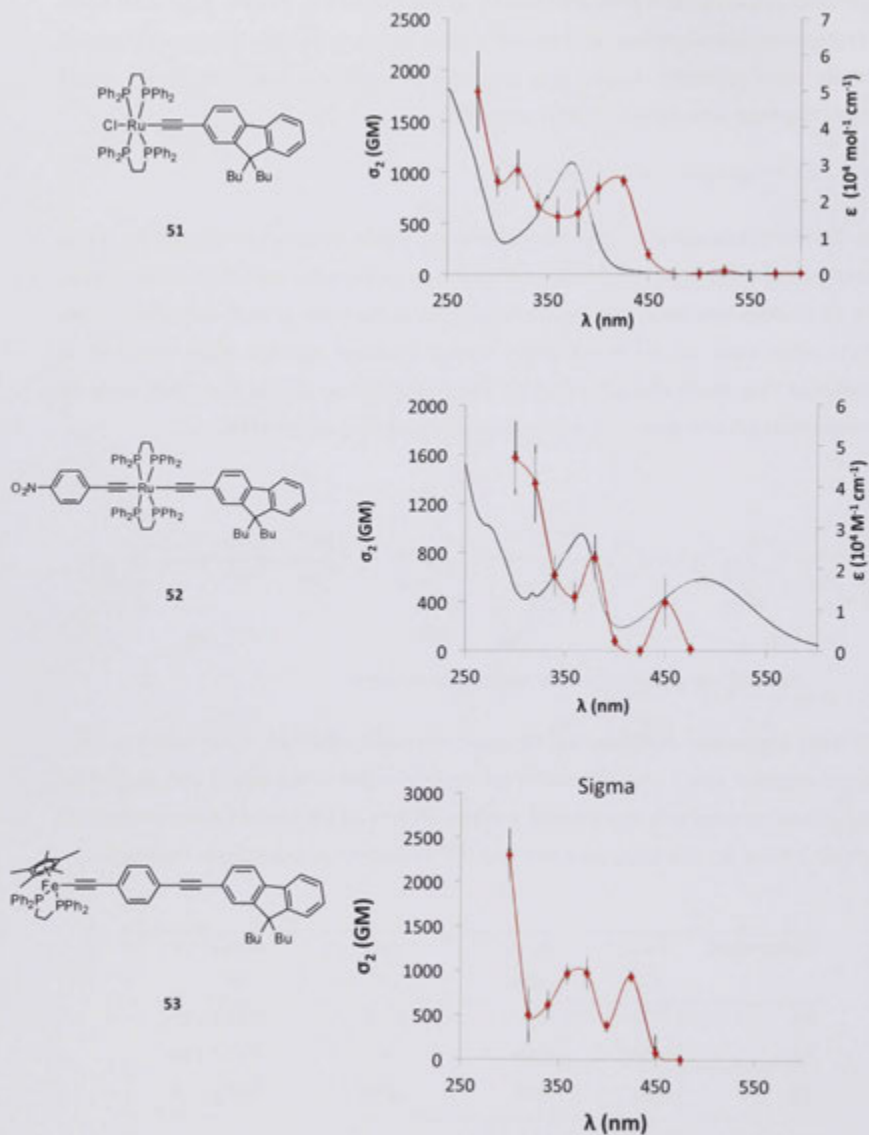


Figure 2.5 - Optical data for fluorene complexes. σ_2 traces are plotted at half the measurement wavelengths and a trend line has been added as a visual aid. The linear spectrum of 53 was not supplied.

The maximal 2PA value of **52** is at 760 nm, corresponding to a linear transition at 380 nm. **51** has a low energy transition at 373 and has a 2PA peak at between 800 and 900, roughly twice the principle absorption. The magnitude of the 2PA cross-section at this peak is less than **51** and is at a shorter wavelength, which suggests addition of the nitro group is unfavorable. **53** has a $2PA_{max}$ at 760 nm which is at a higher energy than the $2PA_{max}$ wavelengths for the other two complexes, with a comparable 2PA magnitude even with the larger π -delocalised system. This is most likely due to the change in metal resulting in diminished orbital overlap with the alkynyl ligand. This is also shown in the UV-Visible spectrum, where the MLCT band is blue-shifted compared to the MLCT of the ruthenium complex.

2.2.4 Dendrimers

Many ruthenium alkynyl dendrimers have been synthesised and characterised by wavelength dependence Z-scan.^{46,53-56} They show very large 2PA cross-sections as well as large γ_{real} values. However it has been shown that in certain scaling methods for NLO property comparison these underperform compared to smaller organometallic molecules. NLO response per cost of synthesis is one such measure in which metalated dendrimers are not the most efficient NLO material. Bandar Babgi has synthesised a number of first generation dendrimers containing functional group modification on the periphery to gain some insight into the effect of unsymmetrical electronic tuning on the NLO response of dendrimers which have until now been symmetrical at each branching point. The structures of the molecules are shown in Figure 2.6.

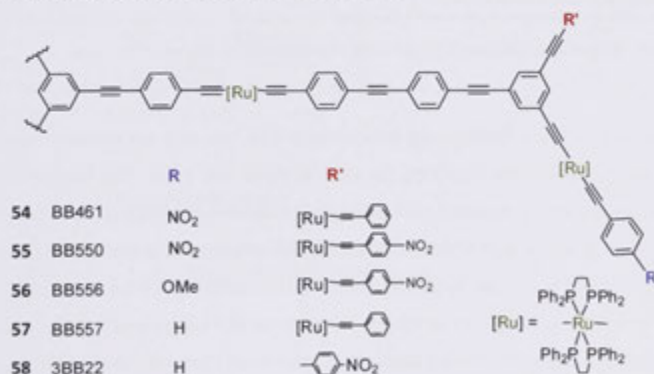


Figure 2.6 - Structure of the dendrimers measured.

Compounds **54**, **56** and **58** contain unsymmetrical branching points with either a nitro acceptor, an essentially neutral non-substituted phenyl, or a electron-donating methoxy group. For comparison **55** and **57** are symmetrical and substituted with the functional groups listed above. Z-scan measurements were conducted between 500 and 820 nm, the wavelength being restricted due to problems with the OPA. The results are presented in Table 2.4 and the σ_2 values are plotted in Figure 2.7.

Compound	λ	$\gamma_{\text{imag}} (10^{-36} \text{ esu})$	$\gamma_{\text{real}} (10^{-36} \text{ esu})$	$\sigma_2 \text{ (GM)}$
57	600	78 000 \pm 26 000	-572 000 \pm 120 000	61 400 \pm 26 000
	680	71 900 \pm 20 000	-470 000 \pm 67 000	24 100 \pm 6 800
	760	38 000 \pm 10 000	-16 8 000 \pm 28 000	10 000 \pm 3 000
55	620	493 000 \pm 175 000	-2 180 000 \pm 520 000	199 000 \pm 74 000
	680	187 000 \pm 65 000	-1 443 000 \pm 211 000	62 900 \pm 21 000
	780	104 000 \pm 25 100	-1 080 000 \pm 440 000	26 500 \pm 6000
54	600	53 000 \pm 14 000	-906 000 \pm 20 500	23 000 \pm 8900
	680	188 000 \pm 40 000	-1 002 000 \pm 140 000	63 100 \pm 13 000
	800	104 000 \pm 7 000	-826 000 \pm 75 000	25 900 \pm 7 100
56	600	341 000 \pm 70 000	-2 320 000 \pm 380 000	147 000 \pm 30 300
	680	178 000 \pm 55 000	-1 720 000 \pm 523 000	58 000 \pm 18 000
	760	140 000 \pm 54 000	-251 000 \pm 220 000	37 000 \pm 14 000
58	600	91 000 \pm 25 000	-770 000 \pm 180 000	39 000 \pm 11 000
	680	24 000 \pm 7 000	-140 000 \pm 41 000	8106 \pm 2600
	760	29 000 \pm 9 000	-129 000 \pm 39 000	7 900 \pm 2 600

120 mm focal length lens employed

Table 2.4 - Nonlinear optical data for dendrimer complexes **54-58** at selected wavelengths.

The γ_{real} values of all five dendrimers maximise at 620 nm, and are roughly an order of magnitude larger than those reported for similar sized and structured compounds. The errors are large at the γ_{real} maxima so meaningful comparison is difficult to carry out. The γ_{imag} values for the nitro- containing compounds are negative at wavelengths below 540 nm. In Figure 2.8 the γ_{imag} trace is plotted with the UV-Visible spectrum for compound **54**. The negative values occur at an absorptive region of the compound's linear spectrum. Saturable absorption occurs and the absorptive trace from channel 3 (see setup on pg. 13) is inverted, with an increase in transmission at the focal point. This is common in alkynyl-ruthenium compounds which contain nitro- groups, as the MLCT band is shifted to a much longer wavelength and into the Z-scan measurement window. This occurs for **55** and **54**

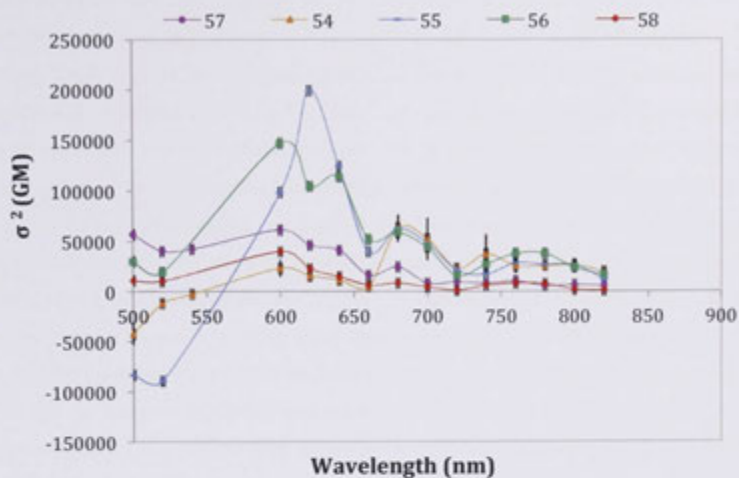


Figure 2.7 - σ_2 traces for compounds 54-58. A coloured trend line has been added as a visual aid only.

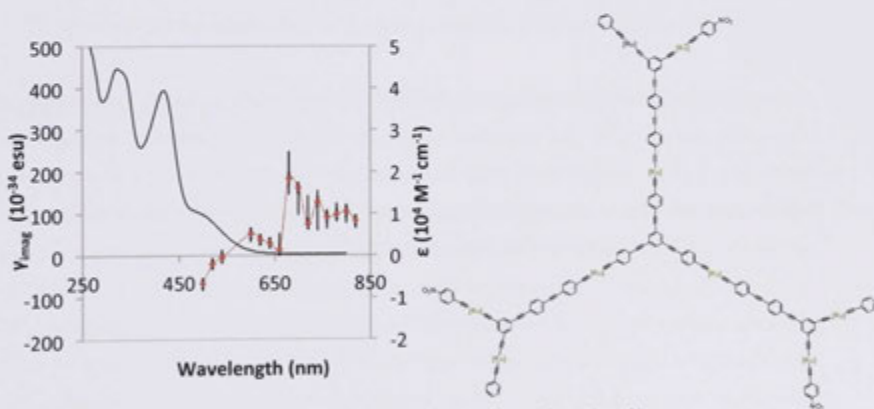


Figure 2.8 - V_{3mag} trace for compound 54 showing negative σ_3 values at the region of linear absorption overlap. A trend line has been added to the V_{3mag} trace as a visual aid.

where there is a nitrophenylethynyl ligand. The distance between metal and nitro- for **58** and the presence of an adjacent electron donor for **56** seems to eliminate this outcome. The 2PA cross-section values for all five dendrimers are compared in Figure 2.7. **56** has the largest σ_2 value which is at 600 nm, the same as all except **55** which maximises at 620 nm, probably due to the lower energy λ_{max} and the nitro- functionality. **54** has a comparatively low σ_2 value throughout the range 500-640 nm, but increases to a magnitude common to all five dendrimers at ca. 680 nm. There may be some dampening associated with the linear absorption through this region, although this isn't observed with **55** which has two distinct nitro- groups. Altering the donor and acceptor nature at the periphery of these dendrimers appears to tune the wavelength of the 2PA maximum, as shown by **55** with the more electron withdrawing cap giving the lower 2PA max. When one acceptor group is switched for an electron donor (the OMe on **56**), the band splits and a local maximum is created at 640 nm, but maintains the common peak at 600 nm possessed by the other complexes. The σ_2 values at 800 nm are not of comparable magnitude to the previously measured 1st generation dendrimer (**45**), despite the latter being structurally identical to **57**. The 600 nm comparison is more promising with the bis-NO₂ complex (**55**) having the highest TPA cross-section followed in magnitude by the unsymmetrical donor-acceptor complex (**56**). The values are near doubled at this wavelength compared to the value for **45**. **58** has the smallest TPA value as this compound has three less metal centres than the others, while **54** and **57** underperform as well.

Overall, the breaking of symmetry of the peripheral capping groups seems to diminish the TPA cross-section, with the exception of the donor-acceptor containing analogue **56**, which has a slight reduction at peak and a concomitant generation of a lower energy maximum. A bis-OMe analogue would be interesting to compare to this set, to confirm that symmetry in **55** is the source of the better TPA cross-section.

Compound	λ	σ_2 (GM)
57	800	$6490 \pm 1\ 300$
	600	$61\ 400 \pm 26\ 000$
55	800	$25\ 800 \pm 7\ 000$
	620	$199\ 000 \pm 74\ 000$
54	800	$25\ 890 \pm 7\ 000$
	600	$23\ 000 \pm 8\ 900$
56	800	$23\ 600 \pm 6\ 200$
	600	$147\ 000 \pm 30\ 300$
58	800	$1\ 800 \pm 600$
	600	$39\ 000 \pm 11\ 000$
45	800	$11\ 800 \pm 1\ 000$
	560*	$14\ 000 \pm 2\ 100$

* TPA local maximum

Table 2.5 - Scaled nonlinear optical data for dendrimer complexes.

2.2.5 Metal content of dendrimers

Organometallic NLO materials tend to have larger linear absorption and larger two-photon absorption cross-sections than organic based counterparts.¹⁹ This seems to be due to electron donation from the electron-rich metal into the organic π -delocalised system. To develop an understanding on the extent of the enhancement organic systems obtain in these compounds, Alistair Watson and later Peter Simpson synthesised compounds with increasing metal number in the phenylethynyl 'scaffold' of a first-generation dendrimer. Three compounds were measured through the range 540 - 1100 nm and the results are shown in Figure 2.10 and Table 2.6.

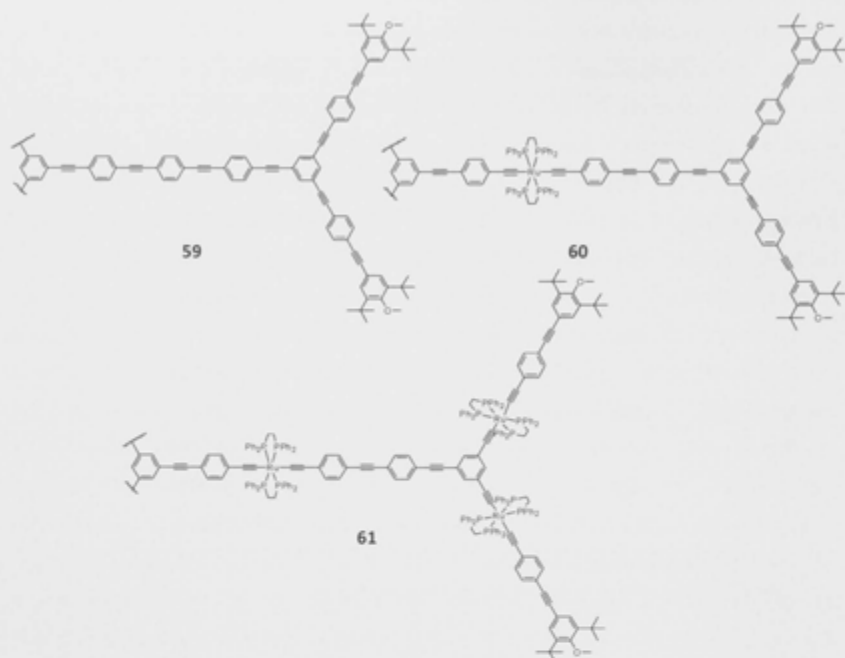


Figure 2.9 – The molecular structures of dendrimers 59-61 with varying metal content investigated in this section.

The three compounds have a 2PA maximum at 800 nm as well as another peak at 680 nm. The peaks are consistent with the linear absorption bands for **60**, but are slightly off-resonant for the other two. The band at 424 nm is most likely a MLCT band, whereas the 333 nm band is a mix of the $\pi-\pi^*$ in either the phenylethynyl ligand or the auxiliary dppe phenyl rings. **61** has a very broad $\pi-\pi^*$ absorption covering the MLCT, with the 2PA maximum likely corresponding to a linear absorption under this broad $\pi-\pi^*$ band. The all organic **59** has a 2PA band at a wavelength longer than expected when compared to the UV maximum; the 2PA band at 800 nm is anomalous as there isn't a corresponding linear band at ca. 400 nm.

	λ_{max}	λ_{σ_2max} (nm)	γ_{imag} (10^{-36} esu)	γ_{real} (10^{-36} esu)	σ_2 (GM)	σ_2/M (GM/amu)
59	365 (sh)	800	$14\,000 \pm 4000$	$-14\,000 \pm 4\,300$	3300 ± 970	0.98
	341	680	9560 ± 2000	$-111\,000 \pm 16\,000$	3210 ± 760	0.96
60	424	800	$26\,600 \pm 8500$	$-9\,150 \pm 1\,000$	6450 ± 2000	1.05
	333	680	$79\,500 \pm 12\,000$	$-179\,000 \pm 15\,000$	26700 ± 4300	4.37
61	423 (sh)	800	$136\,000 \pm 38\,000$	$-66\,100 \pm 17\,000$	$33\,000 \pm 9000$	2.83
	391	680	$218\,000 \pm 60\,000$	$-681\,000 \pm 160\,000$	$73000 \pm 22\,000$	6.29

120 mm focal length employed

Table 2.6 - Third-order NLO data at selected wavelengths for dendrimer complexes 59, 60 and 61.

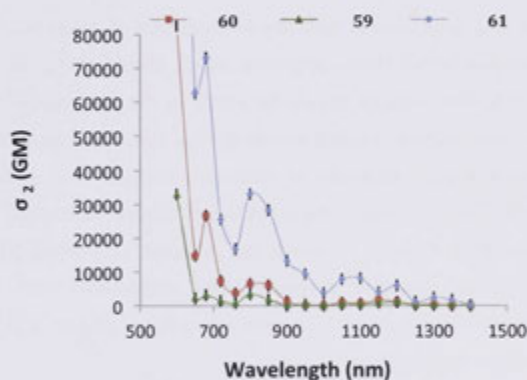
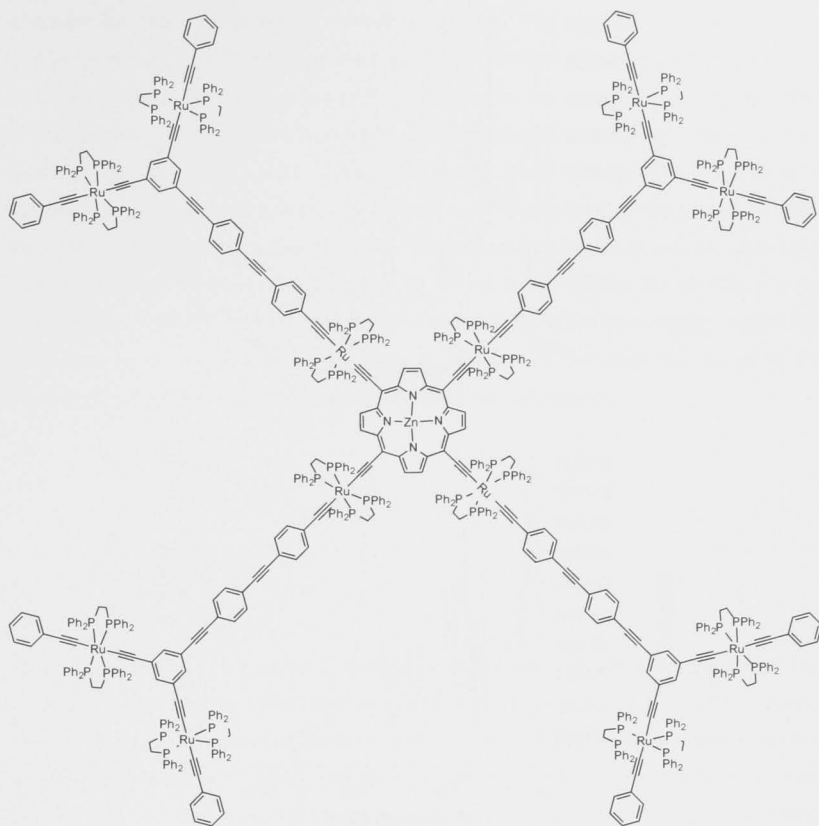


Figure 2.10 - σ_2 plot for dendrimer complexes 59, 60 and 61. A trend line has been added as a visual aid only.

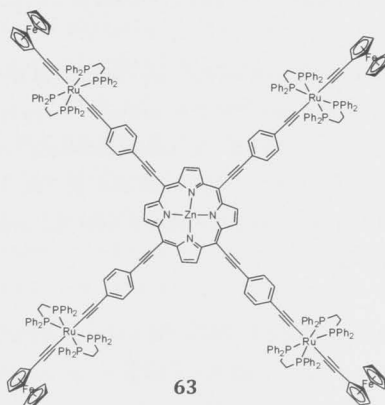
Comparison of the data reveals an increase of σ_2 with increasing metal number in the dendrimer. The nona-ruthenium complex has a 5-fold greater σ_2 value than the tri-ruthenium and a 10-fold greater σ_2 value than the organic analogue. When scaled by molecular weight the increase isn't as great, with **61** at 2.8 GM/amu, **60** at 1.05 and the organic **59** is 0.95 GM/amu. It is important to scale by weight in this set as the metals bring additional chromophores in the form of the auxillary ligands. The additional mass added to the molecule needs to be justified in terms of NLO output. There is a benefit to the NLO response above the linear contribution of making the molecule larger, ie a 4-fold increase in mass (**59** to **61**) gives a 10-fold increase in the σ_2 value.

2.2.6 Porphyrin Complexes

Porphyrins have long been used as dyes and have also found use as NLO materials. They are highly absorptive in the visible spectrum which should mean that the 2PA peaks corresponding to visible maxima should be firmly in the NIR region. This is of great interest as telecommunications exploit wavelengths in this region, and 2PA or 3PA in this window could lead to a development of molecular switches from such materials. The combination of the redox and large 2PA properties of alkynyl-ruthenium complexes with the large absorption coefficients of porphyrins promises interesting NLO effects. Areej Merhi has synthesised two zinc porphyrin-cored dendrimers with four peripheral ruthenium-ferrocene conjugates or tri-ruthenium wedges (Figure 2.11) and a limited range Z-scan study was therefore performed.



62



63

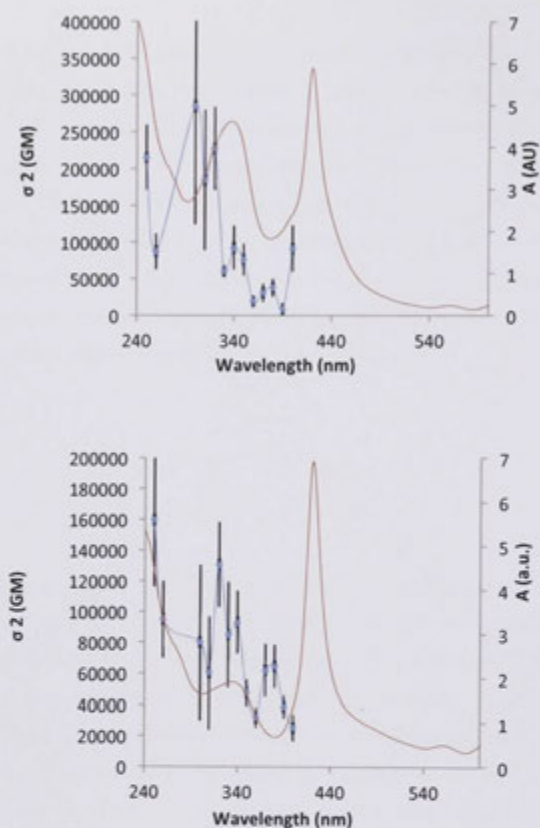


Figure 2.11- UV-Vis data (red) for compounds **62** (top) and **63** (bottom) overlaid with σ_2 data (blue) plotted at half the wavelength. A trend line has been added as a visual aid only.

Z-scan measurements were performed on the two compounds between 500 and 800 nm with some difficulty. In this range the measurement is competing with the linear absorption in these compounds, which can cause problems with accurate fitting. To accomplish this the concentration of the solutions of the samples were reduced significantly; usually a 0.2 % w/w concentration is used for large dendritic species but here a 0.007 % w/w was used.

Strong 2PA peaks are observed near to twice the linear absorption wavelength for both complexes. The maximal σ_2 value for **62** has a large error margin as it falls in the low-energy absorption region. This value could probably be discounted in favor of the 680 nm which aligns better with twice the wavelength of the corresponding linear absorption and has a smaller error margin. **63** has a blue-shifted 2PA maximum at

640 nm (130 000 GM); the smaller σ_2 value is expected due to a smaller π -conjugated structure and the less absorptive ferrocenyl moieties. The 2PA trace is suggestive of a further maximum beyond 800 nm in **62**, possibly a 2PA peak corresponding to the zinc-porphyrin subunit. Previous studies of porphyrin containing compounds reveal significant saturable absorption behaviour below 640 nm due to the strong linear absorption at these wavelengths. The fitting traces of the data shown above do show the beginnings of saturable absorption behaviour (gradual increase in transmission) at the periphery of the trace, however as the focal point of the laser is reached the two-photon absorption processes appear to dominate. This may be an effect intrinsic to the structure of the compounds reviewed or perhaps the result of the high dilution of the samples required for good data to be obtained. Further study is required to ascertain the cause of this discrepancy of behaviour between structurally similar compounds.

2.2.7 Protic Switching

63 has the potential for redox switching of states with different optical properties. Molecules which can be reversibly switched would have a greater utility in optical devices as multiple states can perform multiple roles. Many different types of optical property switching exist, which can be accessed by a multitude of stimuli.⁵⁷ Protic switching occurs using a proton source to bind to a target area on a compound to change the optical property. This has been used commonly in alkynyl ruthenium complexes, as the β carbon on the metal bound alkynyl ligand is susceptible to electrophilic addition. After proton addition there is a strong molar extinction coefficient change and the MLCT band of the complex (typically at 380-400 nm) diminishes. Such strong linear optical property changes are associated with changes in the 2PA properties, with a blue shift of σ_2 max associated with the removal of the MLCT band. Matthew Walkey of the Koutsantonis research group at UWA has synthesised a ruthenium alkynyl complex bearing a spiropyran moiety. Treatment of **64** with trifluoroacetic acid protonates both the alkynyl and the pyran units which forms **64a**, drastically altering the optical properties of the compound. It is even possible to selectively deprotonate the generated vinylidene complex to create **64b**, giving a three mode protic switch.

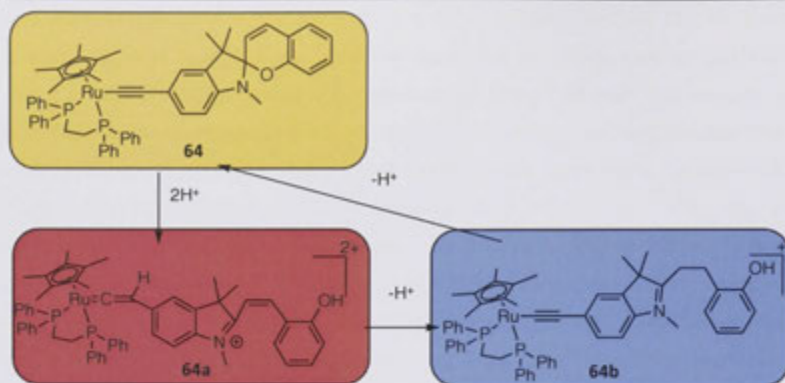


Figure 2.12- The three accessible forms of **64**. The box represents the colour of each complex. Compound **64b** was too thermally unstable for UV or Z-scan measurements

Each version of the complex has a different colour. The neutral species is yellow, the diprotic is red and the monoprotic is a deep blue. The compound **64b** is quite unstable at room temperature, but stable for a least an hour in a dry ice/acetone bath (*ca.* -78 °C). Unfortunately, optical investigation into this species was not possible with the facilities available. A low-temperature UV or Z-scan cell is required, as the phenol is quite nucleophilic and rapidly reverts to the starting material at room temperature. The mechanism is not known, but it appears that it generates a fourth, colourless compound (most likely **64** with a protonated amine group), which can then regenerate the yellow starting complex by the addition of base (triethylamine). Z-scan measurements were run on **64** and **64a** at two wavelengths (500 nm and 610 nm).

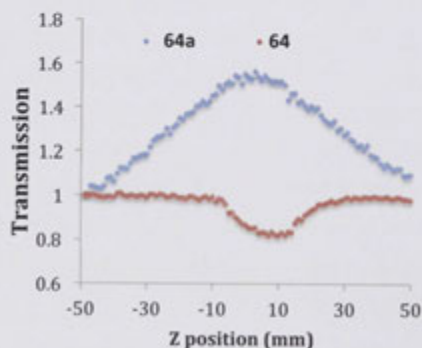


Figure 2.13 - Open aperture experiment traces for **64** (red) and **64a** (blue) at 500 nm

λ (nm)		64	64a
500	$\gamma_{\text{imag}} (10^{-36} \text{ esu})$	870 ± 60	-780 ± 70
	$\gamma_{\text{real}} (10^{-36} \text{ esu})$	$-3\,600 \pm 1\,500$	$-4\,300 \pm 300$
	σ_2 (GM)	540 ± 50	-485 ± 70
610	$\gamma_{\text{imag}} (10^{-36} \text{ esu})$	770 ± 100	23 ± 2
	$\gamma_{\text{real}} (10^{-36} \text{ esu})$	$-2\,700 \pm 250$	$-2\,400 \pm 230$
	σ_2 (GM)	323 ± 40	10 ± 3

Table 2.7 - Tabulated third-order NLO data of **64** and **64a** at 500 and 610 nm (bottom).

The neutral complex appears to have quite a large σ_2 value for such a small complex at both wavelengths, but as this measurement was carried out on a ns pulsed laser, some excited-state absorption is almost certainly present which will cause overestimation of the value. The protonated analogue has a nearby broad absorption band centered at 490 nm and a non-zero absorption at about 590 nm. The compound is a strong saturable absorber at wavelengths up to 600 nm; at 610 nm, it is a weak nonlinear absorber. This compound is promising as a protic switch but a method is required for analysis of **64b** in order to increase its potential as a molecular switch. It may be possible to generate this state *in situ* in a low temperature cell, a possibility currently being investigated.

2.2.8 Molybdenum and Niobium cluster complexes

2.2.8.1 Molybdenum cluster complexes

The optical limiting merit of metal clusters has been of great interest as the heavier elements favour intersystem crossing and tend to have more energy sub-levels than organic materials. Both of these properties create a multitude of energy absorption and dissipation mechanisms ideal for intensity dependent beam attenuation. The linear and nonlinear absorptive properties of trimolybdenum clusters has been studied previously by a collaboration of the Llusar and Humphrey groups.^{58,59}

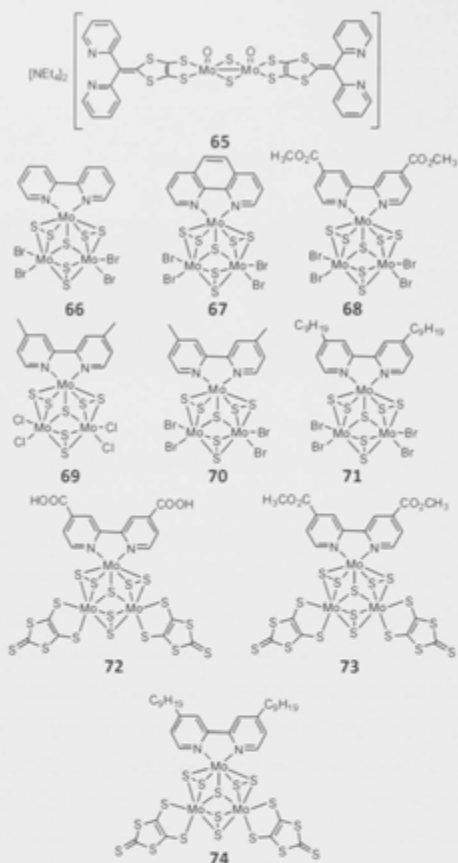


Figure 2.14 - Complexes 65 to 74 used in optical limiting measurements.

New clusters equipped with bipyridine (bpy) and 2-thioxo-1,3-dithiol-4,5,-dithiolato (dmit) ligands were synthesised in an effort to increase the suitability of these complexes for optical limiting by broadening the linear absorption range, with the intention of also increase their optical limiting capacity. The complexes have a similar metal cluster core structure with the exception of **65** which is a di-molybdenum complex with a modified dmit ligand containing two pyridine units instead of a thione. **66-71** have tetra-bromo substitution on the core cluster, except for **69** which has a tetra chloro composition. They all have a bipy ligand with varied functional groups at the 4/4' position on bipy; methyl, carboxyl, methyl carboxylate or a linear nonyl chain. **67** is the exception with a fused backbone with an alkene added to the 5/5' position. **72-74** are composed of the core

cluster with dmit ligands with either carboxyl, methyl carboxylate or a nonyl chain in the 4/4' position on the bipy.

The modification of the bipy has a small effect on the UV-Vis properties of the complex (displayed in Table 2.8). Most of the tetrabromo- and tetrachloro- (**66-71**) compounds have flat, broad transitions from 280 to 650 nm with λ_3 (being the lowest energy transition) at around 450-470 nm. Compound **68** substituted with carboxy groups possess the lowest λ_3 of this set of compounds at around 520 nm, the strongly withdrawing carboxyl presumably lowering the MLCT transition. The addition of the dmit ligand in **72-74** further decreases the energy and increases the molar absorptivity of λ_3 as the π -conjugation per molecule is increased.

The Z-scan experiment was conducted at 570 nm for all compounds as they all have a small absorption at this wavelength without significant linear absorption interfering with the experiment. The experiments were conducted on a nanosecond pulsed laser, as opposed to a femtosecond pulsed laser used in the previous measurements. The measurement of **65** was troublesome at this wavelength as sufficient nonlinear absorption is not present. The concentration for this compound was then increased until satisfactory results were obtained. The open aperture experiment trace was converted to transmittance vs. fluence graphs to obtain the $F_{15\%}$ value in Table 2.8, and this value used for the calculation of the excited state cross-sections. The threshold limiting fluence (in this case the $F_{15\%}$ value) is used to measure limiting ability.

Cluster	Optical abs λ , nm ($\epsilon \times 10^4 \text{ dm}^3 \text{ mol}^{-1} \text{ cm}^{-1}$)				$F_{15\%}$ (J cm^{-2})**	Cross Section (10^{-18} cm^2)	
	$\lambda_1 (\epsilon_1)$	$\lambda_2 (\epsilon_2)$	$\lambda_3 (\epsilon_3)$	$\lambda_m (\epsilon_m)^*$		Ground state, σ_0	Excited State, σ_{eff}
65	341 (3.2)	423 (sh,1.01)	525 (0.24)	570 (1590)	0.32	6.1	5.5
66	313 (1.6)	370 (0.52)	471 (0.24)	570 (790)	0.13	3.0	3.2
67	304 (sh,1.4)	352(sh, 0.61)	493 (Sh, 0.19)	570 (820)	0.20	3.1	3.9
68	329 (sh, 1.91)	406 (0.42)	519 (sh, 0.36)	570 (2100)	0.18	8.0	8.7
69	320 (sh, 1.1)	370 (sh, 0.53)	450 (0.23)	570 (310)	0.25	1.2	2.1
70	313 (sh, 2.1)	375 (sh, 0.75)	461 (0.37)	570 (830)	0.14	3.2	3.4
71	314 (2.4)	371 (sh, 0.71)	466 (sh, 0.34)	570 (420)	0.23	1.6	1.8
72	311 (sh, 2.48)	335 (sh, 1.7)	500 (0.97)	570 (3060)	0.20	11.6	12.7
73	332 (sh, 1.7)	407 (sh, 0.74)	493 (1.1)	570 (1790)	0.06	6.8	12.4
74	307 (2.7)	-	497 (1.02)	570 (4410)	0.05	16.8	21.3

* Measurement Wavelength (ϵ of complex at λ_m in $\text{dm}^3 \text{ mol}^{-1} \text{ cm}^{-1}$). ** $F_{15\%}$ is the incident fluence which reduces the transmittance by 15 %.

Table 2.8 - UV-Visible and Optical limiting properties of 65-74.

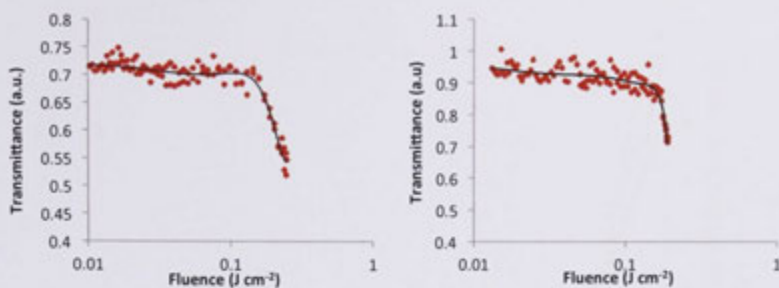


Figure 2.15 - Transmittance-fluence plots of 72 (left) and 68 (right) at 570 nm.

There is a strong inverse correlation between ϵ_m and $F_{15\%}$ in that the more absorptive the complex at the measurement wavelength, the less energy per unit area (fluence) required for a reduction in transmittance. This trend also carries through to the differences between the ground and excited state cross-sections with the complexes with a larger ϵ_{570} having greater ground/excited state cross-section differences. Optical limiting merit increases with the metal content of the clusters, and lower energy absorption bands due to increasing π -conjugated ligand content (dmit addition) and subsequent tuning by functional group modification (electron-donating substituent's being favoured here). This is evident from the $F_{15\%}$ trend: $74 \approx 73 < 66 \approx 70 < 68 \approx 72 \approx 67 \approx 71 < 69 < 65$.

2.2.8.2 Niobium cluster complexes

Niobium clusters with similar bipy ligands as those in 2.2.8.1 (**75-77**) were also investigated for optical limiting ability. The complexes feature an unsaturated nonyl chain (**76**) and methyl carboxylate substituted ligands (**77**), as well as unfunctionalised bipy on a binuclear Nb core (**75**).

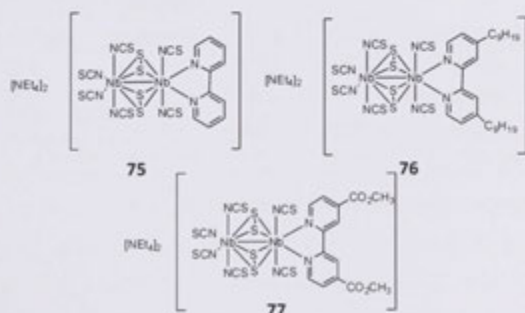


Figure 2.16 - Niobium clusters 75-77.

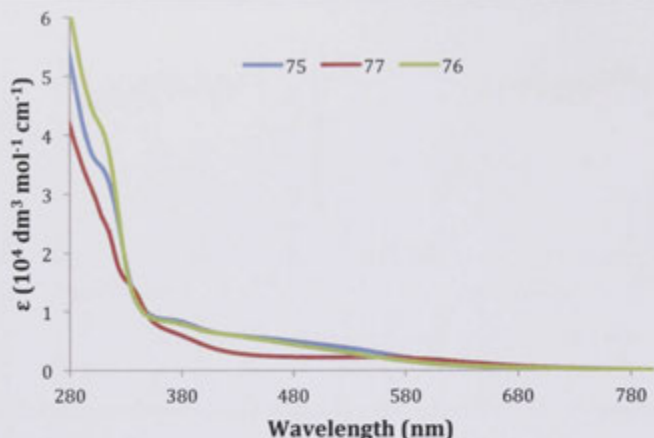


Figure 2.17 - UV-Visible spectra of 75-77.

The optical and optical limiting data for these complexes is displayed in Table 2.9 and the UV-Visible spectra in Figure 2.17. The linear optical profile of complexes 75-77 is broad and flat from 370 to around 680 nm. 600 nm was selected as a wavelength with a good response and was used for measurement of these compounds. The absorptivity at this wavelength for the niobium clusters is greater than for the molybdenum clusters, which indicates that they may be more suitable materials for optical limiting at this wavelength. The threshold optical limiting fluence is of the same order as for the tetrabromo- Mo clusters (68-72, 0.25-0.3 J cm⁻²), however, the ground state to excited state cross-section difference is much greater, the excited state having an order or two greater cross section than the ground state. This seems to suggest the ground state rapidly saturates to favour excited state absorption, a beneficial mechanism for the dissipation of energy, as discussed in the introduction.

Cluster	λ_{max} , nm (ϵ^A)	ϵ_{600}^A	$F_{15\%}^B$	Cross Section (10^{-18} cm ²)	
				Ground, σ_0	Excited, σ_{eff}
75	465 (sh, 0.5)	1750	0.253	0.66	6.47
76	465 (sh, 0.4)	1137	0.33	0.43	15.3
77	558 (sh, 0.6)	1919	0.236	0.73	2.48

^A units - dm³ mol⁻¹ cm⁻¹. ^B Fluence required to reduce transmittance by 15 % (J cm⁻²).

Table 2.9 – UV-Vis and optical limiting properties of compounds 75-77.

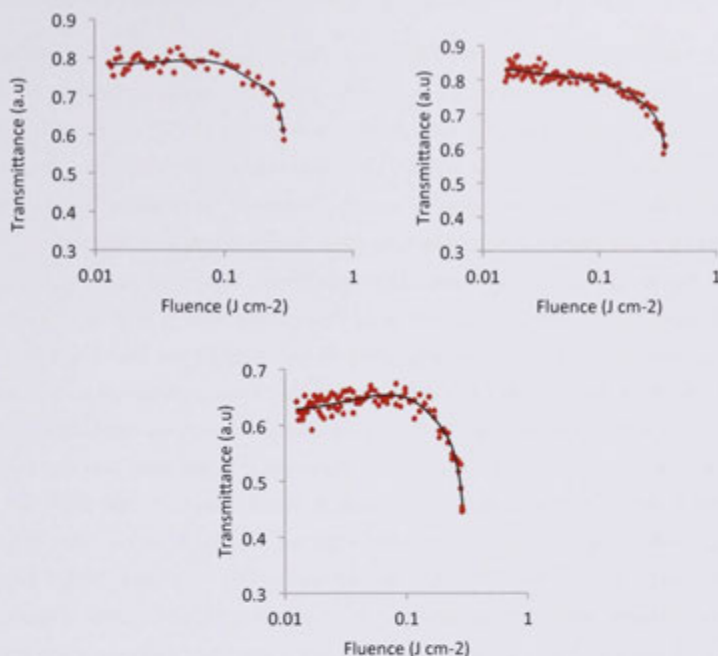


Figure 2.18 - Transmittance-fluence plots of **75** (top left), **76** (top right) and **77** (bottom) at 600 nm.

The nonyl functionalised **76** seems to have a weaker nonlinear absorption response at this wavelength requiring more energy to reduce transmittance than the other two. **76** also has less linear absorption at this wavelength, both details contrary to what was observed for this ligand in the molybdenum cluster, **74**. The order of threshold saturation fluence is $77 \approx 75 < 76$, the electron-withdrawing carboxylate-containing cluster possessing the lowest fluence threshold.

2.3 Experimental

2.3.1.1 Materials

Measurements were conducted on solutions of material in either CH_2Cl_2 (**47-64b**) or DMF (**65-77**) placed in 1 mm glass cells. CH_2Cl_2 was distilled over CaH_2 and deoxygenated subsequently by sparging under N_2 , DMF was dried using 4Å molecular sieves. The concentrations of all samples varied but were typically around 0.10-0.20 % w/w; 0.007 % and 0.01 % w/w were used for **62** and **63**, and 0.35 % for **65**.

2.4.1.2 Methods and Instrumentation

Spectral dependence Z-scan experiments were run using a light source consisting of a Quantronix Integra-C3.5F pumping a Quantronix Palitra-FS optical parametric amplifier, tuneable over a wavelength range from 460 nm to 900 nm or 1400 nm (were specified). The output delivered 130 fs pulse with a 1 kHz repetition rate. Coloured glass filters and a Thorlabs polarizing filter were used to remove unwanted wavelengths and the power adjusted by use of neutral density filters to obtain nonlinear phase shifts between 0.1 to 1.3 rad. The focal length of the beam at the experiment was either 120 mm or 75 mm (where specified), obtained by the use of an appropriate lens. A 120 mm lens gave a Gaussian beam waist of 25-60 mm (depending on wavelength) and the 75 mm lens gave 25-45 mm beam waist, both of which give Rayleigh lengths longer than the sample thickness. Samples travelled down the Z axis on a Thorlabs motorised stage between 0 and 100 mm with a 120 mm lens, and between 5-45 mm with a 75 mm lens. Data was collected by three Thorlabs photodiodes, 500-900 with Si based detectors, 900-1300 nm with InGaAs detectors and 1300-2000 nm with amplified InGaAs detectors. Data from the detectors were collected by a Tektronix oscilloscope feeding a custom LabVIEW program (written by Marek Samoc) permitting fitting of a theoretical trace. A sample of CH_2Cl_2 was run at each wavelength as an aid in referencing to a 3 mm fused silica plate; the real and imaginary components of the second hyperpolarisability (γ) of the materials were calculated assuming additivity to these reference samples.

UV-Vis traces for optical limiting samples were run on samples in DMF in 1 cm quartz cells on a Varian Cary 5 spectrophotometer over a 270 to 800 nm range. The optical limiting experiments were performed with a light source from a Opolette (HE) 355 II (Opotek) ns laser system tuneable to a range from 400- 2200 nm (20 Hz repetition rate, 5 ns pulses). The power of the beam was moderated using a polarising filter to obtain a power that wouldn't damage the sample and was recorded with a Coherent Fieldmate laser power meter. The open aperture Z-scan data was converted into transmittance vs fluence plots assuming Gaussian character of the beam, with the beam waist being derived from the closed aperture experiment.

Chapter 3 - Core Modification in Ruthenium Alkynyl Stars

3.1 Introduction

Ruthenium alkynyl compounds have been used extensively in the development of materials with large nonlinear optical responses.^{7,18,26,56,60} These range in structural diversity from linear complexes to hyperbranched dendrimers (Figure 3.1), the latter showing large TPA values with generational increase. Dendrimers have typically used a 1,3,5 substitution pattern at the core^{61,62} and branching points of the molecule mainly due to steric considerations, as well as maintaining the octupolar substructure for maximising the NLO effects.⁶³

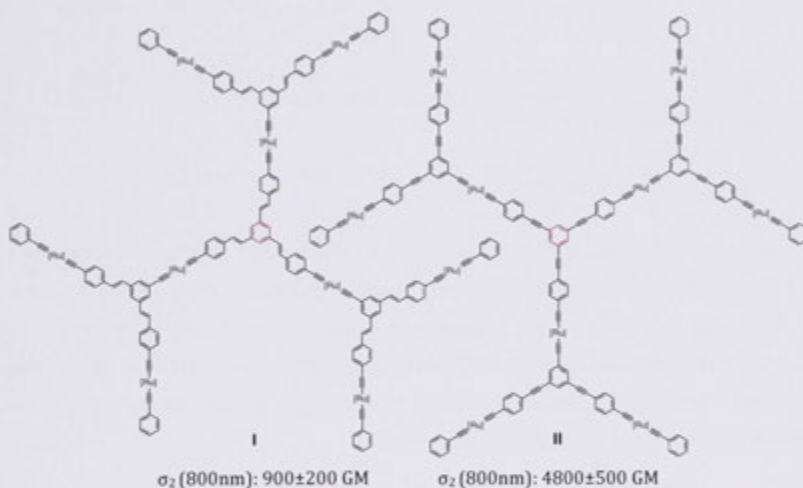


Figure 3.1- Two dendrimers with a 1,3,5-substituted core synthesised for investigation of two-photon absorption properties.^{56,61,74} [Ru] = Ru(dppe)₂

Modifying the core structure of dendrimers or star shaped compounds has been undertaken with heteroatoms (B⁹, N⁵, P¹⁰), hexagonally arranged donor or acceptor groups (isocyanurates⁴⁸, triazine⁶⁴) and finally metal complex cored compounds (porphyrin⁶⁵, Ru(bipy)₃¹⁷) with promising NLO results. With a focus on compounds with a benzene core, we are limited to modification of substitution and therefore symmetry of the core. The substitutions previously studied mainly cover (1,3)-⁶⁶; (1,4)-^{60,66}; (1,3,5)-^{61,66}; (1,2,4,5)-⁶⁷; and hexa⁶⁸⁻⁷⁰ substitutions, but not all twelve possible 'substitutional' variants as displayed in Figure 3.2. This area is of interest to expand the possible modifications on existing dendrimer structures to widen the design for materials with large NLO properties. This Chapter will focus on the synthesis and properties of linearly extended cores only, which should be adequate to demonstrate the effect of modification without the need for the preparation of dendrimers.

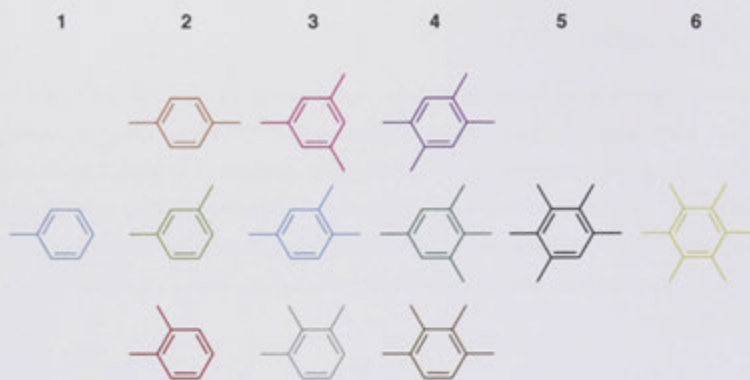


Figure 3.2 - The twelve possible benzene substitutional variants. The colour of the benzene in this diagram is assigned to all compounds with this core substitution pattern throughout this chapter for both structure and UV-Vis traces.

3.1.1 Core substitution level in NLO materials

Kondo *et al.* carried out the first NLO investigations of substitutionally varied compounds in 1995.⁶⁹ They tested 3 core substitutions of a simple tolane structure (Figure 3.3) with the degenerate four-wave mixing technique to determine the $\chi^{(3)}$ value in chloroform solutions. Values increase from the 1,3,5 to the 1,2,4,5 and again to the hexa-substituted compound. The authors linked the increased π -conjugation through the molecule to the observed increase in third-order NLO properties.

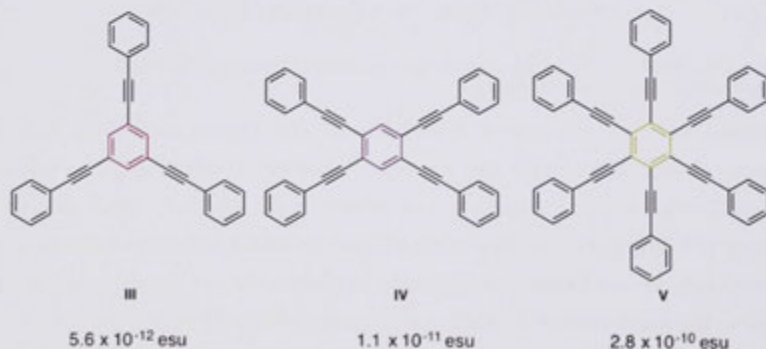


Figure 3.3 - Compounds studied by Kondo *et al.* showing increased NLO behaviour with core substitution change.⁶⁹

Multi-annulene compounds with varied core substitution have also been synthesised.⁷¹ Bhasker *et al.* synthesised annulenes with (1,4)-, (1,2,3,4)-, (1,2,4,5)- and hexa-substituted cores (Figure 3.4).

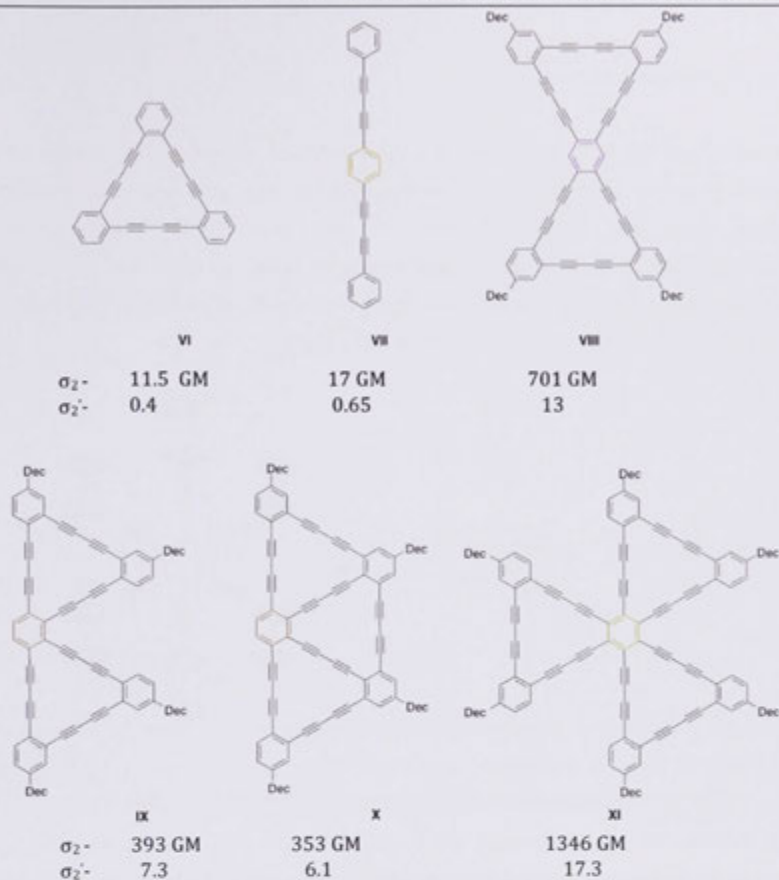
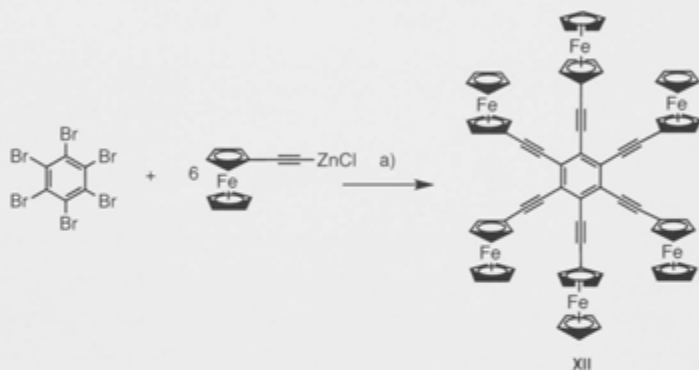


Figure 3.4 - Butadiyne linked compounds with core modification synthesised by Bhasker *et. al.*⁷¹ The 2PA cross section is shown to increase with core geometry change. This has been scaled per π -electron (σ_2') to accurately compare large and small compounds.

Two-photon absorption cross-sections were measured by the two-photon excited fluorescence technique which showed the higher symmetry substitution gives the higher TPA cross-sections. The elimination of the effect of having more chromophoric elements (more butadiyne linkers) was achieved by dividing the TPA cross-section values by the number of π -electrons in the molecule. This seemed to suggest that the symmetry plays a role in NLO properties of a molecule, as shown by the difference between **IX** and **VIII** ((1,2,3,4)- and (1,2,4,5)-isomers). The only apparent difference between the two structures is core substitution, however the efficacy of core conjugation is not considered and may become important in further study.

3.1.2 Organometallic compounds

Research into the NLO properties of core substituted organometallic compounds is limited. Hexa-substituted compounds with organometallic groups have been synthesised before, with the NLO properties of only one having been measured. Hexakis(ferrocenylethynyl)benzene synthesized by Diallo *et al* shows the solubility problems that occur when incorporating metals into hexaethynylbenzene, the red solid **XII** being insoluble in most common solvents (Scheme 3.1).⁷²



Scheme 3.1- Diallo *et al.* synthesis of hexakis(ferrocenylethynyl)benzene. a) Pd(PPh₃)₄, toluene, THF, 7 days.⁷²

Huang *et al.* synthesised a hexa-metallated compound with Au(PCy₃) around the periphery.⁶⁸ This required phenylethynyl extended spacers to accommodate six bulky metal centres around the core. The tri(cyclohexyl)phosphine auxiliary ligand on the gold centre was used to aid the solubility of the complex. This compound was resynthesised by the Humphrey group for NLO studies, in which wavelength dependence two-photon absorption studies were conducted.⁷³ The two-photon absorption cross-section maximizes at 600 nm for both complexes with a large difference in σ_2 value (**XIII**: 80 GM, **XIV**: 9000 GM) (Figure 3.1).

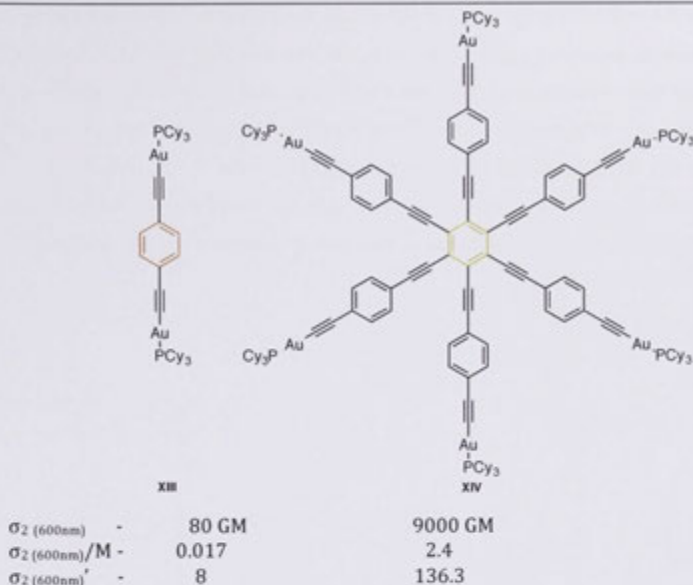


Figure 3-5 - Alkynylgold compounds measured by Corkery *et al.*^{73,74} σ_2 values have been scaled by molar mass (σ_2/M) and π -electrons (σ_2^r).

When scaled by molar mass the hexa-substituted compound outperformed the linear compound.⁷⁴ For consistency of comparison with the compounds reported by Bhasker *et al.* this data has been scaled by π -electrons (Figure 3.4) and the value is still two orders of magnitude greater. This was a promising result for organometallics with modified core structures but to increase the utility of the compounds ruthenium metal centres were desired. Ruthenium groups containing two 1,2-(diphenylphosphino)ethane ligands were identified as the best for use as complexes employing this *trans*-Ru(dppe)₂ can be extended to larger dendrimers and have reversible redox properties useful for electrochemical switching.

3.1.3 Previous work with alkynylruthenium compounds

In 2009-2010, PhD student Chris Corkery attempted to synthesise a series of organometallic stars to investigate the NLO response upon changing the substitution pattern around a benzene core. He targeted the symmetric analogues: (1)-, (1,4)-, (1,3,5)-, (1,2,4,5)- and hexa substitution patterns (Figure 3.6).⁷⁴ The structure of the three stars and two linear molecules in Figure 3.6 were kept as similar as possible in order to

investigate the effect of changing substitution pattern around the core. Solubilising ethoxy groups were incorporated into the arms to aid the solubility of the complexes. The Sonogashira cross-coupling of hexabromobenzene and the bulky ethoxy arm to form **XV** was hampered by a side reaction where protonation of the benzene core occurs after the cross-coupling addition of five acetylene arms (**XX**) en route to **XV** (Scheme 3.2). This side reaction has been investigated extensively and resolved by Neirle *et al.* by coupling an aryl iodide arm to a hexaethynylbenzene core rather than an extended acetylene arm to hexabromobenzene.⁷⁵

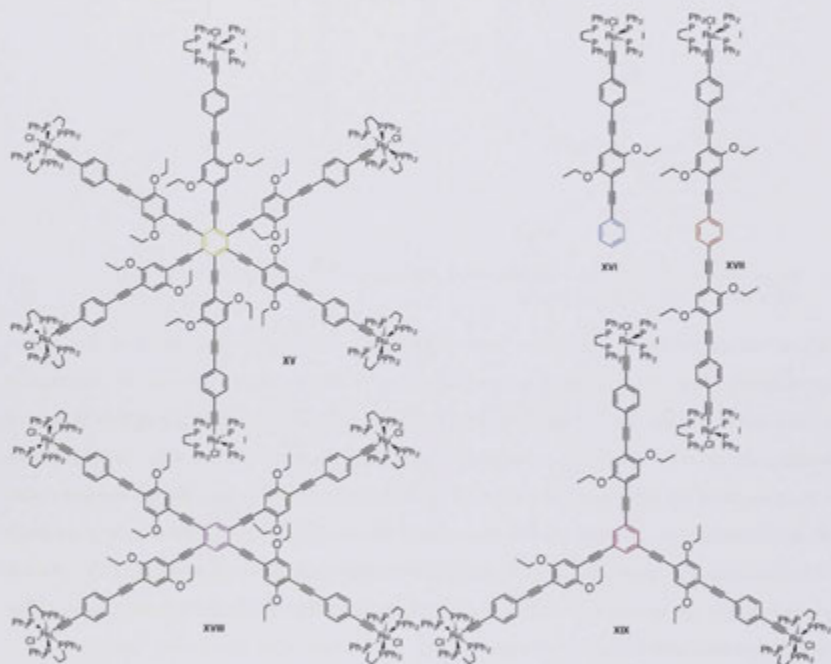
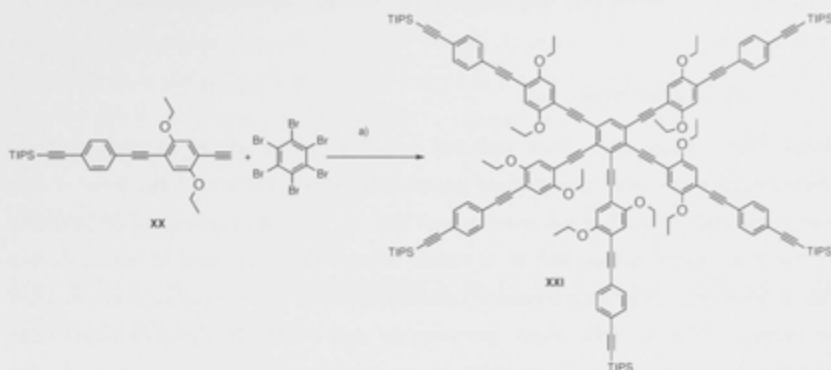


Figure 3.6 – Corkery's target compounds.



Scheme 3.2 – Corkery's attempted synthesis of XV. a) PdCl₂(PPh₃)₂, CuI, NEt₃.

3.1.2 Synthetic considerations

3.1.2.1 Hexaethynylbenzene

Many syntheses of compounds containing a hexaethynylbenzene moiety exist and some of these are presented here to assess their viability for use in this synthesis.⁷⁵⁻⁷⁹ The synthesis of the hexa analogue of any suite of compounds for this investigation is the most difficult, and the design of the set of compounds needs to satisfy these demands. The first synthesis of hexaethynylbenzene was by Peter Vollhardt and coworkers using a Sonogashira cross-coupling reaction on hexabromobenzene with either trimethylsilylacetylene or dimethylpropargylalcohol (DMPA).⁷⁹ Deprotection of the TMS protected species with K₂CO₃ yielded the heat, air and light sensitive hexaethynylbenzene. The DMPA protected species was less successful, requiring heat and a stronger base for deprotection. Nierle and coworkers used this methodology to add phenylacetylene to bromobenzene with little success, generating instead the pentaethynyl species, originating from protonation of the core after pentasubstitution.⁷⁵ They changed procedure, accessing the hexatolane through a two-step procedure of addition of a smaller acetylene (TMSA), deprotection and subsequent Sonogashira coupling to access the desired compound. Sonada *et al.* used a Negishi cross-coupling reaction to access TMS-protected hexaethynylbenzene.⁷⁶ They reported higher yields than previously obtained by the Sonogashira method but didn't discuss why this is observed. Haley *et al.* in 2001 modified the standard Sonogashira coupling to allow the functionalisation of hexaiodobenzene

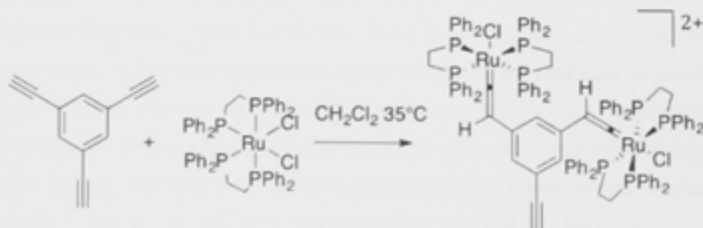
using a catalyst with a much higher reactivity and a favorable solvent system to enhance solubility.⁷⁷ This methodology was trialed in the present study with no success.

3.1.2.2 Solubilising functional groups

Solubilising groups have been included into the design of many large organic, organometallic and hexaethynyl-cored compounds.^{44,70,71,73} These take the form of long linear aliphatic or branched functional groups with the purpose of increasing the solubility of the final compound as well as synthetic intermediates for ease of synthesis and characterisation. Many characterisation techniques require solutions of materials in order to measure, such as NMR, mass spectrometry and Z-scan. Phenylethynyl-containing compounds can become quite insoluble as the chain lengthens, mainly due to the flat structure of the compounds. The incorporation of solubilising groups into these high symmetry compounds gives the added bonus of providing a H or C NMR 'handle' to aid characterisation, as well as the main purpose, namely to increase the solubility of the compounds. The 2,6-diethyl containing ring was incorporated into the design of the present series of compounds to maintain symmetry and increase the solubility.

3.1.2.3 Chain length

The "spacer" between the metal and the core benzene needs to be at least 2 phenyleneethynylene units long.⁷⁴ In his PhD Thesis, Chris Corkery reported Spartan modelling to assess the feasibility of putting the desired $\text{RuCl}(\text{dppe})_2$ units around hexaethynylbenzene. The vinylidene intermediate for generation of the alkynyl-ruthenium species is more sterically demanding than the product itself. This is shown in the synthesis of the dendritic wedge (branching unit) that is commonly employed by the Humphrey group (Scheme 3.3).⁶¹ The steric bulk of the first two vinylidenes prevent the coordination of the third.



Scheme 3.3 – Metallation of 1,3,5-triethynylbenzene with $\text{RuCl}(\text{dppe})_2$ showing the sterically demanding intermediate.⁶¹

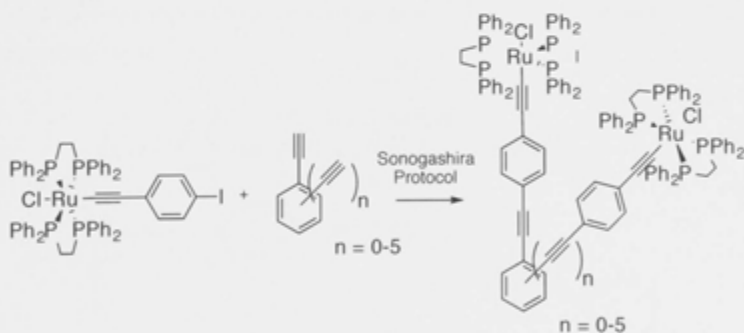
The solubilising group can impose steric demands.⁷³ The 2,5-bis-(2-ethylhexyl) solubilising group previously utilised by the Humphrey group has such a requirement: an additional phenyleneethynylene “spacer” between the metal and the core.⁴⁴ The 2,6-diethyl- solubilising group also requires a spacer to accommodate the vinylidene intermediates of the organic bridge.

3.2 Synthesis

Note: Full structures and numbering legend can be found in foldout figures in the appendix 4.3 (pg 273).

3.2.1 Synthetic design

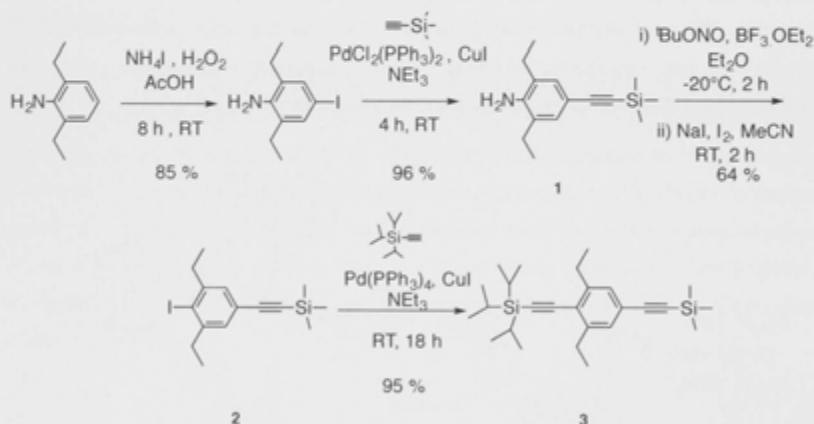
To minimise the number of synthetic steps in total, a strategy that reduces the manipulations after core attachment is desired. The straightforward method for synthesis would be to add a metalated tri(phenyleneethynylene) arm to each of the 12 ethynyl benzene substitution variants (Scheme 3.4). This may be a viable procedure for bis-alkynyl complex where attachment to the metal is blocked by the presence of another acetylide ligand, but for mono-alkynyl complexes, the target alkyne can coordinate to the ruthenium. The next shortest route is to add silyl-protected tri(phenyleneethynylene) moieties to the ethynyl-functionalised core, subsequent deprotection and then metallation, and this was the procedure that was ultimately employed.



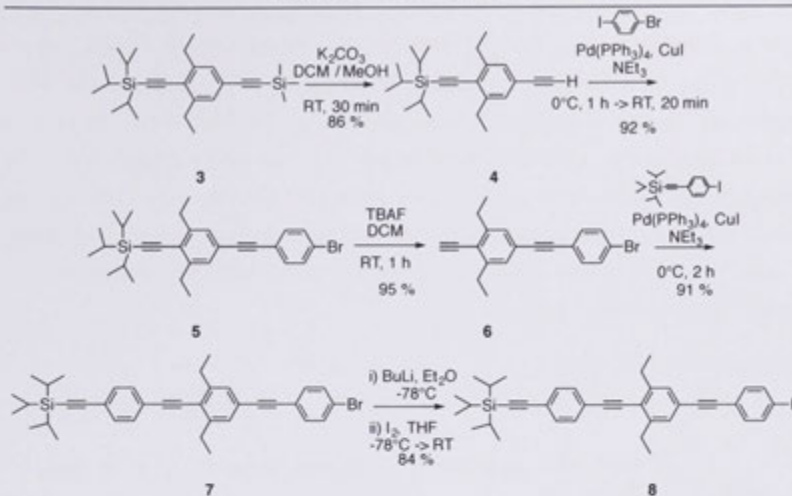
Scheme 3.4 - The ideal preparation of target compounds. Unlikely to work due to the labile chloride ligand

3.2.2 Preparation of a tri(Phenyleneethynylene) containing arm

The synthesis of the tri(phenyleneethynylene) arm was achieved by a series of deprotections and selective Sonogashira reactions. By design, the final silyl protecting group on the compound was a triisopropylsilyl group to aid solubility of the larger organic compounds assembled using the arm. The iodide terminal group was also desired to obtain high yields from the Sonogashira reaction with the core-ethynylbenzenes, in particular hexaethynylbenzene, which is heat, light and oxygen sensitive.⁷⁹ Starting with 2,6-diethylaniline, the para-position was iodinated with an in-situ generated iodonium acetate (Scheme 3.5).⁸⁰ This was then reacted via a Sonogashira cross-coupling with trimethylsilylacetylene to afford **1**. This was then reacted with tert-butyl nitrite to obtain the diazonium salt, which was immediately reacted with sodium iodide to afford the iodinated compound **2**. A further Sonogashira reaction, this time with triisopropylsilylacetylene gave **3**. This reaction was best carried out with heat, as the iodide is sterically hindered by the adjacent ethyl groups. This hindrance prevents cross-coupling with larger acetylenes (such as 4-triisopropylsilylethynylphenylacetylene, which would reduce the overall steps required).⁷³

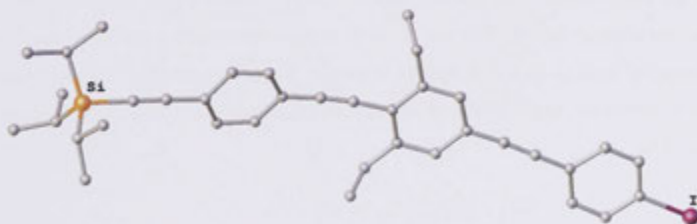


Scheme 3.5 - The preparation of compounds 1-3



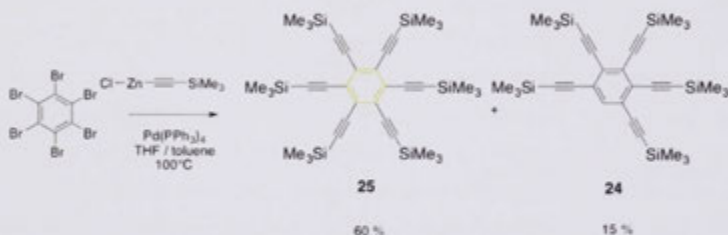
Scheme 3.6 - The preparation of 4-8.

Selective deprotection of the TMS group occurred rapidly with a mild base to give **4**, which was then reacted under Sonogashira conditions with 1-bromo-4-iodobenzene at 0°C to bias substitution at the iodide (Scheme 3.6). **5** was then deprotected with TBAF to give the free acetylene **6**, which was reacted via another selective Sonogashira reaction at 0°C with 1-(trimethylsilyl)-2-(4-iodophenyl)ethyne. *Trans*-halogenation gave the desired tri(phenyleneethynylene) iodide **8**. Crystals of **8** suitable for diffraction were grown from diffusion of MeOH into a CH₂Cl₂ solution (Figure 3.7). All three phenyl groups are in a planar arrangement.

Figure 3.7 - The crystal structure of **8** solved by Dr Graeme Moxey.

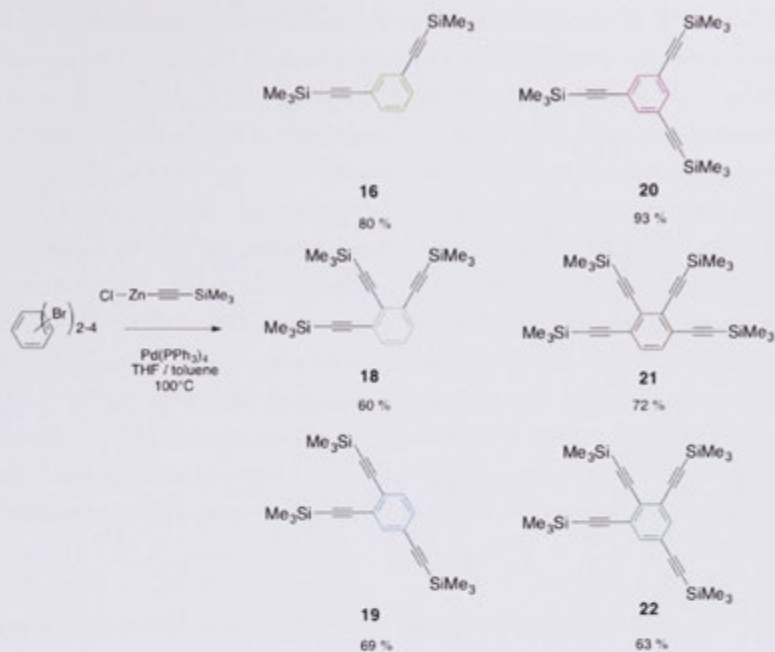
3.2.3 TMS-protected cores

Sonada *et al.* have prepared the TMS protected hexaethynylbenzene using a Negishi coupling to hexabromobenzene.⁷⁶ This seemed to be the best route into the hexaethynylbenzene, as this removes the protons generated in Sonogashira type coupling as well as the need for the copper co-catalyst. Sonada *et al.* also reported generation of the penta-substituted species although at a lower yield (10%).⁷⁶ The source of the penta species is unclear, but it may be possible that the palladated pentaethynyl species is stable, and exists in an appreciable amount upon workup, while the excess zinc chloride is quenched with the addition of acid.

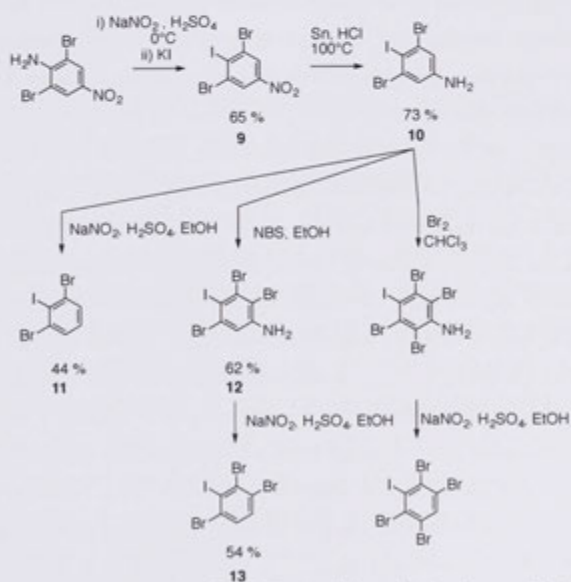


Scheme 3.7 - The synthesis of hexa- and pentaethynylbenzene.

The hexa- (**25**) and penta- (**24**) substituted TMS-protected cores were synthesised from the same Negishi reaction and separated by column chromatography (Scheme 3.7). The reaction can be upscaled to multigram levels but requires at least two chromatography columns to separate large amounts. Several other TMS-protected cores were synthesised by this method (**16**, **18**, **19**, **20**, **21** and **22** (Scheme 3.9)), as reaction times tend to be quicker. Using Sonogashira reactions with aryl bromides usually required multiple additions of alkyne due to a competing homocoupling reaction at high temperatures. This depleted the acetylenes before the reaction had gone to completion and is thought to be due to the presence of copper. The use of the Negishi cross-coupling protocol removed the requirement for copper, as the acetylene proton is already removed. This also made the acetylene more stable, as even after 4 days at 100°C the chloro-zinc alkynyl complex can still be present.



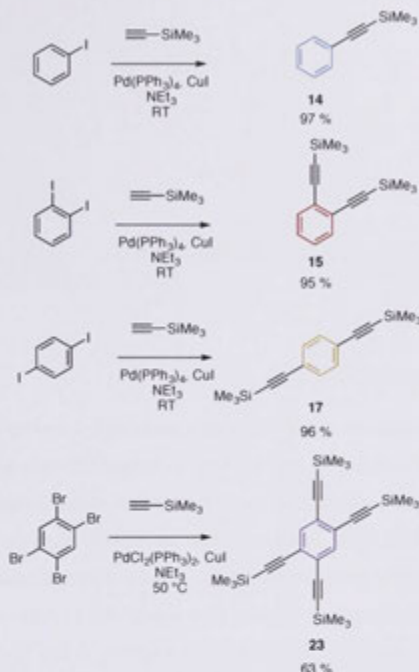
Scheme 3.9 - The Negishi reaction was preferred for the cross coupling to aryl bromides (**18** and **21**) were synthesised from **11** and **13**).



Scheme 3.8 - The preparation of **9-13**. The pentahalogeno analogue is also accessible by this route.

Compounds **18**, **21** and **22** have unique core geometries. The bromobenzene precursors, while commercially obtainable, were not available for this synthesis. 1,2,3-Tri and 1,2,3,4-tetra chloride analogues were obtained and cross-coupling attempted on these compounds using methodology applied by Langer *et al.*⁸¹ on the hexachloro analogue. This approach was found to be inappropriate probably due to the choice of acetylene used. Langer *et al.* used mainly phenyl-substituted acetylenes which are less volatile; the TIPS- and TMS-protected acetylenes used here yielded no product. Aryl-chloride Kumada cross-coupling as outlined in Sonada *et al.* was also unsuccessful.⁷⁶ Bromo- or iodo- containing analogues of these compounds were then synthesised (Scheme 3.9). Starting from 2,6-dibromo-4-nitroaniline all three compounds can be accessed by reduction, halogenation or deamination reactions. This also provides a route to prepare the (1,2,3,5)- and the penta-halogenated core, both of which were ultimately not required. **22** was prepared by tri-bromination of aniline with molecular bromine and a subsequent Sandmeyer reaction to install an iodine. Compound **9**, **10** and **11** have previously been synthesised by different routes.⁸²

The amine on 2,6-dibromo-4-nitroaniline was replaced with iodine by a standard Sandmeyer reaction protocol for a moderate yield of **9** (previously synthesised by a different method)⁸³. Iodine was preferred because quenching the diazonium salt with potassium iodide generates considerable diatomic iodine, which does not react further, whereas diatomic bromine can undergo electrophilic ring substitution leading to undesirable side products. Bromine addition was attempted with standard methodologies to minimize diatomic bromine generation (urea to quench residual nitrous acid; dilution of the diazonium solution; use of copper bromide as a halogen source) but to no avail. Reduction to the aniline **10** was facile. Deamination to give **11** was rapid with good conversion that is not reflected in the yield. A side product was formed in this procedure, thought to be the reaction of surplus nitrous acid with the benzene ring. This impurity gave a singlet in the ¹H NMR consistent with an aryl-nitroso moiety and repeated recrystallization from hexane the only successful way to remove it. This compound was also previously reported by Karim *et al.* although synthesised by a different method.⁸⁴ The authors performed a Sandmeyer reaction on commercially sourced 2,6-dibromoaniline, which resulted in higher yields than achieved in the method shown in Scheme 3.9. Mono-bromination of **10** gives **12**, which works best in EtOH; CHCl₃ or MeCN gives multiple halogenation products. Deamination to give **13** does not give any problematic side product as this procedure did for compound **11**.



Scheme 3.10 - The synthetic protocol for compounds 14, 15, 17 and 23.

14, **15**, **17** and **23** were prepared by standard Sonogashira coupling (Scheme 3.10). **14**, **15** and **17** were prepared from the aryl iodide, which occurs rapidly at room temperature and avoids the homocoupling problem seen in the aryl-bromide case. **23** was made from the aryl bromide by normal Sonogashira reaction. **14** wasn't required for the synthesis of the corresponding alkyne (commercially derived phenyl acetylene was used), but was synthesised for comparison of optical properties to other TMS-containing cores. The reported physical data for many of the TMS-protected cores are also inconsistent and thus collating this data may be helpful.⁶⁵ The NMR data for these compounds were very useful for aiding the assignment of the NMR spectra of the larger extended organic analogues. Therefore ¹H NMR, ¹³C NMR, EI mass spectrometry and UV-Visible data for all twelve TMS protected core compounds is provided in the experimental section. Only **18** and **22** are previously unreported compounds, with **18** being crystallised for X-ray diffraction from the slow evaporation of solvent from a methanolic solution. Crystals of **22** were also obtained by this method but the X-ray diffraction data could not be refined past a confirmation of atomic composition and bond connectivity.

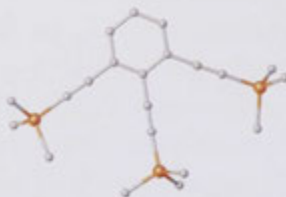
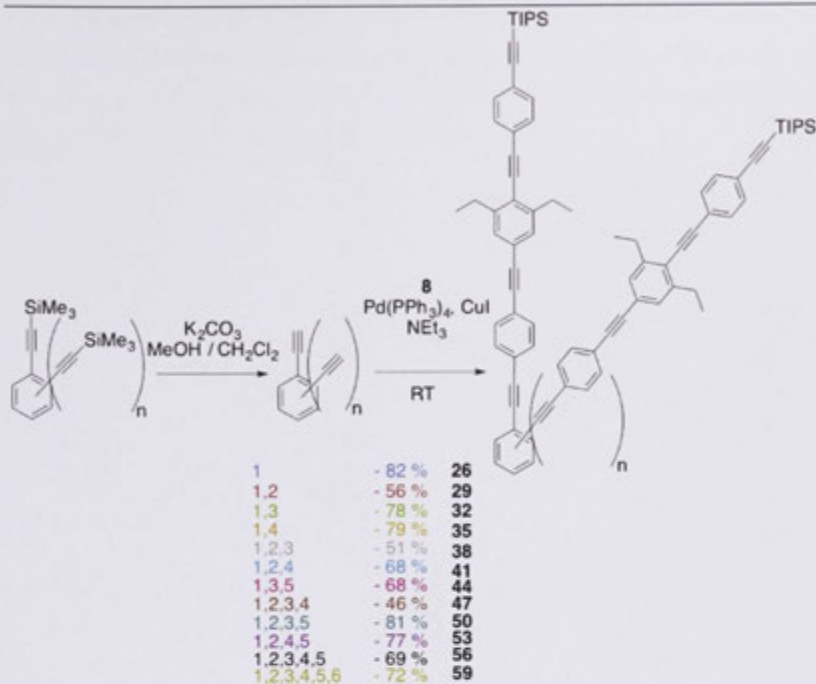


Figure 3.8 - Crystal structure of **18** collected by Dr Graeme Moxey.

3.2.4 Core synthesis and metallation

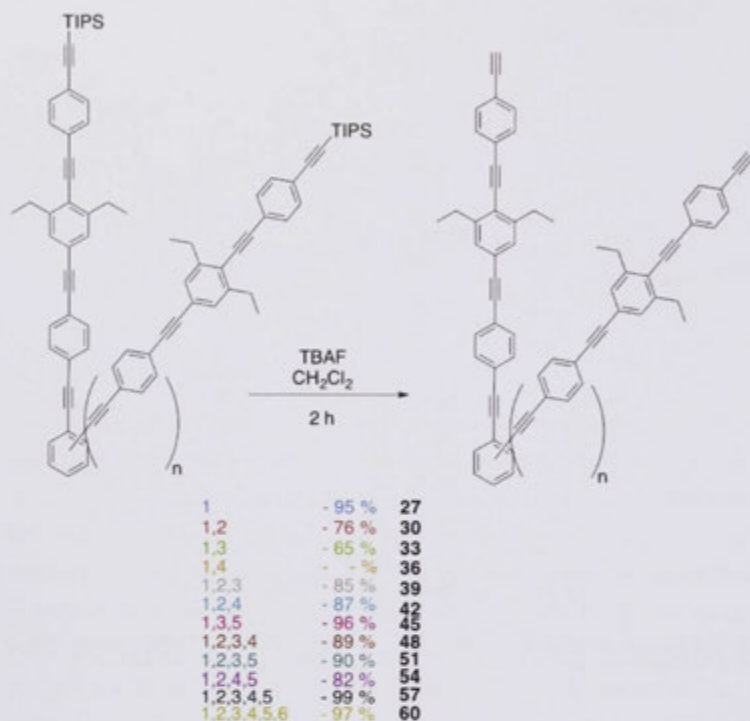
The assembly of the organic cores starts with a Sonogashira cross-coupling reaction of the appropriate ethynyl-substituted core and the tri(phenyleneethynylene) (**8**). Some of the required ethynyl benzenes are air and light sensitive, which necessitates fresh preparation with exclusion from air and light, similar to the procedure used by Schmittl *et al.*⁷⁸ Vollhardt noted this sensitivity in his first synthesis of hexaethynylbenzene.⁷⁹ This is also a property of the higher substituted analogues (the penta, the (1,2,3)- and the (1,2,3,4)-). The (1,3,5)- and (1,2,4,5)- analogues have been used before in the Humphrey group and are reported as having stability for days under standard lab conditions. This seems to suggest that the (1,2,3)- arrangement is behind this sensitive behavior. Desilylation of the TMS-protected cores was carried out with K_2CO_3 over 2 hours in a mixture of deoxygenated CH_2Cl_2 and MeOH (Scheme 3.11). The workup and solvent removal was also carried out under an inert atmosphere. 1H NMR was used to monitor the extent of reaction to ensure complete desilylation of the material, by looking for the disappearance of the 0.25 ppm TMS peak and the introduction of a terminal acetylene peak in the range of 3.1 ppm to 3.3 ppm. Incomplete deprotection was never observed.



Scheme 3.11 - Synthesis of the extended organic cores from the appropriate TMS cores. The first column of values are the core benzene substitution pattern, the second column is the yield of reaction over two steps.

For several species two or three acetylenic proton peaks were observed, as in the case of the (1,2,3)- analogue, which has the expected 2:1 integration, as the magnetic environment of the central ethynyl proton is influenced by the two adjacent ethynyl groups, causing it to shift downfield. The ethynylbenzenes were then added to a mixture of the catalyst and the tri(phenyleneethynylene) (**8**) by cannula. The reaction time was varied depending on extent of substitution, the singly and doubly substituted versions needing shorter reaction times. The yields of these reactions are moderate, no clear trend being observed.

The extended cores were then desilylated using tetra-*n*-butylammonium fluoride (Scheme 3.12). The (1,4)- example (**36**) has extremely low solubility in common solvents so was not fully characterised and used without purification in the metallation step. The deprotection reaction is high yielding, with an easy clean-up. Methanol was added to precipitate the compound, which was recovered by filtration. Thorough washing with methanol removed the residual silane and TBAF. Column chromatography was not needed, but was employed for the lower substitution levels. These compounds appear to have a low stability over time which precluded characterisation by microanalysis.

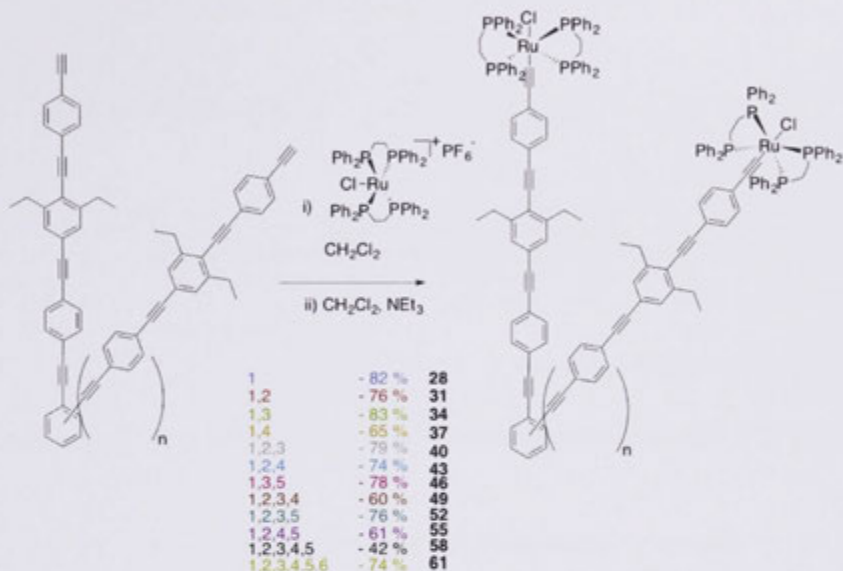


Scheme 3.12 - Desilylation of the extended organic cores. The first column of values are the core benzene substitution pattern, the second column is the yield of reaction.

Finally metallation of the organic cores (Scheme 3.13) with the five-coordinate species $[\text{RuCl}(\text{dppe})_2]\text{PF}_6$ under an inert atmosphere formed the vinylidene complexes which were subsequently converted to the alkynyl complexes with triethylamine. It was necessary that the vinylidene complex was isolated by precipitation to prevent the formation of unwanted products, such as bis-alkynyl complexes or *trans*- $[\text{RuCl}_2(\text{dppe})_2]$ which can form following base addition. The reaction was also conducted with excess $[\text{RuCl}(\text{dppe})_2]\text{PF}_6$ to ensure the complete reaction of all ethynyl groups. The vinylidenes were washed with MeOH to remove NaCl and the surplus metal species before addition to CH_2Cl_2 and NEt_3 . The resulting metal complexes are passed through a short pad of alumina to remove the triethylammonium hexafluorophosphate salts.

The yields are diminished for the higher substitutions, even after a longer reaction time. A possible explanation is that reactions of the higher substituted complexes were carried out on a much smaller scale and therefore have a higher mechanical loss, or lose more

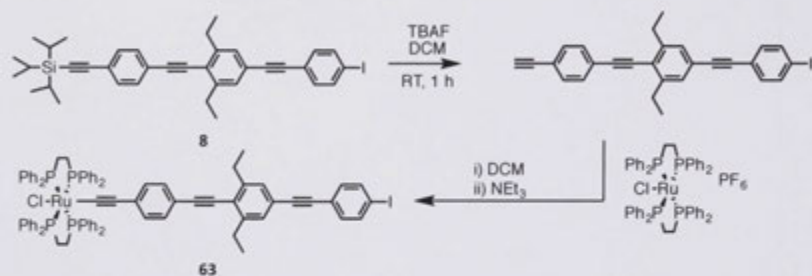
substance at the precipitation step. The synthesis of **37** was marred by the insolubility of the intermediate terminal acetylene as previously discussed. Compound **28** was obtained as a bright yellow solid whereas **61** is a red-brown colour. The compounds in between progressively darken upon increased substitution.



Scheme 3.13 - Metallation of the deprotected organic cores. The first column of values are the core benzene substitution pattern, the second column is the yield of reaction.

Crystals of the singly substituted compound (**28**) were grown from a slow infusion of petrol into a dichloromethane solution (Figure 3.9). Crystallisation of the larger metallated compounds was attempted but was unsuccessful. The compounds were characterised by ^1H , ^{13}C and ^{31}P NMR spectroscopies, however, mass spectrometry was again difficult for the complexes larger than **28**. Due to the large molecular weight of the compounds, ESI mass spectrometry is required and a spectrum was obtained only for compound **28**. ESI mass spectrometry of the other compounds was unsuccessful, most likely due to the lack of solubility in solvents required for ES ionization (MeCN and MeOH used at the ANU MS unit). Attempts to obtain mass analysis resulted in the observation of peaks with mass corresponding to the free $\text{RuCl}(\text{dppf})_2$ with acetonitrile or carbonyl ligands denoting degradation of the complex.

Compound **8** was deprotected with TBAF to form the terminal acetylene (**62**) for coupling to a ruthenium metal centre to form **63**. The structure of **63** was elucidated from a single-crystal x-ray diffraction study for which suitable crystals were obtained by a diffusion of petrol into a solution of CH_2Cl_2 .



Scheme 3.14 – The preparation of **63**.

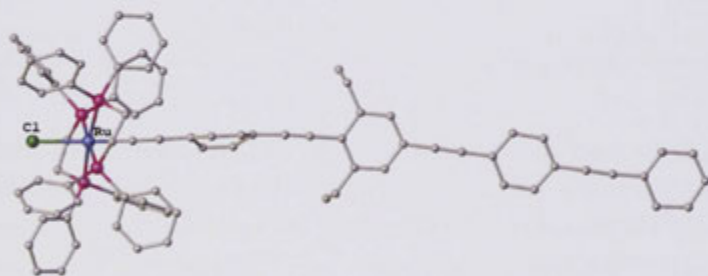


Figure 3.9 - The molecular structure of **28**. Hydrogen atoms and the lattice dichloromethane molecule are omitted for clarity. Selected bond lengths (Å) and angles (°): Ru1-C1 1.992(3), Ru1-P1 2.3943(8), Ru1-P2 2.3596(8), Ru1-P3 2.3597(8), Ru1-P4 2.3626(8), Ru1-Cl1 2.5065(8), C1-Ru1-Cl1 175.21(8), C1-Ru1-P1 85.56(8), P1-Ru1-Cl1 98.44(2), C1-Ru1-P2 83.49(8), P2-Ru1-Cl1 99.61(2), P2-Ru1-P1 82.23(2), C1-Ru1-P3 91.04(8), P3-Ru1-Cl1 85.01(2), P3-Ru1-P1 176.42(3), P2-Ru1-P3 96.29(3), C1-Ru1-P4 91.29(8), P4-Ru1-Cl1 85.54(2), P1-Ru1-P4 98.39(2), P2-Ru1-P4 174.68(3), P3-Ru1-P4 82.77(3). Structure collected by Dr Graeme Moxey

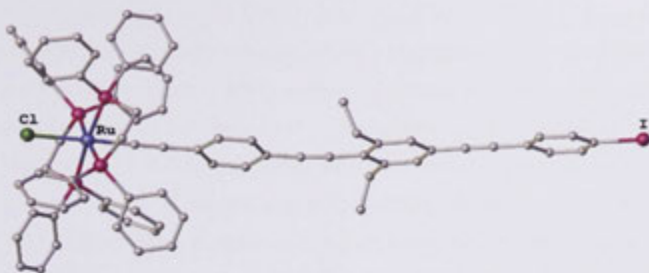


Figure 3.10- The molecular structure of **63**. Hydrogen atoms and the lattice dichloromethane molecule are omitted for clarity. Selected bond lengths (Å) and angles (°): Ru1-C1 1.992(3), Ru1-P1 2.3943(8), Ru1-P2 2.3596(8), Ru1-P3 2.3597(8), Ru1-P4 2.3626(8), Ru1-Cl1 2.5065(8), C1-Ru1-Cl1 175.21(8), C1-Ru1-P1 85.56(8), P1-Ru1-Cl1 98.44(2), C1-Ru1-P2 83.49(8), P2-Ru1-Cl1 99.61(2), P2-Ru1-P1 82.23(2), C1-Ru1-P3 91.04(8), P3-Ru1-Cl1 85.01(2), P3-Ru1-P1 176.42(3), P2-Ru1-P3 96.29(3), C1-Ru1-P4 91.29(8), P4-Ru1-Cl1 85.54(2), P1-Ru1-P4 98.39(2), P2-Ru1-P4 174.68(3), P3-Ru1-P4 82.77(3). Collected by Dr Graeme Moxey.

3.3 NMR analysis

Note: a foldout figure with atom labeling can be found in appendix 4.3 (from pg. 273).

3.3.1 Extending arm

The ^1H and ^{13}C NMR spectra of compounds **1** to **8** are included in the Appendix. They are mostly unremarkable with the exception of those of **7** and **8**. The major difference between **7** and **8** is the AA'BB' spin system in the aryl region from protons H_{16} and H_{17} . The aryl iodide has a larger ppm difference between the two pseudo-doublets than does the aryl bromide (d at 7.25 and 7.69 ppm (I) vs d at 7.35 and 7.62 ppm (Br)), which is due to heavy atom effects. This enables rapid assessment of completion for later stage reactions as the peaks are clear of the aryl protons of the product (Figure 3.11).

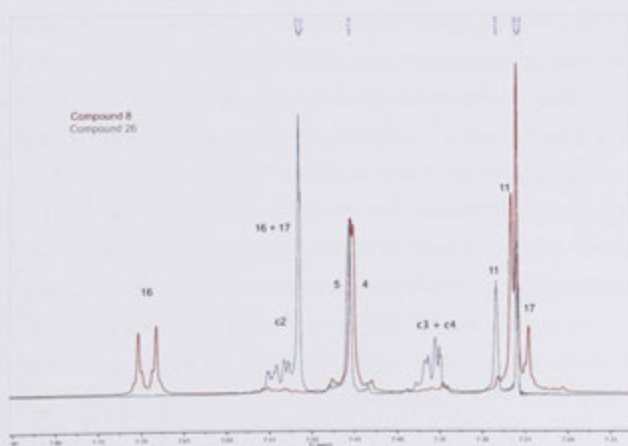


Figure 3.11 - ^1H NMR comparison of **8** and **26**.

H₁₆ and H₁₇ converge to either a singlet or a multiplet after coupling to the ethynyl core. The solubilising group is useful for correct assignment of the carbon environments in the compound. With three linked phenyl-ethynyl units, the proton and carbon environments become difficult to distinguish, particularly the acetylenic carbons. Assignment for compound **8** started with H₄ and H₅ which appear as a singlet, however there is some second-order coupling occurring and some very fine splitting. Inspection of the ¹³C NMR shows the parent carbon environments are different (by 1 ppm) and HMBC permits absolute assignment from ³J_{C-H} coupling to the very different C₂ and C₇ acetylenic environments. Here H₄ is very slightly upfield in the ¹H NMR and C₄ is downfield in the ¹³C NMR. Assignment of the quaternary phenyl environments is not possible as C₃ and C₆ are too near to discern. There is distortion in the cross peak between the H₄/H₅ resonance and the C₃/C₆ peaks which would suggest C₆ more downfield than C₃ but higher resolution is required. HMBC can be subsequently used to assign all acetylene peaks (88 – 104 ppm) except for C₈ which is more than 4 bonds from the nearest ¹H due to the ethyl substituent. Fully annotated spectra for compounds **1** to **8** can be found in the Appendix.

3.3.2 TMS cores

The TMS-substituted cores have very different ¹³C NMR spectra, yet similar ¹H NMR spectra. At the upfield end of the spectrum, compounds **14-25** have from 1 to 3 TMS resonances, depending on the symmetry of the molecule. For instance, the (1,2,4)-analogue has three resonances (one at 0.23 and two at 0.26 ppm [0.01 ppm separation]) stemming from the different magnetic environments around the core; the upfield resonance at 0.23 ppm corresponds to the TMS group attached to the 4 position, while the other two resonances correspond to the 1 and 2 positions deshielded by the C=C triple bonds attached to the adjacent TMS group. The TMS group on arm 2 appears downfield from that of arm 1 due to its (1,3)- substitution compared to arm 4. This is consistent for all compounds that exhibit a (1,3)- arrangement. The mono-substituted TMS core (**14**) has a resonance corresponding to the TMS group in the ¹H NMR spectrum at 0.25, as does the (1,4)- arranged analogue (**17**). Taking this as a "baseline" chemical shift for TMS protected ethynyl benzenes, compounds with a 1,2 arrangement (**15**, **18**, **19**, **21** and **22**) are downfield-shifted to 0.26 ppm while the (1,3)- substituted (**16**, **20**) appear an upfield-shifted at 0.24 ppm and the internal TMS group in a (1,2,3)- arrangement resonates at 0.28-0.29 ppm. Combinations of these effects rationalize the more complex arrangements; the (1,2,3,5)- (**22**) has 2 TMS groups with an effective (1,2)- arrangement, one with a

(1,3)- and one with a (1,2,3)-. The spectrum then shows three TMS peaks with a 1:2:1 ratio at 0.29 (1,2,3)-, 0.26 and 0.23 ppm. This pattern is present also in the ^{13}C NMR for the TMS methyl environments. The greater the resonance for a TMS environment is shifted downfield in the ^1H NMR, the further it appears downfield in the ^{13}C NMR spectrum.

The aryl protons from the TMS cores behave as expected. The spectrum of **14** has two multiplets as per an AA'MM'X spin system for monosubstituted phenyl rings. **15** has AA'BB' multiplet with H_{c2} being the downfield resonance. **16** and **19** have complex AMX systems, which leads to H_{c2} in **16** and H_{c3} in **19** superficially appearing as singlets, but displaying fine splitting due to long range coupling to protons on the other side of the aryl ring (H_{c4} in **16** and H_{c5} in **19**). The spectra of both compounds have an apparent doublet upfield; **16** also has an apparent triplet and **19** a doublet of doublets. The spectrum of **18** exhibits a doublet and a triplet, which don't appear to have any second-order coupling, while those of **20-24** all have singlets in the aryl region and that of **25** hasn't any aryl ^1H resonances.

Considering the mono-substituted (**14**) as a baseline for resonances in the ^{13}C NMR of the TMS-substituted cores, the acetylene carbons of **15** have both shifted due to the close proximity of the ethynyl groups. C_{19} , the alkynyl carbon furthest from the core is shifted downfield while C_{20} is shifted upfield from that of the mono- analogue. The equivalent environments in **16**, **17** and **20** resonate at the same chemical shift as that of **14** due to the distance between them. In **18** the (1,2,3)- relationship gives a 2:1 ratio of C_{20} and C_{19} environments, with C_{192} and C_{202} shifted downfield. **19** has the least symmetry and therefore the most resonances in the NMR; the chemical shifts of C_{194} and C_{204} are similar to those of **14** for the acetylene in the 4 position, while C_{20} and C_{202} are upfield and C_{192} / C_{19} resonances are downfield. With **21** and **22** the C_{202} resonances appear downfield of the C_{20} , as seen for the (1,2,3)- analogue. The spectrum of **23** is similar to **15** as it is essentially two fused (1,2)- systems, however the (1,3)- disposition gives a further upfield shift for C_{20} and downfield shift for C_{19} resulting in the two resonances being very close (101.9 and 100.8 ppm). This is also the case for C_{20} and C_{19} in the penta-substituted species (101.8 and 101.9 ppm). Surprisingly C_{202} is downfield of C_{203} . The hexa-substituted compound has only one environment for each arm carbon, with C_{20} at the same chemical shift as in **14** but C_{19} significantly downfield (to 94 ppm). The ^{13}C resonances of the quaternary core carbons resonate between 123 - 128 ppm, the more substituted species having the more downfield resonances. The tertiary carbons of the core resonate in the region 128-132 ppm, the most downfield resonances being those between two acetylene groups.

3.3.3 Organic cores

The ^1H NMR spectra for the organic cores are similar to those of the individual arm with some notable differences. Most carbon environments ($\text{C}_1\text{-C}_{13}$) remain the same as the tri(phenyleneethynylene) (**8**) starting material. Unsurprisingly there is the introduction of the core proton environments which are usually obscured by the aryl protons of the tri(phenyleneethynylene) (the H_{16} and H_{17} multiplet). For the less substituted compounds (**26-35**) the core protons resonate with the same multiplicity and chemical shift as those in the TMS core analogues. The arm protons H_{16} and H_{17} shift from the wide pseudo-doublets of the AA'BB' coupling system at 7.25 and 7.79 ppm to either a singlet (as in **26**, **32**, **35** and **44**) at around 7.52 ppm or a pseudo-quartet (actually a AA'BB' system) at 7.57 (**29**, **38**, **41**, **47**, **50**, **53**, **56** and **59**). This multiplicity is caused by having a (1,2)-arrangement in the molecule, as the proximity to the other phenyl rings around the core cause small differences in the magnetic environment. Obtaining the ^1H NMR spectrum of the larger systems can be difficult as the compounds have relatively few proton environments considering the size of the molecule and unfortunately running the spectrum at high concentrations causes shimming difficulties and therefore broadening of peaks.

^{13}C NMR spectra were obtained for these compounds and were assigned with the aid of a few HSQC and HMBC 2D NMR experiments of some of the smaller analogue compounds. TIPS and ethyl carbons resonate between 14 and 29 ppm, alkynyl carbons from 89-95 ppm (terminal acetylenes upon TIPS deprotection at 78), quaternary phenyl carbons at 120-124 ppm and the tertiary phenyl carbons at 125-131 ppm. Acquiring the ^{13}C NMR spectra was hampered by the solubility limitations of the compounds, as well as an abundance of quaternary carbon environments, some with a single environment per molecule (for instance **41** has 6 individual core carbon environments with three of them quaternary). The carbon environments from C_1 to C_{13} didn't change significantly from the tri(phenyleneethynylene) (**8**) and were used to guide assignment. C_{14} to C_{20} were shifted by the proximity of the phenyl-ethynyl units of the other arms on the compound and the core carbons underwent similar change. This is related to symmetry, with the more symmetrical compounds having fewer peaks. Full assignment of the (1-), (1,2)-, (1,3)- and (1,4)- was achieved using HSQC and HMBC 2D NMR techniques as these compounds are sufficiently soluble, and the carbon environments are populated by more than one atom per molecule allowing for sufficient signal. Knowing the assignment for the (1,2,4)-analogue it is then useful for assigning the larger complexes as it has common resonances

and magnetic environments exhibited by the others. The HMBC technique was used for this core arrangement but the benzene core, alkyne and quaternary phenyl carbons were insufficiently abundant to ascertain coupling cross-peaks for assignment. These resonances were assigned based on the assignments of the smaller bis-substituted compounds.

As shown in Figure 3.12, assignment of C₁₉ and C₂₀ in compound **41** can be achieved by comparison with **29** and **35**. C₂₀ appears to become three different environments in compound **41**. It has a peak at 91.6 ppm (C₂₀₄), which is the same as the C₂₀ environment in **35**, one at 93.9 ppm (C₂₀), which is the same as the C₂₀ in **29** and C₂₀₂ which is further downfield due to the influence from both extending arms at the 1 and 4 positions. C₁₉ follows the same trend except the shift is upfield and C₁₄ and C₁₃ have smaller differences consistent with their increased distance from the other arms. The quaternary phenyl carbons are difficult to accurately assign due to weak coupling to distant protons. C₉ can be assigned by coupling to H₁₀₁ of the methylene protons and C₁₂ is within 3 bonds of H₁₁. C₃ and C₆ can be assigned by coupling with H₄ and H₅ as with C₁₅ and C₁₈ to H₁₆ and H₁₇. C₁₈ and C₁₅ show multiple resonances.

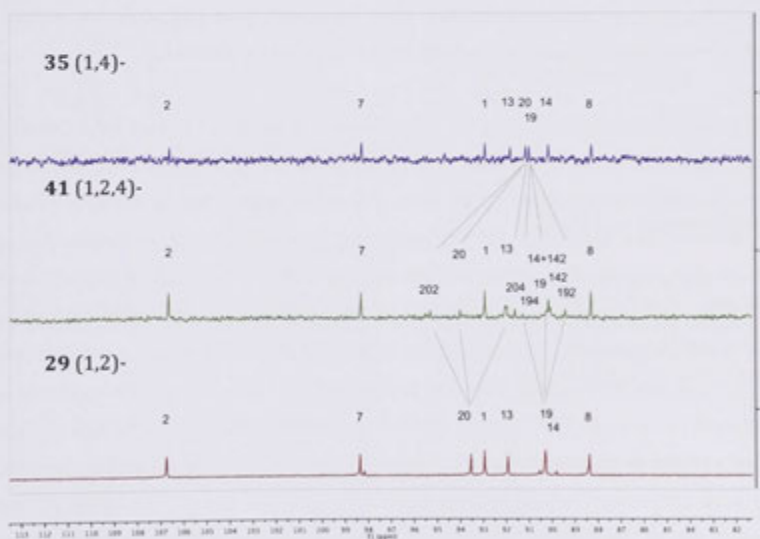


Figure 3.12 - Alkynyl carbon resonances for Compounds **29**, **35** and **41**.

Deprotection of the TIPS protected organics to form the terminal alkynyl compounds is characterised in the ¹H NMR by the formation of an alkyne peak at 3.19 ppm and the

disappearance of the 1.15 ppm TIPS protons. This results in an upfield shift of C₁ and C₂ to 78.9 and 83.3 ppm, respectively. The removal of the electron donating silyl group also causes C₃ (the quaternary phenyl peak) to shift upfield 3 ppm due to the same magnetic anisotropic effects.

3.3.4 Ruthenium alkynyl compounds

Metallation of the terminal acetylene results in little change in the ¹H NMR except the addition of the dppe aryl protons and the loss of the alkyne proton. H₄ is shifted upfield to 6.5 ppm due to the proximity of the ruthenium centre and the shielding by the dppe-bound phenyl groups. H₅ also has a shift upfield to around 7.00 ppm, which is obscured by the dppe proton environments but can be shown by HSQC techniques. Torsten Schwich has investigated these complexes in great detail in his 2013 thesis with full assignment of all peaks of both mono- and bis- acetylide complexes.⁴⁴ He showed that subtle electronic differences between the alkynyl and the chloride ligands cause a doubling of the dppe aryl peaks in both the carbon and proton NMR. The phenyl groups on the same side as the alkynyl ligand (assuming division along the Ru-P plane) are shifted downfield relative to those on the chloride side. This seems to affect the ortho- and meta- positions more than the para- (which has a very small change) as these are held closer to the metal and ligand. The doubling of these peaks disappears upon bis-substitution and a return to local symmetry (the acetylide ligands may still be unsymmetrically substituted).

The ¹³C NMR spectra were obtained for all complexes however all carbon environments were only observed for the complexes up to the tetra-substitutions. The hexa and penta analogues were soluble enough to only see a few of the alkynyl and quaternary phenyl peaks, however the dppe derived ¹³C peaks are characteristic of mono-substituted ruthenium alkynyl complex. Upon metallation the terminal acetylene carbon peaks (C₁ and C₂) shift downfield though C₁ is typically not observed. The literature shows this carbon couples to the phosphorus atoms around the metal and should exist as a quintet around 131 ppm.⁸⁶ It is therefore a small peak and probably obscured by the aryl environment in the molecule. C₄ and C₅ shift slightly upfield upon metallation as do C₃ and C₆, the quaternary phenyl environments on the ring immediately adjacent to the metal. The dppe ligands have two ortho- carbon resonances at 136 ppm (for the same reasons for the doubling of the corresponding protons) and meta- resonances at 126 ppm; the alkynyl facing rings possess the most downfield resonance. The para positions appear at 128 as a singlet. The carbon backbone of the dppe (C_b) and the ipso- position of the dppe aryl rings are multiplets (due to C-P coupling) and appear at 30.6 ppm (C_b) and 136 or 135 (C₁₁ and C₁₂ respectively).

The alkynyl ruthenium complexes all have the same ^{31}P NMR resonance at 49.3 ppm, which is evidence that the core arrangement has little effect on the metal centre. ^{31}P NMR is a useful technique for monitoring the progress of metal alkynyl addition. Ligand substitution on the metal leads to large change in chemical shift and is a good preliminary measure of purity during synthesis. Many possible side reactions or impurities can be formed in these couplings, mostly due to reaction of oxygen, solvents or adventitious chloride generation from chlorinated solvents. Throughout the synthesis of ruthenium dppe complexes the chemical shift of various side products and even products have been documented and tabulated in Table 3.1.

^{31}P Shift (ppm)	Species	Notes (removal)
-11.6	dppe free ligand	
34.0	$t\text{-[Ru(C=CHC}_6\text{H}_4\text{-4-NO}_2\text{)Cl(dppe)}_2\text{]PF}_6$	Vinylidene
34.7	$t\text{-[RuCl}_2\text{(dppeO)}_2\text{]}$	May also be a single P-oxide (Column: alumina or THF / MeOH cryst.)
35	$t\text{-[Ru(C=CHC}_6\text{H}_5\text{)Cl(dppe)}_2\text{]PF}_6$	Vinylidene
36.8	$t\text{-[Ru(C}\equiv\text{CC}_6\text{H}_5\text{)(C=CHC}_6\text{H}_5\text{)(dppe)}_2\text{]PF}_6$	Vinylidene
37.6 (t), 52.3 (t)	$c\text{-[RuCl}_2\text{(dppe)}_2\text{]}$	
41.8 (s)	$t\text{-[Ru(CO)Cl(dppe)}_2\text{]}$	Cleavage/oxidation of vinylidene (Column: alumina or acetone ppt'n).
42.		
45.7 (s)	$t\text{-[RuCl}_2\text{(dppe)}_2\text{]}$	2:1:0.5 P/D/NEt ₃ wash off Al
49.2 (s)	$t\text{-[RuC}\equiv\text{CC}_6\text{H}_4\text{-4-NO}_2\text{)Cl(dppe)}_2\text{]}$	
49.9 (s)	$t\text{-[Ru(C}\equiv\text{CC}_6\text{H}_5\text{)Cl(dppe)}_2\text{]}$	
52.3 (t) 37.6 (t)	$c\text{-[RuCl}_2\text{(dppe)}_2\text{]}$	(2:1:0.5 P/D/NEt ₃ column: Alumina or acetone ppt'n)
54.5 (s)	$t\text{-[Ru(C}\equiv\text{CC}_6\text{H}_5\text{)}_2\text{(dppe)}_2\text{]}$	
56.9 (t) 84.8 (t)	$[\text{RuCl(dppe)}_2\text{]PF}_6$	
59.2 (t) 60.0 (t)	$c\text{-[Ru(O}_2\text{C}_2\text{H}_5\text{)(dppe)}_2\text{]}$	Impure NaPF ₆ from recryst. acetate from impure MeCN.
60.0 (t) 59.2 (t)	$c\text{-[Ru(O}_2\text{C}_2\text{H}_5\text{)}_2\text{(dppe)}_2\text{]}$	β -elimination of MeOH
68.0 (s)	$t\text{-[Ru(C}\equiv\text{CC}_6\text{H}_5\text{)H(dppe)}_2\text{]}$	(2:1:0.5 P/D/NEt ₃ Column: alumina)
84.8 (t) 56.9 (t)	$[\text{RuCl(dppe)}_2\text{]PF}_6$	MeOH ppt'n

Table 3.1 – A list of common ^{31}P NMR impurities observed in alkynyl ruthenium complex syntheses (for bis-dppe auxiliary ligands only).

For the complexes synthesised in this chapter the most common impurity was the generation of *trans*-[RuCl₂(dppe)₂], which was removed by precipitation from acetone, or residual [RuCl(dppe)₂]PF₆, which was removed by precipitation from MeOH. Acetone may

be unsuitable for compounds with smaller alkynyl ligands but works well for mono-acetylides with over three phenylethynylene units in the ligand.

3.4 Linear optical properties

3.4.1 UV-Visible properties

The UV-Visible spectra of the TMS-protected core compounds, the TIPS-protected compounds and the metal complexes were obtained. There is a substantial change in the UV-Vis spectra between the different core substitutions, which was expected for the TMS cores due to the observation of Sonada *et al.* with phenyleneethynylene substituted compounds.⁷⁶

3.4.2 TMS cores

The UV-Visible data for the TMS-protected cores are provided in two figures for clarity (Figure 3.13 and Figure 3.14). They all exhibit a similar absorption at 260 nm with a similar shape, which is similar to the UV-Vis spectra of the tolanes synthesised by Kondo *et al.* although the lack of distinct low energy transitions is reduced because of the relative similarity of π -electron density (Kondo *et al.* had phenyl substitution).¹⁸ The molar absorptivity also increases with a higher substitution level, which is expected as the effective π -conjugation is increased. **15** has a unique intense peak at 241 nm where **17** has two lower energy peaks (279 and 294 nm). This may be due to the ease of conjugation through the core benzene, as the (1,4)- has the lowest energy barrier for resonance through the core. Compound **19** also has this band but at lower energy, owing to the larger π -conjugation as well as a (1,4)- substitution motif. Both **16** and **20** have a (1,3)-arrangement and also exhibit near identical absorption profiles. **18** has a weak absorption at 284 nm which is similar to the lowest energy band of **15**, which may suggest a transition with (1,2)- nature.

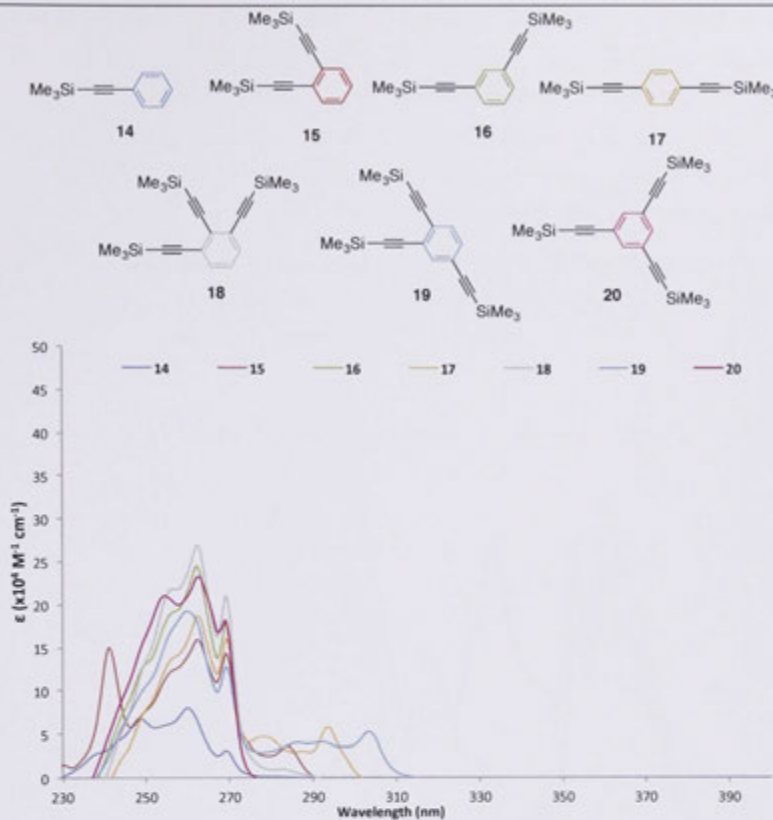


Figure 3.13 - Molecular structure (top) and UV-Vis spectra (bottom) of compounds 14-20.

Compound **21** has a (1,4)- substitution motif, and has a low energy transition at 309 nm (similar to other (1,4)- motif containing compounds). The lowest energy transition is common to the penta- (**24**) and hexa- (**25**) at 324 nm. The biggest difference between these spectra is the second lowest energy band at 305 nm for **25** and 290 nm for **24**. The level of substitution is fundamental to this difference. In the compounds with at least one (1,4)- arrangement the lowest transition energy decreases as a function of the number of (1,4)- relationships and the increase of π conjugation (ie. **17** > **19** > **21** \approx **22** > **23** > **24** \approx **25**).

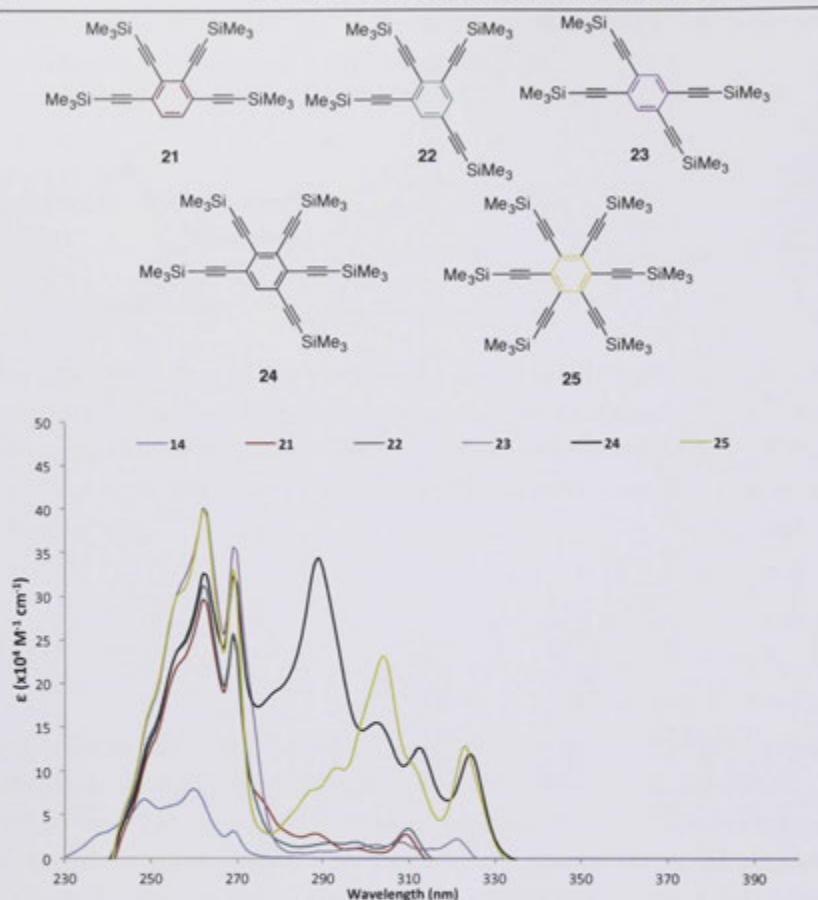


Figure 3.14 - Molecular structure (top) and UV-Vis spectra of compounds 21-25 (14 included for comparison).

3.4.3 TIPS-protected organic cores

During synthesis, the TIPS-protected organics were found to be highly fluorescent with some effects observed in natural light. **59** gives a strong green sheen on exposure, to natural light so UV-Visible and fluorescence measurements were conducted. In the UV-Vis spectra of the TIPS-protected compounds there appears to be three overlapping transitions, which are difficult to assign. The spectra (Figure 3.15) again display a bathochromic shift as the substitution level increases, as well as corresponding increases in molar absorptivity as was observed with the TMS-protected core compounds. There is also a shift of about 10 nm on increasing the extent of (1,4)- substitution at the core (increasing the ease of conjugation through the core of the compound). **53**, which contains effectively two (1,4)- relationships, has a much lower energy transition than **47** or **50**,

which have only one (1,4)-disposed arrangement, even though they are all tetra-substituted. The same transitions in the spectra of compounds **26** and **29** are much higher in energy than the spectra of **35**. This is also seen with the tri- and tetra- substitution groups. **59** has the highest λ_{max} as it has a larger π -conjugation. There is a clear separation of the two major peaks, which may be due to steric influences in the molecule, causing rotation of an arm and effectively breaking the conjugation path. This will be discussed further in later sections.

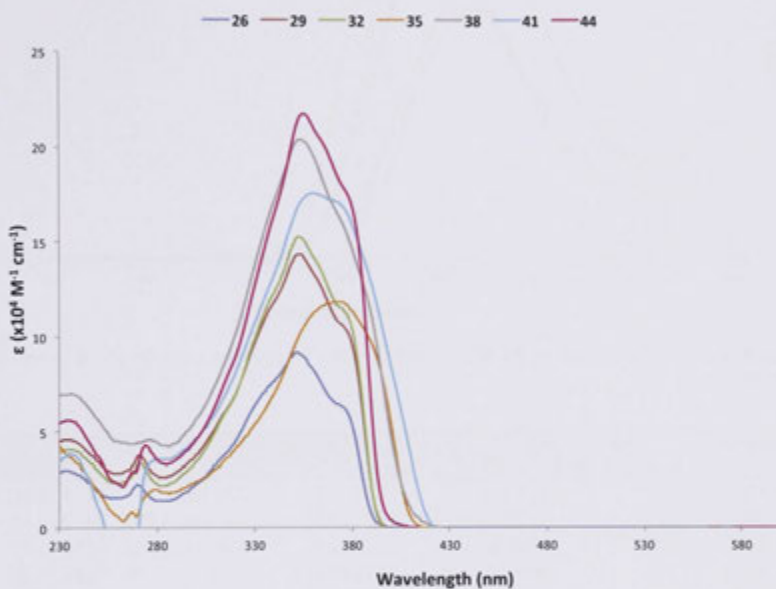


Figure 3.15 - UV-Vis spectra of the mono-, bis- and tris-TIPS-protected core compounds.

A summary of peak data for these compounds is given in Table 3.2. **26**, **29** and **32** are quite similar which is anomalous considering the differences observed in the TMS core compounds of the same substitution (**15** and **16**).

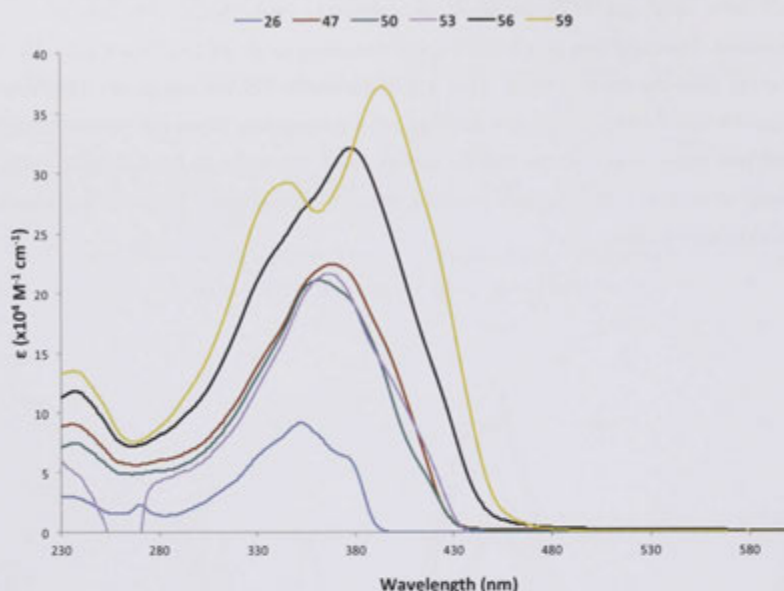


Figure 3.16 - The UV-Vis spectra for the tetra-, penta- and hexa-TIPS-protected cores (26 (mono-) added for comparison).

Compound	Core arrangement	λ (nm) [ϵ ($10^4 \text{ M}^{-1} \text{ cm}^{-1}$)]				
26	(1)-	376 [sh, 6.2]	352 [9.2]	339 [sh, 7.3]	274 [1.8]	
29	(12)-	379 [sh, 9.9]	357 [13.9]	340 [sh, 11.9]	274 [3.4]	
32	(13)-	378 [sh, 11.1]	356 [14.9]	338 [sh, 12.0]	274 [3.5]	
35	(14)-	389 [sh, 9.8]	378 [11.6]	-	288 [2.8]	
38	(123)-	378 [sh, 16.2]	358 [19.9]	-	280 [4.4]	
41	(124)-	377 [sh, 16.6]	362 [17.5]	-	275 [3.2]	
44	(135)-	367 [sh, 19.8]	359 [21.2]	-	271 [3.9]	
47	(1234)-	395 [sh, 15.6]	372 [22.2]	-	-	
50	(1235)-	378 [sh, 19.3]	366 [20.8]	-	-	
53	(1245)-	401 [sh, 11.9]	372 [21.3]	-	-	
56	(12345)-	397 [sh, 25.4]	383 [31.6]	335 [22.6]	-	
59	(123456)-	420 [sh, 24.8]	397 [36.6]	348 [26.1]	-	

Table 3.2 - Summary of UV-Vis optical absorption maxima data for the TIPS protected organic cores.

The fluorescence of the TIPS-protected cores was analysed by measuring the excitation and emission maxima for each compound. The excitation maxima differ from the absorption maxima of the complex, in that the emission scan displays the optimal input wavelength for the largest resultant emission. The compounds show excitation bands from 380 nm to 420 nm. Compounds containing more than four substitutions have two excitation peaks. The emission peaks for all compounds have a low-energy shoulder at *ca.*

400 to 430 nm for most, with the penta- and hexa- substituted compounds having the lowest emission maximum at 448 and 472 nm, respectively.

Compound	Core arrangement	Excitation Maximum	Emission Maximum
26	(1)-	390	408
29	(1,2)-	406	418
32	(1,3)-	351	408
35	(1,4)-	381	406
38	(1,2,3)-	393	409
41	(1,2,4)-	373	417
44	(1,3,5)-	391	410
47	(1,2,3,4)-	406	430
50	(1,2,3,5)-	407	434
53	(1,2,4,5)-	407	433
56	(1,2,3,4,5)-	423	448
59	(1,2,3,4,5,6)-	390	472

Table 3.3 - Fluorescence data for the TIPS-protected cores (26-59).

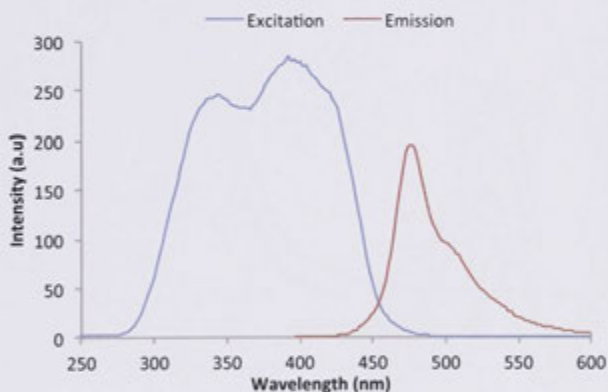


Figure 3.17 - The excitation (blue) and emission (red) traces for compound 59.

The difference between the excitation and emission peaks (Stokes shift) loosely represents the non-radiative energy loss of the excited state. Thus, the hexa-substituted compound has the largest Stokes shift of around 80 nm, while the others have Stokes shifts of 20-30 nm. There is little correlation in the tabulated data to the UV absorption maxima. It should be noted that the excitation spectra differs from the absorption maxima. Again, the core geometry influences the excitation energy for all compounds. Compounds with a (1,2)- structural motif appear to have a lower excitation energy with **29**, **47**, **50** and **53** all having similar energies; the exception is the (1,2,3)-substituted (**38**). **56** has the lowest at 423 nm but **59** strangely is similar to **26**. **32** has the highest excitation energy,

possibly related to the (1,3)- substitution, however **44** is closer to the other trisubstituted (**38** and **41**) and even the (1,4)-substituted (**35**). The excitation-emission spectrum for **59** is shown in Figure 3.17. As previously stated the excitation has two peaks and the emission shows a major peak at 472 nm, which has a shoulder peak of a possible vibrational transition at ca. 490 nm. Time resolved fluorescence measurements are probably needed to comment further as there may be more effects contributing to these values.

3.4.4 Metallated cores

The UV-Visible spectra of the metallated species (Figure 3.18 and Figure 3.19) are quite similar to those of the precursor organic compounds with an additional MLCT band at around 420-430 nm. Erandi Kulasekera has modeled the UV-Vis spectra of these compounds computationally with good agreement to experimental values, which may make some assignments possible.⁸⁷

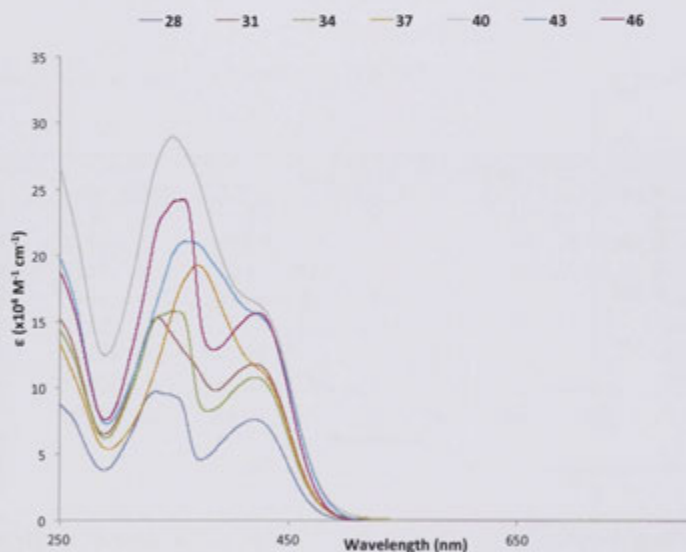


Figure 3.18 - UV-Vis spectra of the mono-, bis- and trisubstituted alkynyl ruthenium complexes (**28**,**31**,**34**,**37**,**40** and **46**).

The compounds with lower metal content (**28**, **31**, **34**, **37**, **40** and **43**) clearly show the MLCT band at 420 nm (Figure 3.18). There is surprisingly little change of the MLCT transition wavelength as the extent of core substitution increases. It would be expected that as the overall π -conjugation length increases the energy levels would change, resulting in a lower transition energy. This may suggest that the metal centre is isolated from the core electronically, which is likely due to out of plane rotation of the phenyl rings

relative to each other. The crystal structure of **28** (Figure 3.9) would seem to support this. The larger compounds (**46-61**) possess blue shifted MLCT bands in this region (420-390 nm), which seem to be an overlap of several different bands. There is a continuing decrease in energy of the $\pi-\pi^*$ transition bands as the extent of substitution increases to a point where the band in **61** overlaps the MLCT band entirely and has a much higher molar absorptivity. Based on the lack of change in the smaller complexes it is most likely there is no change in the MLCT band and the $\pi-\pi^*$ band obscures the direct observation. This is applicable to complexes **58** and **61**.

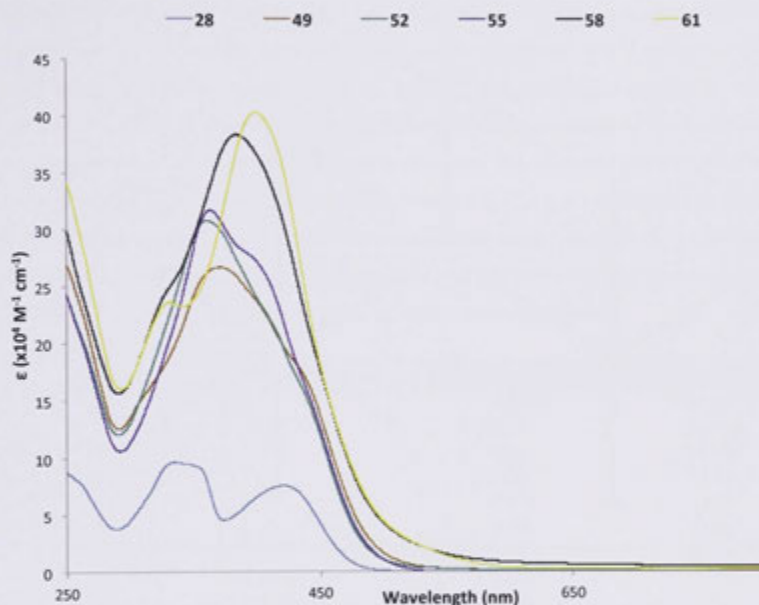


Figure 3.19 - UV-Vis spectra of the tetra-, penta- and hexa-substituted alkynyl ruthenium complexes (mono- (**28**) for comparison).

Cmpd	Core arrangement	λ (nm) [ϵ ($10^4 \text{ M}^{-1} \text{ cm}^{-1}$)]			
28	(1)-	426 [7.46]	367 [sh,9.1]	341 [9.5]	254 [sh, 7.5]
31	(1,2)-	425 [11.7]	369 [sh,12.0]	342 [15.1]	257 [sh,13.6]
34	(1,3)-	428 [11.6]	367 [12.1]	341 [15.4]	254 [sh,14.1]
37	(1,4)-	432 [sh,10.6]	378 [18.5]	-	-
40	(1,2,3)-	429 [sh,15.3]	353 [28.8]	-	-
43	(1,2,4)-	431 [sh,14.9]	368 [20.9]	-	-
46	(1,3,5)-	430 [15.0]	357 [24.0]	-	-
49	(1,2,3,4)-	430 [sh,18.4]	375 [26.6]	315 [sh,16.3]	-
52	(1,2,3,5)-	434 [sh,16.2]	355 [30.7]	-	-
55	(1,2,4,5)-	436 [sh,16.5]	404 [26.5]	369 [31.1]	-
58	(1,2,3,4,5)-	388 [sh,38.0]	-	332 [25.]	-
61	(1,2,3,4,5,6)-	406 [sh,39.7]	-	335 [23.4]	-

Table 3.4 - Summary of UV-Vis data for the alkynyl ruthenium complexes 28-61.

The band at around 340 nm can be assigned as a $\pi\text{-}\pi^*$ transition localized on the organic phenylethynyl ligand. There is a slight blue shift in this band upon addition of a metal. The hexa- and penta-substituted compounds have a second $\pi\text{-}\pi^*$ transition at a high energy, at a similar energy to the third transition of the mono-substituted compound. This may be a transition caused by isolation of a single arm from the core since it is mainly observed in the more sterically demanding compounds. This is also observed in the (1,2,3,4)-

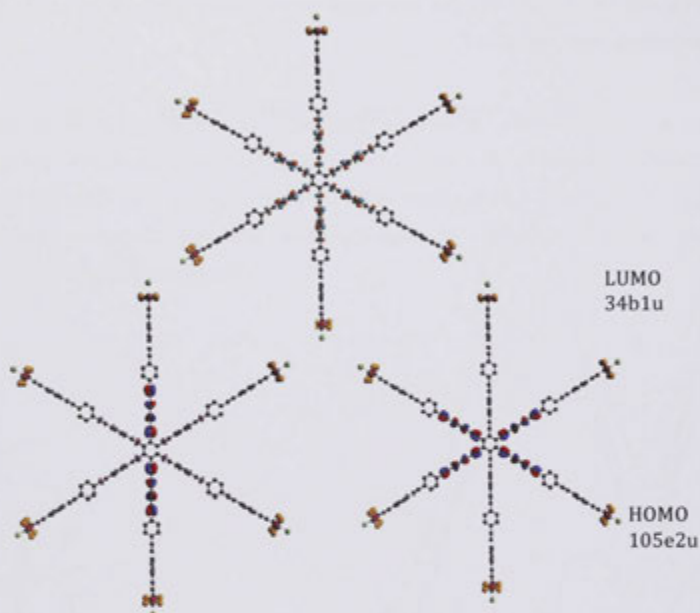


Figure 3.20 - HOMO and LUMOs in the hexa-substituted compound (61) that align with the 335 nm transition (calculations performed by Erandi Kulasekera).

substituted compound, although it is weaker and is obscured in the (1,2,3)- analogue by the primary $\pi\text{-}\pi^*$ band.

The complexes have similar features to the complexes Chris Corkery had made (Figure 3.6). The MLCT bands are at *ca.* 400 - 430 nm (*cf.* 405 - 445 nm of the Corkery set). This is inconsistent with precedents in which replacement of ethyl with ethoxy groups usually resulting in a blue shift in the MLCT bands. The $\pi\text{-}\pi^*$ transitions in his complexes also show the bathochromic shift upon substitution level increase; the (1,4)-substituted however is outlying of this trend. The UV-Vis $\pi\text{-}\pi^*$ maxima of the ethoxy compounds appear at 308 nm for the (1)- substituted, 326 nm for the (1,4)-, 315 nm for the (1,3,5)- and 320 nm for the (1,2,4,5)-substituted. Based on the trend observed for the ethyl solubilised complexes the (1,4)- should be at higher energy than the (1,2,4,5)- due to a longer effective π -conjugation in the latter complex. This would suggest that inclusion of

the ethoxy moiety changes the conjugation through the core due to steric effects, therefore the larger complexes would have a higher energy π - π^* transition.

3.5 Electrochemistry

3.5.1 Cyclic voltammetry and spectroelectrochemistry

Cyclic voltammetry data of the ruthenium complexes are summarised in Table 3.5. Cyclic voltammetry studies for all complexes revealed a reversible process at around 0.6 V. The voltammograms also show irreversible processes at around 1.5 V common to these complexes, probably an oxidation of the organic component. Employing a switching potential of 1.6 V with these complexes can lead to misshapen peaks on the reverse sweep due to deposition of the degraded compounds onto the electrodes. To counter this, a preliminary run is carried out in the potential range 1.6 V to -1.6 V to observe all processes followed by cleaning of the electrode before the next scan. A limited scan was then run from 0 to 1.2 V which afforded processes satisfying the reversibility / quasi-reversibility conditions, from which $E_{1/2}$ and reversibility values were calculated.

Compound	Core arrangement	$E_{1/2}$ RuII/III (V)	$[i_{pc}/i_{pa}]$
28	(1)-	0.58	[0.90]
31	(1,2)-	0.59	[0.95]
34	(1,3)-	0.59	[0.95]
37	(1,4)-	0.59	[1.0]
40	(1,2,3)-	0.60	[1.0]
43	(1,2,4)-	0.59	[1.0]
46	(1,3,5)-	0.61	[0.96]
49	(1,2,3,4)-	0.59	[0.96]
52	(1,2,3,5)-	0.58	[0.95]
55	(1,2,4,5)-	0.58	[0.90]
58	(1,2,3,4,5)-	0.62	[1.0]
61	(1,2,3,4,5,6)-	0.59	[1.0]

Table 3.5 – Summary of cyclic voltammetry data for ruthenium complexes.

The oxidation potentials of these complexes are in a similar range to previously reported values for ruthenium mono-alkynyl complexes with auxiliary dppe ligands (usually 0.50 – 0.58 V).^{41,42} There doesn't seem to be any trend in the CV data as the core structure is altered, which is further evidence that the phenylethynyl ligand has little effect on the metal centre. Alterations on the ligand can lead to changes in the oxidation potential in the metal centre, as seen in Rigamonti *et al.* with studies on lengthening the phenylethynyl chain.⁴³ The researchers had a nitro- functionalized ligand which exhibited lower oxidation potentials as the bridge length was increased, which is most likely due to increasing rotation of the oligo(phenyleneethynylene) rings isolating and eventually

decoupling the metal donor and nitro- acceptor. Figure 3.1 shows the reversibility of complex **28**, with multiple scans at different rates.

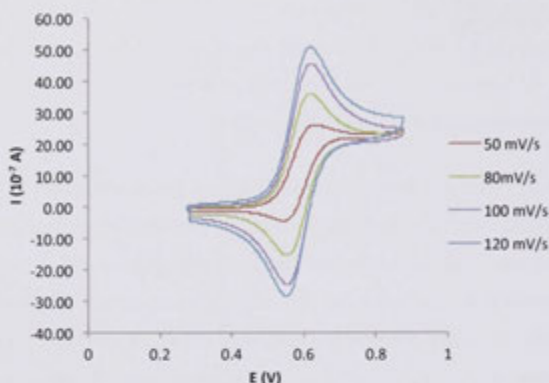


Figure 3.21- Cyclic voltammetry of the mono-complex (**28**) run at four different rates

The complexes do not behave reversibly in the OTTLE cell (Figure 3.22) when run at room temperature. Complexes **28**, **31**, **37**, **46**, **55** and **61** were used for spectroelectrochemistry measurements as these have the highest symmetry (**31** excepted) and are representative of each substitution group. When running the experiment the absorptions at 426-430 nm (MLCT bands) and 341 nm reduce and new bands at 487 nm and 922-935 nm grow in on oxidation. The voltage is increased progressively from 0.5 to 1.2 V to oxidise the metal centre with sufficient speed. Upon switching the voltage back to 0 V to regenerate the starting complex the 426-430 nm peak grows back in very slowly and the 920 - 930 nm band reduces. The poor reversibility is probably an issue with the OTTLE cell used, as the cell isn't constantly under a flow of argon. It is also possible that the complex just isn't stable for long periods of time oxidized at room temperature. This type of measurement is preferably run at greatly reduced temperature to prevent complex degradation. The new bands formed are lowest for **37** at 935 nm, 933 nm for **28**, 929 nm for **31** and **61**, 922 nm for **46** and 909 nm for **55**. The difference in the wavelength is probably of little significance however, **55** was run after **61**, which had significant deposition on the electrode during the scan. The **55** trace is therefore contorted and oxidation is incomplete which gives the strange, broad shaped peak at 909 nm. The reported value for this peak should then be regarded with caution.

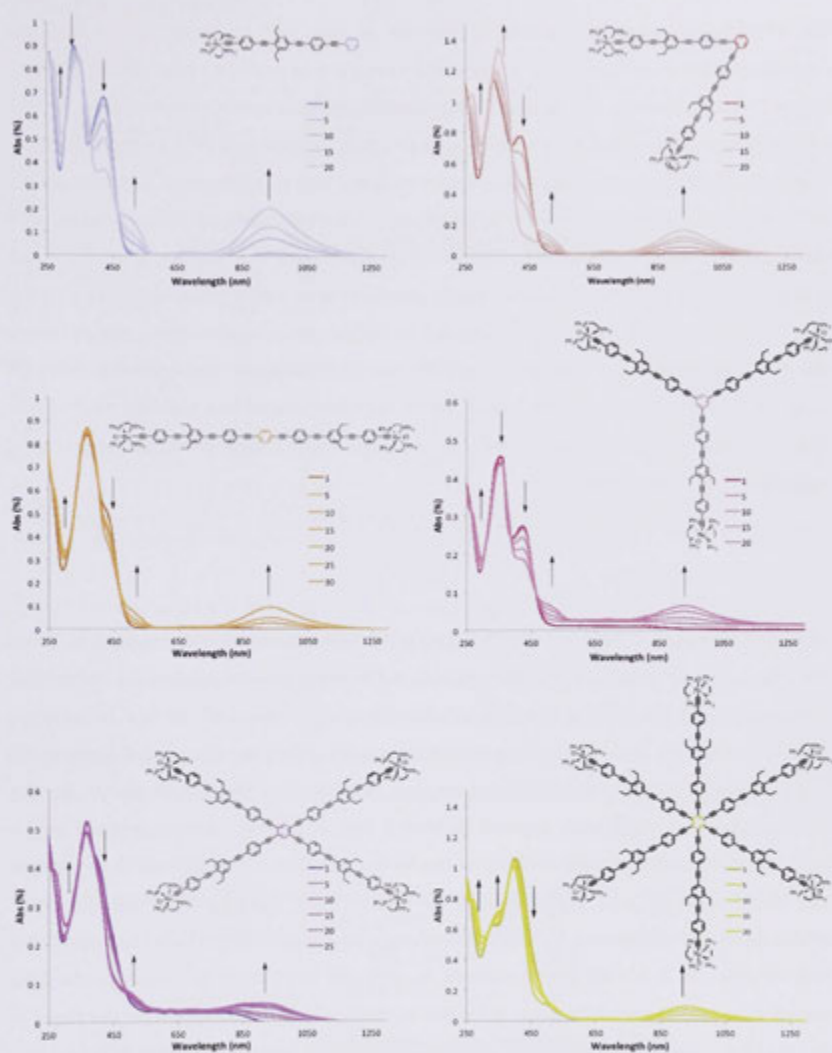


Figure 3-22 - Six spectroelectrochemical plots of complexes 28, 31, 37, 46, 55 and 61. Arrows denote changes in absorbance with oxidation of the complexes. 55 is distorted due to incomplete oxidation and optical interference from deposited compounds.

3.6 Nonlinear optical properties

The third-order nonlinear optical properties of the TIPS-protected cores and the ruthenium alkynyl complexes were measured over a broad spectral range (500-1800 nm) by the Z-scan technique. The access to long wavelengths was a recent development for the RSC laser set-up and difficulty was encountered fitting the traces at very long wavelengths within the limited sample progression width with the lens focal length of 120 mm. As the wavelength of the beam increases the beam waist also increases, which correspondingly increases the size of the closed and open aperture traces. This created problems with fitting curves above 1500 nm as the closed aperture curve peaks got progressively closer to the window edge. A 75 mm lens was used for subsequent measurements, which meant the TIPS-protected cores are run with a 75 mm lens, whereas the ruthenium alkynyl complexes are run with a 120 mm lens. This means the comparison between the organic and organometallic compounds is difficult, although comparison within the organics or organometallics permissible.

3.6.1 TIPS-protected cores

The nonlinear optical data for the TIPS-protected compounds are summarised in Table 3.6. Data are reported at the two-photon absorption maximum for the respective compound (580 nm for **26** and 620 nm for the rest). Compound **35** had insufficient solubility in CH_2Cl_2 at a high enough concentration for measurement. γ_{real} values broadly increase as the extent of substitution increases, maximising with compound **59**. **41**, the least symmetrical compound, appears to have a high γ_{real} value surpassing those of the other tris-substituted as well as those of the tetra-substituted. It is difficult to rationalise this observation as these values tend to have large error margins at wavelengths with strong nonlinear absorption. The γ_{real} value shown for compound **38** should be considered with caution, as it is very low compared to even the bis-substituted compounds. This carries over into the absolute γ value for this material; the majority following the trend of increased substitution leading to an increase in value. The compounds were typically self-defocusing from 500 – 900 nm, switching to self-focusing at longer wavelengths. The two-photon absorption maximum for the smallest compound (**26**) is at 580 nm where the rest appear at 620 nm. This is expected as the π -delocalisation is greater for the others, however this doesn't go further, as one could imagine the largest (**59**) having a 2PA max at longer wavelength than the rest. The two-photon absorption cross-section also increases as the extent of substitution increases, the largest value being for **59** at 5600 GM. This is a large value for an organic compound.

	Core arrangement	λ_{\max} (nm)	2PA $_{\max}$ λ (nm)	γ_{real} (10^{-36} esu)	γ_{imag} (10^{-36} esu)	$\langle\gamma\rangle$ (10^{-36} esu)	$\sigma_{2,\max}$ (GM)
26	(1)-	352	580	-3 195	1 503	3 531	694 ± 80
29	(1,2)-	357	620	-8 200	2 800	8 665	1 135 ± 120
32	(1,3)-	356	620	-9 780	3 550	10 404	1 438 ± 190
35*	(1,4)-	378					
38	(1,2,3)-	358	620	-810	4 849	4 916	1 959 ± 270
41	(1,2,4)-	362	620	-14 900	5 410	15 860	2 197 ± 210
44	(1,3,5)-	359	620	-10 400	4 691	11 409	1 895 ± 210
47	(1,2,3,4)-	372	620	-7 114	7 300	10 193	2 949 ± 490
50	(1,2,3,5)-	366	620	-15 445	7 758	17 284	3 134 ± 630
53	(1,2,4,5)-	372	620	-10 300	8 410	13 297	3 397 ± 440
56	(1,2,3,4,5)-	383	620	-30 478	10 414	32 208	4 207 ± 870
59	(1,2,3,4,5,6)-	397	620	-37 596	13 955	40 102	5 638 ± 850

*35 had insufficient solubility in CH_2Cl_2 for the experiment requirements. 75 mm lens utilised.

Table 3.6 - NLO data for the TIPS-protected organic compounds at the TPA maximum.

The 2PA cross-section is also highest for the most symmetrical species (59 and 53) with the exception of 44 (1,3,5-substituted), which is comparable to or smaller than other tris-compounds. In this case the (1,2,4)- compound is slightly larger which may due to the 1,4-disposed moiety, as all compounds with at least one 1,4 substitution have a 2PA cross-section above 2000 GM. This proposition would be stronger with the data for compound 35. The relative efficiency of two-photon absorption for each TIPS-protected compound is shown in Table 3.7.

	Core arrangement	$\sigma_{2,\max}$ (GM)	$\sigma_{2,\max} / \pi e^-$ (GM/e)	$\sigma_{2,\max} / M$ (GM/amu)
26	(1)-	694 ± 80	34.7	1.1
29	(1,2)-	1135 ± 120	32.4	1.0
32	(1,3)-	1438 ± 190	41.1	1.2
35*	(1,4)-			
38	(1,2,3)-	1959 ± 270	39.2	1.2
41	(1,2,4)-	3076 ± 330	43.9	1.3
44	(1,3,5)-	1895 ± 210	37.9	1.1
47	(1,2,3,4)-	2949 ± 490	45.4	1.3
50	(1,2,3,5)-	3134 ± 630	48.2	1.4
53	(1,2,4,5)-	3397 ± 440	52.3	1.5
56	(1,2,3,4,5)-	4207 ± 870	52.6	1.5
59	(1,2,3,4,5,6)-	5638 ± 850	59.3	1.7

Table 3.7 - TPA efficiency data of the TIPS-protected organics scaling by σ_2 , per π -electron or molecular weight.

The best performing compound by these metrics is the hexa-substituted complex with values of 59 GM per π -electron. The (1,2,4,5) configuration (**53**) has a comparable efficiency to the penta-substituted (**56**).

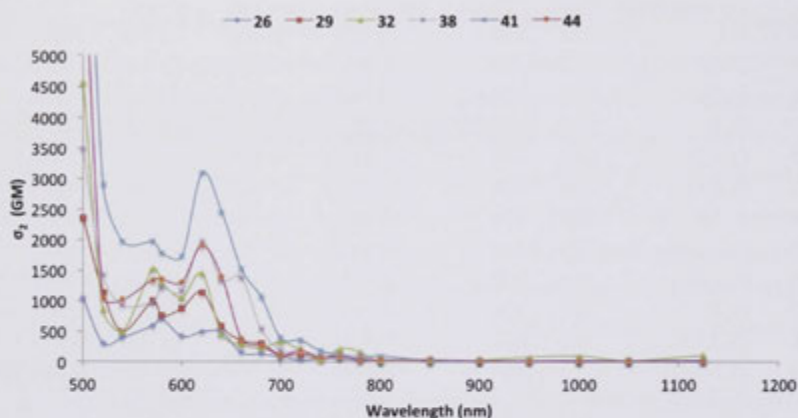


Figure 3.23 - TPA cross-section traces for mono-, bis-, and tris-substituted TIPS-protected organic compounds (**28**, **29**, **32**, **38**, **41** and **44**). A trend line has been added as a visual aid.

Comparative plots of the 2PA cross-section (σ_2) traces between the TIPS-protected complexes are plotted in Figure 3.23 and Figure 3.24. Error bars have been omitted for clarity. All traces show the maximum 2PA cross-section at 620 nm (580 nm for **28**) as well as local maxima at 560 nm. There is also a common maximum at 700 nm for the larger compounds, most prominent in **53**, **56** and **59**. These compounds have 2 (or more) (1,4)-

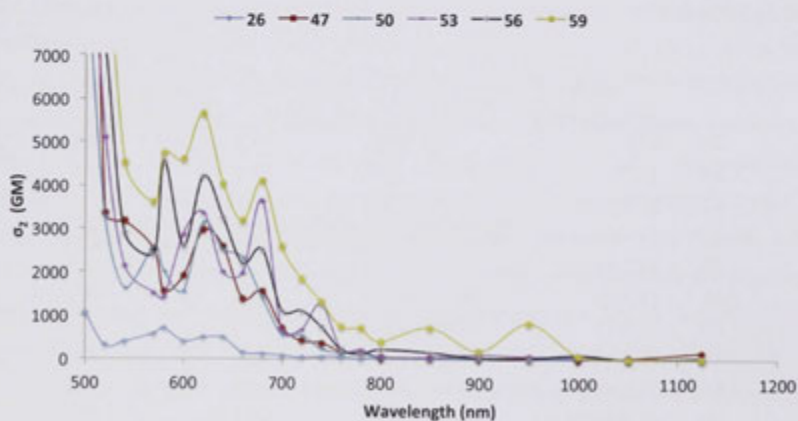


Figure 3.24 - TPA cross-section traces for mono-, tetra-, penta-, and hexa-substituted TIPS-protected organic compounds (**28**, **47**, **50**, **53**, **56** and **59**). A trend line has been added as a visual aid.

disposed arms which may be the cause of this maximum. During the measurement of these compounds some two-photon fluorescence was observed in the infrared wavelengths (700-1100 nm). At the intersection of the beam with the sample deep blue or aqua light emission was observed, which correlates well with the excitation-emission data discussed previously (part 3.4.3), the larger compounds having a lower energy emission. Second harmonic generation was ruled out, as the emission colour did not change with a change in wavelength, suggesting the two-photon excitation degrades to a common energy level before radiative emission to the ground state.

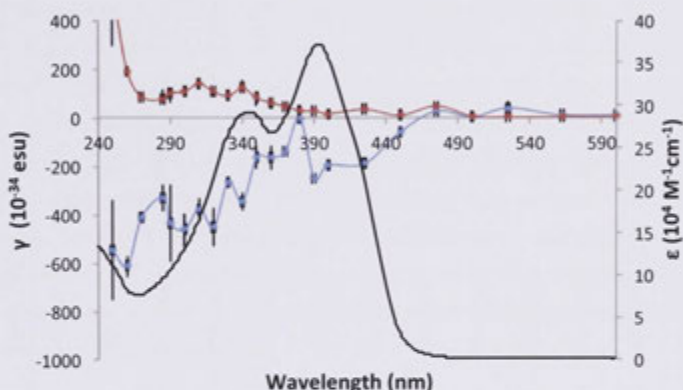


Figure 3.25 - γ_{real} (blue) and γ_{imag} (red) values for 59 at half the measurement wavelength overlaid on the UV-Vis spectrum (black). A trend line has been added to the γ traces as a visual aid.

Based on the limited scaling factors considered, the highest 2PA_{max} efficiency TIPS-protected core is the hexa-substituted core, closely followed by the penta- and tetra-substituted cores ($59 > 56 \sim 53 > 50 > 47$). This follows 2PA cross-section trends observed by Bhasker *et al.* for the authors symmetrically varied annulenes discussed in the introduction.⁷¹

3.6.2 Ruthenium alkynyl complexes

A summary of the third-order NLO properties of the ruthenium alkynyl complexes at the two-photon absorption maxima is shown in Table 3.8. All twelve complexes have two local maxima at 660-740 nm and 850 nm with the 850 nm being consistent with other ruthenium alkynyl complexes (see Chapters 1 and 2). The values at 850 nm are similar between complexes with the same extent of substitution, in particular the bis-substituted around 4000 GM and the tetra-substituted around 8000 GM.

Complex	Core arrangement	λ_{\max} (nm)	First σ_2 maximum			Second σ_2 maximum		
			$\lambda_{TPA\max}$ (nm)	$\langle\gamma\rangle$ (10^{-36} esu)*	σ_2 (GM)	$\lambda_{TPA\max}$ (GM)	$\langle\gamma\rangle$ (10^{-36} esu)*	σ_2 (GM)
28	(1)-	426	680	47 600	$2\,080 \pm 430$	850	21 920	$2\,240 \pm 800$
31	(1,2)-	425	680	103 400	$5\,540 \pm 660$	850	94 360	$4\,410 \pm 1200$
34	(1,3)-	428	680	132 500	$3\,770 \pm 690$	850	50 910	$4\,960 \pm 1300$
37	(1,4)-	432	660	42 400	$3\,060 \pm 900$	850	21 450	$3\,770 \pm 1030$
40	(1,2,3)-	429	680	159 000	$5\,810 \pm 1140$	850	71 270	$3\,840 \pm 3840$
43	(1,2,4)-	431	680	256 600	$9\,570 \pm 1940$	850	165 200	$7\,550 \pm 2860$
46	(1,3,5)-	430	680	149 400	$6\,990 \pm 1190$	850	237 230	$4\,630 \pm 1320$
49	(1,2,3,4)-	434	740	107 000	$10\,080 \pm 2370$	850	310 720	$7\,570 \pm 3200$
52	(1,2,3,5)-	434	720	121 400	$8\,580 \pm 2280$	850	248 940	$7\,660 \pm 3400$
55	(1,2,4,5)-	436	700	229 000	$15\,430 \pm 2840$	850	274 500	$7\,970 \pm 2200$
58	(1,2,3,4,5)-	388	740	159 300	$13\,560 \pm 4560$	850	251 250	$8\,390 \pm 2060$
61	(1,2,3,4,5,6)-	406	700	355 000	$11\,910 \pm 1823$	850	265 190	$10\,800 \pm 2160$

* Error margins for these values are on the order of 20-25 %. Experiment utilised a 120 mm lens.

Table 3.8 - Third-order nonlinear optical data for alkynyl ruthenium complexes.

The TPA cross-section values broadly increase with increase in extent of substitution, with **61** having the largest TPA value (10 800 GM). **43** doesn't follow this trend with a 2PA value almost twice that of the other tris-substituted compounds.

There doesn't appear to be any observable trend in the TPA cross-section data at the first σ_2 maximum. The smaller complexes from mono- to tris-substitution tend to have the maximum at 680 nm, with the tetra-, penta- and hexa- having erratically trending values (from 700 – 740 nm). Here the (1,2,4,5)-substituted (**55**) has the larger cross-section (15 000 GM) followed by the penta- (**58**) then the hexa-. The complexes were typically self-focusing on the closed-aperture experiment. A 120 mm lens was used for this set of compounds and, as discussed in Chapter 2, the longer focal length lens typically causes overestimation of the Y_{real} values due to increased transmission through the aperture. This may be reflected in the $\langle Y \rangle$ values displayed in Table 3.8 which shows no clear trend at the first σ_2 maximum, however those at the second max increase with extent of substitution. The 680 – 740 nm range correlates well to twice the $\pi-\pi^*$ transition in these complexes, which may be the origin of this maxima, however this would require accurate comparison to the organic analogues, which further requires measurement with a 75 mm lens. This is currently underway.

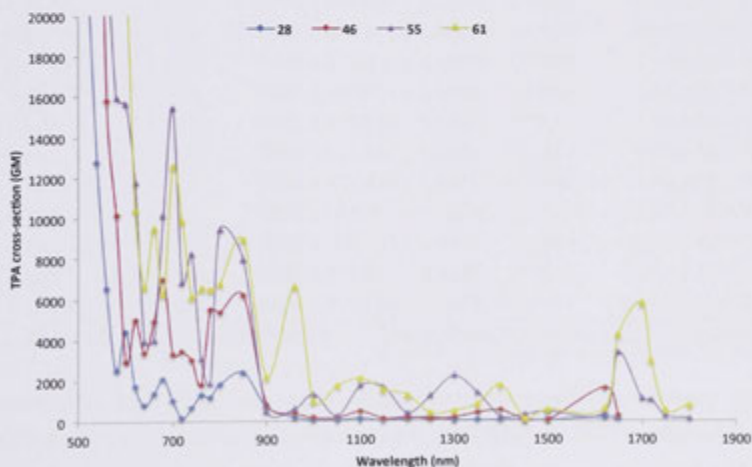


Figure 3.26 - 2PA cross-section comparison for compounds **28**, **46**, **55** and **61**.

A 2PA comparison plot of compounds **28**, **46**, **55** and **61** is displayed in Figure 3.26. These four compounds were chosen as these are the most commonly used core structures in ruthenium alkynyl complexes for nonlinear optics, and assessing the NLO response for

each will help for future investigations. The high symmetry of these compounds is desirable for the ease of synthesis and characterisation as discussed earlier in this Chapter. **55** has the highest 2PA cross-section at 700 nm yet **61** is highest at 850 nm. **46**, **55** and **61** all have a very long wavelength maximum between 1600 and 1700 nm. Considering the gradient of the open-aperture trace at this wavelength it is very likely this is a combination of multi-photon absorption events. The magnitude of the band at 1700 nm for compound **61** appears a bit extreme as it is over twice that for the other complexes. The (1,2,4,5)- and hexa-substituted cores outperform the (1,3,5)- at most wavelengths for 2PA cross-section values. This would suggest their utilisation in alkynyl ruthenium dendrimers would be beneficial to the 2PA properties of such complexes. The 2PA efficiency of the complexes are shown in Table 3.9 and appear to show the hexa-substituted complex does not perform the best when judged by these metrics. 2PA cross-section per π -electron or mass appears to favor the (1,2,4)-substituted complex, which is hard to justify on a structural basis. The σ_2 value is very high compared to the other trisubstituted compounds and seems to be overestimated. Further investigation is required to rationalise this result; the ability to compare between the organic and organometallic analogue would be ideal.

Core	λ_{\max} (nm)	2PA $_{\max}$ λ (nm)	$\sigma_{2,\max}$ (GM)	$\sigma_{2,\max} / \pi e^-$ (GM/e) ^a	$\sigma_{2,\max} / M$ (GM/amu)
28 (1)-	426	850	2 240 ± 512	53.3	1.6
31 (1,2)-	425	850	4 413 ± 1214	59.6	1.6
34 (1,3)-	428	850	4 966 ± 1667	67.1	1.8
37 (1,4)-	432	850	3 771 ± 1037	51.0	1.4
40 (1,2,3)-	429	850	3 844 ± 1383	36.3	1.0
43 (1,2,4)-	431	850	7 553 ± 2860	71.3	1.9
46 (1,3,5)-	430	850	4 633 ± 1320	43.7	1.2
49 (1,2,3,4)-	430	850	7 573 ± 3280	54.9	1.4
51 (1,2,3,5)-	434	850	8 330 ± 3650	55.5	1.4
55 (1,2,4,5)-	436	850	7 968 ± 2380	57.7	1.5
58 (1,2,3,4,5)-	388	850	8 389 ± 2070	49.3	1.3
61 (1,2,3,4,5,6)-	406	850	10 800 ± 2160	53.5	1.4

^a120 nm lens utilised. Ruthenium considered as contributing 2 electrons

Table 3.9 - 2PA efficiency at the cross-section maximum.

The three-photon absorption cross-section values for the twelve complexes were calculated from 1100 nm to 1800 nm and the maximum displayed in Table 3.10. The $\sigma_{3,\max}$ values have two maxima, the largest at 1700 nm, in a region expecting four-photon absorption (roughly four times λ_{\max}), and another at 1250-1300 nm (three times λ_{\max}). The σ_3 values at 1250-1300 nm are comparable in magnitude to previously characterised ruthenium alkynyl complexes ($2.5 \times 10^{-77} \text{ cm}^6 \text{ s}^2$)⁴⁴ with the exception of the (1,2,3,5)-analogue which is at 8.5×10^{-77} although the error for this value is considerable. There

seems to be no common structural motif between **40**, **46** and **58** to explain the maximum at 1250 nm rather than 1300 nm. **61** has a longer wavelength maximum at 1400 nm. The nature of the second peak is difficult to assign. It is within the expected region for four-photon absorption, however the fitting of the open aperture trace at this wavelength is indicative of more than one multi-photon absorption event, or perhaps excited-state absorption in combination with one of the effects mentioned previously. Further investigation is required to deconvolute the processes occurring here, however for discussions sake, assume three-photon absorption. The σ_3 values for **46**, **49** and **51** maximise at 1650 nm rather than 1700 nm as the others do. This may be an issue with the sample size utilised at the IR wavelengths (measurements at every 50 nm). It may be that the maximum is between 1650 and 1700 nm as seen in the σ_3 plot of the **43**, **46**, **49**, **51** and **55** where there are only small differences between the values at the two measured wavelengths. Due to the long times required to obtain measurements for a single wavelength it isn't realistic to measure at smaller sampling rates, however wavelength of interest may be sampled at a more frequent rate. This wavelength range will be investigated over more points in the subsequent measurements for these compounds.

Core	λ_{\max} (nm)	First		Second	
		λ (nm)	σ_3 ($10^{-77} \text{ cm}^6 \text{ s}^2$)	λ (nm)	σ_3 ($10^{-77} \text{ cm}^6 \text{ s}^2$)
28 (1)-	426	1300	0.08 ± 0.03	1700	1.54 ± 0.05
31 (1,2)-	425	1300	3.87 ± 2.04	1700	10.85 ± 0.27
34 (1,3)-	428	1300	1.20 ± 0.47	1700	3.86 ± 0.09
37 (1,4)-	432	1300	2.35 ± 1.19	1700	1.18 ± 0.03
40 (1,2,3)-	429	1250	1.34 ± 0.11	1700	6.64 ± 0.17
43 (1,2,4)-	431	1300	6.38 ± 3.57	1700	1.80 ± 0.05
46 (1,3,5)-	430	1250	1.27 ± 0.25	1650	4.68 ± 0.11
49 (1,2,3,4)-	430	1300	3.40 ± 1.80	1650	8.55 ± 1.13
51 (1,2,3,5)-	434	1300	8.52 ± 4.23	1650	10.07 ± 0.29
55 (1,2,4,5)-	436	1300	5.64 ± 2.84	1700	10.52 ± 0.28
58 (1,2,3,4,5)-	388	1250	1.61 ± 0.03	1700	12.48 ± 0.35
61 (1,2,3,4,5,6)-	406	1400	2.83 ± 0.79	1700	84.10 ± 2.03

Table 3.9 - 3PA cross-sections of the alkynyl ruthenium complexes.

The hexa-substituted (**61**) has the largest σ_3 at 1700 nm, eight times that of the tetra- (**49**, **51**, **55**) and penta- (**58**) and the (1,2)-substituted (**31**), which has a value on the same order as these complexes. The (1,2,4)- complex (**43**), which shows a large 2PA cross-section and high 2PA efficacy underperforms as a 3PA material at 1700 nm, but has the second highest value at 1300 nm, albeit with a large margin of error.

The ruthenium alkynyl complexes have larger 2PA cross-sections than the organic analogues and they follow the same trend of increasing 2PA values with increasing core substitution. However, the efficacy of 2PA, considering the two scaling metrics used, does not follow as the hexa-substituted complex performs worse by these metrics than lower substituted complexes. There is no straightforward trend between similarly sized complexes of different substitution pattern in the observed NLO responses. This is also the case for the 3PA data, in which the larger complexes have considerably larger cross-sections, a topic requiring further investigation.

3.7 Concluding remarks

A series of star-shaped ruthenium alkynyl complexes with twelve different core substitution patterns were synthesised. The composition of the complexes and precursor compounds were confirmed by ^1H , ^{13}C and ^{31}P NMR techniques. Differences in the ^1H and ^{13}C NMR spectra between each substitution pattern were limited to the nuclei on and around the core; those on the periphery remain the same. ^{31}P NMR chemical shifts were equivalent for all core substitutions. All compounds except the linear analogue were too large for analysis by the mass spectrometry techniques available. The UV-vis spectra were collected and compared. The energy of the main $\pi\text{-}\pi^*$ transition was lowered upon increased substitution level as well as increased conjugation through the core in the form of 1,4-substitution moieties. The MLCT in the alkynyl ruthenium complexes is unaffected by core substitution, suggesting that there is appreciable isolation from the core. Longer conjugation lengths afforded by favorable core conjugation paths should lower the MLCT band, as seen in other ruthenium alkynyl examples. The electrochemical behaviour of the ruthenium alkynyl complexes are similar to others previously synthesised, with oxidation potentials at around 0.6 V; isolation from the molecular core results in identical potentials. The electrochemical properties were also similar with an introduction of an absorption band at around 900 nm upon oxidation. The third-order NLO properties of the TIPS-protected organic compounds and the ruthenium alkynyl complexes were obtained by the Z-scan technique. The TIPS-protected organic molecules have large 2PA cross-sections, which maximize at 620 nm (580 nm for the smallest molecule (**26**)) with the hexa-substituted compound having the largest σ_2 value of the set. The hexa-substituted compound maintains σ_2 supremacy even when scaled for molecular weight and π -electron number. The 1,4-disposed analogue was not soluble enough for a concentration sufficient for Z-scan analysis. The alkynyl ruthenium complexes show large 2PA cross-sections at

850 nm, and substantial 3PA at longer wavelengths. In absolute terms, the hexa-substituted complex has the highest 2PA value and would be an interesting structural motif to incorporate in larger dendrimer complexes. When 2PA cross-section is scaled for molecular mass and π -electron count the (1,2,4)-substituted complex (**43**) has higher 2PA efficiency, which may make a case for future investigations into low symmetry complexes. The ability to accurately compare the organic and organometallic complexes synthesised would shed light on this result, and Z-scan measurements are currently being conducted on a 75 mm lens set-up.

3.8 Experimental section

3.8.1 Atom labeling

Protons and carbons are labeled 1 through 20 from the terminal acetylene (1) to the arene core-attached acetylene (20). The ethyl solubilising groups' C and H atoms are labeled by the carbon number to which they are attached to (10) followed by the number of carbons from the attached atom (1 or 2). The **silyl** protecting groups' Hs and Cs are labeled 's' to denote silyl attachment, followed by the carbon number the to which the silyl is attached (e.g. 7) and finally the number of carbons from the silicon (i.e. 1 for the methyne and 2 for the methyl moiety on TIPS). The **ruthenium dppe** Hs and Cs are labeled with a letter denoting the phenyl position (i.e. i for the P-bound ipso position), followed by a number designating which side the phenyl group sits on the metal and phosphorus group plane: 1 is for the alkynyl-bound face and 2 for the chloro-bound face. b denotes the dppe backbone H or C. The arene **core** labeling starts with 'c' denoting a core derived atom, followed by a number (1-6) based on counting around the ring in the standard IUPAC fashion. Magnetically equivalent atoms are assigned the same label. An example is provided for the (1,2,4)-substituted core. In some instances, atoms are magnetically inequivalent with others in a similar structural environment in the molecule (e.g. C₁₇-C₂₀ in the 1,2,4- substituted core). A number denoting core carbon number attachment is added to the end of the atom label (i.e. C₂₀ attached to C₂ on the core becomes C₂₀₂).

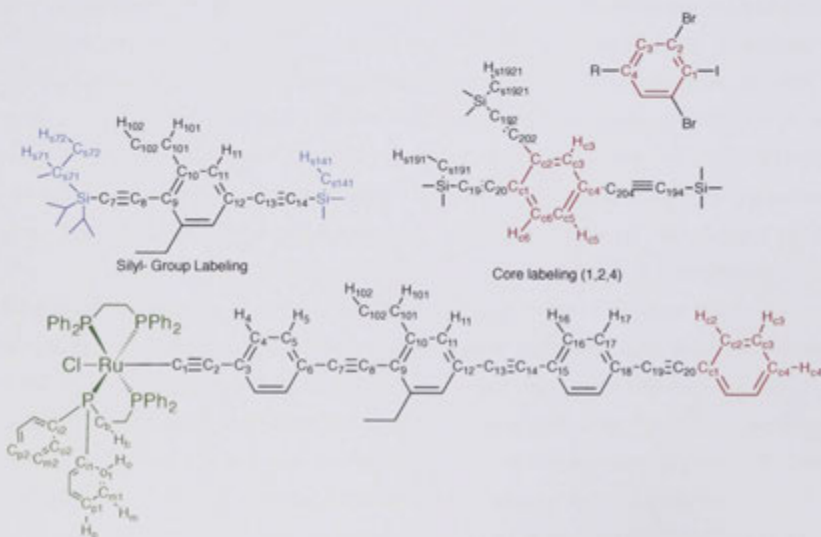


Figure 3.21 – Atom assignment in NMR spectra.

3.8.2 Materials

All commercially available materials were used as received with the exception of ZnCl_2 which was desiccated at 110 °C under vacuum for 18 h prior to use. The compounds $[\text{RuCl}(\text{dppe})_2]\text{PF}_6^{88}$ and (2-(4-iodophenyl)ethynyl)triisopropylsilane⁸⁹ were prepared following literature procedures. All reactions were carried out under Schlenk conditions unless otherwise stated. Diethyl ether, toluene and THF were dried by distilling over sodium/benzophenone before use. CH_2Cl_2 was dried by distillation over CaH_2 . Petrol refers to a fraction of petroleum spirits with a boiling range 60 – 80 °C. Chromatography was on silica gel (230-400 mesh) or basic alumina.

3.8.3 Instrumentation

Mass spectra were recorded by the ANU Mass Spectrometry Unit staff using a Micromass/Waters LC-ZMD single quadrupole liquid chromatograph-MS ((ESI⁺) MS, both unit resolution and HR on acetonitrile solutions), a VG Quattro II triple quadrupole MS (EI MS, unit resolution on CH_2Cl_2 solutions) and a VG AutoSpec M series sector (EBE) MS (HRMS (EI⁺) on CH_2Cl_2 solutions). Unit resolution EI⁺ data are reported as m/z (fragment, abundance (a.u.)); HR EI⁺ and ESI⁺ are reported as m/z (calcd [elemental composition] m/z). UV-vis spectra were recorded in CH_2Cl_2 in 1 cm quartz cells using a Cary 5 spectrophotometer and are reported in the form wavelength (nm) [extinction coefficient ($10^4 \text{ M}^{-1} \text{ cm}^{-1}$)]. Microanalyses were carried out by either the Microanalytical Unit staff at the Research School of Chemistry at the Australian National University or at London Metropolitan University. Instability precluded analysis of the terminal alkyne species of the organic cores. ¹H-NMR spectra were recorded using a Varian MR-400 FT NMR spectrometer or a Bruker Avance-400 HD FT NMR spectrometer; spectra are referenced to residual chloroform (7.26 ppm). ¹³C-NMR spectra were recorded using a Varian MR-400 FT NMR spectrometer and are referenced to *d*-chloroform (77.0 ppm). ³¹P-NMR spectra were recorded using a Bruker Avance-400 HD FT NMR spectrometer and are referenced to external 85% H_3PO_4 (0.0 ppm). HMBC and HSQC NMR Spectra were obtained with a Varian MR-400 FT NMR spectrometer. Fluorescence data were obtained using a Cary Eclipse fluorescence spectrophotometer in 1 cm quartz vials using solutions in distilled CH_2Cl_2 . Cyclic voltammetric measurements were recorded using a MaLab 400 interface and potentiostat from eDAQ. Measurements were performed on CH_2Cl_2 solutions containing 0.1 M $(\text{Bu}_4\text{N})\text{PF}_6$ with ca. 5 mg of complex, using Pt working, Pt auxiliary and

Ag-AgCl reference electrodes. All scans were performed under an argon atmosphere. Scan rates of 50, 80, 100 and 120 mV s⁻¹ were used to ascertain reversibility ratios. E_{1/2} values are referenced to an internal sample of ferrocene (E_{1/2} = 0.56 V). UV-Vis spectra of the oxidised species were obtained at 298 K by generation in an OTTLE cell at potentials above the E_{1/2} of the complex with 0.1 M (Bu₄N)PF₆ as supporting electrolyte.

Spectral dependence Z-scan experiments were run using a light source consisting of a Quantronix Integra-C3.5F pumping a Quantronix Palitra-FS optical parametric amplifier, tuneable over a wavelength range from 460 nm to 1600 nm, which was confirmed by a Ocean optics USB2000+ spectrometer (500-1000 nm) or an Ocean optics NIR-Quest spectrometer (1000-1800 nm). The output delivered 130 fs pulse with a 1 kHz repetition rate. Coloured glass filters and a Thorlabs polarizing filter were used to remove unwanted wavelengths and the power adjusted by use of neutral density filters to obtain nonlinear phase shifts between 0.1 to 1.3 rad. The focal length of the beam at the experiment was either 120 mm or 75 mm (where specified), obtained by the use of an appropriate lens. A 120 mm lens gave a Gaussian beam waist of 25-60 μm (depending on wavelength) and the 75 mm lens gave 25-45 μm beam waist, both of which give Rayleigh lengths longer than the sample thickness. Samples travelled down the Z axis on a Thorlabs motorised stage between 0 and 100 mm with a 120 mm lens, and between 5-45 mm with a 75 mm lens. Data was collected by three Thorlabs photodiodes, 500-900 with Si based detectors, 900-1300 nm with InGaAs detectors and 1300-2000 nm with amplified InGaAs detectors. Data from the detectors were collected by a Tektronix oscilloscope feeding a custom LabVIEW program (written by Marek Samoc) permitting fitting of a theoretical trace. A sample of CH₂Cl₂ was run at each wavelength as an aid in referencing to a 3 mm fused silica plate; the real and imaginary components of the second hyperpolarisability (γ) of the materials were calculated assuming additivity to these reference samples.

3.8.4 Experimental data for compounds 1 - 61

Synthesis of 2,6-diethyl-4-((trimethylsilyl)ethynyl)aniline (1)

2,6-Diethyl-4-iodoaniline (3.1 g, 11.3 mmol) was added to a mixture of PdCl₂(PPh₃)₂ (20 mg, 1.37 mmol) and CuI (19 mg, 0.50 mmol) in deoxygenated triethylamine (50 mL). Trimethylsilylacetylene (1.6 mL, 11.4 mmol) was added and the mixture stirred at room temperature for 12 h. The mixture was filtered to remove the precipitate and the filtrate added to ether and then extracted with an aqueous solution of NH₄Cl and then brine. The solvent was removed from the organic phase under vacuum and the residue purified by column chromatography on silica, eluting with a mixture of *n*-hexane and ethyl acetate (10:1). The

solvent was removed to give a waxy brown solid, which was then crystallised from methanol and water. 2,6-Diethyl-4-((trimethylsilyl)ethynyl)aniline was obtained as light brown crystals (2.45 g, 88 %). R_f (hexane:EtOAc, 10:1) - 0.15. MS (EI^+): 245.1 ($[M]^+$, 92), 230.1 ($[M - Me]^+$, 100). HRMS (EI^+): $[M]^+$ 245.1603 (calcd $[C_{15}H_{23}NSi]$ 245.1603). *Anal.* calcd for $C_{15}H_{23}NSi$: C, 73.41; H, 9.44; N, 5.71. Found: C, 73.42; H, 9.65; N, 5.82. 1H NMR (δ , 400 MHz, $CDCl_3$): 0.23 (s, 9H, H_{Si41}), 1.25 (t, 6H, H_{102} , $J_{HH} = 7.6$ Hz), 2.48 (q, 4H, H_{101} , $J_{HH} = 7.6$ Hz), 3.79 (bs, 2H, NH_2), 7.11 (s, 2H, H_{11}). ^{13}C NMR (δ , 101.5 MHz, $CDCl_3$): 0.2 (C_{Si41}), 12.7 (C_{102}), 23.9 (C_{101}), 90.7 (C_{14}), 106.8 (C_{13}), 111.9 (C_{12}), 127.1 (C_{10}), 129.9 (C_{11}), 142.3 (C_9).

Synthesis of (3,5-diethyl-4-iodophenyl)ethynyltrimethylsilane (2)

2,6-Diethyl-4-((trimethylsilyl)ethynyl)aniline (2.15 g, 10.7 mmol) was added to distilled ether (60 mL) and the resultant mixture cooled to -20 °C in a dry ice / acetone bath. $BF_3 \cdot (OEt)_2$ (12 mL, 45.5 mmol, 50% solution in ether) was added to the mixture dropwise over 30 min. *tert*-Butyl nitrite (4.4 mL, 34.1 mmol) was then added and the mixture stirred at -20 °C for 30 min and then allowed to warm to 5 °C over 10 min. Cold ether (50 mL) was added and a yellow precipitate was formed after 20 min stirring. This was collected by filtration, washed with cold ether and then added to MeCN (20 mL). A mixture of NaI (3.2 g, 21.6 mmol) and I_2 (0.2 g, 0.8 mmol) in MeCN (10 mL) was then added dropwise and the mixture stirred overnight. An aqueous solution of $Na_2S_2O_3$ was then added to the stirring mixture. The product was extracted with ether and the organic layer dried with Na_2SO_4 . The solvent was removed and the residue purified by column chromatography using silica, eluting with hexane. The solvent was removed from the eluate under reduced pressure to give (3,5-diethyl-4-iodophenyl)ethynyltrimethylsilane as a colourless solid (2.07 g, 64 %). R_f (hexane) - 0.64. MS (EI^+): 356.1, ($[M]^+$, 60), 341.0 ($[M - Me]^+$, 100). HRMS (EI^+): $[M]^+$ 356.0464 (calc. $[C_{15}H_{21}ISi]$ 356.0464). *Anal.* calcd for $C_{15}H_{21}ISi$: C, 50.56; H, 5.94. Found: C, 50.89; H, 6.08. 1H NMR (δ , 400 MHz, $CDCl_3$): 0.24 (s, 9H, H_{Si41}), 1.21 (t, 6H, H_{102} , $J_{HH} = 7.6$ Hz), 2.77 (q, 4H, H_{101} , $J_{HH} = 7.6$ Hz), 7.14 (s, 2H, H_{11}). ^{13}C NMR (δ , 101.5 MHz, $CDCl_3$): 0.1 (C_{Si41}), 14.5 (C_{102}), 35.4 (C_{101}), 94.7 (C_{14}), 104.5 (C_{13}), 107.9 (C_9), 122.9 (C_{12}) 129.0 (C_{11}), 147.3 (C_{10}).

Synthesis of $Pr_3SiC \equiv CC_6H_2-2,6-Et_2-4-C \equiv CSiMe_3$ (3)

3,5-Diethyl-4-iodophenyl)ethynyltrimethylsilane (2.05 g, 5.75 mmol) was added to triethylamine (40 mL) and the resultant mixture deoxygenated. $Pd(PPh_3)_4$ (20 mg, 0.01 mmol) and CuI (30 mg, 0.15 mmol) were added and the mixture stirred at room temperature for 5 min. Triisopropylsilylacetylene (1.35 mL, 5.8 mmol) was then added and the mixture stirred at room

temperature for 12 h. The solvent was removed under reduced pressure and the residue purified by column chromatography on silica, eluting with petrol. The solvent was removed to give ${}^1\text{Pr}_3\text{SiC}\equiv\text{CC}_6\text{H}_2\text{-2,6-Et}_2\text{-4-C}\equiv\text{CSiMe}_3$ as a colourless solid (2.25 g, 95 %). R_f (petrol) - 0.50. MS (EI^+): 410.3 ($[\text{M}]^+$, 40), 395.3 ($[\text{M} - \text{Me}]^+$, 20), 367.2 ($[\text{M} - \text{Pr}]^+$, 100). HRMS (EI^+): 410.2825 (calcd $[\text{C}_{26}\text{H}_{42}\text{Si}_2]$ 410.2825). *Anal.* calcd for $\text{C}_{26}\text{H}_{42}\text{Si}_2$: C, 76.02; H, 10.31. Found: C, 75.89; H, 10.38. ${}^1\text{H}$ NMR (δ , 400 MHz, CDCl_3): 0.24 (s, 9H, H_{Si141}), 1.13 (s, 21H, $\text{H}_{\text{C71}} + \text{H}_{\text{C72}}$), 1.22 (t, 6H, H_{102} , $J_{\text{HH}} = 7.6$ Hz), 2.81 (q, 4H, H_{101} , $J_{\text{HH}} = 7.6$ Hz), 7.16 (s, 2H, H_{11}). ${}^{13}\text{C}$ NMR (δ , 101.5 MHz, CDCl_3): 0.1 (C_{Si141}), 11.4 (C_{C71}), 14.7 (C_{102}), 18.6 (C_{C72}), 28.1 (C_{101}), 94.9 (C_{14}), 100.2 (C_8), 103.2 (C_{13}), 105.387 (C_7), 122.3 (C_{12}), 122.5 (C_9), 128.8 (C_{11}), 146.9 (C_{10}).

Synthesis of ${}^1\text{Pr}_3\text{SiC}\equiv\text{CC}_6\text{H}_2\text{-2,6-Et}_2\text{-4-C}\equiv\text{CH}$ (4)

(Note: This reaction was not conducted under an inert atmosphere.)

${}^1\text{Pr}_3\text{SiC}\equiv\text{CC}_6\text{H}_2\text{-2,6-Et}_2\text{-4-C}\equiv\text{CSiMe}_3$ (1.77 g, 4.30 mmol) was added to a mixture of CH_2Cl_2 and methanol (1:1, 30 mL) followed by K_2CO_3 (0.7 g, 5.1 mmol) and the mixture stirred for 2 h. Water was added, the product was extracted with CH_2Cl_2 and the organic phase was dried with Na_2SO_4 . After filtration, the solvent was removed from the filtrate under reduced pressure to give ${}^1\text{Pr}_3\text{SiC}\equiv\text{CC}_6\text{H}_2\text{-2,6-Et}_2\text{-4-C}\equiv\text{CH}$ as a colourless liquid (1.26 g, 86 %). R_f (hexane) - 0.57. MS (EI^+): 338.2 ($[\text{M}]^+$, 40), 295.2 ($[\text{M} - \text{Pr}]^+$, 100). HRMS (EI^+): $[\text{M}]^+$ 338.2432 (calcd $[\text{C}_{23}\text{H}_{34}\text{Si}]$ 338.2430). ${}^1\text{H}$ NMR (δ , 400 MHz, CDCl_3): 1.15 (s, 21H, $\text{H}_{\text{C71}} + \text{H}_{\text{C72}}$), 1.25 (t, 6H, H_{102} , $J_{\text{HH}} = 7.6$ Hz), 2.81 (q, 4H, H_{101} , $J_{\text{HH}} = 7.6$ Hz), 3.10 (s, 1H, H_{14}), 7.19 (s, 2H, H_{11}). ${}^{13}\text{C}$ NMR (δ , 101.5 MHz, CDCl_3): 11.5 (C_{C71}), 14.9 (C_{102}), 18.8 (C_{C72}), 28.2 (C_{101}), 77.9 (C_{14}), 84.1 (C_{13}), 100.8 (C_8), 103.2 (C_7), 121.5 (C_{12}), 122.8 (C_9), 129.1 (C_{11}), 147.1 (C_{10}).

Synthesis of ${}^1\text{Pr}_3\text{SiC}\equiv\text{CC}_6\text{H}_2\text{-2,6-Et}_2\text{-4-C}\equiv\text{CC}_6\text{H}_4\text{-4-Br}$ (5)

${}^1\text{Pr}_3\text{SiC}\equiv\text{CC}_6\text{H}_2\text{-2,6-Et}_2\text{-4-C}\equiv\text{CH}$ (2.9 g, 12.1 mmol) and 4-bromoiodobenzene (3.40 g, 12.1 mmol) were added to deoxygenated triethylamine (40 mL) and the solution cooled in an ice bath. $\text{Pd}(\text{PPh}_3)_4$ (25 mg, 0.02 mmol) and CuI (16 mg, 0.08 mmol) were then added and the mixture stirred for 3 h maintaining the temperature at 0 °C. The solvent was then removed under vacuum and the residue passed through a short pad of silica, eluting with petrol. The solvent was removed under vacuum to give ${}^1\text{Pr}_3\text{SiC}\equiv\text{CC}_6\text{H}_2\text{-2,6-Et}_2\text{-4-C}\equiv\text{CC}_6\text{H}_4\text{-4-Br}$ as a colourless liquid (3.1 g, 92 %). R_f (hexane) - 0.48. MS (EI^+): 494.2 ($[\text{M}]^+$, 55), 451.1 ($[\text{M} - \text{Pr}]^+$, 100). HRMS (EI^+): $[\text{M}]^+$, 494.1830 (calcd $[\text{C}_{29}\text{H}_{37}^{81}\text{BrSi}]$ 494.1827). ${}^1\text{H}$ NMR (δ ,

400 MHz, CDCl₃): 1.15 (s, 21H, H₅₇₁ + H₅₇₂), 1.26 (t, 6H, H₁₀₂, *J*_{HH} = 7.6 Hz), 2.84 (q, 4H, C₁₀₁, *J*_{HH} = 7.6 Hz), 7.22 (s, 2H, H₁₁), 7.38 (appd (AA'BB'), 2H, H₁₆, *J*_{AB} = 8 Hz), 7.48 (appd (AA'BB'), 2H, H₁₇, *J*_{AB} = 8 Hz). ¹³C NMR (δ, 101.5 MHz, CDCl₃): 11.3 (C₅₇₁), 14.8 (C₁₀₁), 18.6 (C₅₇₂), 28.0 (C₁₀₁), 89.1 (C₁₄), 90.8 (C₁₃), 100.4 (C₈), 103.2 (C₇), 122.2 (C₁₅ and C₁₈), 122.4 (C₁₄), 122.7 (C₉), 128.4 (C₁₁), 131.6 (C₁₇), 132.9 (C₁₆), 147.0 (C₁₀).

Synthesis of HC≡CC₆H₂-2,6-Et₂-4-C≡CC₆H₄-4-Br (6)

¹Pr₃SiC≡CC₆H₂-2,6-Et₂-4-C≡CC₆H₄-4-Br (10.30 g, 20.87 mmol) followed by TBAF (21 mL, 21 mmol, 1 M in THF) was added to CH₂Cl₂ (30 mL) and the solution stirred for 2 h. Water was added and the organic layer separated, dried with MgSO₄, and the solvent removed under vacuum. The residue was purified using column chromatography on silica, eluting with hexane. The solvent was removed and the residue crystallised by slow diffusion of MeOH into a CH₂Cl₂ solution. HC≡CC₆H₂-2,6-Et₂-4-C≡CC₆H₄-4-Br was isolated as colourless crystals (6.08 g, 95 %). *R*_f(hexane) - 0.42. MS (EI⁺): 338.0 ([M]⁺, 100). HRMS (ESI⁺): [M]⁺, 338.0489 (calcd [C₂₀H₁₇⁸¹Br] 338.0489). *Anal.* calcd for C₂₀H₁₇Br: C, 71.23; H, 5.10. Found: C, 71.29; H, 5.10. ¹H NMR (δ, 400 MHz, CDCl₃): 1.28 (t, 6H, H₁₀₂, *J*_{HH} = 7.8 Hz), 2.82 (q, 4H, H₁₀₁, *J*_{HH} = 7.8 Hz), 3.53 (s, 1H, H₇), 7.23 (s, 2H, H₁₁), 7.37 (appd (AA'BB'), 2H, H₁₇, *J*_{AB} = 8 Hz), 7.48 (appd (AA'BB'), 2H, H₁₆, *J*_{AB} = 8 Hz). ¹³C NMR (δ, 101.5 MHz, CDCl₃): 14.8 (C₁₀₂), 28.0 (C₁₀₁), 80.2 (C₈), 86.14 (C₇), 89.2 (C₁₄), 90.6 (C₁₃), 120.9 (C₁₂), 122.2 (C₉), 122.4 (C₁₈), 122.7 (C₁₅), 128.4 (C₁₁), 131.6 (C₁₇), 132.9 (C₁₆), 147.0 (C₁₀).

Synthesis of ¹Pr₃SiC≡CC₆H₄-4-C≡CC₆H₂-2,6-Et₂-4-C≡CC₆H₄-4-Br (7)

HC≡CC₆H₂-2,6-Et₂-4-C≡CC₆H₄-4-Br (1.14 g, 2.61 mmol) was added to a mixture of Pd(PPh₃)₄ (55 mg, 0.05 mmol), CuI (35 mg, 0.18 mmol), and (2-(4-iodophenyl)ethynyl)triisopropylsilane (0.85 g, 3.0 mmol) in deoxygenated NEt₃ (30 mL) cooled to 0 °C in an ice bath. The mixture was stirred for 2 h. The solvent was then removed and the residue purified by column chromatography on silica, eluting with petrol. ¹Pr₃SiC≡CC₆H₄-4-C≡CC₆H₂-2,6-Et₂-4-C≡CC₆H₄-4-Br was isolated as a colourless solid (1.55 g, 91 %). *R*_f(hexane) - 0.33. MS (EI⁺): 594.2 ([M]⁺, 100), 551.2 ([M - ¹Pr]⁺, 55). HRMS (ESI⁺): [M]⁺ 592.2161 (calcd [C₃₇H₄₁⁷⁹BrSi] 592.2161). *Anal.* calcd for C₃₇H₄₁BrSi: C, 74.85; H, 6.96. Found: C, 75.12; H, 7.29. ¹H NMR (δ, 400 MHz, CDCl₃): 1.14 (s, 21H, H₅₁₁ + H₅₁₂), 1.26 (t, 6H, H₁₀₂, *J*_{HH} = 7.8 Hz), 2.80 (q, 4H, C₁₀₁, *J*_{HH} = 7.8 Hz), 7.25 (s, 2H, H₁₁), 7.35 (appd

(AA'BB'), 2H, H_{17} , $J_{AB} = 8$ Hz), 7.44 (s, 4H, $H_4 + H_5$), 7.62 (appd (AA'BB'), 2H, H_{16} , $J_{AB} = 8$ Hz). ^{13}C NMR (δ , 101.5 MHz, CDCl_3): 11.3 (C_{511}), 14.6 (C_{102}), 18.7 (C_{512}), 27.9 (C_{101}), 88.1 (C_8), 89.4 (C_{13}), 90.9 (C_{14}), 92.9 (C_1), 98.2 (C_7), 106.6 (C_2), 121.8 (C_{12}), 122.2 (C_9), 122.5 (C_{15} and C_{18}), 123.4 (C_3 and C_6), 128.5 (C_{11}), 131.1 (C_5), 131.6 (C_{16}), 132.0 (C_4), 133.0 (C_{17}), 146.5 (C_{10}).

*Synthesis of $^i\text{Pr}_3\text{SiC}\equiv\text{CC}_6\text{H}_4\text{-4-C}\equiv\text{CC}_6\text{H}_2\text{-2,6-Et}_2\text{-4-C}\equiv\text{CC}_6\text{H}_4\text{-4-I}$ (**8**)*

$^i\text{Pr}_3\text{SiC}\equiv\text{CC}_6\text{H}_4\text{-4-C}\equiv\text{CC}_6\text{H}_2\text{-2,6-Et}_2\text{-4-C}\equiv\text{CC}_6\text{H}_4\text{-4-Br}$ (4.00 g, 6.73 mmol) was added to diethyl ether (20 mL) and the mixture was cooled to -78°C in a dry ice / acetone bath. n -Butyl lithium (5.6 mL, 6.95 mmol, 2.5 M in hexane) was slowly added and the mixture stirred for 2 h. Iodine (2.00 g, 7.90 mmol) in THF (25 mL) was added and the mixture warmed to room temperature. Aqueous $\text{Na}_2\text{S}_2\text{O}_3$ (20 mL) was added to the stirring mixture and the product extracted with CH_2Cl_2 , washing well with water. The organic layer was dried with MgSO_4 and the solvent removed. $^i\text{Pr}_3\text{SiC}\equiv\text{CC}_6\text{H}_4\text{-4-C}\equiv\text{CC}_6\text{H}_2\text{-2,6-Et}_2\text{-4-C}\equiv\text{CC}_6\text{H}_4\text{-4-I}$ was obtained as a colourless solid (3.62 g, 84 %). R_f (hexane) - 0.16. MS (EI^+): 640.1 ($[\text{M}]^+$, 100), 597.1 ($[\text{M} - \text{Pr}]^+$, 55). HRMS (EI^+): $[\text{M}]^+$ 640.2018 (calcd $[\text{C}_{37}\text{H}_{41}\text{Si}]$ 640.2022). *Anal.* calcd for $\text{C}_{37}\text{H}_{41}\text{Si}$: C, 69.36; H, 6.45. Found: C, 69.54; H, 6.71. ^1H NMR (δ , 400 MHz, CDCl_3): 1.13 (s, 21H, $H_{511} + H_{512}$), 1.31 (t, 6H, H_{102} , $J_{\text{HH}} = 7.6$ Hz), 2.88 (q, 4H, H_{101} , $J_{\text{HH}} = 7.6$ Hz), 7.25 (appd (AA'BB'), 2H, H_{17} , $J_{AB} = 8$ Hz), 7.27 (s, 2H, H_{11}), 7.45 (s, 4H, $H_4 + H_5$), 7.69 (appd (AA'BB'), 2H, H_{16} , $J_{AB} = 8$ Hz). ^{13}C NMR (δ , 101.5 MHz, CDCl_3): 11.3 (C_{511}), 14.6 (C_{102}), 18.7 (C_{512}), 27.9 (C_{101}), 88.2 (C_8), 89.5 (C_{18}), 91.1 (C_{13}), 92.9 (C_1), 94.2 (C_{14}), 98.2 (C_7), 106.6 (C_2), 121.8 (C_{12}), 122.5 (C_9), 122.7 (C_{15}), 123.4 + 123.42 (C_3 and C_6), 128.5 (C_{11}), 131.1 (C_5), 132.0 (C_{17}), 133.0 (C_4), 137.5 (C_{16}), 146.6 (C_{10}).

*Synthesis of 3,5-dibromo-4-iodo-nitrobenzene (**9**)^{85,90*}*

2,6-Dibromo-4-nitroaniline (7.0 g, 23.4 mmol) was added to 50% H_2SO_4 in H_2O (150 mL) and cooled in an ice bath. A solution of NaNO_2 (2.0 g, 28.9 mmol) in H_2O (25 mL) was added dropwise, ensuring the temperature remained below 3°C . After addition the mixture was stirred for 2 h. A solution of KI (4.8 g, 28.9 mmol) in water (25 mL) was then added dropwise. The mixture was then warmed to room temperature and stirred for 5 h. CH_2Cl_2 was added and the organic layer was recovered, washed with aqueous $\text{Na}_2\text{S}_2\text{O}_3$ and dried with MgSO_4 . After filtration, the solvent was removed under vacuum and the residue was recrystallised from *n*-hexane to give red crystals (6.25 g, 65 %). R_f (5:1, Petrol/ CH_2Cl_2)

- 0.34. MS (EI⁺): 406.7 ([M]⁺, 100), 360.7 ([M - NO₂], 35). HRMS (EI⁺): 406.7469 (calcd [C₆H₂⁷⁹Br₂INO₂] 406.7456). ¹H NMR (δ, 400 MHz, CDCl₃): 8.38 (s, 2H, H_{c4}). ¹³C NMR (δ, 121.5 MHz, CDCl₃): 118.8 (C_{c2}), 125.2 (C_{c4}), 132.1 (C_{c1}), 148.0 (C_{c5}).

*Previously prepared by different methodology in ref. 85 and ref. 90 with no NMR or MS characterisation.

Synthesis of 3,5-dibromo-4-iodoaniline (**10**)^{83*}

3,5-Dibromo-4-iodo-nitrobenzene (7.0 g, 17.2 mmol) was added to concentrated HCl (100 mL) and then tin metal (10.1 g, 86.4 mmol) was added portionwise. A condenser was fitted and the reaction heated to 80 °C for 10 h. Water (100 mL) was added and the pH adjusted to 10 with Na₂CO₃. The product was extracted with CH₂Cl₂ and recrystallised from MeOH and H₂O to give pale yellow crystals of 3,5-dibromo-4-iodoaniline (6.49 g, 73 %). *R*_f (2:1, Petrol/CH₂Cl₂) - 0.44. MS (EI⁺): 376.8 ([M]⁺, 100), 249.8 ([M - I]⁺, 21). HRMS (EI⁺): 375.1655 (calcd [C₆H₆⁷⁹Br₂I] 375.1650). ¹H NMR (δ, 400 MHz, CDCl₃): 3.77 (s, 2H, NH₂), 6.93 (s, 2H, H_{c2}). ¹³C NMR (δ, 101.5 MHz, CDCl₃): 93.3 (C_{c4}), 117.3 (C_{c2}), 131.1 (C_{c3}), 148.0 (C_{c1}).

*Previously synthesised in ref. 83 using an iron and acetic acid reduction methodology. NMR data are consistent.

Synthesis of 1,3-dibromo-2-iodobenzene (**11**)^{84*}

3,5-Dibromo-4-iodoaniline (1.96 g, 5.2 mmol) was added to a solution of H₂SO₄ in EtOH (10% v/v, 40 mL) and the solution heated to 70°C, before NaNO₂ (0.40 g, 5.8 mmol) was added. After 30 min, water (100 mL) was added and the resulting solid collected by filtration. The solid was purified by column chromatography on silica, eluting with hexane. The residue was then recrystallised from hexane to give 1,3-dibromo-2-iodobenzene as a colourless solid (0.80 g, 44 %). *R*_f (Hexane) - 0.75. MS (EI⁺): 361.8 ([M]⁺, 50). HRMS (ESI⁺): 361.7628 (calcd [C₆H₃⁷⁹Br₂I] 361.7626). ¹H NMR (δ, 400 MHz, CDCl₃): 7.07 (t, 1H, H_{c5}, *J*_{HH} = 8 Hz), 7.58 (d, 2H, H_{c4}, *J*_{HH} = 8 Hz). ¹³C NMR (δ, 101.5 MHz, CDCl₃): 109.4 (C_{c2}), 130.3 (C_{c1}), 131.1 (C_{c4}), 131.3 (C_{c3}).

* Previously synthesised in ref. 84 from 2,6-dibromoaniline. The physical data are consistent.

Synthesis of 2,3,5-tribromo-4-iodoaniline (12)

To 3,5-dibromo-4-iodoaniline (1.51 g, 4.01 mmol) in chloroform (30 mL) was added *N*-bromosuccinimide (0.72 g, 4.04 mmol) and the mixture allowed to stir for 3 h. Water (100 mL) was added and the organic layer recovered, drying with MgSO_4 . The solvent was removed under vacuum and the residue recrystallised from petrol. 2,3,5-Tribromo-4-iodoaniline was obtained as bright orange crystals (1.13 g, 62 %). MS (EI⁺): 454.7 ([M]⁺, 100). HRMS (ESI⁺): 454.6836 (calcd [C₆H₅⁷⁹Br₃IN] 454.6840). ¹H NMR (δ, 400 MHz, CDCl₃): 4.37 (bs, 2H, NH₂), 7.10 (s, 1H, H_{C6}). ¹³C NMR (δ, 101.5 MHz, CDCl₃): 93.7 (C₄), 109.7 (C₅), 116 (C₆), 129.6 (C₃), 133.5 (C₂), 146.1 (C₁).

Synthesis of 1,2,4-tribromo-3-iodobenzene (13)

2,3,5-Tribromo-4-iodoaniline (2.0 g, 4.38 mmol) was added to a solution of H₂SO₄ in EtOH (10% v/v, 40 mL) and the solution heated to 70°C before NaNO₂ (0.40 g, 5.79 mmol) was added. After 30 min water (100 mL) was added and the resulting solid collected by filtration. The solid was purified by column chromatography on silica, eluting with hexane. The solvent was removed to give 1,2,4-tribromo-3-iodobenzene as a pale yellow solid (1.1 g, 54 %). *R_f* (Hexane) – 0.74. MS (EI⁺): 439.7 ([M]⁺, 100), 312.7 ([M - I]⁺, 37). HRMS (ESI⁺): 439.6731 (calcd [C₆H₂⁷⁹Br₂⁸¹BrI] 439.6731). ¹H NMR (δ, 400 MHz, CDCl₃): 7.45 (d, 1H, H_{C6}, *J*_{HH} = 8 Hz), 7.48 (d, 1H, H_{C5}, *J*_{HH} = 8 Hz). ¹³C NMR (δ, 101.5 MHz, CDCl₃): 110.7 (C₂), 122.6 (C₄), 129.9 (C₁), 131.7 (C₆), 132.7 (C₃), 133.9 (C₅).

Synthesis of trimethylsilylethynylbenzene (14)^{91,92*}

Iodobenzene (1 mL, 8.96 mmol) was added to triethylamine (20 mL) and the mixture was deoxygenated under vacuum and backfilled with N₂. Pd(PPh₃)₄ (3 mg, 0.003 mmol) and CuI (2 mg, 0.01 mmol) were added followed by (trimethylsilyl)acetylene (1.3 mL, 9.28 mmol) and the mixture stirred for 2 h. The precipitate was removed by filtration, washing with petrol and the filtrate solvent removed under vacuum. The residue was purified by column chromatography on silica eluting with petrol. The solvent was removed under vacuum to give trimethylsilylethynylbenzene as a colourless oil (1.5 g, 97 %). *R_f* (Petrol) - 0.47. MS (EI⁺): 174.1 ([M]⁺, 30), 159.1 ([M - Me]⁺, 100). HRMS (ESI⁺): 174.0862 (calcd

[C₁₁H₁₄Si] 174.0865). UV-Vis: 270 [5.10], 261 [7.56], 241 [6.10]. ¹H NMR (δ, 400 MHz, CDCl₃): 0.25 (s, 9H, H_{s191}), 7.30 (m (AA'BB'X), 3H, H_{c3} + H_{c4}), 7.47 (m (AA'BB'X), 2H, H_{c2}). ¹³C NMR (δ, 101.5 MHz, CDCl₃): -0.02 (C_{s191}), 94.1 (C₁₉), 105.1 (C₂₀), 123.1 (C_{c1}), 128.2 (C_{c3}), 128.4 (C_{c4}), 131.9 (C_{c2}).

* Previously synthesised in ref 91 and ref 92. NMR data are consistent.

Synthesis of 1,2-bis(trimethylsilylethynyl)benzene (15)^{93}*

1,2-Diodobenzene (1.00 g, 3.03 mmol) was added to triethylamine (20 mL) and the mixture deoxygenated under vacuum. Pd(PPh₃)₄ (5 mg, 0.004 mmol) and CuI (2 mg, 0.01 mmol) were added followed by (trimethylsilyl)acetylene (0.85 mL, 6.1 mmol) and the mixture stirred for 2 h. The precipitate was removed by filtration, washing with petrol, and the filtrate solvent was removed under vacuum. The residue was purified by column chromatography on silica, eluting with petrol. The solvent was removed under vacuum to give 1,2-bis(trimethylsilylethynyl)benzene as a pale yellow oil (0.7 g, 85 %). *R_f* (Petrol) - 0.35. MS (EI⁺): 270.1 ([M]⁺, 65), 255.1 ([M - Me]⁺, 100). HRMS (ESI⁺): 270.1260 (calcd [C₁₆H₂₂Si₂] 270.1260). UV-Vis: 285 [2.8], 279 [4.6], 270 [14.7], 263 [18.3]. ¹H NMR (δ, 400 MHz, CDCl₃): 0.27 (s, 18H, H_{s191}), 7.24 (m (AA'BB'), 2H, H_{c3}), 7.44 (m (AA'BB'), 2H, H_{c4}). ¹³C NMR (δ, 101.5 MHz, CDCl₃): -0.04 (C_{s191}), 98.4 (C₁₉), 103.2 (C₂₀), 125.7 (C_{c1}), 128.0 (C_{c3}), 132.3 (C_{c2}).

* Previously synthesised in ref 93. No NMR data is reported.

Synthesis of 1,3-bis(trimethylsilylethynyl)benzene (16)^{94}*

1,3-Dibromobenzene (2.0 g, 8.47 mmol) and Pd(PPh₃)₄ (20 mg, 0.017 mmol) were added to distilled toluene (80 mL) and the mixture deoxygenated under vacuum and backfilled with N₂. (Trimethylsilylethynyl)zinc chloride in THF (50 mL, 0.5 M, 25 mmol) was added by cannula and the mixture heated to 90 °C and stirred for 4 d. Dilute HCl solution (100 mL, 2 M in H₂O) was added and the organic layer recovered, dried with MgSO₄ and the solvent removed under vacuum. The residue was purified by silica column chromatography eluting with petrol to give 1,3-bis(trimethylsilylethynyl)benzene as a colourless solid (1.8 g, 80 %). *R_f* - 0.34 (Petrol). MS (EI⁺): 270.1 ([M]⁺, 35), 255.1 ([M - Me]⁺, 100). HRMS (ESI⁺): 270.1263 (calcd [C₁₆H₂₂Si₂] 270.1260). UV-Vis: 269 [18.0], 263 [23.5], 251 [13.6]. ¹H NMR (δ, 400 MHz, CDCl₃): 0.24 (s, 18H, H_{s191}), 7.58 (t, 1H, H_{c5}, *J*_{HH} = 8 Hz),

7.39 (dd, 2H, H_{C4} , $J_{Hortho} = 8$ Hz, $^3J_{Hmeta} = 1.6$ Hz), 7.22 (t, 1H, H_{C2} , $J_{HH} = 1.6$ Hz). ^{13}C NMR (δ , 101.5 MHz, $CDCl_3$): 0.10 (C_{S191}), 94.8 (C_{19}), 104.0 (C_{20}), 123.3 (C_{C1}), 128.2 (C_{C5}), 131.7 (C_{C4}), 135.4 (C_{C2}).

*Previously synthesised in ref 94 by a different method. A higher field NMR instrument allows for better resolution of the aryl region, as a result the multiplicity is inconsistent.

Synthesis of 1,4-bis(trimethylsilylethynyl)benzene (**17**)^{93*}

1,4-Diiodobenzene (1.5 g, 4.54 mmol) was added to triethylamine (30 mL) and the mixture deoxygenated under vacuum. $Pd(PPh_3)_4$ (7 mg, 0.006 mmol) and CuI (4 mg, 0.02 mmol) were added followed by (trimethylsilyl)acetylene (1.3 mL, 9.3 mmol) and the mixture stirred for 2 h. The precipitate was removed by filtration, washing with petrol, and the solvent of the filtrate was removed under vacuum. The residue was purified by column chromatography on silica, eluting with petrol. The solvent was removed to give trimethylsilylethynylbenzene as a colourless solid (1.18 g, 96 %). R_f (2:1, Petrol/ CH_2Cl_2) - 0.37. MS (EI^+): 270.1 ($[M]^+$, 45), 255.1 ($[M - Me]^+$, 100). HRMS (ESI^+): 270.1259 (calcd [$C_{16}H_{22}Si_2$] 270.1260). UV-Vis: 295 [4.6], 280 [4.4], 270 [14.7], 263 [18.3]. 1H NMR (δ , 400 MHz, $CDCl_3$): 0.25 (s, 18H, H_{S191}), 7.39 (s, 4H, H_{C2}). ^{13}C NMR (δ , 101.5 MHz, $CDCl_3$): 0.10 (C_{S191}), 96.3 (C_{19}), 104.5 (C_{20}), 123.1 (C_{C1}), 131.7 (C_{C2}).

* Previously synthesised in ref 93. No NMR data is reported.

Synthesis of 1,2,3-tris(trimethylsilylethynyl)benzene (**18**)

1,3-Dibromo-2-iodobenzene (1 g, 2.76 mmol) and $Pd(PPh_3)_4$ (15 mg, 0.013 mmol) were added to distilled toluene (60 mL) and the mixture deoxygenated under vacuum and backfilled with N_2 . (Trimethylsilylethynyl)zinc chloride in THF (30 mL, 0.4 M, 12 mmol) was added by cannula and the mixture heated to 90 °C and stirred for 4 d. HCl solution (40 mL, 1 M in H_2O) was added and the organic layer recovered, dried with $MgSO_4$ and the solvent removed under vacuum. The residue was purified by column chromatography on silica, eluting with petrol. The solvent was removed under vacuum to give 1,2,3-tris(trimethylsilylethynyl)benzene as a pale yellow solid (0.60 g, 60 %). R_f (Petrol) - 0.17. MS (EI^+): 366 ($[M]^+$, 100), 351 ($[M - Me]^+$, 60). HRMS (ESI^+): 366.1651 (calcd [$C_{21}H_{30}Si_3$] 366.1655). UV-Vis: 285 [0.7], 269 [21.0], 263 [26.2], 255 [20.9]. 1H NMR (δ , 400 MHz, $CDCl_3$): 0.26 (s, 18H, H_{S191}), 0.29 (s, 9H, H_{S1921}), 7.15 (t, 1H, H_{C4} , $J_{HH} = 8$ Hz) 7.40 (d, 2H, H_{C3} , $J_{HH} = 8$ Hz). ^{13}C NMR (δ , 101.5 MHz, $CDCl_3$): 0.00 (C_{S1921}), 0.12 (C_{S191}), 98.8 (C_{19}), 101.6 (C_{192}), 102.6 (C_{20}), 103.2 (C_{202}), 126.3 (C_{C1}), 127.4 (C_{C5}), 128.0 (C_{C2}), 132.1 (C_{C4}).

Synthesis of 1,2,4-tris(trimethylsilylethynyl)benzene (19)^{95}*

1,2,4-Tribromobenzene (1.0 g, 3.17 mmol) and Pd(PPh₃)₄ (15 mg, 0.013 mmol) were added to distilled toluene (60 mL) and the mixture deoxygenated under vacuum. (Trimethylsilylethynyl)zinc chloride in THF (40 mL, 0.4 M, 16 mmol) was added by cannula and the mixture heated to 90 °C and stirred for 4 d. HCl solution (50 mL, 1 M in H₂O) was added and the organic layer recovered, dried with MgSO₄ and the solvent removed under vacuum. The residue was purified by column chromatography on silica, eluting with petrol. The solvent was removed under vacuum to give 1,2,4-tris(trimethylsilylethynyl)benzene as a pale yellow solid (0.80 g, 69 %). *R_f* (Petrol) - 0.25. MS (EI⁺): 367 ([M + H]⁺, 91), 249.8 ([M - Me]⁺, 100). HRMS (ESI⁺): 366.1654 (calcd [C₂₁H₃₀Si₃] 366.1655). UV-Vis: 305 [4.3], 288 [3.8], 241 [6.1], 269 [12.8], 258 [20.0]. ¹H NMR (δ, 400 MHz, CDCl₃): 0.23 (s, 9H, H_{s1941}), 0.260 (s, 9H, H_{s191}), 0.265 (s, 9H, H_{s1921}), 7.30 (dd, 1H, H_{c5}, *J*_{HH} = 8 Hz, *J*_{HH} = 1.6 Hz), 7.38 (d, 1H, H_{c6}, *J*_{HH} = 8 Hz), 7.57 (d, 1H, H_{c3}, *J*_{HH} = 1.6 Hz). ¹³C NMR (δ, 101.5 MHz, CDCl₃): -0.13 (C_{s1941}), 0.00 (C_{s191} + C_{s1921}), 96.9 (C₁₉₄), 99.2 (C₁₉₂), 100.5 (C₁₉), 102.3 (C₂₀₂), 102.9 (C₂₀), 103.7 (C₂₀₄), 123.0 (C_{c4}), 125.5 (C_{c2}), 125.9 (C_{c1}), 131.2 (C_{c6}), 132.1 (C_{c5}), 135.7 (C_{c3}).

*Previously synthesised by ref 95 with a different methodology. NMR data are consistent.

Synthesis of 1,3,5-tris(trimethylsilylethynyl)benzene (20)^{96}*

1,3,5-Tribromobenzene (2.6 g, 8.2 mmol) and Pd(PPh₃)₄ (15 mg, 0.013 mmol) were added to distilled toluene (80 mL) and the mixture deoxygenated under vacuum. (Trimethylsilylethynyl)zinc chloride in THF (60 mL, 0.5 M, 30 mmol) was added by cannula and the mixture heated to 90 °C for 3 d. HCl solution (30 mL, 1 M in H₂O) was added and the organic layer recovered, dried with MgSO₄ and the solvent removed under vacuum. The residue was purified by column chromatography on silica, eluting with petrol. The solvent was removed under vacuum to give 1,3,5-tris(trimethylsilylethynyl)benzene as a colourless solid (2.8 g, 93 %). *R_f* (petrol) - 0.29. MS (EI⁺): 366 ([M]⁺, 40), 351 ([M - Me]⁺, 100). HRMS (ESI⁺): 366.1655 (calcd [C₂₁H₃₀Si₃] 366.1655). UV-Vis: 269 [18.2], 262 [23.1], 255 [20.9]. ¹H NMR (δ, 400 MHz, CDCl₃): 0.23 (s, 27H, H_{s191}), 7.49 (s, 3H, H_{c2}). ¹³C NMR (δ, 101.5 MHz, CDCl₃): -0.17 (C_{s191}), 95.6 (C₁₉), 103.1 (C₂₀), 123.6 (C_{c1}), 134.9 (C_{c2}).

*Previously synthesised in ref 96.

Synthesis of 1,2,3,4-tetrakis(trimethylsilylethynyl)benzene (21)^{97*}

1,2,4-Tribromo-3-iodobenzene (0.70 g, 1.6 mmol) and Pd(PPh₃)₄ (20 mg, 0.017 mmol) were added to distilled toluene (50 mL) and the mixture deoxygenated. (Trimethylsilylethynyl)zinc chloride in THF (40 mL, 0.2 M, 8.1 mmol) was added by cannula and the mixture heated to 90 °C for 4 d. HCl solution (20 mL, 1 M in H₂O) was added and the organic layer recovered, dried with MgSO₄ and the solvent removed under vacuum. The residue was purified by column chromatography on silica, eluting with a mixture of petrol and CH₂Cl₂ (4:1). The solvent was removed under vacuum to give 1,2,3,4-tetrakis(trimethylsilylethynyl) benzene as a colourless solid (0.53 g, 72 %). *R_f* (4:1, Petrol/CH₂Cl₂) - 0.42. MS (EI⁺): 462 ([M]⁺, 100). HRMS (ESI⁺): 462.2053 (calcd [C₂₆H₃₈Si₄] 462.2051). UV-Vis: 309 [1.7], 290 [2.4], 271 [28.1], 261 [29.1], 235 [22.3]. ¹H NMR (δ, 400 MHz, CDCl₃): 0.26 (s, 9H, H_{s191}), 0.29 (s, 9H, H_{s1921}), 7.31 (s, 2H, H_{c3}). ¹³C NMR (δ, 101.5 MHz, CDCl₃): -0.06 (C_{s191}), 0.07 (C_{s1921}), 100.6 (C₁₉₂), 101.2 (C₁₉), 102.6 (C₂₀₂), 103.5 (C₂₀), 125.9 (C_{c2}), 128.4 (C_{c1}), 131.3 (C_{c3}).

* Previously synthesised in ref 97 by a different methodology.

Synthesis of 1,2,3,5-tetrakis(trimethylsilylethynyl)benzene (22)

1,3,5-Tribromo-2-iodobenzene (0.80 g, 1.85 mmol) and Pd(PPh₃)₄ (15 mg, 0.013 mmol) were added to distilled toluene (50 mL) and the mixture deoxygenated under vacuum. (Trimethylsilylethynyl)zinc chloride in THF (45 mL, 0.24 M, 11 mmol) was added by cannula and the mixture heated to 90 °C for 4 d. HCl (40mL, 1 M in H₂O) was added and the organic layer recovered, dried with MgSO₄ and the solvent removed under vacuum. The residue was purified by column chromatography on silica, eluting with a mixture of petrol and CH₂Cl₂ (2:1). The solvent was removed under vacuum to give 1,2,3,5-tetrakis(trimethylsilylethynyl)benzene as a pale yellow gum (0.53 g, 63 %). *R_f* (2:1, Petrol/CH₂Cl₂) - 0.60. EI MS: 462 ([M]⁺, 100), 447 ([M - Me]⁺, 30). HRMS (ESI⁺): 462.2050 (calcd [C₂₆H₃₈Si₄] 462.2051). UV-Vis: 311 [3.0], 299 [1.1], 270 [23.8], 263 [30.6], 257 [24.0]. ¹H NMR (δ, 400 MHz, CDCl₃): 0.25 (s, 9H, H_{s1951}), 0.26 (s, 18H, H_{s191}), 0.29 (s, 9H, H_{s1921}), 7.50 (s, 2H, H_{c4}). ¹³C NMR (δ, 101.5 MHz, CDCl₃): -0.21 (C_{s1951}), -0.08 (C_{s191}), 0.04 (C_{s1921}), 97.3

(C₁₉), 99.4 (C₁₉₂), 101.2 (C₁₉₅), 102.0 (C₂₀₂), 102.8 (C₂₀₅), 104.9 (C₂₀), 122.7 (C₁₅), 126.5 (C₁₁), 127.5 (C₁₂), 135.0 (C₁₄).

Synthesis of 1,2,4,5-tetrakis(trimethylsilylethynyl)benzene (23)^{98}*

1,2,4,5-Tetrabromobenzene (2.0 g, 5.08 mmol) was added to a deoxygenated mixture of toluene and diisopropylamine (10 %, 80 mL) followed by Pd(PPh₃)₄ (15 mg, 0.013 mmol) and CuI (25 mg, mmol). TMSA (3.4 mL, 24.3 mmol) was added and the mixture was heated to 70 °C for 2 d. The progress was checked by TLC and additional (trimethylsilyl)acetylene (1 mL, 7.14 mmol) was added. The mixture stirred at 70 °C for 1 d. NH₄Cl solution (50 mL, 2 M in H₂O) was added and the organic layer recovered and dried with MgSO₄. The solvent was removed under vacuum. The residue was purified by column chromatography using silica, eluting with a mixture of petrol and CH₂Cl₂ (4:1). The solvent was removed under vacuum to give 1,2,4,5-tetrakis(trimethylsilylethynyl)benzene as a colourless solid (1.5 g, 66 %). *R*_f (4:1, Petrol/CH₂Cl₂) - 0.76. MS (EI⁺): 462 ([M]⁺, 100), 447 ([M - Me]⁺, 38). HRMS (ESI⁺): 462.2051 [calcd [C₂₆H₃₈Si₄] 462.2051]. UV-Vis: 323 [1.5], 309 [1.7], 270 [34.9], 263 [39.5], 256 [30.2]. ¹H NMR (δ, 400 MHz, CDCl₃): 0.25 (s, 36H, H_{Si191}), 7.56 (s, 4H, H_{C2}). ¹³C NMR (δ, 101.5 MHz, CDCl₃): -0.1 (C_{Si191}), 100.8 (C₁₉), 101.9 (C₂₀), 125.3 (C₁₁), 135.9 (C₁₂).

*Previously synthesised in ref 98 by different method.

Synthesis of pentakis(trimethylsilylethynyl)benzene and hexakis(trimethylsilylethynyl)benzene (24 and 25)^{76}*

1,2,3,4,5,6-Hexabromobenzene (2.0 g, 3.6 mmol) and Pd(PPh₃)₄ (100 mg, 0.086 mmol) were added to distilled toluene (80 mL) and the mixture deoxygenated. (Trimethylsilylethynyl)zinc chloride in THF (80 mL, 0.5 M, 40 mmol) was added by cannula and the mixture heated to 90 °C for 5 d. HCl (50 mL, 1 M in H₂O) was added and the organic layer recovered, washed with thoroughly with water, dried with MgSO₄. The solvent removed under vacuum and the residue was purified by column chromatography silica, eluting with a polarity gradient from petrol to 4:1 petrol : CH₂Cl₂ to give 1,2,3,4,5-pentakis(trimethylsilylethynyl)benzene (0.40 g, 16 %) eluting first, followed by 1,2,3,4,5,6-hexakis(trimethylsilylethynyl)benzene (1.2 g, 50 %). Both compounds were pale yellow solids. (24) - *R*_f (4:1, Petrol/CH₂Cl₂) - 0.62. MS (EI⁺): 558 ([M]⁺, 100). HRMS

(ESI⁺): 558.2447 (calcd [C₃₁H₄₆Si₅] 558.2446). UV-Vis: 323 [11.9], 313 [12.4], 300 [14.9], 289 [34.3], 269 [32.9], 263 [34.4]. ¹H NMR (δ, 400 MHz, CDCl₃): 0.25 (s, 9H, H_{s191}), 0.28 (s, 27H, H_{s1921}+H_{s1931}), 7.50 (s, 2H, H_{c6}). ¹³C NMR (δ, 101.5 MHz, CDCl₃): -0.1 (C_{s191}), 0.01 (C_{s192} + C_{s193}), 100.8 (C₁₉), 100.9 (C₁₉₃), 101.0 (C₁₉₂), 101.8 (C₂₀), 103.9 (C₂₀₃), 105.1 (C₂₀₂), 125.5 (C_{c1}), 127.7 (C_{c2}), 128.9 (C_{c3}), 135.1 (C_{c6}). (25) - R_f (4:1, Petrol/CH₂Cl₂) - 0.48. MS (EI⁺): 654 ([M]⁺, 100). HRMS (ESI⁺): 654.2840 (calcd [C₃₆H₅₄Si₆] 654.2841). UV-Vis: 324 [11.9], 312 [9.8], 305 [22.2], 294 [10.3], 269 [32.9], 263 [38.7]. ¹H NMR (δ, 400 MHz, CDCl₃): 0.28 (s, 54H, H_{s191}). ¹³C NMR (δ, 101.5 MHz, CDCl₃): 0.02 (C_{s191}), 100.9 (C₁₉), 105.2 (C₂₀), 127.9 (C_{c1}).

*Methodology applied from ref 76. NMR data are consistent.

Synthesis of ¹Pr₃SiC≡CC₆H₄-4-C≡C-C₆H₂-2,6-Et₂-4-C≡CC₆H₄-4-C≡CPh (26)

¹Pr₃SiC≡CC₆H₄-4-C≡C-C₆H₂-2,6-Et₂-4-C≡CC₆H₄-4-I (0.15 g, 0.27 mmol) was added to NEt₃ (15 mL) and the solution deoxygenated under vacuum. Pd(PPh₃)₄ (16 mg, 0.01 mmol) and CuI (5 mg, 0.02 mmol) were added and the mixture stirred at room temperature for 1 min. Phenylacetylene (28 mg, 0.27 mmol) was then added and the reaction stirred for 1 h. The solvent was removed under vacuum and the residue was purified by column chromatography on silica and eluting with petrol. ¹Pr₃SiC≡CC₆H₄-4-C≡C-C₆H₂-2,6-Et₂-4-C≡CC₆H₄-4-C≡C-Ph was obtained as a colourless solid (0.18 g, 93 %). R_f (Petrol) - 0.55. MS (ESI⁺): 614.3 ([M]⁺, 100). HRMS (ESI⁺): 614.3365 (calc. [C₄₅H₄₆Si] 614.3369). Anal. calc for C₄₅H₄₆Si: C, 87.89; H, 7.54. Found: C, 87.95; H, 7.73. UV-vis: 376 [sh, 6.2], 352 [sh, 9.2], 339 [7.3], 274 [1.8]. ¹H NMR (δ, 400 MHz, CDCl₃): 1.14 (s, 21H, H_{s71} + H_{s72}), 1.32 (t, 6H, H₁₀₂, J_{HH} = 7.2 Hz), 2.89 (q, 4H, H₁₀₁, J_{HH} = 7.2 Hz), 7.28 (s, 2H, H₁₁), 7.34-7.36 (m (AA'BB'X), 2H, H₂₃ + H₂₄), 7.45 (s, 4H, H₄ + H₅), 7.51 (s, 4H, H₁₆ + H₁₇), 7.52-7.55 (m (AA'BB'X), 3H, H₂₂). ¹³C NMR (δ, 101.5 MHz, CDCl₃): 11.3 (C_{s11}), 14.6 (C₁₀₂), 18.6 (C_{s12}), 27.9 (C₁₀₁), 88.2 (C₈), 89.1 (C₁₉), 90.2 (C₁₃), 91.3 (C₂₀), 91.6 (C₁₄), 92.9 (C₁), 98.2 (C₇), 106.6 (C₂), 121.8 (C₁₂), 122.6 (C₉), 123.0 (C₁₈ + C_{c1}), 123.1 (C₁₅), 123.3 (C₆), 123.4 (C₃), 128.4 (C_{c3} + C_{c4}), 128.5 (C₁₁), 131.1 (C₅), 131.5 (C₁₆ + C₁₇), 131.6 (C_{c2}), 132.0 (C₄), 146.7 (C₁₀).

Synthesis of HC≡CC₆H₄-4-C≡CC₆H₂-2,6-Et₂-4-C≡CC₆H₄-4-C≡CPh (27)

¹Pr₃SiC≡CC₆H₄-4-C≡C-C₆H₂-2,6-Et₂-4-C≡CC₆H₄-4-C≡C-Ph (0.31 g, 0.51 mmol) and then TBAF (0.6 mL, 1 M in THF) were added to CH₂Cl₂ (10 mL) and the resultant mixture

stirred for 2 h. Water was added and the product extracted with CH_2Cl_2 . The solvent was removed from the organic phase and the residue purified by column chromatography on silica, eluting with a mixture of petrol and CH_2Cl_2 (2:1). The solvent was removed to give $\text{HC}\equiv\text{CC}_6\text{H}_4\text{-4-C}\equiv\text{C-C}_6\text{H}_2\text{-2,6-Et}_2\text{-4-C}\equiv\text{CC}_6\text{H}_4\text{-4-C}\equiv\text{C-Ph}$ as a light yellow solid (0.25 g, 95 %). R_f (petrol/ CH_2Cl_2 , 2:1) - 0.44. MS (EI⁺): 458.2 ([M]⁺, 100). HRMS (ESI⁺): 458.2028 (calcd [$\text{C}_{36}\text{H}_{26}$] 458.2035). Anal. calcd for $\text{C}_{36}\text{H}_{26}$: C, 94.29; H, 5.71. Found: C, 94.12; H, 5.61. ¹H NMR (δ , 300 MHz, CDCl_3): 1.30 (t, 6H, H_{102} , $J_{\text{HH}} = 7.2$ Hz), 2.86 (q, 4H, H_{101} , $J_{\text{HH}} = 7.2$ Hz), 3.16 (s, 1H, H_1), 7.28 (s, 2H, H_{11}), 7.34-7.36 (m (AA'BB'X), 2H, $\text{H}_{23} + \text{H}_{24}$), 7.45 (s, 4H, $\text{H}_4 + \text{H}_5$), 7.51 (s, 4H, $\text{H}_{16} + \text{H}_{17}$), 7.52-7.55 (m (AA'BB'X), 3H, H_{22}). ¹³C NMR (δ , 101.5 MHz, CDCl_3): 14.6 (C_{102}), 27.9 (C_{102}), 79.1 (C_1), 83.3 (C_2), 88.5 (C_8), 89.1 (C_{14}), 90.3 (C_{19}), 91.4 (C_{13}), 91.6 (C_{20}), 98.0 (C_7), 121.8 (C_9), 121.9 (C_3), 122.8 (C_{21}), 123.0 ($\text{C}_{15} + \text{C}_{10}$), 123.2 (C_{12}), 124.1 (C_6), 128.4 (C_{11}), 128.5 ($\text{C}_{23} + \text{C}_{24}$), 131.2 (C_5), 131.6 ($\text{C}_{16} + \text{C}_{17}$), 131.7 (C_{22}), 132.5 (C_4), 146.7 (C_{10}).

*Synthesis of trans-[RuCl($\text{C}\equiv\text{CC}_6\text{H}_4\text{-4-C}\equiv\text{CC}_6\text{H}_2\text{-2,6-Et}_2\text{-4-C}\equiv\text{CC}_6\text{H}_4\text{-4-C}\equiv\text{CPh}$)(*dpepe*)₂] (28)*

$\text{HC}\equiv\text{CC}_6\text{H}_4\text{-4-C}\equiv\text{CC}_6\text{H}_2\text{-2,6-Et}_2\text{-4-C}\equiv\text{CC}_6\text{H}_4\text{-4-C}\equiv\text{CPh}$ (0.20 g, 0.43 mmol) was added to distilled and deoxygenated CH_2Cl_2 (20 mL). $[\text{RuCl}(\text{dpepe})_2]\text{PF}_6$ (0.48 g, 0.44 mmol) was added and the reaction stirred for 10 h. The solvent level was reduced to 5 mL under vacuum and the mixture added to stirring deoxygenated petrol (100 mL). The yellow solid was collected and dried under a N_2 flow. The solid was then added to a deoxygenated mixture of CH_2Cl_2 and NEt_3 (10:1, 15 mL) and stirred for 10 min. The mixture was then passed through a short pad of alumina, eluting with a mixture of petrol, CH_2Cl_2 and NEt_3 (10:10:1, 150 mL). The solvent was removed under vacuum to give **28** as a yellow powder (0.51 g, 82 %). MS (ESI⁺): 1396.43 ([M - Cl + MeCN]⁺, 100), HRMS (ESI⁺): 1396.4037 (calcd [$\text{C}_{90}\text{H}_{76}\text{NP}_4\text{Ru}$] 1396.3972). Anal. calcd for $\text{C}_{90}\text{H}_{76}\text{ClP}_4\text{Ru}$: C, 75.99; H, 5.29. Found: C, 75.68; H, 5.45. UV-vis: 426 [7.4], 367 [sh,9.1], 341 [9.5], 254 [7.5]. ³¹P NMR (δ , 161 MHz, CDCl_3): 49.3. ¹H NMR (δ , 400 MHz, CDCl_3): 1.35 (t, 6H, H_{102} , $J_{\text{HH}} = 7.2$ Hz), 2.68 (bs, 8H, H_b), 2.93 (q, 4H, H_{101} , $J_{\text{HH}} = 7.2$ Hz), 6.59 (d, 2H, H_a , $J_{\text{HH}} = 8$ Hz), 6.95-7.02 (m, 18H, $\text{H}_{m1} + \text{H}_{m2} + \text{H}_5$), 7.17-7.21 (m, 8H, H_f), 7.28-7.30 (m, 10H, $\text{H}_{11} + \text{H}_{o1}$), 7.35-7.39 (m, 2H, $\text{H}_{c3} + \text{H}_{c4}$), 7.48-7.58 (m, 15H, $\text{H}_{c3} + \text{H}_{o2} + \text{H}_{16} + \text{H}_{17}$). ¹³C NMR (δ , 101.5 MHz, CDCl_3): 14.6 (C_{102}), 27.9 (C_{101}), 30.6 (m, C_b), 86.5 (C_{20}), 89.1 (C_8), 89.9 (C_{14}), 91.2 (C_{19}), 91.8 (C_{13}), 100.1 (C_7), 114.5 (C_3), 117.0 (C_6), 121.8 (C_{12}), 122.8 (C_9), 123.0 ($\text{C}_{c1} + \text{C}_{18}$), 123.2 (C_{15}), 126.9 (C_{o1}), 127.2 (C_{o2}), 128.3 (C_{11}), 128.4 ($\text{C}_{c3} + \text{C}_{c4}$), 128.8 (C_p), 128.8 (C_p), 129.9 (C_6), 130.4 (C_4), 131.2 (C_5), 131.6 ($\text{C}_{16} + \text{C}_{17}$), 131.7 (C_{c2}), 134.2 (C_{m1}), 134.4 (C_{m2}), 135.6 (m, C_{i1}), 136.3 (m, C_{i2}), 146.7 (C_{10}). C_1 not observed.

Synthesis of 1,2-(i Pr₃SiC≡CC₆H₄-4-C≡CC₆H₂-2,6-Et₂-4-C≡CC₆H₄-4-C≡C)₂C₆H₄ (29)

1,2-Bis(trimethylsilylethynyl)benzene (90 mg, 0.33 mmol) was added to deoxygenated CH₂Cl₂ (15 mL) and deoxygenated MeOH (15 mL) was added. K₂CO₃ (0.10 g, 0.72 mmol) was then added and the mixture stirred for 2 h. The mixture was added to deoxygenated water (80 mL) and the organic layer recovered and dried with CaCl₂. The solvent was removed under vacuum and the residue dissolved in deoxygenated NEt₃ (10 mL). The solution was added by cannula to a deoxygenated mixture of **8** (0.41 g, 0.64 mmol), Pd(PPh₃)₄ (25 mg, 0.02 mmol), CuI (25 mg, 0.13 mmol) and NEt₃, (15 mL) and the mixture stirred for 6 h. The solvent was removed under vacuum and the residue was purified by column chromatography on silica, eluting with a mixture of petrol and CH₂Cl₂ (2:1). **29** was obtained as a colourless solid (0.29 g, 76 %). *R_f* (petrol/CH₂Cl₂ (2:1) - 0.36. *Anal.* calcd for C₈₄H₈₆Si₂: C, 87.60; H, 7.53. Found: C, 87.68; H, 7.49. UV-Vis: 379 [sh, 9.9], 357 [13.9], 340 [sh, 11.9], 274 [3.4]. ¹H NMR (δ, 400 MHz, CDCl₃): 1.14 (s, 42H, H₆₇₁ + H₆₇₂), 1.32 (t, 12H, H₁₀₂, *J*_{HH} = 7.6 Hz), 2.89 (q, 8H, H₁₀₁, *J*_{HH} = 7.2 Hz), 7.29 (s, 4H, H₁₁), 7.31-7.35 (m (AA'BB'), 2H, H₁₃), 7.45 (s, 8H, H₄ + H₅), 7.52 (appq (AA'BB'), 8H, H₁₇ + H₁₆, *J*_{AB} = 7.2 Hz), 7.57-7.58 (m (AA'BB'), 2H, H₁₄). ¹³C NMR (δ, 101.5 MHz, CDCl₃): 11.3 (C₆₇₁), 14.6 (C₁₀₂), 18.6 (C₆₇₂), 27.9 (C₁₀₁), 88.3 (C₈), 90.0 (C₁₄), 90.1 (C₁₅), 91.7 (C₁₃), 92.9 (C₁), 93.4 (C₂₀), 98.2 (C₇), 106.6 (C₂), 121.8 (C₉), 122.6 (C₁₂), 123.0 (C₁₅), 123.3 (C₁₈), 123.4 (C₆), 123.5 (C₃), 125.6 (C₁), 128.2 (C₃), 128.5 (C₁₁), 131.1 (C₅), 131.5 (C₁₆ + C₁₇), 131.7 (C₁₂), 132.0 (C₄), 146.6 (C₁₀).

Synthesis of 1,2-(HC≡CC₆H₄-4-C≡CC₆H₂-2,6-Et₂-4-C≡CC₆H₄-4-C≡C)₂C₆H₄ (30)

1,2-(i Pr₃SiC≡CC₆H₄-4-C≡C-C₆H₂-2,6-Et₂-4-C≡CC₆H₄-4-C≡C)₂C₆H₄ (0.070 g, 0.060 mmol) was added to CH₂Cl₂ (15 mL) and TBAF (0.12 mL, 1 M in THF) was then added. The mixture was stirred for 2 h before water was added. The organic layer was recovered and dried with MgSO₄. The solvent was removed and the residue purified by column chromatography on silica, eluting with a mixture of petrol and CH₂Cl₂ (5:1). **30** was obtained as a pale yellow solid (0.035 g, 65 %). *R_f* (petrol/CH₂Cl₂ (2:1) - 0.36. *Anal.* calcd for C₆₆H₄₆: C, 93.36; H, 5.58. Found: C, 93.68; H, 5.76. ¹H NMR (δ, 400 MHz, CDCl₃): 1.32 (t, 6H, H₁₀₂, *J*_{HH} = 7.6 Hz), 2.89 (q, 4H, H₁₀₁, *J*_{HH} = 7.6 Hz), 3.19 (s, 1H, H₁), 7.29 (s, 2H, H₁₁), 7.32 - 7.34 (m, 2H, H₁₃), 7.48 (s, 4H, H₄ + H₅), 7.52 (appq (AA'BB'), 8H, H₁₇ + H₁₆, *J*_{AB} = 8 Hz), 7.57-7.58 (m, 2H, H₁₂). ¹³C NMR (δ, 101.5 MHz, CDCl₃): 14.6 (C₁₀₂), 27.9 (C₁₀₁), 78.9 (C₁),

83.3 (C₂), 88.4 (C₈), 90.1 (C₁₄+C₁₉), 91.8 (C₁₃), 93.4 (C₂₀), 97.9 (C₇), 121.8 (C₉), 121.9 (C₃), 122.6 (C₁₂), 123.0 (C₁₅), 123.3 (C₁₈), 124.0 (C₆), 125.6 (C_{c1}), 128.2 (C_{c3}), 128.5 (C₁₁), 131.2 (C₅), 131.6 (C₁₆), 131.6 (C₁₇), 131.7 (C_{c2}), 132.1 (C₄), 146.6 (C₁₀).

Synthesis of 1,2-(trans-[RuCl(dppe)]₂(C≡CC₆H₄-4-C≡CC₆H₂-2,6-Et₂-4-C≡CC₆H₄-4-C≡C))₂C₆H₄ (31)

1,2-(HC≡CC₆H₄-4-C≡CC₆H₂-2,6-Et₂-4-C≡CC₆H₄-4-C≡C)₂-C₆H₄ (0.05 g, 0.06 mmol) and [RuCl(dppe)]₂PF₆ (0.15 g, 0.14 mmol) were added to distilled and deoxygenated CH₂Cl₂. The mixture was stirred for 8 h and was then poured into deoxygenated petrol (100 mL). The solid was recovered by filtration and washed with deoxygenated MeOH (10 mL). The solid was then dissolved in a deoxygenated mixture of CH₂Cl₂ and NEt₃ (60 mL, 10:1) and stirred for 10 min. The mixture was then passed through a short pad of alumina eluting with a mixture of CH₂Cl₂, petrol and NEt₃ (30 mL, 10:10:1). The solvent was removed from the eluate under vacuum to afford **31** as a yellow solid (0.16 g, 76 %). *Anal.* calcd for C₁₇₀H₁₄₀Cl₂P₈Ru₂: C, 75.52; H, 5.22. Found: C, 75.54; H, 5.42. UV-vis: 425 [11.7], 369 [sh, 12.0], 342 [15.1], 257 [13.6]. ¹H NMR (δ, 400 MHz, CDCl₃): 1.36 (t, 12H, H₁₀₂, J_{HH} = 7.2 Hz), 2.68 (bs, 16H, H_b), 2.93 (q, 8H, H₁₀₁, J_{HH} = 7.2 Hz), 6.59 (bs, 4H, H₄), 6.95-7.02 (m, 32H, H_{m1} + H_{m2}), 7.17-7.21 (m, 16H, H_p), 7.28-7.30 (m, 26H, H_{c3} + H₁₁ + H_{o1} + H₅), 7.48-7.58 (m, 26H, H_{o2} + H₁₆ + H₁₇ + H_{c2}). ³¹P NMR (δ, 161 MHz, CDCl₃): 49.3. ¹³C NMR (δ, 101.5 MHz, CDCl₃): 14.6 (C₁₀₂), 27.9 (C₁₀₁), 30.6 (m, C_b), 86.6 (C₈), 89.9 (C₁₉), 90.1 (C₁₃), 92.1 (C₂₀), 93.5 (C₁₄), 100.1 (C₇), 117.0 (C₆), 121.8 (C₁₂), 122.7 (C₉), 122.9 (C₁₈), 123.5 (C₁₅), 125.7 (C_{c1}), 126.9 (C_{o1}), 127.2 (C_{o2}), 128.2 (C_{c3}), 128.4 (C₁₁), 128.8 (C_{p1}), 128.8 (C_{p2}), 130.1 (C₅), 130.5 (C₄), 131.5 (C₁₆ + C₁₇), 131.6 (C_{c2}), 134.2 (C_{o1}), 134.4 (C_{o2}), 135.5 (m, C_{i1}), 136.3 (m, C_{i2}), 146.7 (C₁₀). C₁, C₂ and C₃ not observed.

Synthesis of 1,3-(ⁱPr₃SiC≡CC₆H₄-4-C≡CC₆H₂-2,6-Et₂-4-C≡CC₆H₄-4-C≡C)₂C₆H₄ (32)

8 (0.36 g, 0.56 mmol) was added to NEt₃ (15 mL) and the solution deoxygenated. Pd(PPh₃)₄ (10 mg, 0.008 mmol) and CuI (10 mg, 0.05 mmol) were added and then a solution of 1,3-diethynylbenzene (36 mg, 0.28 mmol) in NEt₃ (5 mL) was added by cannula. The mixture was stirred for 6 h. The solvent was removed under vacuum and the residue was purified by column chromatography on silica, eluting with a mixture of petrol and CH₂Cl₂ (3:1). **32** was obtained as a light yellow solid (0.25 g, 78 %). *R_f* (petrol/CH₂Cl₂ (3:1)) - 0.15. *Anal.* calcd for C₆₄H₆₆Si₂: C, 87.60; H, 7.53. Found: C, 87.81; H, 7.79. UV-Vis: 378 [sh, 11.1], 356 [14.9], 338 [sh, 12.0], 274 [3.5]. ¹H NMR (δ, 400 MHz, CDCl₃): 1.14 (s, 42H, H_{s11} + H_{s12}), 1.32 (t, 12H, H₁₀₂, J_{HH} = 7.2 Hz), 2.89 (q, 8H, H₁₀₁, J_{HH} = 7.2 Hz), 7.28 (s, 4H,

H₁₁), 7.35 (t, 1H, H_{c4}, *J*_{HH} = 8 Hz), 7.45 (s, 8H, H₄ + H₅), 7.49 (dd, 2H, H_{c3}, *J*_{HH} = 8 Hz, *J*_{HH} = 1.6 Hz), 7.52 (s, 8H, H₁₇ + H₁₆), 7.72 (t, 1H, H_{c2}, *J*_{HH} = 1.6 Hz). ¹³C NMR (δ, 101.5 MHz, CDCl₃): 11.3 (C_{s11}), 14.6 (H₁₀₂), 18.6 (C_{s12}), 27.9 (C₁₀₁), 88.2 (C₈), 89.8 (C₁₉), 90.1 (C₁₃), 90.3 (C₂₀), 91.7 (C₁₄), 92.9 (C₁), 98.2 (C₇), 106.6 (C₂), 121.8 (C₁₂), 122.6 (C₉), 122.8 (C_{c1}), 123.3 (C₁₀), 123.4 (C₆), 123.4 (C₃), 123.5 (C₁₅), 128.4 (C₁₁), 128.5 (C_{c4}), 131.1 (C₅), 131.4 (C_{c3}), 131.5 (C₁₆ + C₁₇), 132.0 (C₄), 134.6 (C_{c2}), 146.6 (C₁₀).

Synthesis of 1,3-(HC≡CC₆H₄-4-C≡CC₆H₂-2,6-Et₂-4-C≡CC₆H₄-4-C≡C)₂C₆H₄ (33)

1,3-(iPr₃SiC≡CC₆H₄-4-C≡CC₆H₂-2,6-Et₂-4-C≡CC₆H₄-4-C≡C)₂C₆H₄ (0.070 g, 0.060 mmol) was added to CH₂Cl₂ (15 mL) and TBAF (0.12 mL, 1 M in THF) was then added. The mixture was stirred for 2 h before water was added. The organic layer was recovered and dried with MgSO₄. The solvent was removed and the residue purified by column chromatography on silica, eluting with petrol and CH₂Cl₂ (5:1). **33** was obtained as a pale yellow solid (0.035 g, 65 %). *R*_f (petrol/CH₂Cl₂ (3:1)) - 0.15. *Anal.* calcd for C₆₆H₄₆: C, 94.47; H, 5.53. Found: C, 94.38; H, 5.56. ¹H NMR (δ, 400 MHz, CDCl₃): 1.32 (t, 12H, H₁₀₂, *J*_{HH} = 8 Hz), 2.89 (q, 8H, H₁₀₁, *J*_{HH} = 8 Hz), 3.18 (s, 2H, H₁), 7.29 (s, 4H, H₁₁), 7.35 (t, 1H, H_{c5}, *J*_{HH} = 8 Hz), 7.45 (m, 10H, H₄ + H₅ + H_{c4}), 7.52 (s, 8H, H₁₇ + H₁₆), 7.72 (t, 1H, H_{c2}, *J*_{HH} = 1.6 Hz). ¹³C NMR (δ, 101.5 MHz, CDCl₃): 14.6 (C₁₀₂), 27.9 (C₁₀₁), 78.9 (C₁), 83.2 (C₂), 88.4 (C₈), 89.8 (C₁₄), 90.1 (C₁₉), 90.3 (C₂₀), 91.7 (C₁₃), 97.9 (C₇), 121.7 (C₃), 121.8 (C₉), 122.7 (C₁₂), 122.8 (C_{c1}), 123.3 (C₁₅ + C₁₀), 123.4 (C₂₁), 123.4 (C₆), 128.5 (C₁₁), 128.6 (C_{c4}), 131.1 (C₅), 131.4 (C_{c5}), 131.6 (C₁₆ + C₁₇), 132.1 (C₄), 134.6 (C_{c2}), 146.6 (C₁₀).

Synthesis of 1,3-(trans-[RuCl(dppe)₂](C≡C-C₆H₄-4-C≡CC₆H₂-2,6-Et₂-4-C≡CC₆H₄-4-C≡C))₂C₆H₄ (34)

1,3-(HC≡CC₆H₄-4-C≡CC₆H₂-2,6-Et₂-4-C≡CC₆H₄-4-C≡C)₂C₆H₄ (0.080 g, 0.090 mmol) was added to deoxygenated and distilled CH₂Cl₂ followed by [RuCl(dppe)₂]PF₆ (0.20 g, 0.18 mmol). The mixture was stirred for 16 h and then poured into deoxygenated petrol (100 mL). The solid was recovered by filtration and washed with deoxygenated MeOH (20 mL). The solid was then dissolved in a deoxygenated mixture of CH₂Cl₂ and NEt₃ (60 mL, 10:1) and stirred for 10 min. The mixture was then passed through a short pad of alumina eluting with a mixture of CH₂Cl₂, petrol and NEt₃ (30 mL, 10:10:1). The solvent was removed to afford **34** as a yellow solid (0.21 g, 83 %). UV-vis: 426 [11.6], 367 [12.1], 341

[15.4], 254 [14.1]. ^1H NMR (δ , 400 MHz, CDCl_3): 1.36 (t, 12H, H_{102} , $J_{\text{HH}} = 7.2$ Hz), 2.68 (bs, 8H, H_b), 2.93 (q, 8H, H_{101} , $J_{\text{HH}} = 7.2$ Hz), 6.59 (d, 4H, H_4 , $J_{\text{HH}} = 8$ Hz), 6.95-7.02 (m, 32H, $\text{H}_{m1} + \text{H}_{m2}$), 7.17-7.21 (m, 16H, H_p), 7.28-7.30 (m, 27H, $\text{H}_{c3} + \text{H}_{c4} + \text{H}_{11} + \text{H}_{o1} + \text{H}_5$), 7.48-7.58 (m, 24H, $\text{H}_{o2} + \text{H}_{16} + \text{H}_{17}$), 7.73 (bs, 1H, H_{c2}). ^{31}P NMR (δ , 161 MHz, CDCl_3): 49.3. ^{13}C NMR (δ , 101.5 MHz, CDCl_3): 14.8 (C_{102}), 28.3 (C_{101}), 86.5 (C_8), 89.8 ($\text{C}_{13} + \text{C}_{19}$), 90.3 (C_{20}), 92.0 (C_{14}), 100.2 (C_7), 114.5 (C_3), 117.0 (C_6), 121.7 (C_{12}), 122.7 (C_9), 122.8 (C_{10}), 123.5 (C_{15}), 126.9 (C_{m1}), 127.2 (C_{m2}), 128.4 (C_{11}), 128.8 (C_{p1}), 128.9 (C_{p2}), 129.9 (C_5), 130.4 (C_{c3}), 130.6 (C_4), 131.5 (C_{c2}), 131.6 ($\text{C}_{16} + \text{C}_{17}$), 134.2 (C_{o1}), 134.4 (C_{o2}), 136.6 (C_{11}), 136.4 (C_{12}), 146.1 (C_{10}). C_1 not observed.

Synthesis of 1,4-(Pr₃Si-C≡CC₆H₄-4-C≡CC₆H₂-2,6-Et₂-4-C≡CC₆H₄-4-C≡C)₂C₆H₄ (35).

1,4-Bis((trimethylsilyl)ethynyl)benzene (0.77 g, 2.85 mmol) was added to a mixture of CH_2Cl_2 and MeOH (30 mL, 1:1) and the mixture deoxygenated. K_2CO_3 (0.80 g, 5.80 mmol) was then added and the mixture stirred for 2 h. The mixture was added to deoxygenated water (100 mL) and the organic layer recovered, drying with MgSO_4 . After filtration, the solvent was removed from the filtrate under vacuum and the residue redissolved in deoxygenated NEt_3 (10 mL). The solution was then added to a mixture of **8** (0.36 g, 0.56 mmol), $\text{Pd}(\text{PPh}_3)_4$ (10 mg, 0.008 mmol), CuI (10 mg, 0.05 mmol) and NEt_3 (20 mL) by cannula. The mixture was stirred for 6 h. The solvent was removed under vacuum and the residue was purified by column chromatography on silica, eluting with a mixture of petrol and CH_2Cl_2 (3:1). **35** was obtained as a light yellow solid (0.25 g, 78 %). *Anal.* calc for $\text{C}_{84}\text{H}_{86}\text{Si}_2$: C, 87.60; H, 7.53. Found: C, 87.53; H, 7.47. UV-Vis: 389 [sh, 9.8], 378 [11.6], 288 [2.8]. ^1H NMR (δ , 400 MHz, CDCl_3): 1.14 (s, 21H, $\text{H}_{s11} + \text{H}_{s12}$), 1.32 (t, 6H, H_{102} , $J_{\text{HH}} = 7.6$ Hz), 2.89 (q, 4H, H_{101} , $J_{\text{HH}} = 7.6$ Hz), 7.28 (s, 2H, H_{11}), 7.46 (s, 4H, $\text{H}_4 + \text{H}_5$), 7.52 (s, 6H, $\text{H}_{17} + \text{H}_{16} + \text{H}_{22}$). ^{13}C NMR (δ , 101.5 MHz, CDCl_3): 11.3 (C_{s11}), 14.6 (C_{102}), 18.6 (C_{s12}), 27.9 (C_{101}), 88.2 (C_8), 89.8 (C_{14}), 90.1 (C_{19}), 90.3 (C_{20}), 91.7 (C_{13}), 92.9 (C_1), 98.2 (C_7), 106.6 (C_2), 121.8 (C_9), 122.6 (C_{12}), 123.3 ($\text{C}_{15} + \text{C}_{10}$), 123.4 (C_{c1}), 123.4 (C_6), 123.5 (C_3), 128.5 (C_{11}), 131.1 (C_5), 131.5 ($\text{C}_{16} + \text{C}_{17} + \text{C}_{c2}$), 132.0 (C_4), 146.6 (C_{10}).

Synthesis of 1,4-(trans-[RuCl(dppe)]₂(C≡CC₆H₄-4-C≡CC₆H₂-2,6-Et₂-4-C≡CC₆H₄-4-C≡C))₂C₆H₄ (37).

1,4-(Pr₃SiC≡CC₆H₄-4-C≡CC₆H₂-2,6-Et₂-4-C≡CC₆H₄-4-C≡C)₂C₆H₄ (**35**) (0.018, 0.014 mmol) and TBAF (0.05 mL, 1 M in THF) was added to deoxygenated CH_2Cl_2 (50 mL) and the mixture stirred for 2 h. MeOH (80 mL) was added and the precipitate was recovered by

filtration. The precipitate was identified as 1,4-(HC≡CC₆H₄-4-C≡CC₆H₂-2,6-Et₂-4-C≡CC₆H₄-4-C≡C)₂C₆H₄ (**36**) by ¹H NMR only, but could not be characterised by other techniques due to solubility limitations. The solid was then added to a mixture of deoxygenated and distilled CH₂Cl₂ and [RuCl(dppe)₂]PF₆ (0.030 g, 0.046 mmol) and the mixture stirred for 2 d. The mixture was added to deoxygenated stirring petrol (100 mL) and the precipitate recovered and washed with methanol (20 mL). The solid was then added to a mixture of deoxygenated CH₂Cl₂ and NEt₃ (20 mL, 10:1). Petrol (10 mL) was added and the mixture passed through a short pad of alumina, eluting with a mixture of CH₂Cl₂, petrol and NEt₃ (2:1:0.1). The solvent was removed from the filtrate under vacuum and the residue dissolved in CH₂Cl₂ (2 mL) and precipitated from MeOH (18 mL). The yellow precipitate was recovered by filtration to afford **37** as a yellow solid (0.027 g, 65 %). *Anal. calc* for C₁₇₀H₁₄₀Cl₂P₈Ru₂: C, 75.52; H, 5.22. Found: C, 75.45; H, 5.08. UV-Vis: 432 [9.8], 378 [18.5]. ¹H NMR (δ, 400 MHz, CDCl₃): 1.36 (t, 12H, H₁₀₂, *J*_{HH} = 8 Hz), 2.69 (b, 16H, H₅), 2.93 (q, 8H, H₁₀₁, *J*_{HH} = 8 Hz), 6.60 (d, 4H, H₄, *J*_{HH} = 8 Hz), 6.90-7.1 (m, 32H, H_{m1} + H_{m2}), 7.20-7.25 (m, 16H, H_p), 7.27-7.30 (m, 24H, H₁₁ + H_{o1} + H₄), 7.47-7.53 (m, 28H, H_{o2} + H₁₆ + H₁₇ + H_{c2}). ³¹P NMR (δ, 161 MHz, CDCl₃): 49.3. ¹³C NMR (δ, 101.5 MHz, CDCl₃): 14.6 (C₁₀₂), 27.9 (C₁₀₁), 30.6 (m, C₅), 86.5 (C₀), 89.8 (C₁₃), 90.9 (C₁₉), 91.2 (C₂₀), 92.0 (C₁₄), 100.1 (C₇), 114.53 (C₆), 117.0 (C₃), 121.8 (C₁₂), 122.7 (C₉), 122.8 (C₁₈), 123.0 (C_{c1}), 123.5 (C₁₅), 127.0 (C_{m1}), 127.2 (C_{m2}), 128.4 (C₁₁), 128.8 (C_{p1}+C_{p2}), 130.0 (C₅), 130.6 (C₄), 131.5 (C₁₆ + C₁₇ + C_{c2}), 134.2 (C_{o1}), 134.4 (C_{o2}), 135.6 (m, C₁₁), 136.3 (m, C₁₂), 146.1 (C₁₀). C₁ not observed.

*Synthesis of 1,2,3-(fPr)₃SiC≡CC₆H₄-4-C≡CC₆H₂-2,6-Et₂-4-C≡CC₆H₄-4-C≡C)₃C₆H₃ (**38**).*

1,2,3-Tris(trimethylsilylethynyl)benzene (0.11 g, 0.28 mmol) was added to a mixture of MeOH and CH₂Cl₂ (30 mL, 1:1) and was deoxygenated thoroughly by sparging with N₂. K₂CO₃ (0.110 g, 0.79 mmol) was added and the mixture stirred for 3 h. The mixture was added to deoxygenated water (100 mL) and the product extracted with deoxygenated CH₂Cl₂, and the organic phase dried with MgSO₄. After filtration, the solvent was removed from the filtrate under vacuum and the residue dissolved in deoxygenated NEt₃ (20 mL). The solution was then added via cannula to a deoxygenated mixture of Pd(PPh₃)₄ (20 mg, 0.017 mmol), CuI (30 mg, 0.15 mmol) and **8** (0.55 g, 0.86 mmol) in NEt₃ (30 mL). The mixture was stirred for 12 h before the solvent was removed. The residue was purified by column chromatography on silica, eluting with a gradient of solvent polarity from petrol to a mixture of petrol and CH₂Cl₂ (3:1). The eluate was removed under vacuum to afford **38** as a yellow solid (0.18 g, 36 %). *R_f* (3:1 petrol/CH₂Cl₂) - 0.35. *Anal. calcd* for C₁₂₃H₁₂₆Si₃: C, 87.49; H, 7.52. Found: C, 87.38; H, 7.60. UV-Vis: 378 [sh. 16.2], 358 [19.9], 280 [4.4]. ¹H NMR (δ, 400 MHz, CDCl₃): 1.14 (s, 63H, H_{s11} + H_{s12}), 1.32 (t, 18H, H₁₀₂, *J*_{HH} = 8 Hz), 2.90 (q,

12H, C₁₀₁, *J*_{HH} = 8 Hz), 7.30 (s, 6H, H₁₁), 7.33 (d, 2H, H_{C3}, *J*_{HH} = 8 Hz), 7.46 (s, 12H, H₄ + H₅), 7.52-7.60 (m, 13H, H_{C4} + H₁₆ + H₁₇). ¹³C NMR (δ, 101.5 MHz, CDCl₃): 11.3 (C_{S11}), 14.6 (C₁₀₂), 18.6 (C_{S12}), 27.9 (C₁₀₁), 88.2 (C₈), 89.3 (C₁₉₂), 89.8 (C₁₉), 90.2 (C₁₃), 91.9 (C₁₄), 92.0 (C₁₄₂), 92.9 (C₁), 93.8 (C₂₀), 97.8 (C₂₀₂), 98.3 (C₇), 106.6 (C₂), 121.8 (C₁₂), 122.6 (C₉), 122.8 (C₁₅), 123.1 (C₁₅₂), 123.4 (C₆), 123.4 (C₃), 123.5 (C₁₈), 123.6 (C₁₈₂), 126.1 (C_{C1}), 127.9 (C_{C2}), 128 (C_{C4}), 128.5 (C₁₁), 131.1 (C₅), 131.5 (C_{C3}), 131.6 + 131.7 (C₁₆ + C₁₇), 132.0 (C₄), 146.7 (C₁₀).

Synthesis of 1,2,3-(HC≡C-C₆H₄-4-C≡CC₆H₂-2,6-Et₂-4-C≡CC₆H₄-4-C≡C)₃C₆H₃ (39).

1,2,3-(¹Pr₃SiC≡CC₆H₄-4-C≡CC₆H₂-2,6-Et₂-4-C≡CC₆H₄-4-C≡C)₃C₆H₃ (0.070 g, 0.040 mmol) and TBAF (0.12 mL, 1 M in THF) were added to CH₂Cl₂ (15 mL) and the mixture was stirred for 2 h. MeOH (80 mL) was added and the resultant precipitate was recovered by filtration and washed with MeOH. **39** was obtained as a yellow solid (0.048 g, 90 %). ¹H NMR (δ, 400 MHz, CDCl₃): 1.32 (t, 12H, H₁₀₂, *J*_{HH} = 8 Hz), 2.89 (q, 8H, H₁₀₁, *J*_{HH} = 8 Hz), 3.18 (s, 3H, H₁), 7.30 (s, 4H, H₁₁), 7.33 (t, 1H, H_{C3}, *J*_{HH} = 8 Hz), 7.48 (s, 12H, H₄ + H₅), 7.50-7.59 (m, 13H, H₄ + H₁₇ + H₁₆). ¹³C NMR (δ, 101.5 MHz, CDCl₃): 14.6 (C₁₀₂), 27.9 (C₁₀₁), 78.9 (C₁), 83.3 (C₂), 88.4 (C₈), 89.4 (C₁₉₂), 89.8 (C₁₉), 90.2 (C₁₃), 91.9 + 92.0 (C₁₄ + C₁₄₂), 93.8 (C₂₀), 97.8 (C₂₀₂), 98.0 (C₇), 121.7 (C₁₂), 121.9 (C₃), 122.7 (C₉), 122.9 (C₁₈), 123.1 (C₁₈₂), 123.5 (C₁₅), 123.6 (C₁₅₂), 124.0 (C₆), 126.1 (C_{C1}), 127.8 (C_{C2}), 128.5 (C₁₁ + C_{C4}), 131.2 (C₅), 131.5 (C_{C5}), 131.6 (C₁₆ + C₁₇), 132.1 (C₄), 146.6 (C₁₀).

Synthesis of 1,2,3-(trans-[RuCl(dppe)]₂(C≡CC₆H₄-4-C≡CC₆H₂-2,6-Et₂-4-C≡CC₆H₄-4-C≡C))₃C₆H₃ (40).

39 (0.035 g, 0.03 mmol) was added to deoxygenated and distilled CH₂Cl₂ (15 mL). [RuCl(dppe)₂]PF₆ (0.10 g, 0.090 mmol) was then added and the mixture stirred for 16 h. The solution was then poured into rapidly stirring deoxygenated petrol (150 mL) and the precipitate recovered. The solid was washed with MeOH (30 mL) and then added to a deoxygenated mixture of CH₂Cl₂ and NEt₃ (20 mL, 10:1) and stirred for 20 min. The solution was passed through a short pad of alumina, eluting with a mixture of CH₂Cl₂ and NEt₃ (10:1). **40** was obtained as an orange solid (0.086 g, 79 %). UV-Vis: 429 [15.3], 353 [28.8]. ¹H NMR (δ, 400 MHz, CDCl₃): 1.39 (t, 18H, H₁₀₂, *J*_{HH} = 8 Hz), 2.71 (bs, 24H, H_b), 2.97 (q, 12H, H₁₀₁, *J*_{HH} = 8 Hz), 6.62 (d, 6H, H₄), 6.97-7.00 (m, 48H, H_{m1} + H_{m2}), 7.22 (m, 24H, H_p), 7.33 (m, 32H, H₁₁ + H_{o1} + H_{o4}), 7.48-7.59 (m, 43H, H₅ + H_{C5} + H_{o2} + H₁₆ + H₁₇). ³¹P NMR (δ, 161 MHz, CDCl₃): 49.3. ¹³C NMR (δ, 101.5 MHz, CDCl₃): 14.6 (C₁₀₂), 27.9 (C₁₀₁), 30.6 (C_b),

86.5 (C₈), 89.7 (C₁₉₂), 89.8 (C₁₃ + C₁₉), 89.9 (C₁₄ + C₁₄₂), 93.8 (C₂₀), 97.9 (C₂₀₂), 101.2 (C₇), 114.5 (C₆), 117.0 (C₃), 121.7 (C₁₂), 122.7 + 122.8 (C₉ + C₁₈), 122.9 (C₁₈₂), 123.7 (C₁₅), 123.8 (C₁₅₂), 126.9 (C_{C1}), 127.2 (C_{m1}), 128.4 (C_{m2}), 128.4 (C₁₁), 128.8 (C_{p1} + C_{p2}), 129.9 (C₄), 130.1 (C_{C4}), 130.6 (C₅), 131.6 (C₁₆ + C₁₇), 134.2 (C₀₁), 134.3 (C₀₁), 135.5 (C₁₂), 136.3 (C₁₂), 146.1 (C₁₀). C₁, C₂ and C₅ not observed.

Synthesis of 1,2,4-(Pr₃SiC≡CC₆H₄-4-C≡CC₆H₂-2,6-Et₂-4-C≡CC₆H₄-4-C≡C)₃C₆H₃ (41).

1,2,4-Tris(trimethylsilylethynyl)benzene (0.10 g, 0.27 mmol) in a mixture of MeOH and CH₂Cl₂ (30 mL, 1:1) was deoxygenated thoroughly by sparging with N₂. K₂CO₃ (0.12 g, 0.86 mmol) was added and the mixture stirred for 2 h. The mixture was added to deoxygenated water (100 mL) and the solvent extracted with deoxygenated CH₂Cl₂, drying with MgSO₄. The solvent was removed under vacuum and the residue dissolved in deoxygenated triethylamine (20 mL). The mixture was then added via cannula to a deoxygenated mixture of Pd(PPh₃)₄ (20 mg, 0.017 mmol), CuI (30 mg, 0.15 mmol) and **8** (0.52 g, 0.81 mmol) in NEt₃ (30 mL). The mixture was stirred for 12 h before the solvent was removed under vacuum. The residue was purified by column chromatography on silica, eluting with a gradient solvent polarity from petrol to a mixture of petrol and CH₂Cl₂ (3:1). **41** was obtained as a yellow solid (0.31 g, 68 %). *R_f*(petrol)- 0.21. *Anal.* calcd for C₁₂₃H₁₂₆Si₃: C, 87.42; H, 7.63. Found: C, 87.49; H, 7.42. UV-Vis: 377 [16.6], 362 [17.5], 275 [3.2]. ¹H NMR (δ, 400 MHz, CDCl₃): 1.14 (s, 63H, H_{s11} + H_{s12}), 1.32 (t, 18H, H₁₀₂, *J*_{HH} = 8 Hz), 2.89 (q, 12H, H₁₀₁, *J*_{HH} = 8 Hz), 7.29 (s, 6H, H₁₁), 7.45 (s, 13H, H₄ + H₅ + H_{C5}), 7.50-7.59 (m, 13H, H₁₇ + H₁₆ + H_{C6}), 7.75 (bs, 1H, H_{C3}). ¹³C NMR (δ, 101.5 MHz, CDCl₃): 11.3 (C_{s11}), 14.6 (C₁₀₂), 18.6 (C_{s12}), 27.9 (C₁₀₁), 88.2 (C₈), 89.3 (C₁₉₂), 89.9 (C₁₉), 90.1 (C₁₃), 90.2 (C₁₉₄), 91.4 (C₂₀₄), 91.9 (C₁₄₄), 91.5 (C₁₄), 91.6 (C₁₄₂), 92.9 (C₁), 93.9 (C₂₀), 95.2 (C₂₀₂), 98.3 (C₇), 106.6 (C₂), 121.8 (C₁₂), 122.6 (C₉), 122.8 (C₁₈ + C₁₈₂), 123.1 (C₁₈₄), 123.37 (C₆), 123.41 (C₃), 123.42 (C₁₅₄), 123.6 (C₁₅-C₁₅₂), 125.4 (C_{C1}), 126.0 (C_{C2}), 128.48 (C_{C4}), 128.5 (C₁₁), 131.1 (C₅), 131.5 (C_{C6}), 131.6 (C₁₆ + C₁₇), 131.8 (C_{C5}), 132.0 (C₄), 134.7 (C_{C3}), 146.7 (C₁₀).

Synthesis of 1,2,4-(HC≡CC₆H₄-4-C≡CC₆H₂-2,6-Et₂-4-C≡CC₆H₄-4-C≡C)₃C₆H₃ (42).

1,2,4-(Pr₃SiC≡CC₆H₄-4-C≡CC₆H₂-2,6-Et₂-4-C≡CC₆H₄-4-C≡C)₃C₆H₃ (0.020 g, 0.012 mmol) and TBAF (0.5 mL, 1 M in THF) were added to deoxygenated CH₂Cl₂ (10 mL) and the mixture was stirred for 2 h. MeOH (80 mL) was added and the resulting precipitate was recovered by filtration and washed with MeOH. **42** was obtained as a yellow solid

(0.013 g, 87 %). ^1H NMR (δ , 400 MHz, CDCl_3): 1.33 (t, 18H, H_{102} , $J_{\text{HH}} = 8$ Hz), 2.90 (q, 12H, H_{101} , $J_{\text{HH}} = 8$ Hz), 3.19 (s, 3H, H_1), 7.29 (s, 12H, H_{11}), 7.45 (s, 12H, $\text{H}_4 + \text{H}_5$), 7.50-7.59 (m, 14H, $\text{H}_{c5} + \text{H}_{c6} + \text{H}_{17} + \text{H}_{16}$), 7.75 (bs, 1H, H_{c3}). ^{13}C NMR (δ , 101.5 MHz, CDCl_3): 14.6 (C_{102}), 27.9 (C_{101}), 78.9 (C_1), 83.3 (C_2), 88.4 (C_8), 89.9 (C_{13}), 90.2 (C_{194}), 91.60 + 91.65 ($\text{C}_{19} + \text{C}_{192}$), 94.6 (C_{204}), 94.6 ($\text{C}_{14} + \text{C}_{144}$), 94.6 (C_{14}), 95.2 (C_7), 98.0 (C_7), 98.9 (C_{20}), 100.7 (C_{202}), 121.7 (C_{12}), 121.9 (C_6), 122.7 (C_9), 122.8 ($\text{C}_{18} + \text{C}_{182}$), 123.1 (C_{184}), 123.37 (C_6), 123.41 (C_3), 123.42 (C_{154}), 123.6 ($\text{C}_{15} + \text{C}_{152}$), 125.4 (C_{c1}), 126.0 (C_{c2}), 128.48 (C_{c4}), 128.5 (C_{11}), 131.2 (C_5), 131.6 (C_{c6}), 131.7 ($\text{C}_{16} + \text{C}_{17}$), 132.1 (C_4), 134.7 (C_{c5}), 137.2 (C_{c3}), 146.6 (C_{10}).

Synthesis of 1,2,4-(trans-[RuCl(dppe)]₂ (C≡CC₆H₄-4-C≡CC₆H₂-2,6-Et₂-4-C≡CC₆H₄-4-C≡C))₃C₆H₃ (43).

1,2,4-(HC≡CC₆H₄-4-C≡CC₆H₂-2,6-Et₂-4-C≡CC₆H₄-4-C≡C)₃C₆H₃ (0.034 g, 0.028 mmol) was added to distilled CH_2Cl_2 (10 mL) and the mixture deoxygenated by sparging with N_2 . $[\text{RuCl}(\text{dppe})_2]\text{PF}_6$ (0.10 g, 0.093 mmol) was then added and the mixture stirred for 12 h. The solution was then added by cannula to deoxygenated rapidly stirring petrol (150 mL) and the precipitate recovered. The solid was washed with MeOH (15 mL) and then added to a mixture of deoxygenated CH_2Cl_2 and NEt_3 (20 mL, 10:1) and stirred for 20 min. The solution was filtered through a short pad of alumina eluting with a mixture of CH_2Cl_2 and NEt_3 (10:1). **43** was obtained as a yellow solid (0.068 g, 74 %). UV-Vis: 431 [14.9], 368 [20.9]. ^1H NMR (δ , 400 MHz, CDCl_3): 1.36 (t, 18H, H_{102} , $J_{\text{HH}} = 8$ Hz), 2.68 (bs, 24H, H_6), 2.83 (q, 12H, C_{101} , $J_{\text{HH}} = 8$ Hz), 6.60 (appd (AA'BB'), H_4 , $J_{\text{AB}} = 7.96$), 7.00 (m, 48H, $\text{H}_{m1} + \text{H}_{m2}$), 7.20 (m, 24H, H_p), 7.29 (s, 2H, Ar), 7.31 (m, 31H, $\text{H}_{o1} + \text{H}_5 + \text{H}_{c5}$), 7.50 (m, 25H, $\text{H}_{o2} + \text{H}_{c6}$), 7.56 (m (AA'BB'), 12H, $\text{H}_{16} + \text{H}_{17}$), 7.77 (apps, 1H, H_{c3}). ^{31}P NMR (δ , 161 MHz, CDCl_3): 49.3. ^{13}C NMR (δ , 101.5 MHz, CDCl_3): 14.6 (C_{102}), 27.9 (C_{101}), 78.9 (C_1), 83.3 (C_2), 88.4 (C_8), 89.9 (C_{13}), 90.2 (C_{194}), 91.60 + 91.65 ($\text{C}_{19} + \text{C}_{192}$), 94.6 (C_{204}), 94.6 ($\text{C}_{14} + \text{C}_{144}$), 94.6 (C_{14}), 95.2 (C_7), 98.0 (C_7), 98.9 (C_{20}), 100.7 (C_{202}), 121.7 (C_{12}), 121.9 (C_6), 122.7 (C_9), 122.8 ($\text{C}_{18} + \text{C}_{182}$), 123.1 (C_{184}), 123.37 (C_6), 123.41 (C_3), 123.42 (C_{154}), 123.6 ($\text{C}_{15} + \text{C}_{152}$), 125.4 (C_{c1}), 126.0 (C_{c2}), 128.48 (C_{c4}), 128.5 (C_{11}), 128.8 (C_4), 130.6 (C_5), 131.6 (C_{c6}), 131.6 ($\text{C}_{16} + \text{C}_{17}$), 132.1 (C_4), 134.3 (C_{m1}), 134.4 (C_{m2}), 135.7 (C_{11}), 136.4 (C_{c2}), 146.1 (C_{10}). C_{c3} , C_{c5} not observed.

Synthesis of 1,3,5-(Pr₃SiC≡CC₆H₄-4-C≡CC₆H₂-2,6-Et₂-4-C≡CC₆H₄-4-C≡C)₃C₆H₃ (44).

8 (0.93 g, 1.45 mmol) was added to NEt_3 (30 mL) and the solution deoxygenated under vacuum. $\text{Pd}(\text{PPh}_3)_4$ (10 mg, 0.008 mmol) and CuI (10 mg, 0.05 mmol) was added followed

by a deoxygenated solution of 1,3,5-triethynylbenzene (73 mg, 0.49 mmol) in NEt₃ (5 mL) added by cannula. The reaction was stirred for 6 h. The solvent was removed under vacuum and the residue was purified by column chromatography on silica, eluting with a gradient of solvent polarity from petrol to petrol and CH₂Cl₂ (3:1). **44** was obtained as a light yellow solid (0.63 g, 77 %). *R_f*(petrol) - 0.15. *Anal.* calcd for C₁₂₃H₁₂₆Si₃: C, 87.49; H, 7.52. Found: C, 87.39; H, 7.64. UV-Vis: 353 [sh., 17.1], 367 [sh., 19.8], 359 [21.2], 271 [3.9]. ¹H NMR (δ, 400 MHz, CDCl₃): 1.16 (s, 63H, H_{s11} + H_{s12}), 1.35 (t, 18H, H₁₀₂, *J*_{HH} = 8 Hz), 2.92 (q, 4H, H₁₀₁, *J*_{HH} = 8 Hz), 7.31 (s, 6H, H₁₁), 7.54 (s, 12H, H₄ + H₅), 7.67 (s, 12H, H₁₇ + H₁₆), 7.67 (s, 3H, H_{c2}). ¹³C NMR (δ, 101.5 MHz, CDCl₃): 11.3 (C_{s11}), 14.6 (C₁₀₂), 18.6 (C_{s12}), 27.9 (C₁₀₁), 88.3 (C₈), 89.6 (C₁₉), 90.1 (C₁₃), 90.4 (C₁₄), 91.9 (C₂₀), 92.9 (C₁), 98.3 (C₇), 106.7 (C₂), 121.8 (C₁₂), 122.5 (C₉), 122.6 (C₁₈), 123.4 (C₆), 123.5 (C₃), 123.6 (C₁₅), 123.9 (C_{c1}), 128.5 (C₁₁), 131.1 (C₅), 131.6 (C₁₆), 131.7 (C₁₇), 132.0 (C₄), 134.1 (C_{c2}), 146.7 (C₁₀).

*Synthesis of 1,3,5-(HC≡CC₆H₄-4-C≡CC₆H₂-2,6-Et₂-4-C≡CC₆H₄-4-C≡C)₃C₆H₃ (**45**).*

1,3,5-(Pr₃SiC≡CC₆H₄-4-C≡CC₆H₂-2,6-Et₂-4-C≡CC₆H₄-4-C≡C)₃C₆H₃ (0.07 g, 0.04 mmol) and TBAF (0.15 mL, 1 M in THF) were added to CH₂Cl₂ (15 mL) and the resultant mixture was stirred for 2 h. Water (30 mL) was added and the organic layer recovered and dried with MgSO₄. The solvent was removed under vacuum and the residue purified by column chromatography on silica, eluting with petrol and CH₂Cl₂ (2:1). **44** was obtained as a pale yellow solid (0.03 g, 96 %). ¹H NMR (δ, 400 MHz, CDCl₃): 1.33 (t, 18H, H₁₀₂, *J*_{HH} = 8 Hz), 2.90 (q, 12H, H₁₀₁, *J*_{HH} = 8 Hz), 3.19 (s, 3H, H₁), 7.29 (s, 6H, H₁₁), 7.48 (s, 12H, H₄ + H₅), 7.53 (s, 12H, H₁₇ + H₁₆), 7.66 (s, 3H, H_{c2}). ¹³C NMR (δ, 101.5 MHz, CDCl₃): 14.6 (C₁₀₂), 27.9 (C₁₀₁), 78.9 (C₁), 83.3 (C₂), 88.4 (C₈), 89.6 (C₁₃), 90.1 (C₁₉), 90.4 (C₂₀), 91.8 (C₁₄), 98.0 (C₇), 121.7 (C₁₂), 121.9 (C₃), 122.5 (C₉), 122.7 (C_{c1}), 123.5 (C₁₈), 123.9 (C₁₅), 124.0 (C₆), 128.5 (C₁₁), 131.2 (C₅), 131.6 (C₁₆ + C₁₇), 132.0 (C₄), 134.1 (C_{c2}), 146.6 (C₁₀).

*Synthesis of 1,3,5-(trans-[RuCl(dppe)]₂(C≡C-C₆H₄-4-C≡CC₆H₂-2,6-Et₂-4-C≡CC₆H₄-4-C≡C))₃C₆H₃ (**46**).*

1,3,5-(HC≡CC₆H₄-4-C≡CC₆H₂-2,6-Et₂-4-C≡CC₆H₄-4-C≡C)₃C₆H₃ (0.030 g, 0.028 mmol) was added to deoxygenated and distilled CH₂Cl₂ (10 mL). [RuCl(dppe)]₂PF₆ (0.10 g, 0.093 mmol) was then added and the mixture stirred for 12 h. The solution was then added to

deoxygenated rapidly stirring petrol (150 mL) and the precipitate recovered by filtration under an N₂ flow. The solid was washed with MeOH (20 mL) and then added to a mixture of CH₂Cl₂ and NEt₃ (10:1) and stirred for 20 min. The solution was then filtered through a short pad of alumina eluting with a mixture of CH₂Cl₂ and NEt₃ (10:1). **46** was obtained as a yellow solid (0.07 g, 74 %). *Anal.* calc for C₂₅₂H₂₀₇Cl₃P₁₂Ru₃: C, 75.36; H, 5.19. Found: C, 75.27; H, 5.13. UV-Vis: 430 [15.0], 357 [24.0]. ¹H NMR (δ, 400 MHz, CDCl₃): 1.36 (t, 18H, H₁₀₂, J_{HH} = 8 Hz), 2.68 (bs, 18H, H₅), 2.93 (q, 12H, H₁₀₁, J_{HH} = 8 Hz), 6.60 (d, 6H, H₄), 6.95-7.02 (m, 48H, H_{m1} + H_{m2}), 7.17-7.21 (m, 24H, H_p), 7.28-7.30 (m, 36H, H₅ + H₁₁ + H_{o1}) 7.45-7.58 (m, 36H, H_{o2} + H₁₆ + H₁₇), 7.69 (s, 3H, H_{c2}). ³¹P NMR (δ, 161 MHz, CDCl₃): 49.3. ¹³C NMR (δ, 101.5 MHz, CDCl₃): 14.6 (C₁₀₂), 27.9 (C₁₀₁), 30.6 (m, C_b), 86.5 (C₈), 89.5 (C₁₃), 90.4 (C₂₀), 92.1 (C₁₄), 100.1 (C₇), 114.5 (C₃), 116.9 (C₆), 121.7 (C₁₂), 122.4 (C₉), 122.8 (C₁₈), 123.6 (C₁₅), 123.9 (C_{c1}), 126.9 + 127.22 (C_{m1} + C_{m2}), 128.5 (C₁₁), 128.8 (C_{p1} + C_{p2}), 129.9 (C₄), 130.6 (C₅), 131.6 (C₁₆ + C₁₇), 132.1 (C_{c2}), 134.2 (C_{o1}), 134.6 (C_{o2}), 135.7 (m, C_{i1}), 136.3 (m, C_{i2}), 146.1 (C₁₀).

*Synthesis of 1,2,3,4-(¹Pr₃SiC≡CC₆H₄-4-C≡CC₆H₂-2,6-Et₂-4-C≡CC₆H₄-4-C≡C)₄C₆H₂ (**47**).*

1,2,3,4-Tetrakis(trimethylsilylethynyl)benzene (0.090 g, 0.190 mmol) in a mixture of MeOH and CH₂Cl₂ (30 mL, 1:1) was deoxygenated thoroughly by sparging with N₂. K₂CO₃ (0.12 g, 0.86 mmol) was added and the mixture stirred for 3 h. The mixture was added to deoxygenated water (100 mL) and the solvent extracted with CH₂Cl₂, drying with MgSO₄. The solvent was removed under vacuum and the residue dissolved in deoxygenated NEt₃ (20 mL). The mixture was then added via cannula to a deoxygenated mixture of Pd(PPh₃)₄ (15 mg, 0.012 mmol), CuI (25 mg, 0.13 mmol) and **8** (0.51 g, 0.79 mmol) in triethylamine (30 mL) and stirred for 12 h. The solvent was removed under vacuum and the residue purified by column chromatography on silica, eluting with a gradient solvent polarity from petrol to a mixture of petrol and CH₂Cl₂ (3:1). **47** was obtained as a yellow solid (0.19 g, 46 %). *R_f* 0.31 (3:1, petrol/CH₂Cl₂). *Anal.* calc for C₁₆₂H₁₆₆Si₄: C, 87.43; H, 7.52. Found: C, 87.41; H, 7.46. UV-Vis: 395 [15.6], 372 [22.2]. ¹H NMR (δ, 400 MHz, CDCl₃): 1.15 (s, 84H, H_{s11} + H_{s12}), 1.33 (t, 24H, H₁₀₂, J_{HH} = 8 Hz), 2.90 (q, 16H, C₁₀₁, J_{HH} = 8 Hz), 7.30 (s, 8H, H₁₁), 7.46 (s, 16H, H₄ + H₅), 7.52-7.60 (m, 13H, H_{c5} + H₁₆ + H₁₇). ¹³C NMR (δ, 101.5 MHz, CDCl₃): 11.3 (C_{s11}), 14.6 (C₁₀₂), 18.6 (C_{s12}), 27.9 (C₁₀₁), 88.2 (C₈), 89.3 (C₁₉₂), 89.8 (C₁₉), 90.2 (C₁₃), 91.9 (C₁₄), 92.0 (C₁₄₂), 92.9 (C₁), 93.8 (C₂₀), 97.8 (C₂₀₂), 98.3 (C₇), 106.6 (C₂), 121.8 (C₁₂), 122.6 (C₉), 122.8 (C₁₅), 123.1 (C₁₅₂), 123.4 (C₆), 123.4 (C₃), 123.5 (C₁₈), 123.6 (C₁₈₂), 126.1 (C_{c1}), 127.9 (C_{c2}), 128.0 (C_{c5}), 128.5 (C₁₁), 131.1 (C₅), 131.5 (C_{c3}), 131.6 + 131.7 (C₁₆ + C₁₇), 132.0 (C₄), 146.7 (C₁₀).

Synthesis of 1,2,3,4-(HC≡CC₆H₄-4-C≡CC₆H₂-2,6-Et₂-4-C≡CC₆H₄-4-C≡C)₄C₆H₂ (**48**).

1,2,3,4-(Pr₃SiC≡CC₆H₄-4-C≡CC₆H₂-2,6-Et₂-4-C≡CC₆H₄-4-C≡C)₄C₆H₂ (0.040 g, 0.017 mmol) and TBAF (0.10 mL, 1 M in THF) were added to CH₂Cl₂ (10 mL). The mixture was stirred for 2 h, then MeOH (60 mL) was added. The precipitate was recovered by filtration and washed thoroughly with MeOH. **48** was obtained as a yellow solid (0.025 g, 89 %). ¹H NMR (δ, 400 MHz, CDCl₃): 1.31 (t, 24H, H₁₀₂, J_{HH} = 8 Hz), 2.89 (q, 16H, H₁₀₁, J_{HH} = 8 Hz), 3.17 (s, 4H, H₁), 7.47-7.58 (m, 32H, H₄, H₅, H₁₆, H₁₇, H₁₅). ¹³C NMR (δ, 101.5 MHz, CDCl₃): 14.6 (H₁₀₂), 27.9 (H₁₀₉), 79.9 (C₁), 83.4 (C₂), 88.4 (C₆), 89.8 (C₁₉), 90.1 (C₁₉₂), 90.3 (C₁₃), 91.7 (C₂₀), 92.0 (C₁₄), 95.5 (C₂₀₂), 97.9 (C₇), 121.7 (C₁₂), 121.8 (C₃), 122.7 (C₉), 122.8 (C₁₈ + C₁₈₂), 123.6 (C₁₅ + C₁₅₂), 123.4 (C₆), 126.2 (C_{c1} + C_{c2}), 128.5 (C₁₁ + C_{c4}), 131.1 (C₅), 131.5 (C₁₆ + C₁₇), 132.1 (C₄), 146.6 (C₁₀).

Synthesis of 1,2,3,4-(trans-[RuCl(dppe)]₂(C≡CC₆H₄-4-C≡CC₆H₂-2,6-Et₂-4-C≡CC₆H₄-4-C≡C))₄C₆H₂ (**49**).

1,2,3,4-(HC≡CC₆H₄-4-C≡CC₆H₂-2,6-Et₂-4-C≡CC₆H₄-4-C≡C)₄C₆H₂ (0.025 g, 0.015 mmol) was added to deoxygenated and distilled CH₂Cl₂ (10 mL). [RuCl(dppe)]₂PF₆ (0.07 g, 0.065 mmol) was then added and the mixture stirred for 8 h. The solution was then added to rapidly stirring deoxygenated petrol (100 mL) and the precipitate recovered. The solid was washed with deoxygenated MeOH and then added to a mixture of CH₂Cl₂ and NEt₃ (10:1) and stirred for 20 min. The solution was then put through a short pad of alumina, eluting with a mixture of CH₂Cl₂ and NEt₃ (10:1). **49** was obtained as a yellow solid (0.05 g, 60 %). Anal. calcd for C₃₃₄H₂₇₄Cl₄P₁₆Ru₄: C, 75.27; H, 5.18. Found: C, 75.18; H, 5.17. UV-Vis: 430 [18.4], 375 [26.6], 315 [16.3]. ¹H NMR (δ, 400 MHz, CDCl₃): 1.36 (t, 24H, H₁₀₂), 2.68 (bs, 32H, H₆), 2.93 (q, 16H, H₁₀₁), 6.60 (d, 8H, H₄), 6.95-7.00 (m, 64H, H_{m1} + H_{m2}), 7.17-7.21 (m, 32H, H_p), 7.28-7.30 (m, 52H, H₅ + H₁₁ + H₁₀₁), 7.45-7.58 (m, 50H, H₁₆ + H₁₇ + H₁₅). ¹³C NMR (δ, 101.5 MHz, CDCl₃): 14.6 (C₁₀₂), 27.9 (C₁₀₁), 30.6, (m, C₆), 86.5 (C₆), 89.5 (C₁₃), 90.0 (C₁₉), 91.6 (C₂₀), 92.2 (C₁₄), 94.0 (C₇), 100.1 (C₇), 114.5 (C₃), 116.9 (C₆), 121.7 (C₁₂), 122.7 (C₉), 122.8 (C₁₈ + C₁₈₂), 123.6 (C₁₅ + C₁₅₂), 125.9 (C_{c1} + C_{c2}), 126.8 (C_{m1}), 126.9 (C_{m2}), 127.2 (C_{c3}), 128.5 (C₁₁), 128.8 (C_{p1} + C_{p2}), 129.9 (C₄), 130.6 (C₅), 131.6 (C₁₆ + C₁₇), 132.1 (C_{c2}), 134.2 (C₁₀₁), 134.3 (C₁₀₂), 135.7 (m, C₁₁), 136.3 (m, C₁₂), 146.1 (C₁₀).

Synthesis of 1,2,3,5-(Pr₃SiC≡CC₆H₄-4-C≡CC₆H₂-2,6-Et₂-4-C≡CC₆H₄-4-C≡C)₄C₆H₂ (**50**).

1,2,3,5-Tetrakis(trimethylsilylethynyl)benzene (0.050 g, 0.120 mmol) in a mixture of MeOH and CH₂Cl₂ (1:1, 20 mL) was deoxygenated by sparging with N₂. K₂CO₃ (0.11 g, 0.79 mmol) was added and the mixture stirred for 4 h. The mixture was added to deoxygenated water (100 mL) by cannula and the product extracted with deoxygenated CH₂Cl₂, drying with MgSO₄. The solvent was removed under vacuum and the residue dissolved in deoxygenated triethylamine (20 mL). The mixture was then added via cannula to a deoxygenated mixture of Pd(PPh₃)₄ (20 mg, 0.017 mmol), CuI (30 mg, 0.15 mmol) and **8** (0.33 g, 0.51 mmol) in triethylamine (50 mL). The mixture was stirred for 12 h before the solvent was removed under vacuum. The residue was purified by column chromatography using silica, eluting with a gradient solvent polarity from petrol to a mixture of petrol and CH₂Cl₂ (3:1). **50** was obtained as a yellow solid (0.17 g, 64 %). R_f (3:1, petrol/CH₂Cl₂) - 0.25. Anal. calcd for C₁₆₂H₁₆₆Si₄: C, 87.43; H, 7.52. Found: C, 87.38; H, 7.61. UV-Vis: 378 [19.3], 366 [20.8]. ¹H NMR (δ, 400 MHz, CDCl₃): 1.14 (s, 63H, H_{s11} + H_{s12}), 1.32 (t, 18H, H_{10z}, J_{HH} = 8 Hz), 2.90 (q, 12H, C₁₀₁, J_{HH} = 8 Hz), 7.30 (s, 6H, H₁₁), 7.33 (d, 2H, H_{c3}), 7.46 (s, 12H, H₄ + H₅), 7.52-7.60 (m, 13H, H_{c4} + H₁₆ + H₁₇). ¹³C NMR (δ, 101.5 MHz, CDCl₃): 11.3 (C_{s11}), 14.6 (C_{10z}), 18.6 (C_{s12}), 27.9 (C₁₀₁), 88.2 (C₈), 89.3 (C_{19z}), 89.8 (C₁₉), 90.2 (C₁₃), 91.9 (C₁₄), 92.0 (C_{14z}), 92.9 (C₁), 93.8 (C₂₀), 97.8 (C_{20z}), 98.3 (C₇), 106.6 (C₂), 121.8 (C₁₂), 122.6 (C₉), 122.8 (C₁₅), 123.1 (C_{15z}), 123.4 (C₆), 123.4 (C₃), 123.5 (C₁₈), 123.6 (C_{18z}), 126.1 (C_{c1}), 127.9 (C_{c2}), 128 (C_{c4}), 128.5 (C₁₁), 131.1 (C₅), 131.5 (C_{c3}), 131.6 (C₅), 131.7 (C₁₆ + C₁₇), 132.0 (C₄), 146.7 (C₁₀).

Synthesis of 1,2,3,5-(H-C≡C-C₆H₄-4-C≡CC₆H₂-2,6-Et₂-4-C≡CC₆H₄-4-C≡C)₄C₆H₂ (**51**).

1,2,3,5-(Pr₃SiC≡CC₆H₄-4-C≡CC₆H₂-2,6-Et₂-4-C≡CC₆H₄-4-C≡C)₄C₆H₂ (0.080, 0.035 mmol) and TBAF (0.10 mL, 1 M in THF) were added to CH₂Cl₂ (40 mL) and the mixture was stirred for 2 h. MeOH (100 mL) was added and the precipitate was recovered by filtration and washed thoroughly with MeOH. **51** was obtained as a yellow solid (0.051 g, 90 %). ¹H NMR (δ, 400 MHz, CDCl₃): 1.35 (t, 24H, H_{10z}, J_{HH} = 8 Hz), 2.92 (q, 16H, H₁₀₁, J_{HH} = 8 Hz), 3.21 (s, 4H, H₁), 7.33 (s, 8H, H₁₁), 7.56 (s, 1H, H₄ + H₅), 7.57-7.63 (m, 16H, H₁₆ + H₁₇), 7.72 (s, 2H, H_{c4}). ¹³C NMR (δ, 101.5 MHz, CDCl₃): 14.6 (C_{10z}), 27.9 (C₁₀₁), 78.9 (C₁), 83.28 (C₂), 88.4 (C₈), 88.4 (C₁₉), 88.9 (C_{19z} + C_{19z}), 90.3 (C₂₀), 90.1 (C₁₃), 92.1 (C₁₄), 94.2 (C₂₀), 98.4 (C₇), 99.4 (C_{20z}), 121.8 (C₁₂), 121.9 (C₆), 122.7 (C₉), 123.1 (C₁₈), 123.7 (C₁₅ + C_{15z} + C_{15z}), 124.0 (C_{c4} + C₆), 126.4 (C_{c1}), 127.5 (C_{c2} + C_{c5}), 128.5 (C₁₁), 131.2 (C₅), 131.7 (C₁₆ + C₁₇), 131.6 (C_{2z}), 132.1 (C₄), 134.1 (C_{c4}), 146.6 (C₁₀).

Synthesis of 1,2,3,5-(trans-[RuCl(dppe)₂(C≡CC₆H₄-4-C≡CC₆H₂-2,6-Et₂-4-C≡CC₆H₄-4-C≡C]))₄C₆H₂ (52).

1,2,3,5-(HC≡CC₆H₄-4-C≡CC₆H₂-2,6-Et₂-4-C≡CC₆H₄-4-C≡C)₄C₆H₂ (0.040 g, 0.025 mmol) was added to deoxygenated and distilled CH₂Cl₂ (15 mL). [RuCl(dppe)₂]PF₆ (0.11 g, 0.11 mmol) was then added and the mixture stirred for 8 h. The solution was then added to rapidly stirring deoxygenated petrol (100 mL) and the precipitate recovered. The solid was washed with deoxygenated MeOH and then added to a mixture of CH₂Cl₂ and NEt₃ (10:1) and stirred for 20 min. The solution was then passed through a short pad of alumina, eluting with a mixture of CH₂Cl₂ and NEt₃ (10:1). **52** was obtained as an orange solid (0.10 g, 76 %). *Anal.* calcd for C₃₃₄H₂₇₄Cl₄P₁₆Ru₄: C, 75.27; H, 5.18. Found: C, 75.33; H, 5.14. UV-Vis: 434 [16.2], 404 [26.5], 369 [31.1]. ¹H NMR (δ, 400 MHz, CDCl₃): 1.36 (t, 24H, H₁₀₂, J_{HH} = 8 Hz), 2.68 (bs, 32H, H_b), 2.93 (q, 16H, H₁₀₁, J_{HH} = 8 Hz), 6.60 (d, 8H, H₄), 7.02–7.22 (m, 96H, H_{m1} + H_{m2} + H_p), 7.31–7.60 (m, 91H, H_{o1} + H_{o2} + H₁₆ + H₁₇), 7.69 (s, 2H, H_{ε4}). ³¹P NMR: 49.3. ¹³C NMR (δ, 101.5 MHz, CDCl₃): 14.6 (C₁₀₂), 27.9 (C₁₀₁), 30.6 (m, C_b), 126.8 (C_{m2}), 126.9 (C_{m1}), 128.5 (C₁₁), 128.8 (C_{p1} + C_{p2}), 129.9 (C₄), 130.6 (C₅), 131.6 (C₁₆ + C₁₇), 134.2 (C_{o1}), 134.3 (C_{o2}), 135.7 (m, C₁₁), 136.3 (m, C₁₂), 146.1 (C₁₀). Quaternary and core carbon environments not observed.

Synthesis of 1,2,4,5-(Pr₃SiC≡CC₆H₄-4-C≡CC₆H₂-2,6-Et₂-4-C≡CC₆H₄-4-C≡C)₄C₆H₂ (53).

1,2,4,5-Tetrakis(trimethylsilylethynyl)benzene (0.090 g, 0.190 mmol) in a mixture of MeOH and CH₂Cl₂ (1:1, 30 mL) was deoxygenated thoroughly by sparging with N₂. K₂CO₃ (0.110 g, 0.79 mmol) was added and the mixture stirred for 3 h. The mixture was added to deoxygenated water (100 mL) and the product extracted with CH₂Cl₂, drying the organic layer with MgSO₄. After filtration, the solvent was removed from the filtrate under vacuum and the residue dissolved in deoxygenated NEt₃ (20 mL). The mixture was then added via cannula to a deoxygenated mixture of Pd(PPh₃)₄ (15 mg, 0.013 mmol), CuI (25 mg, 0.13 mmol) and **8** (0.50 g, 0.78 mmol) in NEt₃ (30 mL). The mixture was stirred for 12 h before the solvent was removed under vacuum. The residue was purified by column chromatography on silica, eluting with a gradient solvent polarity from petrol to a mixture of petrol and CH₂Cl₂ (3:1). **53** was obtained as a yellow solid (0.33 g, 77 %). *R_f* (petrol/CH₂Cl₂ (3:1)) - 0.21. *Anal.* calcd for C₁₆₂H₁₆₆Si₄: C, 87.43; H, 7.52. Found: C, 87.48; H, 7.52. UV-Vis: 401 [11.9], 372 [21.3]. ¹H NMR (δ, 400 MHz, CDCl₃): 1.14 (s, 84H, H_{s11} + H_{s12}),

1.34 (t, 24H, H_{102} , $J_{HH} = 7.6$ Hz), 2.90 (q, 16H, H_{101} , $J_{HH} = 7.6$ Hz), 7.29 (s, 8H, H_{11}), 7.45 (s, 16H, $H_4 + H_5$), 7.52 (s, 16H, $H_{17} + H_{16}$), 7.72 (s, 2H, H_{C3}). ^{13}C NMR (δ , 101.5 MHz, $CDCl_3$): 11.3 (C_{511}), 14.6 (C_{102}), 18.6 (C_{512}), 27.9 (C_{101}), 88.2 (C_8), 89.3 (C_{19}), 90.1 (C_{13}), 92.13 (C_{20}), 92.9 (C_{14}), 95.5 (C_1), 98.3 (C_7), 106.6 (C_2), 121.9 (C_{12}), 122.6 ($C_9 + C_{10}$), 123.3 + 123.4 ($C_3 + C_6$), 123.7 (C_{15}), 125.7 (C_{C1}), 128.5 (C_{11}), 131.1 (C_5), 131.6 ($C_{16} + C_{17}$), 132.0 (C_4), 134.8 (C_{C3}), 146.6 (C_{10}).

Synthesis of 1,2,4,5-(HC \equiv CC $_6$ H $_4$ -4-C \equiv CC $_6$ H $_2$ -2,6-Et $_2$ -4-C \equiv CC $_6$ H $_4$ -4-C \equiv C) $_4$ C $_6$ H $_2$ (54).

1,2,4,5-(Pr $_3$ SiC \equiv CC $_6$ H $_4$ -4-C \equiv CC $_6$ H $_2$ -2,6-Et $_2$ -4-C \equiv CC $_6$ H $_4$ -4-C \equiv C) $_4$ C $_6$ H $_2$ (0.021 g, 0.009 mmol) and TBAF (0.05 mL, 1 M in THF) were added to CH_2Cl_2 (15 mL) and the mixture was stirred for 2 h. MeOH (80 mL) was then added and the precipitate was recovered by filtration and washed with MeOH. **54** was obtained as a yellow solid (0.017 g, 82 %). 1H NMR (δ , 400 MHz, $CDCl_3$): 1.32 (t, 24H, H_{102} , $J_{HH} = 7.6$ Hz), 2.90 (q, 16H, H_{101} , $J_{HH} = 7.6$ Hz), 3.19 (s, 4H, H_1), 7.29 (s, 8H, H_{11}), 7.48 (s, 16H, $H_4 + H_5$), 7.54 (s, 16H, $H_{17} + H_{16}$), 7.76 (s, 2H, H_{C3}). ^{13}C NMR (δ , 101.5 MHz, $CDCl_3$): 14.6 (C_{102}), 27.9 (C_{101}), 78.9 (C_1), 83.3 (C_2), 88.4 (C_8), 89.3 (C_{14}), 90.1 (C_{13}), 92.1 (C_{20}), 95.5 (C_{19}), 98.0 (C_7), 121.7 (C_9), 121.9 (C_6), 122.6 (C_{10}), 122.7 (C_{15}), 123.7 (C_3), 124.1 (C_{12}), 125.3 (C_{C1}), 128.5 (C_{11}), 131.2 (C_5), 131.6 ($C_{16} + C_{17}$), 132.1 (C_4), 134.8 (C_{C3}), 146.6 (C_{10}).

Synthesis of 1,2,4,5-(trans-[RuCl(dppe) $_2$](C \equiv CC $_6$ H $_4$ -4-C \equiv CC $_6$ H $_2$ -2,6-Et $_2$ -4-C \equiv CC $_6$ H $_4$ -4-C \equiv C)) $_4$ C $_6$ H $_2$ (55).

1,2,4,5-(HC \equiv CC $_6$ H $_4$ -4-C \equiv CC $_6$ H $_2$ -2,6-Et $_2$ -4-C \equiv CC $_6$ H $_4$ -4-C \equiv C) $_4$ C $_6$ H $_2$ (0.017 g, 0.01 mmol) was added to distilled CH_2Cl_2 (15 mL) and the mixture deoxygenated under vacuum, backfilling with N_2 . [RuCl(dppe) $_2$]PF $_6$ (0.050 g, 0.046 mmol) was then added and the mixture stirred for 8 h. The solution was then added to deoxygenated petrol (150 mL) and the precipitate recovered. The solid was washed with deoxygenated MeOH (30 mL) and then added to a mixture of CH_2Cl_2 and NEt_3 (10:1) and stirred for 20 min. The solution was passed through a short pad of alumina eluting with a mixture of CH_2Cl_2 and NEt_3 (10:1). **55** was obtained as an orange solid (0.034 g, 61 %). UV-Vis: 436 [16.5], 404 [26.5], 369 [31.1]. 1H NMR (δ , 400 MHz, $CDCl_3$): 1.35 (t, 24H, H_{102} , $J_{HH} = 8$ Hz), 2.68 (bs, 32H, H_b), 2.94 (q, 16H, H_{101} , $J_{HH} = 8$ Hz), 6.60 (d, 8H, H_4), 6.95-7.02 (m, 64H, $H_{m1} + H_{m2}$), 7.17-7.21 (m, 32H, H_p), 7.28-7.30 (m, 52H, $H_5 + H_{11} + H_{01}$), 7.45-7.58 (m, 48H, $H_{02} + H_{16} + H_{17}$), 7.69 (s, 2H, H_{C3}). ^{13}C NMR (δ , 101.5 MHz, $CDCl_3$): 14.6 (C_{102}), 27.9 (C_{101}), 30.6, (m, C_b), 86.5 (C_8), 89.5

(C₁₃), 90.0 (C₁₉), 91.6 (C₂₀), 92.2 (C₁₄), 94.0 (C₇), 100.1 (C₇), 114.5 (C₃), 116.9 (C₆), 121.7 (C₁₂), 122.4 (C₉), 122.7 (C₉), 122.8 (C₁₈), 123.6 (C₁₅), 125.9 (C_{c1}), 126.8 (C_{m2}), 126.9 (C_{m1}), 127.2 (C_{c3}), 128.5 (C₁₁), 128.8 (C_{p1} + C_{p2}), 129.9 (C₄), 130.6 (C₅), 131.6 (C₁₆ + C₁₇), 132.1 (C_{c2}), 134.2 (C₀₁), 134.3 (C₀₂), 135.7 (m, C₁₁), 136.3 (m, C₁₂), 146.1 (C₁₀).

Synthesis of 1,2,3,4,5-(^tPr₃SiC≡C₆H₄-4-C≡CC₆H₂-2,6-Et₂-4-C≡CC₆H₄-4-C≡C)₅C₆H (56).

1,2,3,4,5-Pentakis(trimethylsilylethynyl)benzene (0.053 g, 0.095 mmol) in a mixture of MeOH and CH₂Cl₂ (50 mL, 1:1) was deoxygenated thoroughly by sparging with N₂. K₂CO₃ (0.070 g, 0.51 mmol) was added and the mixture stirred for 3 h. The mixture was added to deoxygenated water (100 mL) and the organic layer recovered, drying with CaCl₂. After filtration, the solvent was removed from the filtrate under vacuum and the residue dissolved in deoxygenated NEt₃ (20 mL). The mixture was then added via cannula to a deoxygenated mixture of Pd(PPh₃)₄ (30 mg, 0.026 mmol), CuI (50 mg, 0.26 mmol) and **8** (0.33 g, 0.51 mmol) in NEt₃ (30 mL). The mixture was stirred for 12 h at room temperature before the solvent was removed. The residue was purified by column chromatography on silica and eluting with a gradient solvent polarity from petrol to a mixture of petrol and CH₂Cl₂ (3:1). **56** was obtained as a yellow solid (0.18 g, 69 %). R_f(petrol/CH₂Cl₂ (3:1))= 0.15. UV-Vis: 397 [sh, 25.4], 383 [31.6], 335 [22.6]. ¹H NMR (δ, 400 MHz, CDCl₃): 1.15 (s, 105H, H_{s11} + H_{s12}), 1.32 (t, 30H, H₁₀₂, J_{HH} = 8 Hz), 2.89 (q, 20H, C₁₀₁, J_{HH} = 8 Hz), 7.28 (s, 10H, H₁₁), 7.46 (s, 20H, H₄ + H₅), 7.52-7.59 (m, 20H, H₁₇ + H₁₆), 7.72 (s, 1H, H_{e6}). ¹³C NMR (δ, 101.5 MHz, CDCl₃): 11.3 (C_{s11}), 14.6 (C₁₀₂), 18.6 (C_{s12}), 27.9 (C₁₀₁), 88.2 (C₈), 88.9 (C₁₉), 89.2 (C₁₉₂ + C₁₉₃), 90.1 (C₁₃), 92.1 + 92.2 + 92.3 (C₁₄ + C₁₄₂ + C₁₄₃), 92.8 (C₇), 95.3 (C₂₀), 98.3 (C₁), 99.4 (C₂₀₂ + C₂₀₃), 106.6 (C₂), 121.8 (C₉), 122.5 (C₁₈₂ + C₁₈₃), 122.6 (C₁₂), 122.8 (C₁₅₂ + C₁₅₃), 123.3 + 123.4 (C₃ + C₆) 123.7 (C₁₈), 123.8 (C₁₅), 125.3 (C_{c1}), 127.5 (C_{c2} + C_{c3}), 128.5 (C₁₁), 131.1 (C₅), 131.4 (C_{c5}), 131.6 (C₁₆ + C₁₇), 132.0 (C₄), 133.8 (C_{e6}), 146.6 (C₁₀).

Synthesis of 1,2,3,4,5-(HC≡CC₆H₄-4-C≡CC₆H₂-2,6-Et₂-4-C≡CC₆H₄-4-C≡C)₅C₆H (57).

1,2,3,4,5-(^tPr₃SiC≡CC₆H₄-4-C≡CC₆H₂-2,6-Et₂-4-C≡CC₆H₄-4-C≡C)₅C₆H (0.032 g, 0.012 mmol) and TBAF (0.11 mL, 1 M in THF) were added to CH₂Cl₂ (10 mL) and the mixture was stirred for 2 h. MeOH (70 mL) was added and the precipitate was recovered by filtration and washed with MeOH. **56** was obtained as a yellow solid (0.023 g, 99 %). ¹H NMR (δ, 400 MHz, CDCl₃): 1.32 (t, 30H, H₁₀₂, J_{HH} = 8 Hz), 2.89 (q, 20H, H₁₀₁, J_{HH} = 8 Hz), 3.18

(s, 5H, H₁), 7.29 (s, 10H, H₁₁), 7.35-7.60 (m, 41H, H₄ + H₅ + H₁₆ + H₁₇ + H₁₆). ¹³C NMR (δ, 101.5 MHz, CDCl₃); 14.6 (C₁₀₂), 27.9 (C₁₀₁), 78.9 (C₁), 83.28 (C₂), 88.4 (C₈), 89.0 + 89.8 + 89.2 (C₁₉), 90.2 (C₁₃), 92.1 + 92.2 (C₁₄ + C₁₄₂ + C₁₄₃), 95.5 (C₂₀), 98.0 (C₇), 99.4 (C₂₀₂ + C₂₀₃), 121.7 (C₃), 121.8 (C₁₂), 122.5 (C₁₈), 122.7 (C₉), 122.8 (C₁₀₂ + C₁₀₃), 123.7 (C₁₅ + C₁₅₂ + C₁₅₃), 124.0 (C₆), 125.3 (C₁₁), 127.4 (C₁₂ + C₁₃), 128.5 (C₁₁), 131.1 (C₅), 131.6 (C₁₆ + C₁₇), 132.0 (C₄), 133.8 (C₆), 146.6 (C₁₀).

Synthesis of 1,2,3,4,5-(trans-[RuCl(dppe)]₂(C≡CC₆H₄-4-C≡CC₆H₂-2,6-Et₂-4-C≡CC₆H₄-4-C≡C))₅C₆H (58).

1,2,3,4,5-(HC≡CC₆H₄-4-C≡CC₆H₂-2,6-Et₂-4-C≡CC₆H₄-4-C≡C)₅C₆H (0.011 g, 0.005 mmol) was added to distilled and deoxygenated CH₂Cl₂ (10 mL). [RuCl(dppe)]₂PF₆ (0.028 g, 0.026 mmol) was then added and the mixture stirred for 14 h. The solution was then added to rapidly stirring deoxygenated petrol (150 mL) and the precipitate recovered by filtration. The solid was washed with deoxygenated MeOH (30 mL) and then added to a mixture of CH₂Cl₂ and NEt₃ (10:1) and stirred for 10 min. The solution was added dropwise to stirring MeOH (100 mL) and the precipitate recovered by filtration. The solid was washed with acetone (10 mL) and dried under vacuum to give **58** as an orange solid (0.014 g, 42 %). UV-Vis: 388 [38.0], 332 [25.2]. ¹H NMR (δ, 400 MHz, CDCl₃): 1.39 (t, 30H, H₁₀₂, J_{HH} = 8 Hz), 2.70 (bs, 40H, H₆), 2.98 (q, 20H, H₁₀₁, J_{HH} = 8 Hz), 6.60 (d, 10H, H₄), 6.95-7.02 (m, 80H, H_{m1} + H_{m2}), 7.17-7.21 (m, 40H, H₉), 7.28-7.30 (m, 60H, H₅ + H₁₁ + H₁₀₁), 7.45-7.58 (m, 61H, H₁₀₂ + H₁₆ + H₁₇ + H₁₆), 7.69 (s, 2H, H₁₃). ³¹P NMR: 49.9. ¹³C NMR (δ, 101.5 MHz, CDCl₃): 14.6 (C₁₀₂), 27.9 (C₁₀₁), 30.6, (m, C₆), 126.8 (C_{m2}), 126.9 (C_{m1}), 128.5 (C₁₁), 128.8 (C_{p1} + C_{p2}), 129.9 (C₄), 130.6 (C₅), 131.6 (C₁₆ + C₁₇), 134.2 (C₁₀₁), 134.3 (C₁₀₂), 135.7 (m, C₁₁), 136.3 (m, C₁₂), 146.1 (C₁₀). Quaternary and core carbon environments not observed.

Synthesis of 1,2,3,4,5,6-(ⁱPr₃SiC≡CC₆H₄-4-C≡CC₆H₂-2,6-Et₂-4-C≡CC₆H₄-4-C≡C)₆C₆ (59).

1,2,3,4,5,6-Hexakis(trimethylsilylethynyl)benzene (0.015 g, 0.023 mmol) in a mixture of MeOH and CH₂Cl₂ (1:1, 30 mL) was deoxygenated thoroughly by sparging with N₂. K₂CO₃ (0.040 g, 0.28 mmol) was added and the mixture stirred for 2 h. The mixture was added to deoxygenated water (100 mL) and organic layer recovered, drying with MgSO₄. The solvent was removed under vacuum and the residue dissolved in deoxygenated NEt₃ (20 mL). The mixture was then added via cannula to a deoxygenated mixture of Pd(PPh₃)₄ (5 mg, 0.043 mmol), CuI (10 mg, 0.052 mmol) and **8** (0.10 g, 0.86 mmol) in triethylamine (30

mL). The mixture was stirred for 12 h before the solvent was removed under vacuum. The residue was purified by column chromatography on silica, eluting with a gradient solvent polarity from petrol to a mixture of petrol and CH_2Cl_2 (3:1). **59** was obtained as a yellow solid (0.055 g, 74 %). R_f (3:1 Petrol/ CH_2Cl_2) - 0.35. *Anal.* calcd for $\text{C}_{240}\text{H}_{246}\text{Si}_6$: C, 87.38; H, 7.52. Found: C, 87.31; H, 7.58. UV-Vis: 420 [sh, 24.8], 397 [36.6], 348 [26.1]. ^1H NMR (δ , 400 MHz, CDCl_3): 1.14 (s, 126H, $\text{H}_{511} + \text{H}_{512}$), 1.28 (t, 36H, H_{102} , $J_{\text{HH}} = 8$ Hz), 2.90 (q, 24H, H_{101} , $J_{\text{HH}} = 8$ Hz), 7.30 (s, 12H, H_{11}), 7.46 (s, 24H, $\text{H}_4 + \text{H}_5$), 7.52-7.60 (m (AA'BB'), 24H, ($\text{H}_{16} + \text{H}_{17}$)). ^{13}C NMR (δ , 101.5 MHz, CDCl_3): 11.3 (C_{511}), 14.6 (C_{102}), 18.6 (C_{512}), 27.9 (C_{101}), 88.3 (C_8), 89.8 (C_{19}), 90.2 (C_{13}), 92.3 (C_{14}), 92.9 (C_{20}), 98.3 (C_1), 98.5 (C_7), 106.6 (C_2), 121.8 (C_{12}), 122.6 (C_{12}), 122.8 (C_9), 123.3 (C_{18}), 123.4 ($\text{C}_3 + \text{C}_6$), 123.5 (C_{15}), 127.4 (C_{e1}), 128.5 (C_{11}), 131.1 (C_5), 131.6 ($\text{C}_{16} + \text{C}_{17}$), 132.0 (C_4), 146.7 (C_{10}).

*Synthesis of 1,2,3,4,5,6-(HC = CC₆H₄-4-C ≡ CC₆H₂-2,6-Et₂-4-C ≡ CC₆H₄-4-C ≡ C)₆C₆ (**60**).*

1,2,3,4,5,6-($\text{Pr}_3\text{SiC} \equiv \text{CC}_6\text{H}_4-4-\text{C} \equiv \text{CC}_6\text{H}_2-2,6-\text{Et}_2-4-\text{C} \equiv \text{CC}_6\text{H}_4-4-\text{C} \equiv \text{C}$)₆C₆ (0.040 g, 0.012 mmol) and TBAF (0.12 mL, 1 M in THF) were added to CH_2Cl_2 (5 mL) and the mixture was stirred for 2 h. MeOH (50 mL) was then added and the precipitate was recovered by filtration and washed with MeOH. **60** was obtained as an orange solid (0.028 g, 97 %). ^1H NMR (δ , 400 MHz, CDCl_3): 1.32 (t, 36H, H_{102} , $J_{\text{HH}} = 8$ Hz), 2.89 (q, 24H, H_{101} , $J_{\text{HH}} = 8$ Hz), 3.18 (s, 6H, H_1), 7.33 (s, 12H, H_{11}), 7.50 (s, 24H, $\text{H}_4 + \text{H}_5$), 7.55-7.70 (appq (AA'BB'), 24H, $\text{H}_{16} + \text{H}_{17}$). ^{13}C NMR (δ , 101.5 MHz, CDCl_3): 14.5 (C_{102}), 27.9 (C_{101}), 78.9 (C_1), 83.3 (C_2), 88.5 (C_8), 89.6 (C_{19}), 90.4 (C_{13}), 92.1 (C_{14}), 97.9 (C_7), 99.2 (C_{20}), 121.6 (C_{12}), 121.7 (C_3), 122.8 (C_9), 123.0 (C_{18}), 123.5 (C_{15}), 124.0 (C_6), 127.3 (C_{e1}), 128.4 (C_{11}), 131.1 (C_5), 131.5 ($\text{C}_{16} + \text{C}_{17}$), 132.1 (C_4), 134.6 (C_{02}), 146.6 (C_{10}).

*Synthesis of 1,2,3,4,5,6-(trans-[RuCl(dppe)]₂(C≡CC₆H₄-4-C≡CC₆H₂-2,6-Et₂-4-C≡CC₆H₄-4-C≡C)₆C₆ (**61**).*

1,2,3,4,5,6-($\text{HC} \equiv \text{CC}_6\text{H}_4-4-\text{C} \equiv \text{CC}_6\text{H}_2-2,6-\text{Et}_2-4-\text{C} \equiv \text{CC}_6\text{H}_4-4-\text{C} \equiv \text{C}$)₆C₆ (0.013 g, 0.006 mmol) was added to distilled and deoxygenated CH_2Cl_2 (15 mL) followed by $[\text{RuCl}(\text{dppe})_2]\text{PF}_6$ (0.041 g, 0.038 mmol). The mixture was stirred for 16 h. The solution was then added to rapidly stirring deoxygenated petrol (100 mL) and the precipitate recovered by filtration. The solid was washed with MeOH (30 mL) and then added to a mixture of CH_2Cl_2 and NEt_3 (10:1) and stirred for 20 min. The solution was filtered through a short pad of alumina eluting with a mixture of CH_2Cl_2 and NEt_3 (10:1). **61** was obtained as a red solid (0.035 g,

74 %). *Anal.* calcd for $C_{498}H_{408}Cl_6P_{24}Ru_6$: C, 75.19; H, 5.17. Found: C, 74.99; H, 5.19. UV-Vis: 406 [39.7], 335 [23.4]. 1H NMR (δ , 400 MHz, $CDCl_3$): 1.26 (t, 36H, H_{102} , $J_{HH} = 8$ Hz), 2.83 (q, 24H, H_{10} , $J_{HH} = 8$ Hz), 6.61 (d, 12H, H_4 , $J_{HH} = 8$ Hz), 6.9-7.10 (m, 96H, $H_{m1} + H_{m2}$), 7.20 (m, 48H, H_p), 7.30-7.42 (m, 60H, $H_{11} + H_{01}$), 7.50-7.63 (m, 56H $H_5 + H_{02}$), 7.65-7.69 (m, 16H, $H_{16} + H_{17}$). ^{13}C NMR (δ , 101.5 MHz, $CDCl_3$): 14.6 (C_{102}), 27.9 (C_{101}), 30.6, (m, C_b), 126.8 (C_{m2}), 126.9 (C_{m1}), 128.5 (C_{11}), 128.8 ($C_{p1} + C_{p2}$), 129.9 (C_4), 130.6 (C_5), 131.6 ($C_{16} + C_{17}$), 134.2 (C_{01}), 134.3 (C_{02}), 135.7 (m, C_{11}), 136.3 (m, C_{12}), 146.1 (C_{10}). Quaternary and core carbon environments not observed.

References

- (1) Saleh, B. E. A.; Teich, M. C. *Fundamentals of Photonics*; John Wiley & Sons, 2007.
- (2) Zyss, J. In *Nonlinear Optical Materials*; Kuhn, H., Robillard, J., Eds.; CRC Press: 1992; Vol. 1, p 3.
- (3) Zyss, J. *Molecular Nonlinear Optics: Materials, Physics and Devices*; Academic Press: Boston, 1994.
- (4) Sutherland, R. L. *Handbook of Nonlinear Optics*; Marcel Dekker: New York, 1996.
- (5) He, G. S. *Nonlinear Optics and Photonics*; Oxford University Press: Oxford, 2015 (In press; early access online).
- (6) Torea, G.; Vazquez, P.; Agullo-Lopez, F.; Torres, T. *Chem. Rev.* **2004**, *104*, 3723.
- (7) Grelaud, G.; Cifuentes, M. P.; Paul, F.; Humphrey, M. G. *J. Organomet. Chem.* **2014**, *751*, 181.
- (8) Nalwa, H. S.; Miyata, S. *Nonlinear Optics of Organic Molecules and Polymers*; CRC Press, 1997.
- (9) He, G. S.; Tan, L. S.; Zheng, Q.; Prasad, P. N. *Chem. Rev.* **2008**, *108*, 1245.
- (10) Chemla, D. S.; Zyss, J. *Nonlinear Optical Properties of Organic Molecules and Crystals*; Academic Press: London, 1987.
- (11) Wolff, J. J.; Gredel, F.; Oeser, T.; Irngartinger, H.; Pritzkow, H. *Chem. Eur. J.* **1999**, *5*, 29.
- (12) Radhakrishnan, T. P. *Acc. Chem. Res.* **2008**, *41*, 367.
- (13) Tykwinski, R. R.; Gubler, U.; Martin, R. E.; Diederich, F.; Bosshard, C.; Gunter, P. *J. Phys. Chem. B* **1998**, *102*, 4451.
- (14) Andraud, C.; Zabulon, T.; Collet, A.; Zyss, J. *Chem. Phys.* **1999**, *245*, 243.
- (15) Kim, H. M.; Cho, B. R. *J. Mater. Chem.* **2009**, *19*, 7402.
- (16) Ohta, K.; Yamada, S.; Kamada, K.; Slepko, A. D.; Hegmann, F. A.; Tykwinski, R. R.; Shirtcliff, L. D.; Haley, M. M.; Salek, P.; Gel'mukhanov, F.; Agren, H. *J. Phys. Chem. A* **2011**, *115*, 105.
- (17) Vance, F.; Hupp, J. *J. Am. Chem. Soc.* **1998**, *121*, 4047.
- (18) Roberts, R. L.; Schwich, T.; Corkery, T. C.; Cifuentes, M. P.; Green, K. A.; Farmer, J. D.; Low, P. J.; Marder, T. B.; Samoc, M.; Humphrey, M. G. *Adv. Mater.* **2009**, *21*, 2318.
- (19) Schwich, T.; Cifuentes, M. P.; Gugger, P. A.; Samoc, M.; Humphrey, M. G. *Adv. Mat.* **2011**, *23*, 1433.
- (20) McDonagh, A. M.; Whittall, I. R.; Humphrey, M. G.; Skelton, B. W.; White, A. H. *J. Organomet. Chem.* **1996**, *519*, 229.

- (21) Naulty, R. H.; Cifuentes, M. P.; Humphrey, M. G.; Houbrechts, S.; Boutton, C.; Persoons, A.; Heath, G. A.; Hockless, D. C. R.; Luther-Davies, B.; Samoc, M. *J. Chem. Soc., Dalton. Trans.* **1997**, 4167.
- (22) Powell, C. E.; Humphrey, M. G.; Cifuentes, M. P.; Morrall, J. P.; Samoc, M.; Luther-Davies, B. *J. Phys. Chem. A* **2003**, *107*, 11264.
- (23) Babgi, B.; Rigamonti, L.; Cifuentes, M. P.; Corkery, T. C.; Randles, M. D.; Schwich, T.; Petrie, S.; Stranger, R.; Teshome, A.; Asselberghs, I.; Clays, K.; Samoc, M.; Humphrey, M. G. *J. Am. Chem. Soc.* **2009**, *131*, 10293.
- (24) McDonagh, A. M.; Whittall, I. R.; Humphrey, M. G.; Hockless, D. C. R.; Skelton, B. W.; White, A. H. *J. Organomet. Chem.* **1996**, *523*, 33.
- (25) Hurst, S. K.; Cifuentes, M. P.; McDonagh, A. M.; Humphrey, M. G.; Samoc, M.; Luther-Davies, B.; Asselberghs, I.; Persoons, A. *J. Organomet. Chem.* **2002**, *642*, 259.
- (26) McDonagh, A. M.; Humphrey, M. G.; Samoc, M.; Luther-Davies, B. *Organometallics* **1999**, *18*, 5195.
- (27) Vallaitis, T.; Bogatscher, S.; Alloatti, L.; Dumon, P.; Baets, R.; Scimeca, M. L.; Biaggio, I.; Diederich, F.; Koos, C.; Freude, W.; Leuthold, J. *Opt. Exp.* **2009**, *17*, 17357.
- (28) Prasad, P. N.; Williams, D. J. *Introduction to Nonlinear Optical Effects in Molecules and Polymers*; John Wiley & Sons, Inc.: New York, 1991.
- (29) Verbiest, T.; Clays, K.; Rodriguez, V. *Second-order Nonlinear Optical Characterisation Techniques: An Introduction*; CRC Press, 2009.
- (30) Sheik-Bahae, M.; Said, A. A.; Wei, T. H.; Hagan, D. J.; Van Stryland, E. W. *IEEE J. Quantum Electron.* **1990**, *26*, 760.
- (31) Myers, L. K.; Ho, D. M.; Thompson, M. E.; Langhoff, C. *Polyhedron* **1995**, *14*, 57.
- (32) Marder, S. R.; Perry, J. W.; Tiemann, B. G.; Gorman, C. B.; Gilmour, S.; Biddle, S. L.; Bourhill, G. *J. Am. Chem. Soc.* **1992**, *115*, 2524.
- (33) Yuan, Z.; Stringer, G.; Jobe, I. R.; Kreller, D.; Scott, K.; Koch, L.; Taylor, N. J.; Marder, T. B. *J. Organomet. Chem.* **1993**, *452*, 115.
- (34) Ghosal, S.; Samoc, M.; Prasad, P. N.; Tufariello, J. J. *J. Phys. Chem.* **1990**, *94*, 2847.
- (35) Blanchard-Desce, M.; Lehn, J. M.; Barzoukas, M.; Runser, C.; Fort, A.; Puccetti, G.; Ledoux, I.; Zyss, J. *Nonlinear Opt.* **1995**, *10*, 23.
- (36) Hurst, S.; Humphrey, M. G.; Isoshima, T.; Wostyn, K.; Asselberghs, I.; Clays, K.; Persoons, A.; Samoc, M.; Luther-Davies, B. *Organometallics* **2002**, *21*, 2024.
- (37) Morrall, J. P. L.; Cifuentes, M. P.; Humphrey, M. G.; Kellens, R.; Robijns, E.; Asselberghs, I.; Clays, K.; Persoons, A.; Samoc, M.; Willis, A. *Inorg. Chim. Acta* **2006**, *359*, 998.
- (38) Dalton, G. T.; Cifuentes, M. P.; Watson, L. A.; Petrie, S.; Stranger, R.; Samoc, M.; Humphrey, M. G. *Inorg. Chem.* **2009**, *48*, 6534.

- (39) McDonagh, A. M.; Cifuentes, M. P.; Whittall, I. R.; Humphrey, M. G.; Samoc, M.; Luther-Davies, B.; Hockless, D. C. R. *J. Organomet. Chem.* **1996**, *526*, 99.
- (40) Hurst, S. K.; Cifuentes, M. P.; Morrall, J. P. L.; Lucas, N. T.; Whittall, I. R.; Humphrey, M. G.; Asselberghs, I.; Persoons, A.; Samoc, M.; Luther-Davies, B.; Willis, A. C. *Organometallics* **2001**, *20*, 4664.
- (41) Whittall, I. R.; Cifuentes, M. P.; Humphrey, M. G. *Organometallics* **1997**, *16*, 2631.
- (42) Garcia, M. H.; Robalo, M. P.; Dias, A. R.; Duarte, T.; Wenseleers, W.; Aerts, G.; Goovaerts, E.; Cifuentes, M. P.; Hurst, S.; Humphrey, M. G.; Samoc, M.; Luther-Davies, B. *Organometallics* **2002**, *21*, 2107.
- (43) Cifuentes, M. P.; Powell, C. E.; Humphrey, M. G.; Heath, G. A.; Samoc, M.; B., L.-D. *J. Phys. Chem. A* **2001**, *105*, 9625.
- (44) Schwich, T. Phd Thesis, ANU, 2011.
- (45) Green, K. A.; Simpson, P. V.; Corkery, T. C.; Cifuentes, M. P.; Samoc, M.; Humphrey, M. G. *Macromol. Rapid Commun.* **2012**, *33*, 573.
- (46) Samoc, M.; Corkery, T. C.; McDonagh, A. M.; Cifuentes, M. P.; Humphrey, M. G. *Aust. J. Chem.* **2011**, *64*, 1269.
- (47) Argouarch, G.; Veillard, R.; Roisnel, T.; Amar, A.; Meghezzi, H.; Boucekkine, A.; Hugues, V.; Mongin, O.; Blanchard-Desce, M.; Paul, F. *Chem. Eur. J.* **2012**, *18*, 11811.
- (48) Trujillo, A.; Veillard, R.; Argouarch, G.; Roisnel, T.; Singh, A.; Ledoux, I.; Paul, F. *Dalton Trans.* **2012**, *41*, 7454.
- (49) Argouarch, G.; Veillard, R.; Roisnel, T.; Amar, A.; Meghezzi, H.; Boucekkine, A.; Hugues, V.; Mongin, O.; Blanchard-Desce, M.; Paul, F. *Chem. Eur. J.* **2012**, *18*, 11811.
- (50) Malvoti, F.; Rouxel, C.; Mongin, O.; Hapiot, P.; Toupet, L.; Blanchard-Desce, M.; Paul, F. *Dalton Trans.* **2011**, *40*, 6616.
- (51) Zheng, Q.; He, G. S.; Lu, C.; Prasad, P. N. *J. Mater. Chem.* **2005**, *15*, 3488.
- (52) Belfield, K. D.; Hagan, D. J.; Van Stryland, E. W.; Schafer, K. J.; Negres, R. A. *Org. Lett.* **1999**, *1*, 1575.
- (53) Powell, C. E.; Morrall, J. P.; Ward, S. A.; Cifuentes, M. P.; Notaras, E. G. A.; Samoc, M.; Humphrey, M. G. *J. Am. Chem. Soc.* **2004**, *126*, 12234.
- (54) Cifuentes, M. P.; Powell, C. E.; Morrall, J. P.; McDonagh, A. M.; Lucas, N. T.; Humphrey, M. G.; Samoc, M.; Houbrechts, S.; Asselberghs, I.; Clays, K.; Persoons, A.; Isoshima, T. *J. Am. Chem. Soc.* **2006**, *128*, 10819.
- (55) Powell, C. E.; Cifuentes, M. P.; Humphrey, M. G.; Willis, A. C.; Morrall, J. P.; Samoc, M. *Polyhedron* **2007**, *26*, 284.
- (56) Jeffery, C. J.; Cifuentes, M. P.; Dalton, G. T.; Corkery, T. C.; Randles, M. D.; Willis, A. C.; Samoc, M.; Humphrey, M. G. *Macromol. Rapid Commun.* **2010**, 846.

- (57) Green, K. A.; Cifuentes, M. P.; Corkery, T. C.; Samoc, M.; Humphrey, M. G. *Angew. Chem. Int. Ed.* **2009**, *48*, 7867.
- (58) Feliz, M.; Garriga, J. M.; Llusar, R.; Uriel, S.; Humphrey, M. G.; Lucas, N. T.; Samoc, M.; Luther-Davies, B. *Inorg. Chem.* **2001**, *40*, 6132.
- (59) Garriga, J. M.; Llusar, R.; Uriel, S.; Vicent, C.; Usher, A. J.; Lucas, N. T.; Humphrey, M. G.; Samoc, M. *Dalton Trans.* **2003**, 4546.
- (60) Dalton, G. T.; Cifuentes, M. P.; Watson, L. A.; Petrie, S.; Stranger, R.; Samoc, M.; Humphrey, M. G. *Inorg. Chem.*, **2008**, *48*, 6534.
- (61) McDonagh, A. M.; Humphrey, M. G.; Samoc, M.; Luther-Davies, B. *Organometallics* **1999**, *18*, 5195.
- (62) Kozaki, M.; Okada, K. *Org. Lett.* **2004**, *6*, 485.
- (63) Zyss, J.; Ledoux, I. *Chem. Rev.* **1994**, *94*, 77.
- (64) Hu, Q. Y.; Lu, W. X.; Tang, H. T.; Sung, H. H. Y.; Wen, T. B.; Williams, I. D.; Wong, G. K. L.; Lin, Z.; Jia, G. *Organometallics* **2005**, *24*, 3966.
- (65) Drouet, S.; Merhi, A.; Yao, D.; Cifuentes, M. P.; Humphrey, M. G.; Wielgus, M.; Olesiak-Banska, J.; Matczyszyn, K.; Samoc, M.; Paul, F.; Paul-Roth, C. O. *Tetrahedron* **2012**, *68*, 10351.
- (66) Weyland, T.; Ledoux, I.; Brasselet, S.; Zyss, J.; Lapinte, C. *Organometallics* **2000**, *19*, 5235.
- (67) Dalton, G. T.; Cifuentes, M. P.; Watson, L. A.; Petrie, S.; Stranger, R.; Samoc, M.; Humphrey, M. G. *J. Am. Chem. Soc.* **2007**, *129*, 11882.
- (68) Huang, C. C.; Lin, Y. C.; Lin, P. Y.; Chen, Y. J. *Eur. J. Org. Chem.* **2006**, *19*, 4510.
- (69) Kondo, K.; Yasuda, S.; Sakaguchi, T.; Miya, M. *J. Chem. Soc., Chem. Commun.* **1995**, 55.
- (70) Piao, M. J.; Chajara, K. Z.; Yoon, S. J.; Kim, H. M.; Jeon, S. J.; Kim, T. H.; Song, K.; Asselberghs, I.; Persoons, A.; Clays, K.; Cho, B. R. *J. Mater. Chem.* **2006**, *16*, 2273.
- (71) Bhasker, A.; Guda, R.; Haley, M. M.; Goodson, T. *J. Am. Chem. Soc.* **2006**, *128*, 13972.
- (72) Diallo, A. K.; Daran, J. C.; Varret, F.; Ruiz, J.; Astruc, D. *Angew. Chem. Int. Ed.* **2009**, *48*, 3141.
- (73) Barlow, A.; Babgi, B.; Samoc, M.; Corkery, T. C.; van Cleuvenbergen, S.; Asselberghs, I.; Clays, K.; Cifuentes, M. P.; Humphrey, M. G. *Aust. J. Chem.* **2012**, *65*, 834.
- (74) Corkery, T. C. PhD Thesis, ANU, 2010.
- (75) Nierle, J.; Barth, D.; Kuck, D. *Eur. J. Org. Chem.* **2004**, 867.
- (76) Sonada, M.; Inaba, A.; Itahashi, K.; Tobe, Y. *Org. Lett.* **2001**, *3*, 2419.
- (77) Wan, W. B.; Haley, M. M. *J. Org. Chem.* **2001**, *66*, 3893.
- (78) Schmittel, M.; Mal, P. *Chem. Commun.* **2008**, 960.

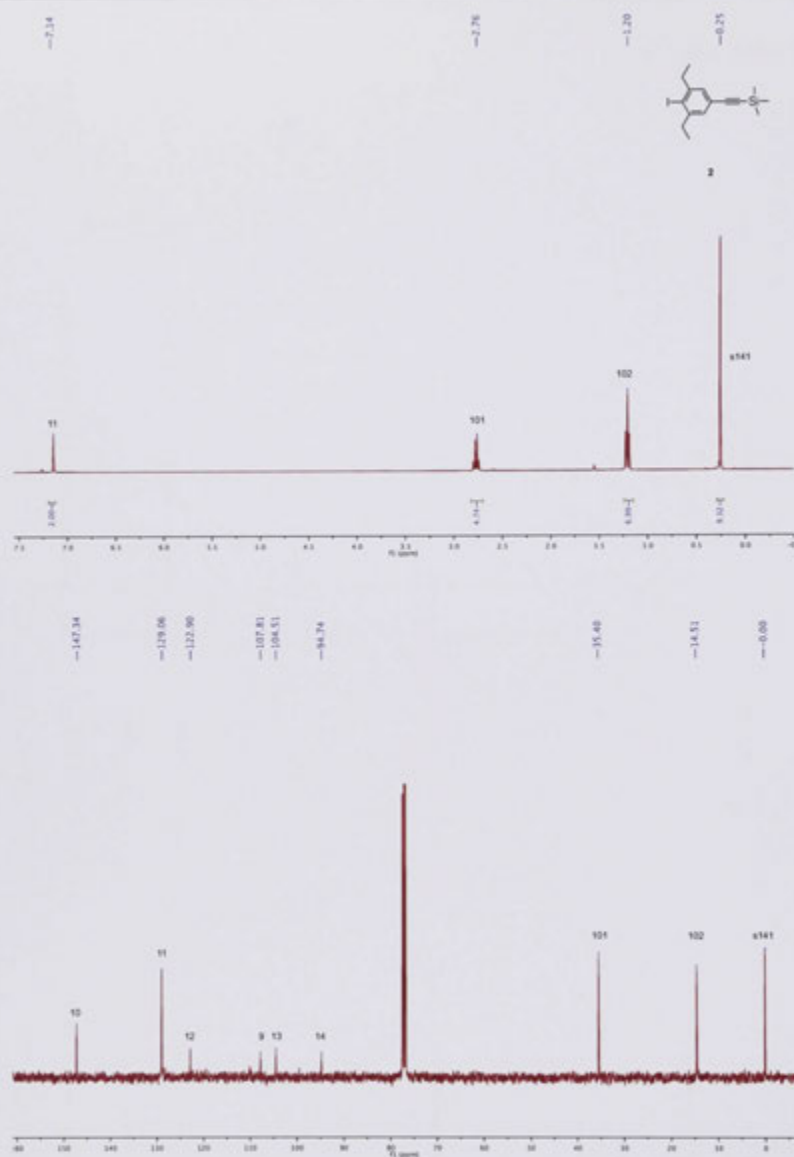
- (79) Diercks, R.; Armstrong, J. C.; Boese, R.; Vollhardt, K. P. C. *Angew. Chem. Int. Ed.* **1986**, *3*, 268.
- (80) Narender, N.; Reddy, K. S. K.; Mohan, K. V. V. K.; Kulkarni, S. J. *Tetrahedron Lett.* **2009**, *48*, 6124.
- (81) Ehlers, P.; Neubauer, A.; Lochbrunner, S.; Villinger, A.; Langer, P. *Org. Lett.* **2011**, *13*, 1618.
- (82) Barbero, M.; Degani, I.; Diulgheroff, N.; Dughera, S.; Fochi, R. *Synthesis* **2001**, *14*, 2180.
- (83) Masatoshi, K.; Keiji, O. *Org. Lett.* **2004**, *6*, 485.
- (84) Karim, A.; Linden, A.; Baldrige, K. K.; Siegel, J. S. *Chem. Sci.* **2010**, *1*, 102.
- (85) Schoutissen, H. A. *J. Am. Chem. Soc.* **1933**, *55*, 4531.
- (86) Rigaut, S.; Monnier, F.; Mousset, F.; Touchard, D.; Dixneuf, P. H. *Organometallics* **2002**, *21*, 2654.
- (87) Kulasekera, E. PhD Thesis, ANU, 2014.
- (88) Morshedi, M.; Simpson, P. V.; Babgi, B.; Green, K. A.; Moxey, G.; Jennaway, M. S.; Cifuentes, M. P.; Humphrey, M. G. *Inorg. Synth.* **2015**, *In Press*.
- (89) Godt, A.; Duda, S.; Unsal, O.; Thiel, J.; Harter, A.; Roos, M.; Tschierske, C.; Diele, S. *Chem. Eur. J.* **2002**, *8*, 5094.
- (90) Barbero, M.; Degani, I.; Diulgheroff, N.; Dughera, S.; Fochi, R. *Synthesis* **2001**, *14*, 2180.
- (91) Stefani, H. A.; Cella, R.; Dorr, F. A.; de Pereira, C. M. P.; Gomes, F. P.; Zeni, G. *Tetrahedron Lett.* **2005**, *46*, 2001.
- (92) Che, C.-M.; Yu, W.-Y.; Chan, P.-M.; Cheng, W.-C.; Peng, S.-M.; Lau, K.-C.; Li, W.-K. *J. Am. Chem. Soc.* **2000**, *122*, 11380.
- (93) Takahashi, S.; Kuroyama, Y.; Sonogashira, K.; Hagihara, N. *Synthesis* **1980**, 627.
- (94) Neenan, T. X.; Whitesides, G. M. *J. Org. Chem.* **1988**, *53*, 2489.
- (95) Mendez, J. D.; Schroeter, M.; Weder, C. *Macromol. Chem. Phys.* **2007**, *208*, 1625.
- (96) Uhl, W.; Bock, H. R.; Breher, F.; Claesener, M.; Haddadpour, S.; Jasper, B.; Hepp, A. *Organometallics* **2007**, *26*, 2363.
- (97) Mohler, D. L.; Kumaraswamy, S.; Stanger, A.; Vollhardt, K. P. C. *Synlett* **2006**, *18*, 2981.
- (98) Berris, B. C.; Hovakeemian, G. H.; Lai, Y.; Mestdagh, H.; Vollhardt, K. P. C. *J. Am. Chem. Soc.* **1985**, *107*, 5670.

Appendix

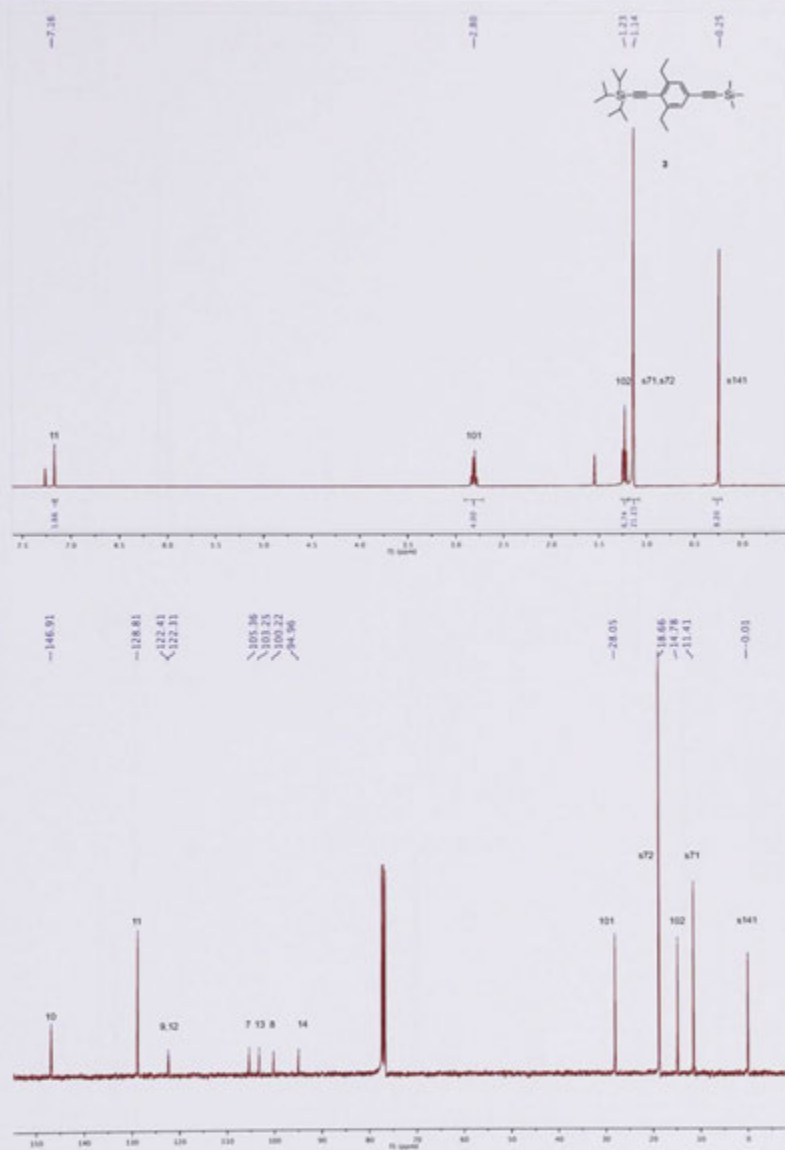
4.1 NMR spectra



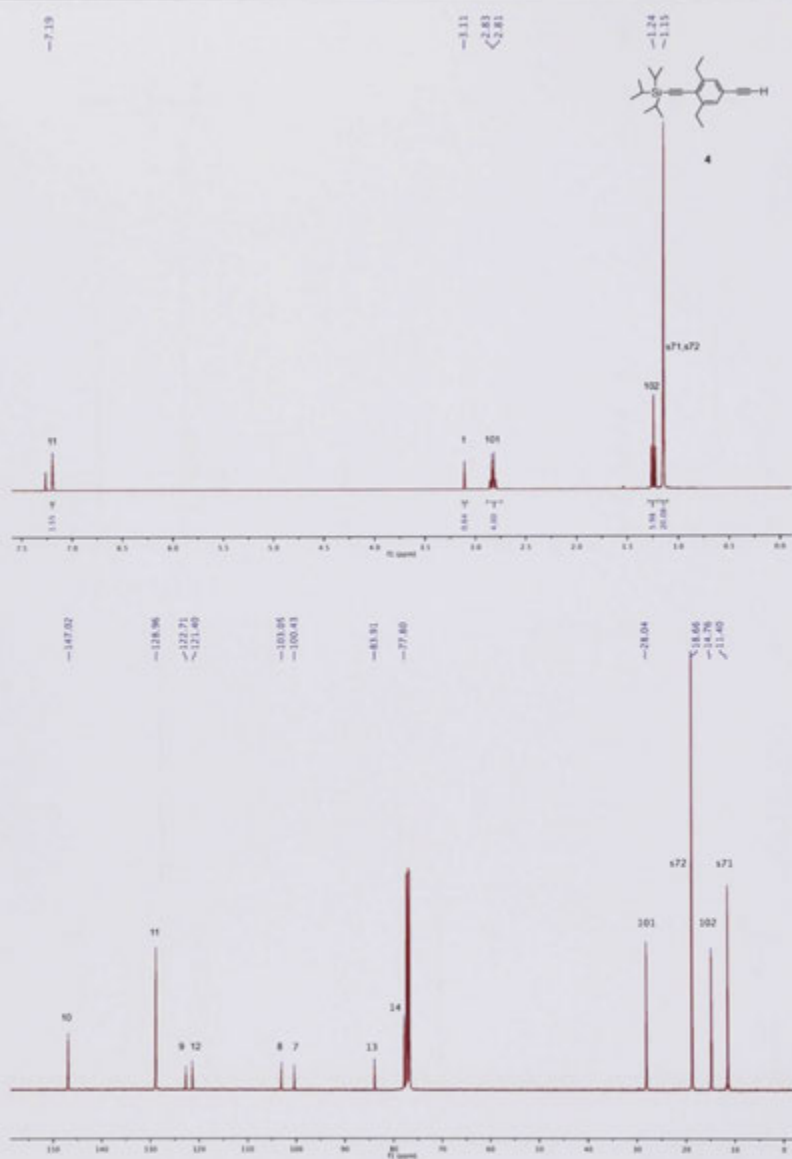
¹H and ¹³C NMR spectra for compound **1**.



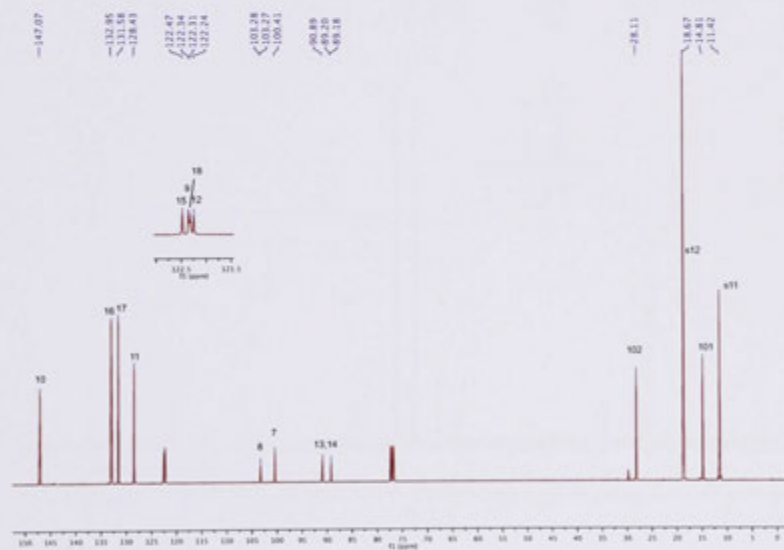
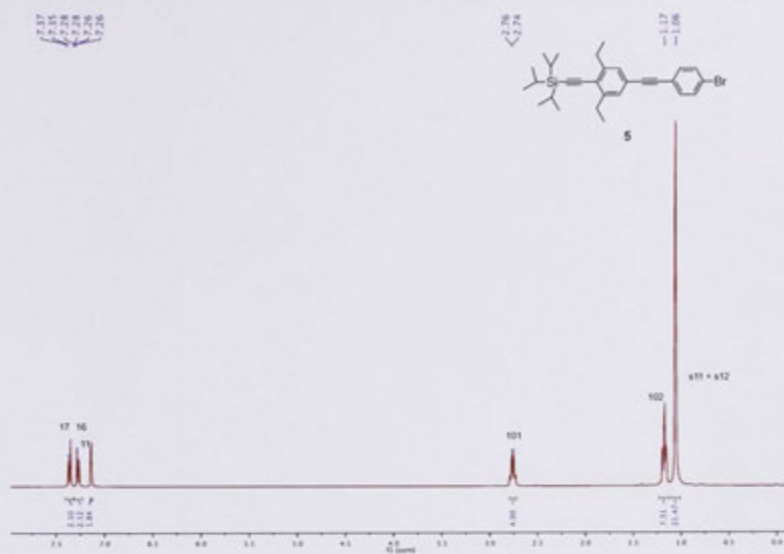
¹H and ¹³C NMR spectra for compound 2.



^1H and ^{13}C NMR spectra for compound 3.

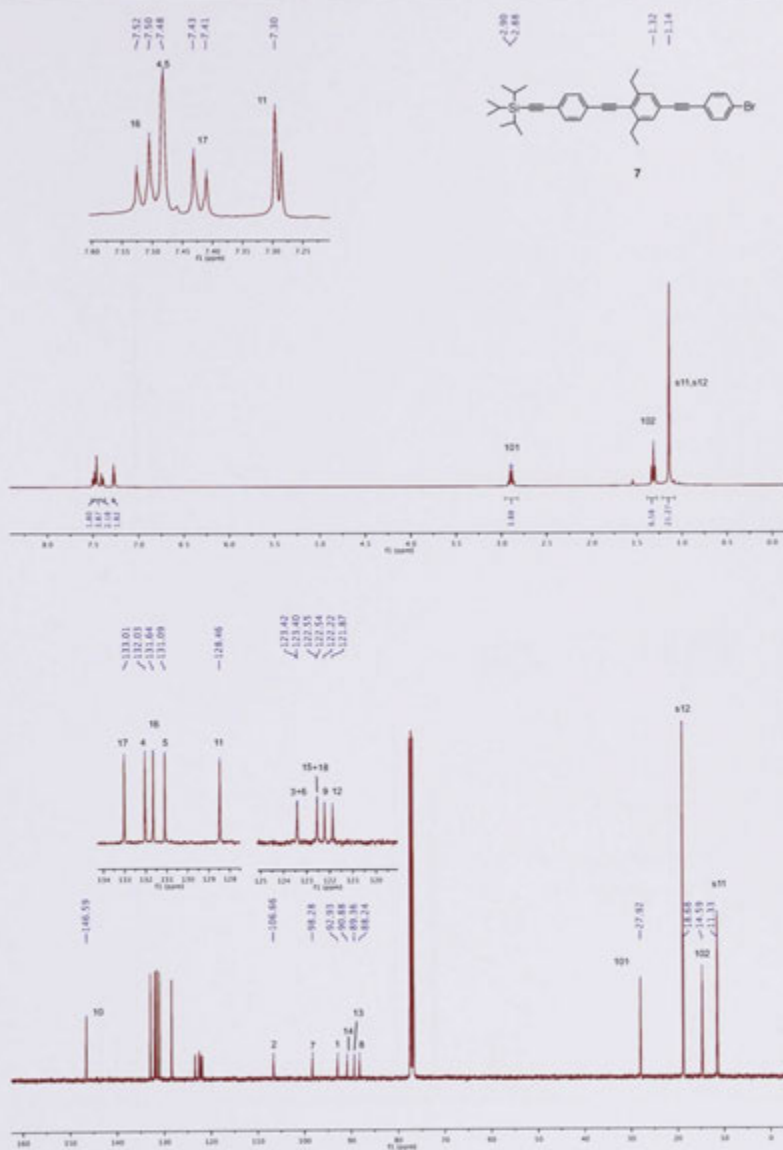


^1H and ^{13}C NMR spectra for compound 4.

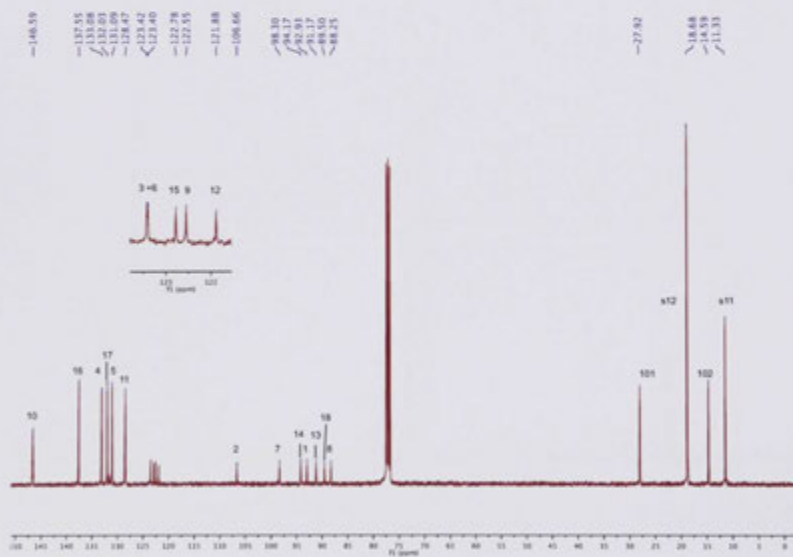
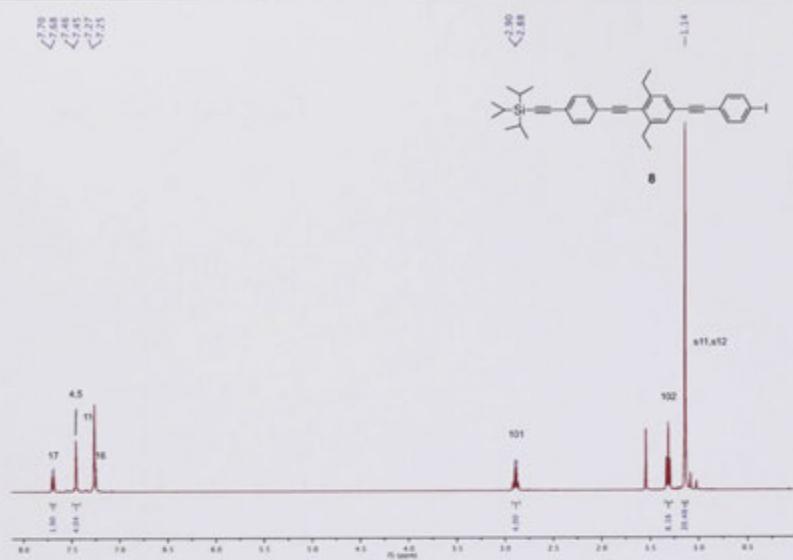


¹H and ¹³C NMR spectra for compound 5.

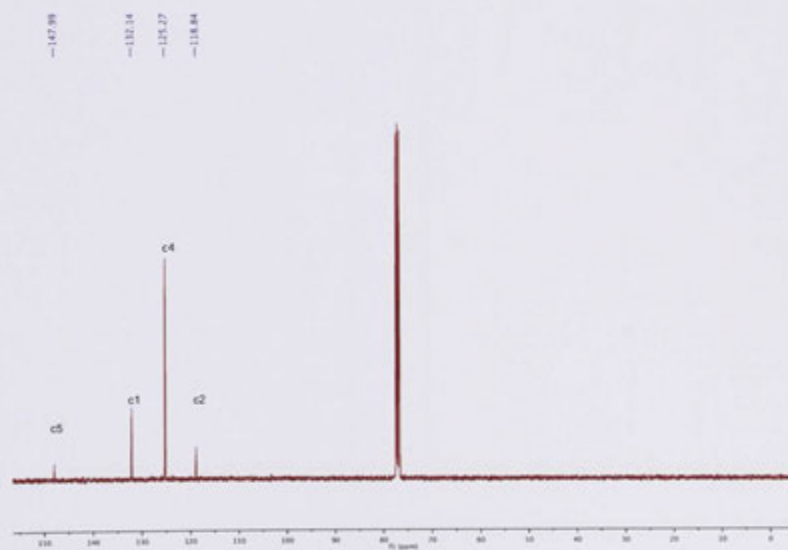
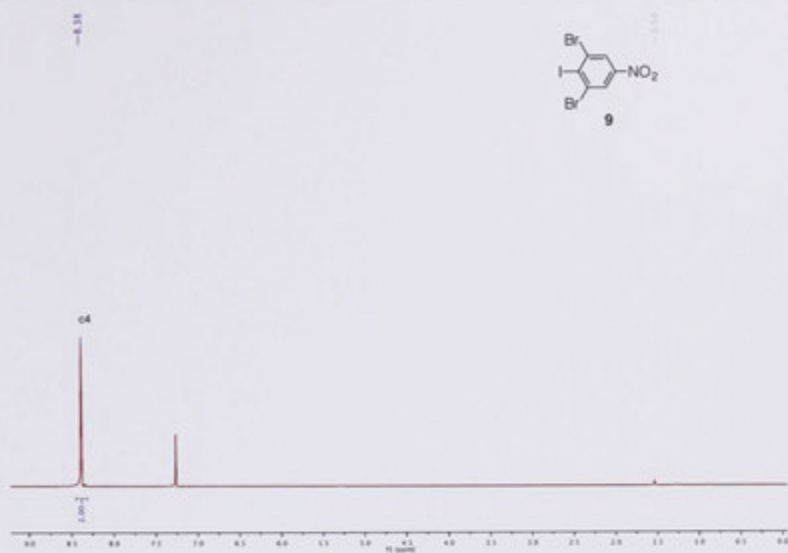
¹H and ¹³C NMR spectra for compound 6.



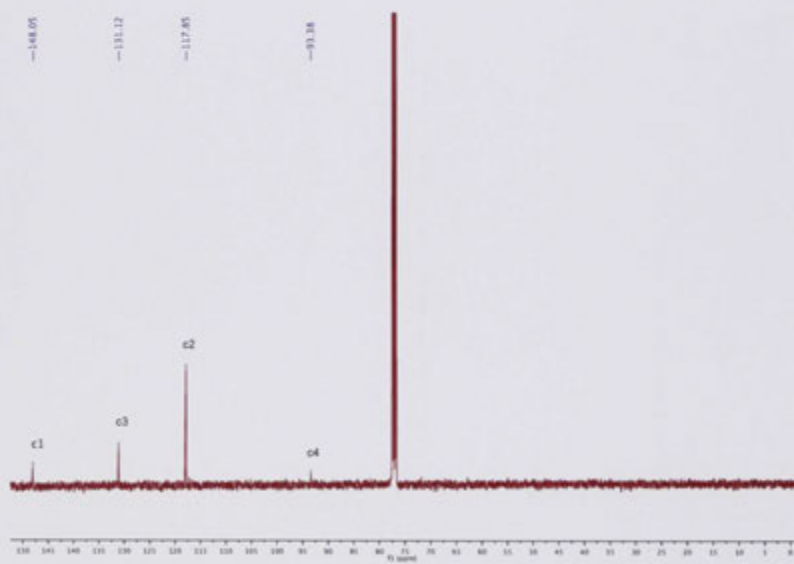
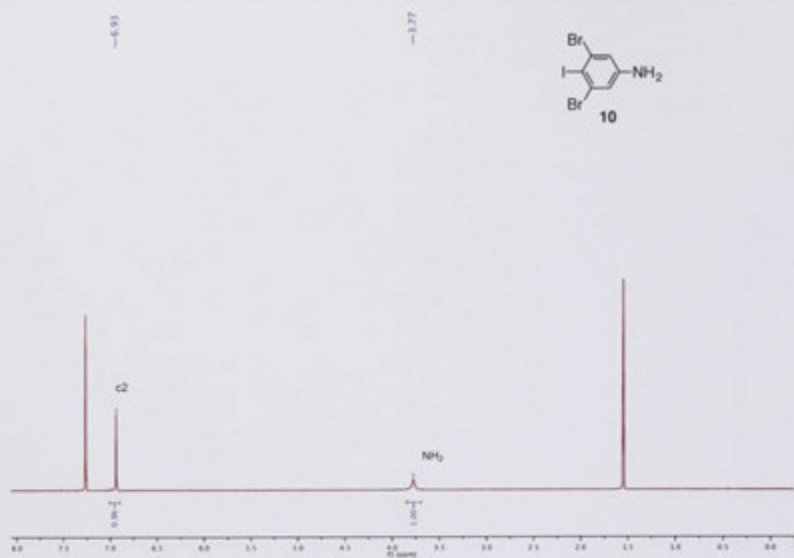
¹H and ¹³C NMR spectra for compound 7.



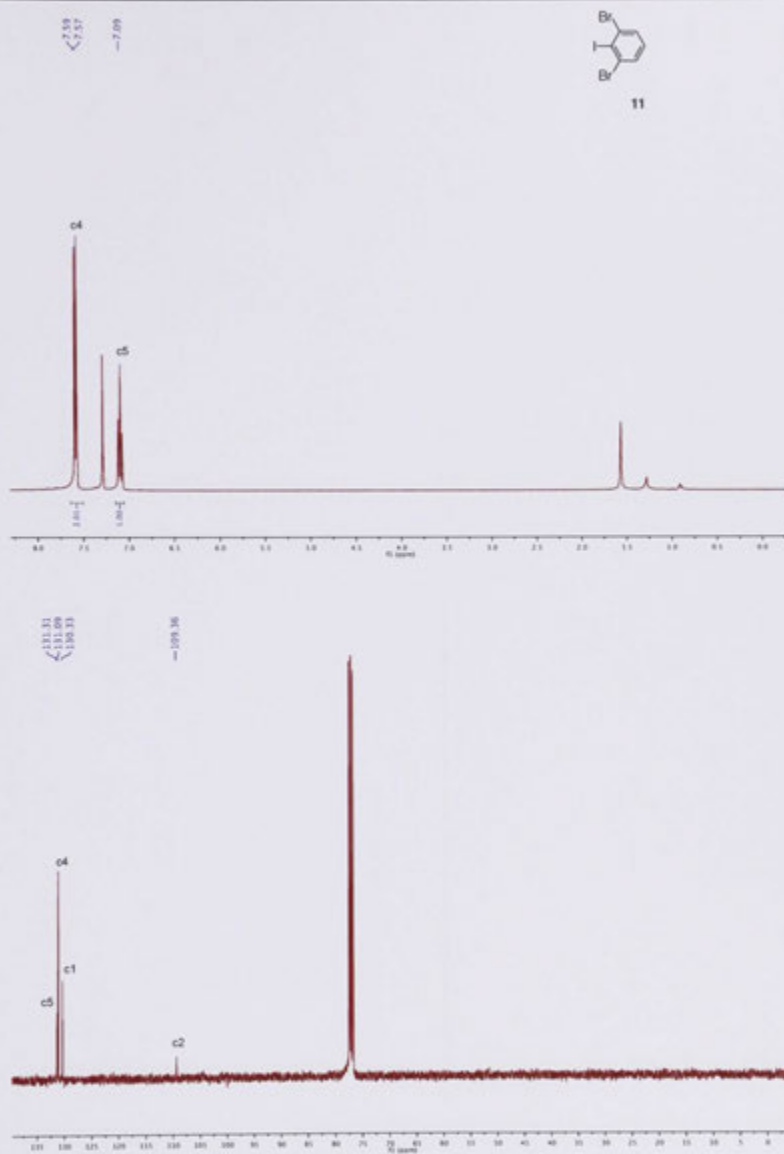
¹H and ¹³C NMR spectra for compound 8.



¹H and ¹³C NMR spectra for compound **9**.



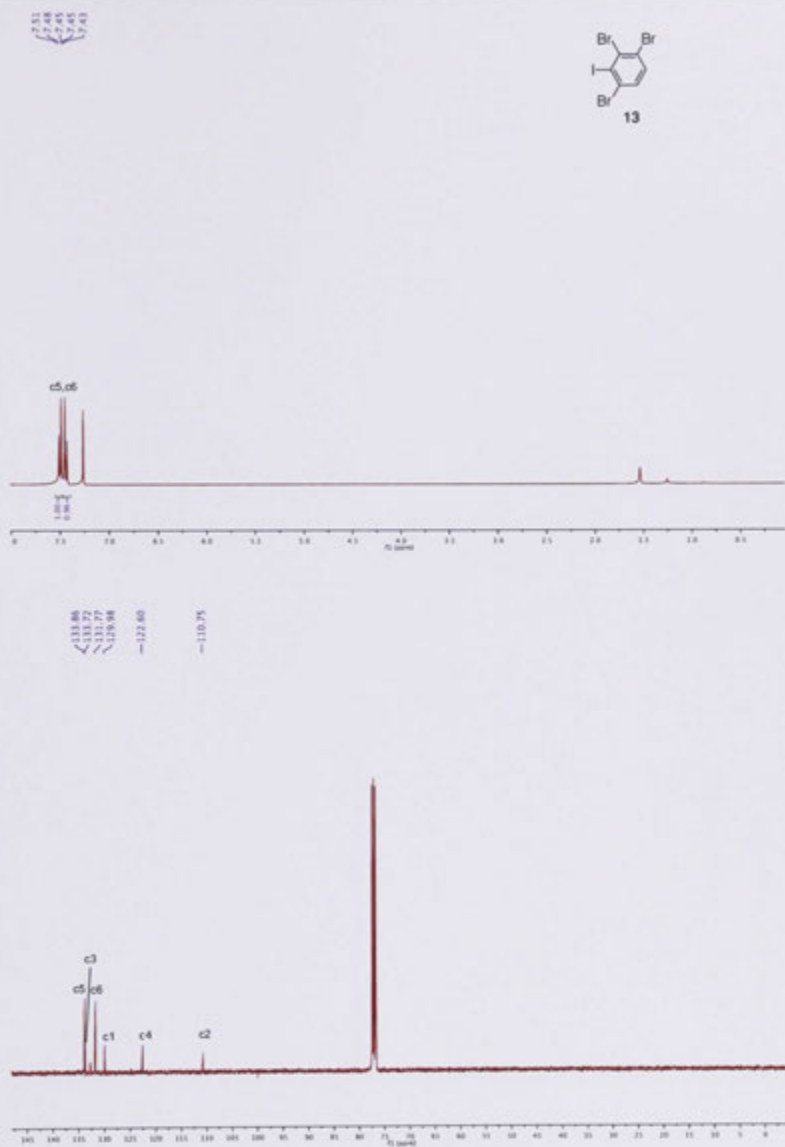
¹H and ¹³C NMR spectra for compound **10**.



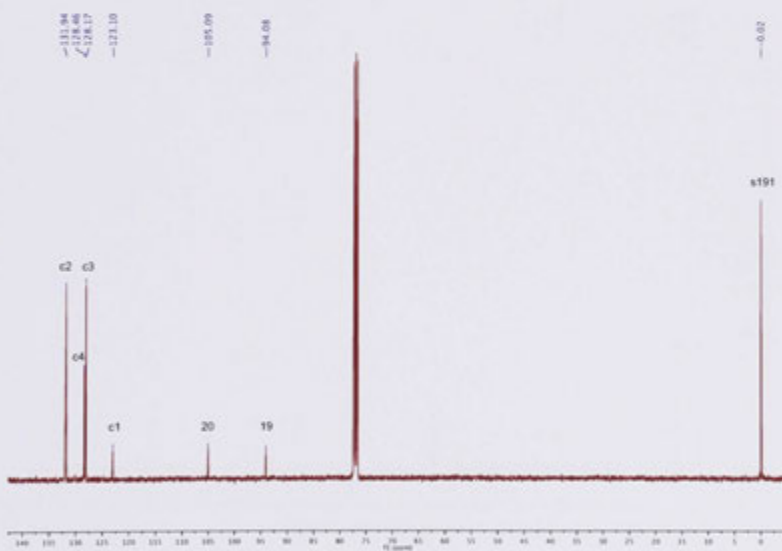
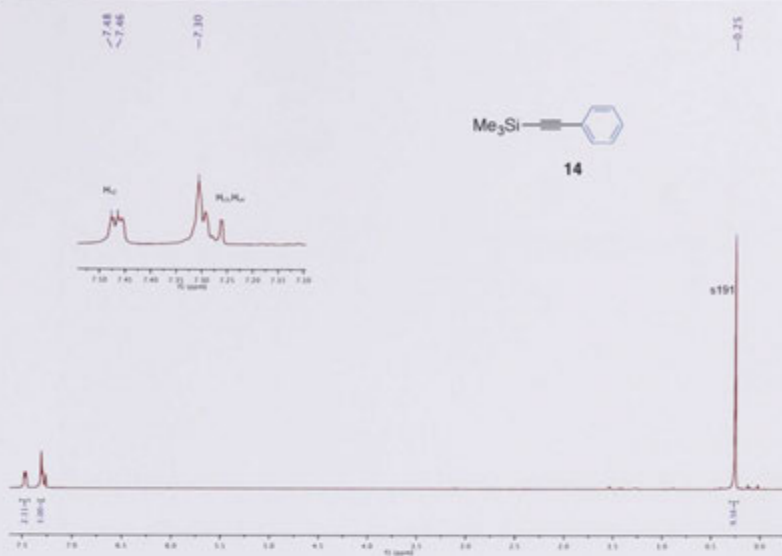
^1H and ^{13}C NMR spectra for compound **11**.



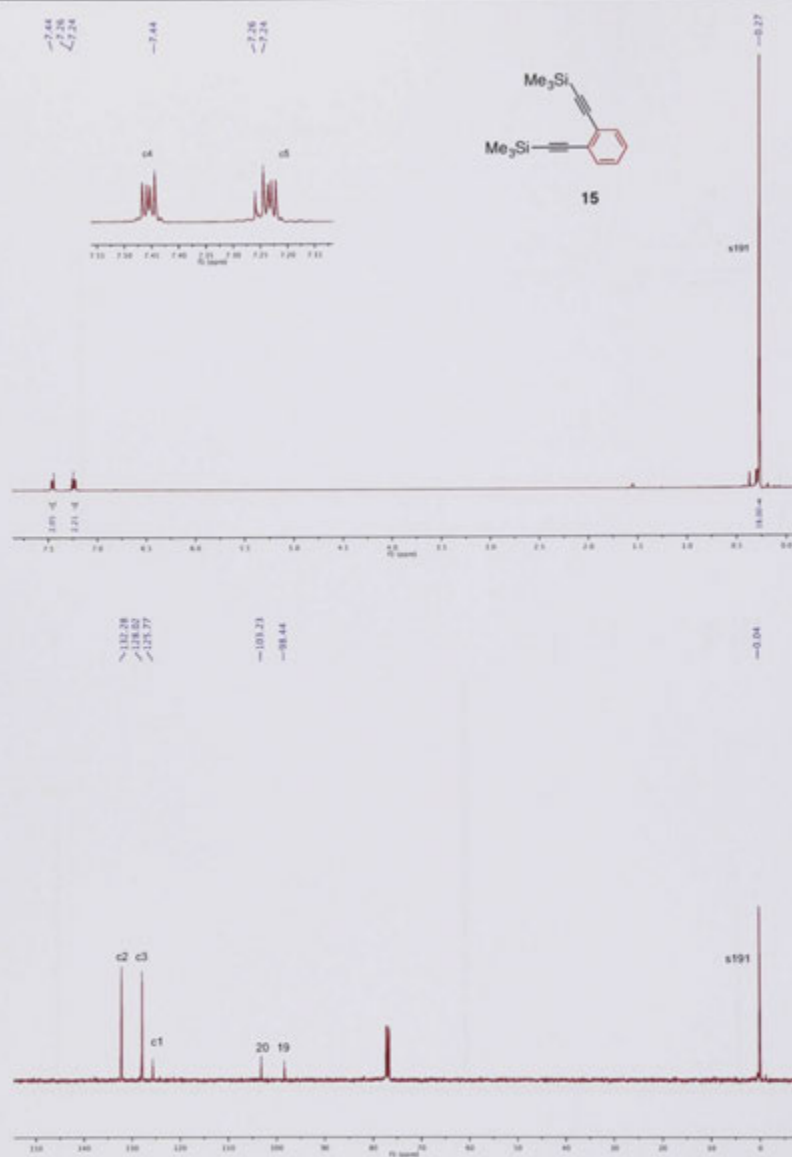
^1H and ^{13}C NMR spectra for compound 12.



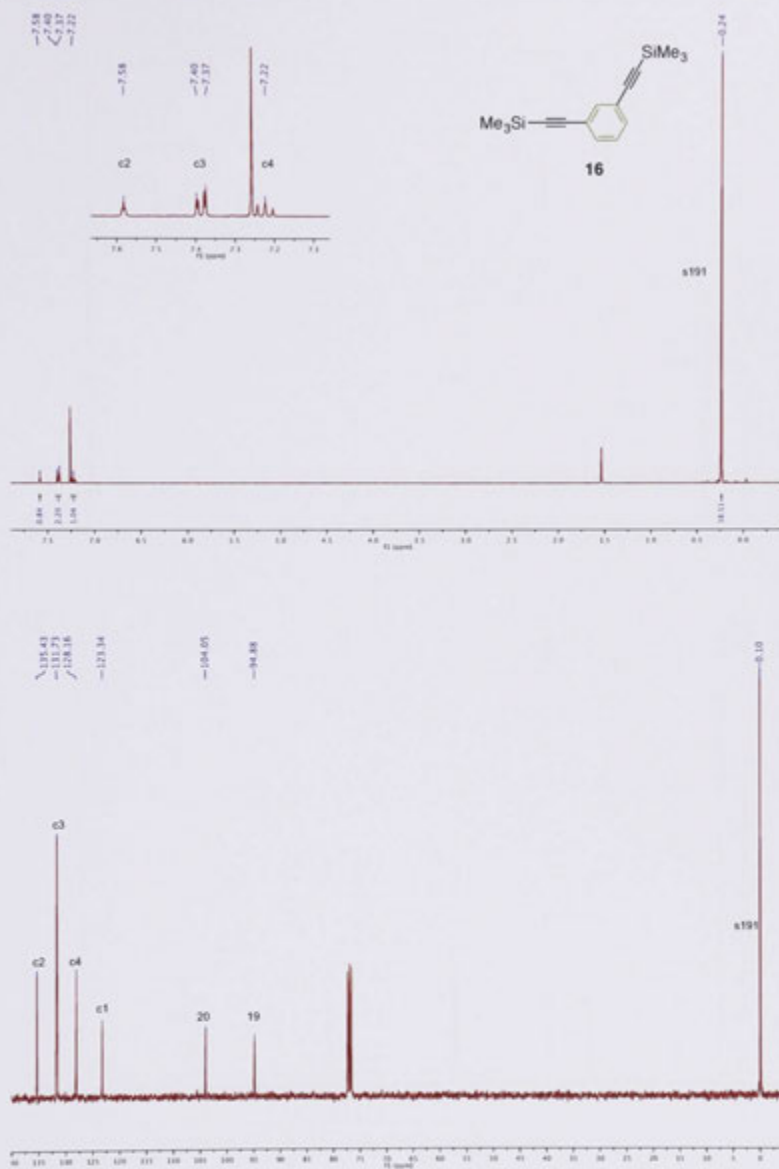
^1H and ^{13}C NMR spectra for compound 13.



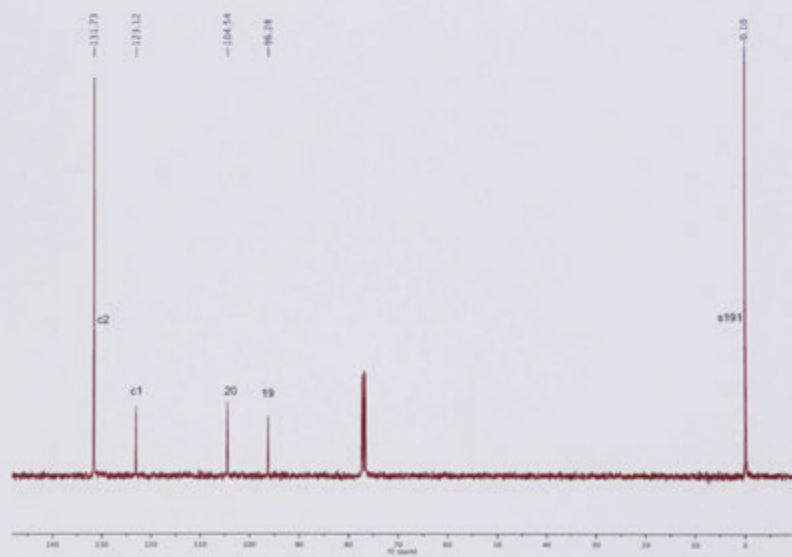
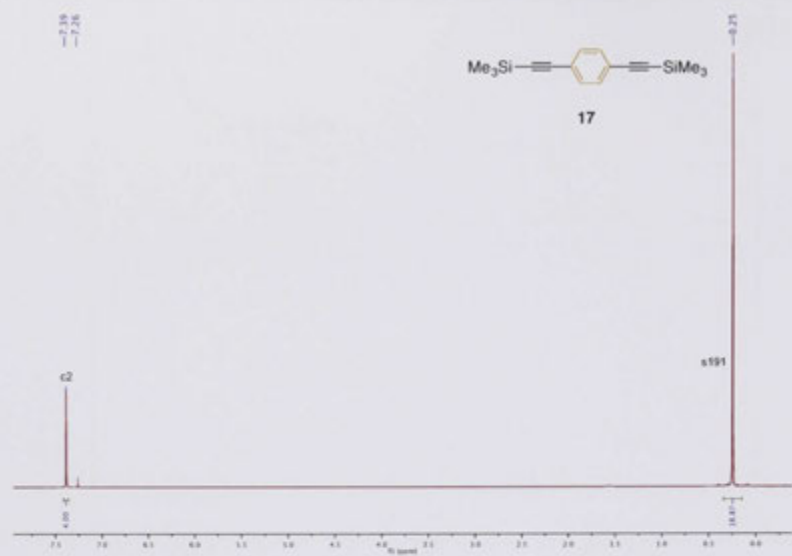
^1H and ^{13}C NMR spectra for compound **14**.



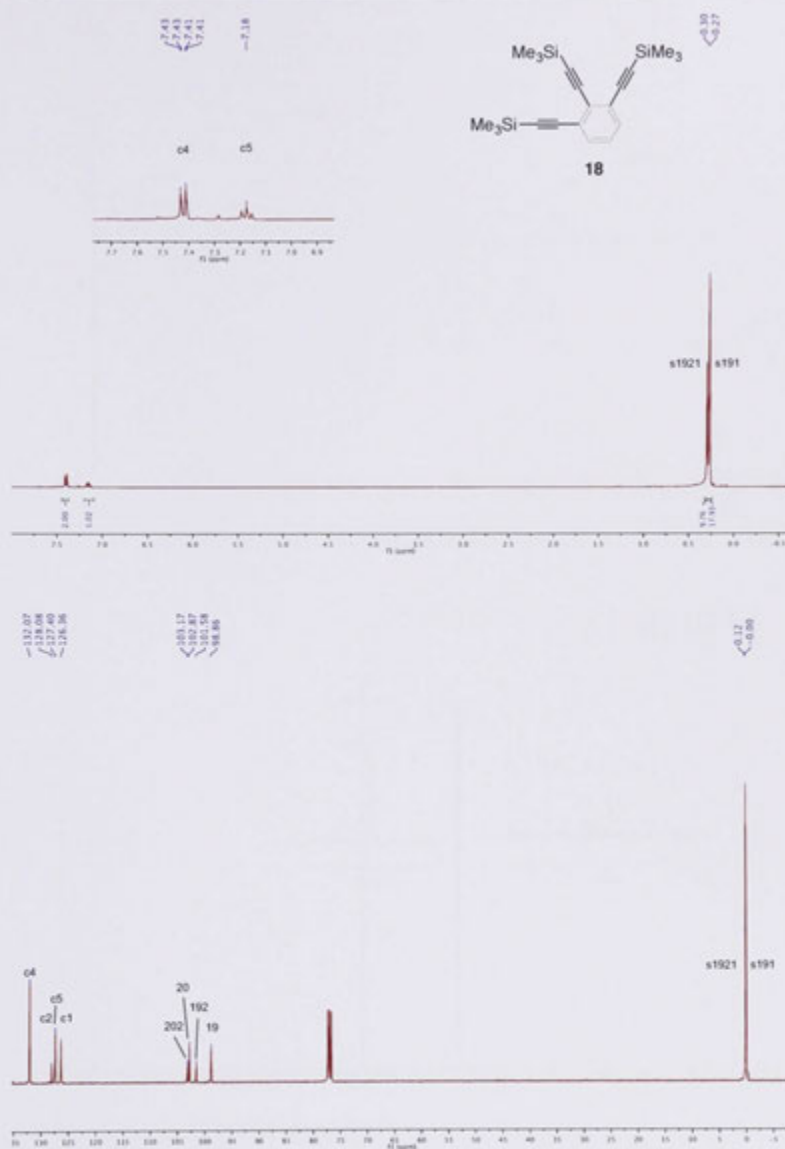
^1H and ^{13}C NMR spectra for compound **15**.



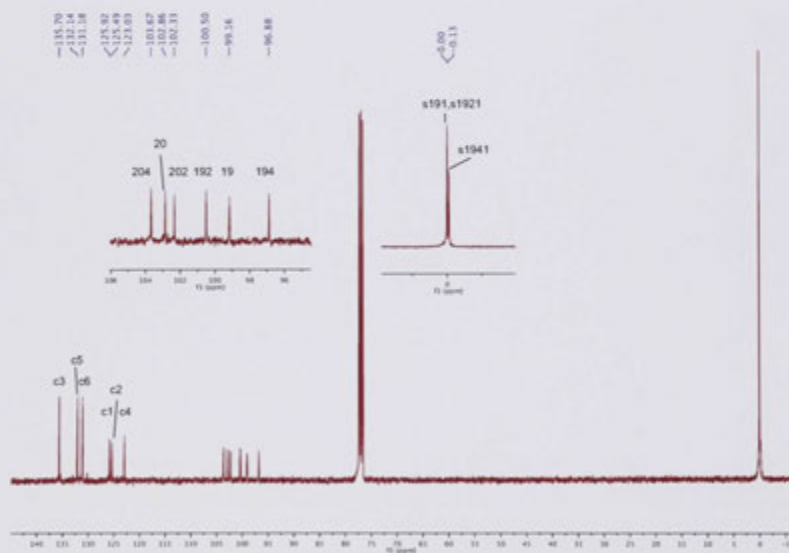
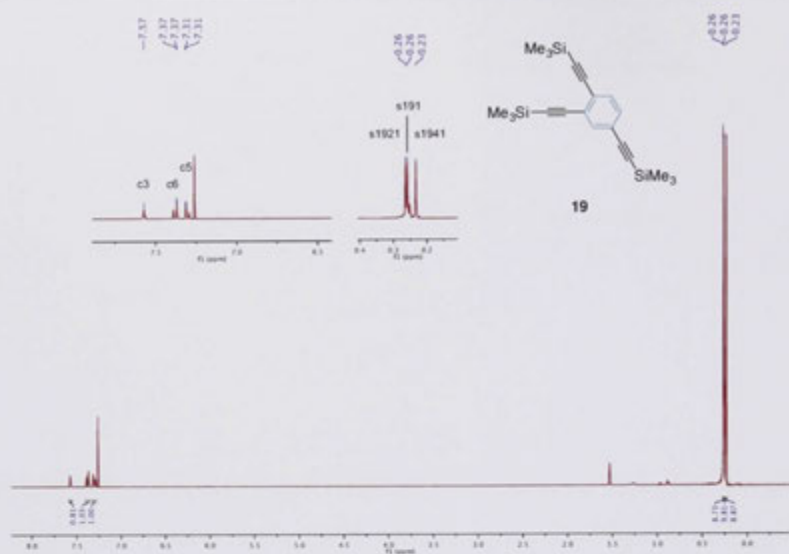
^1H and ^{13}C NMR spectra for compound **16**.



¹H and ¹³C NMR spectra for compound **17**.



^1H and ^{13}C NMR spectra for compound **18**.

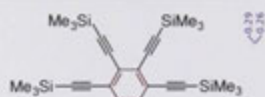


¹H and ¹³C NMR spectra for compound **19**.

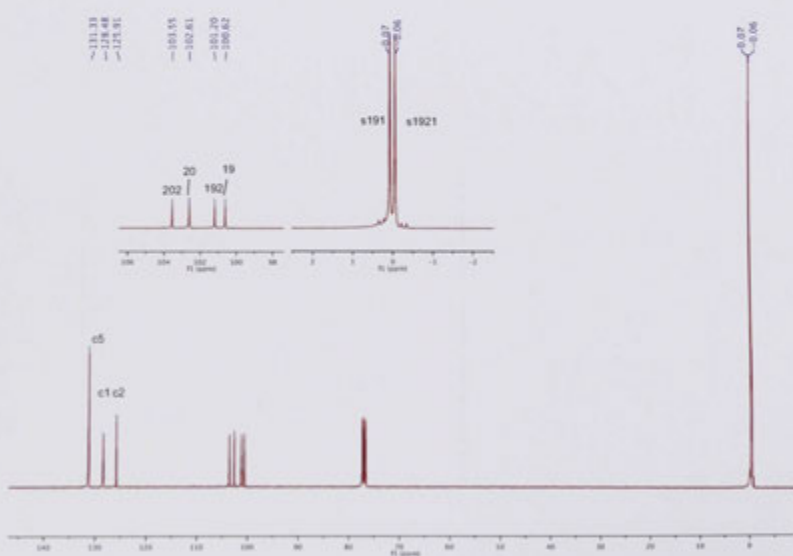
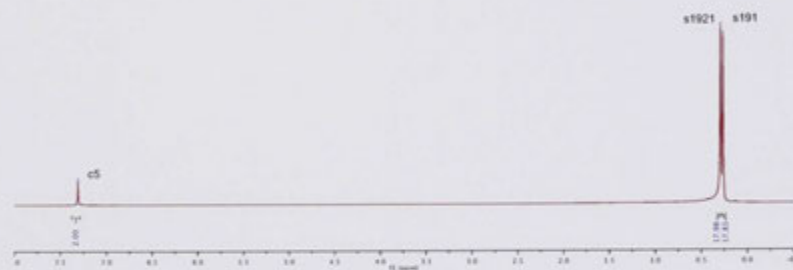


¹H and ¹³C NMR spectra for compound **20**.

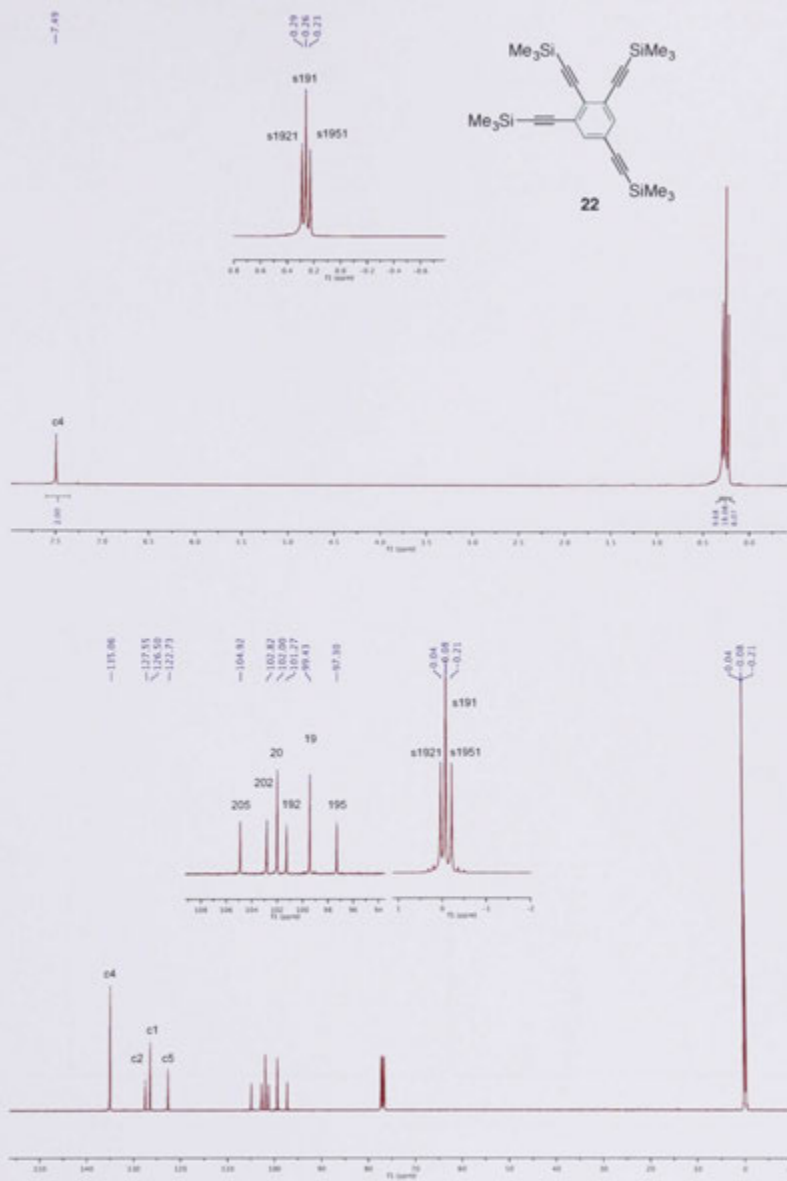
→ 7.31



21



^1H and ^{13}C NMR spectra for compound 21.



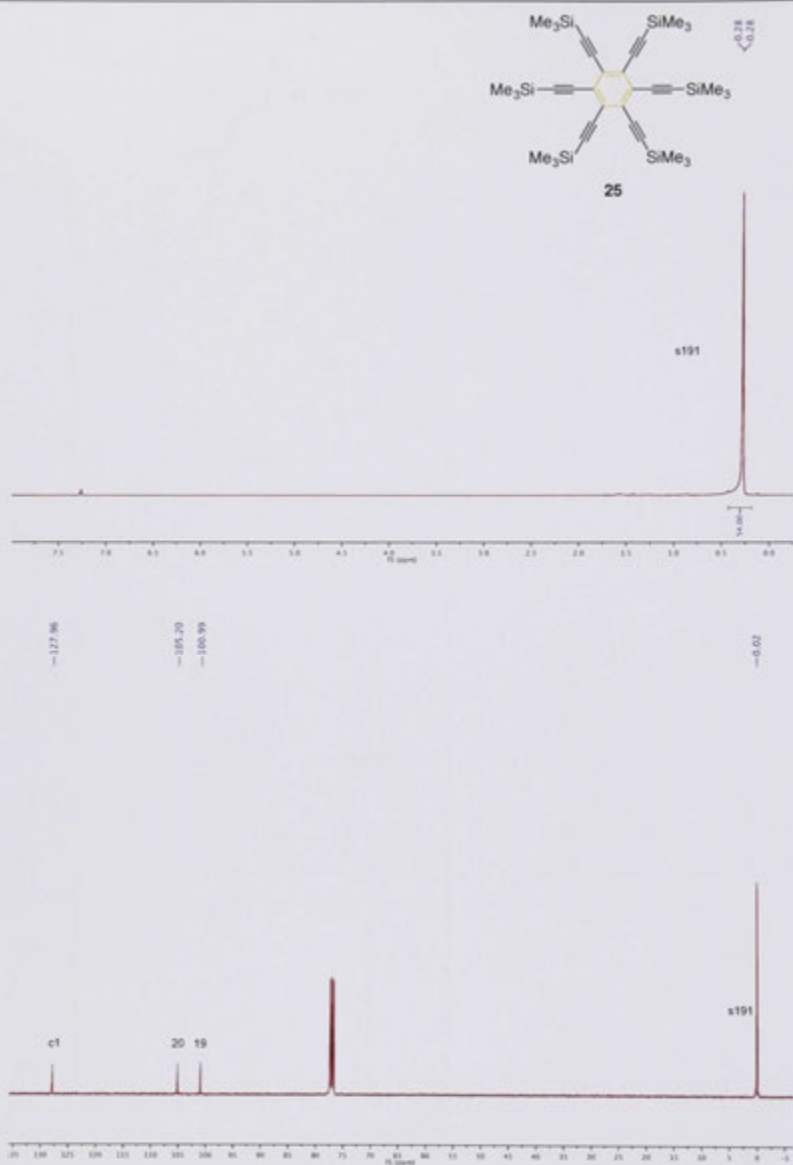
¹H and ¹³C NMR spectra for compound 22.



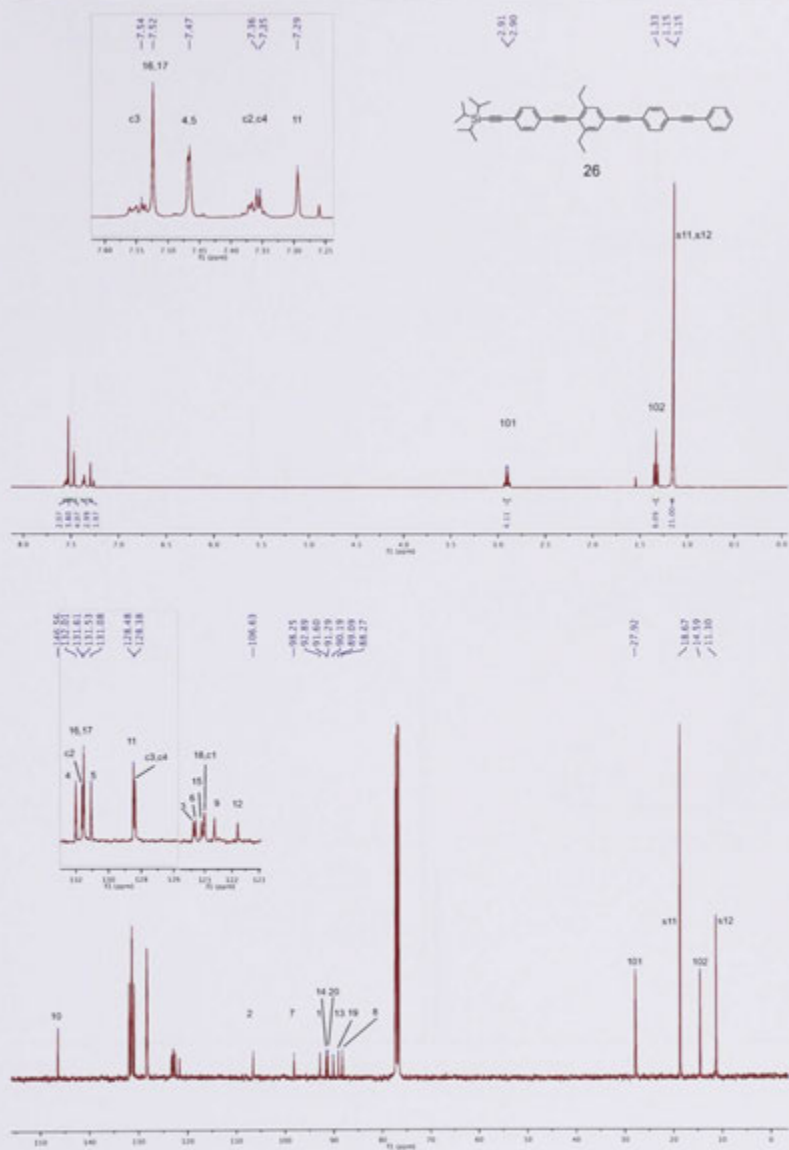
^1H and ^{13}C NMR spectra for compound 23.



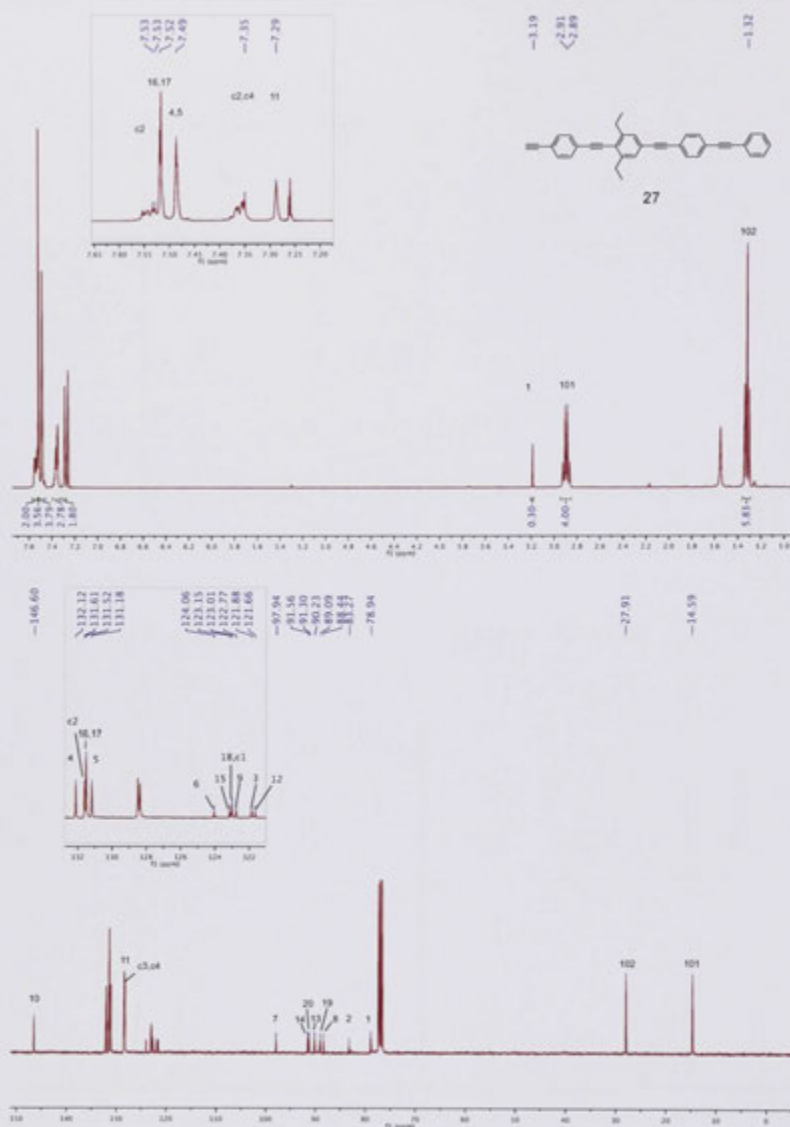
^1H and ^{13}C NMR spectra for compound **24**.



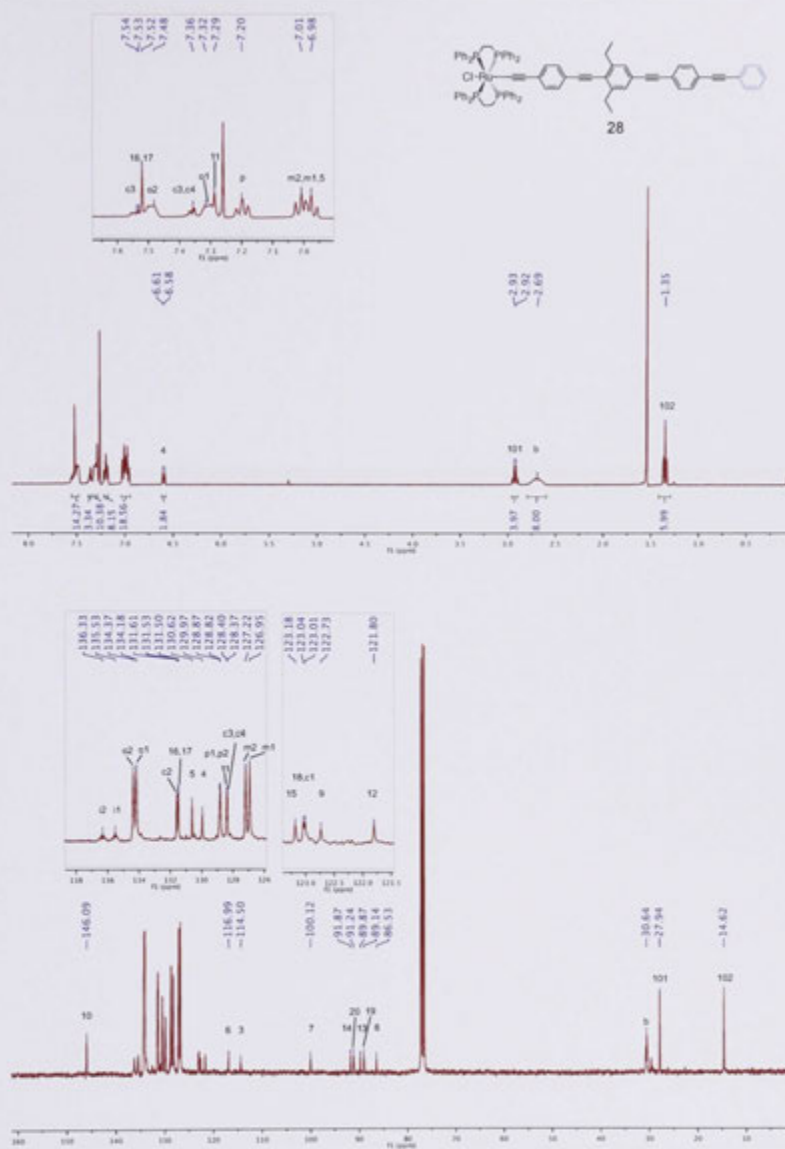
¹H and ¹³C NMR spectra for compound 25.



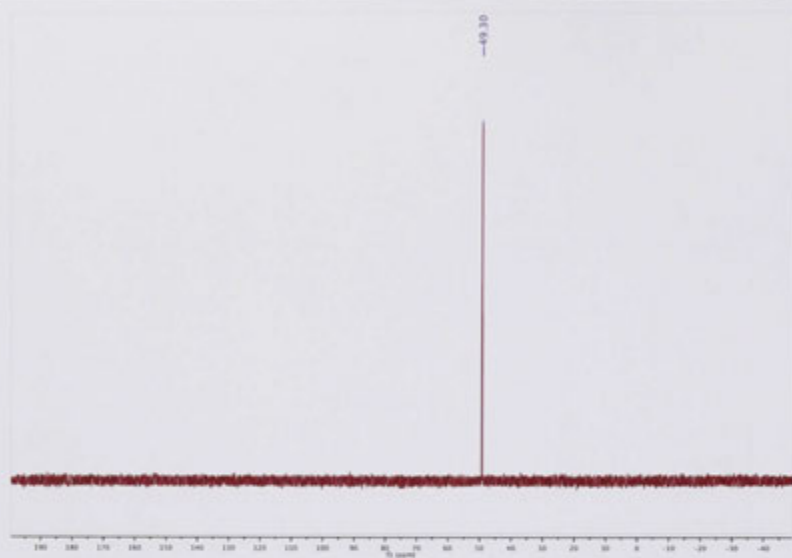
¹H and ¹³C NMR spectra for compound 26.



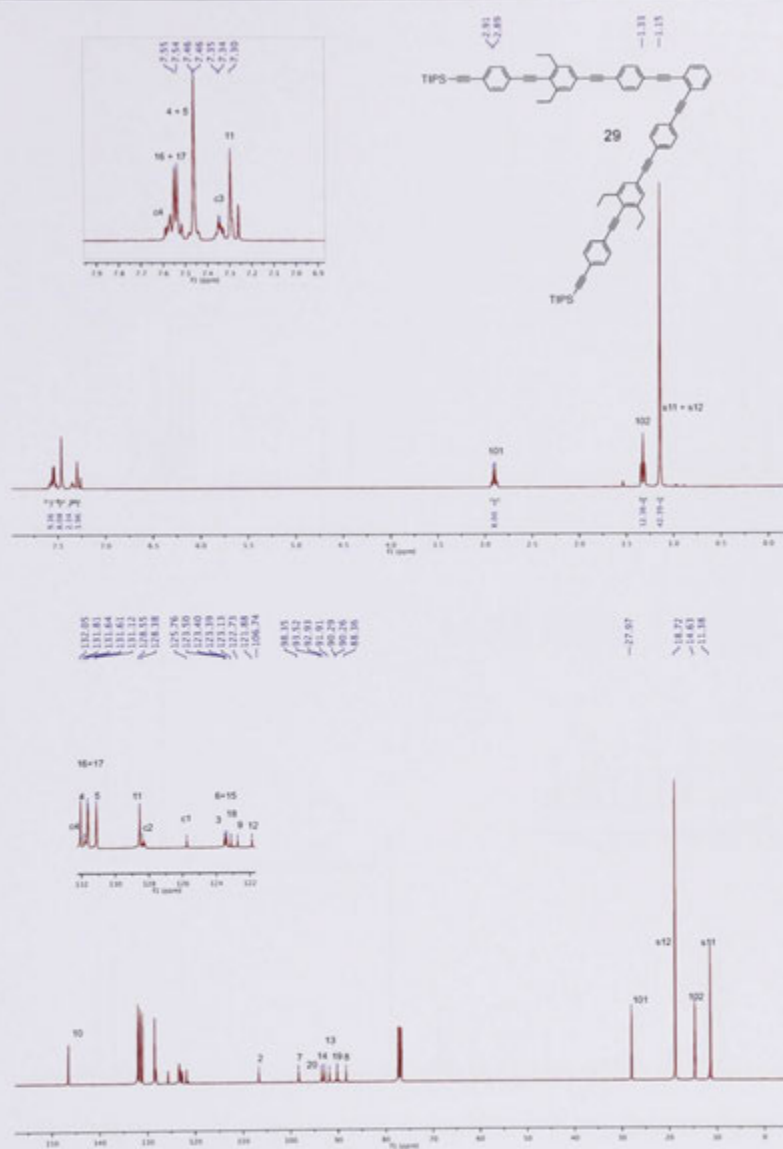
¹H and ¹³C NMR spectra for compound 27.



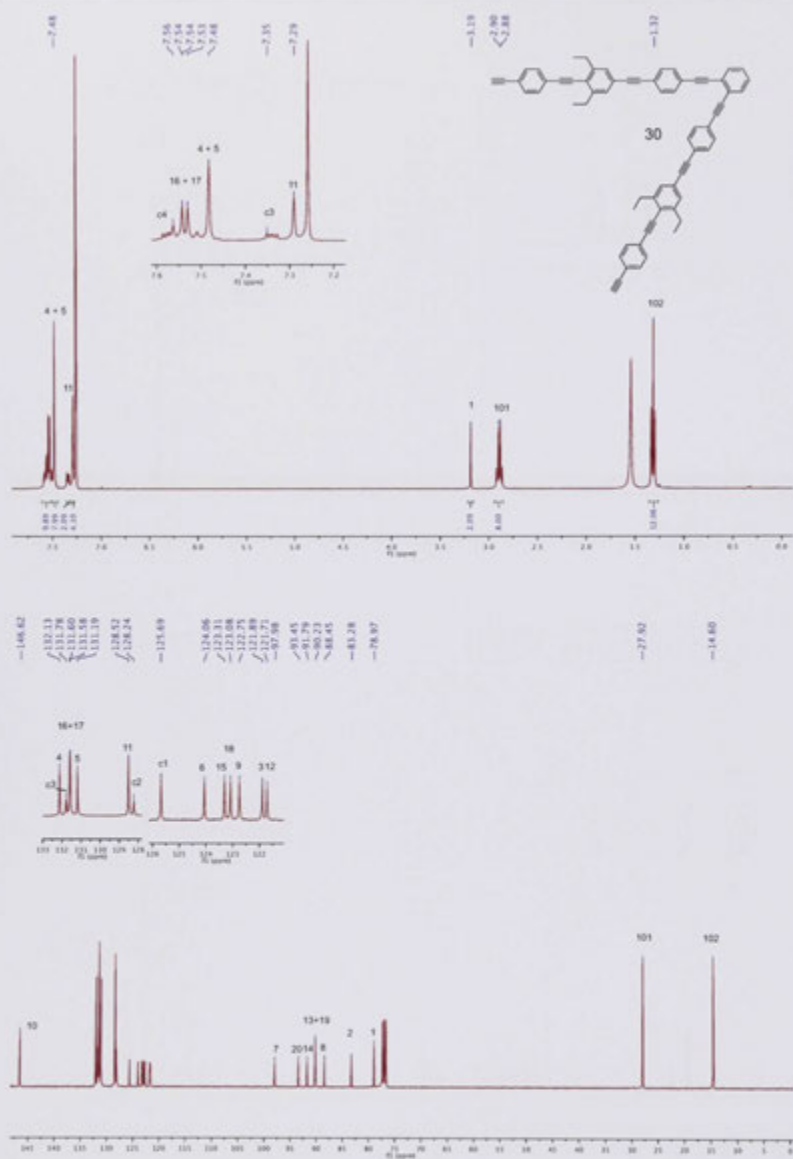
¹H and ¹³C NMR spectra for compound **28**.

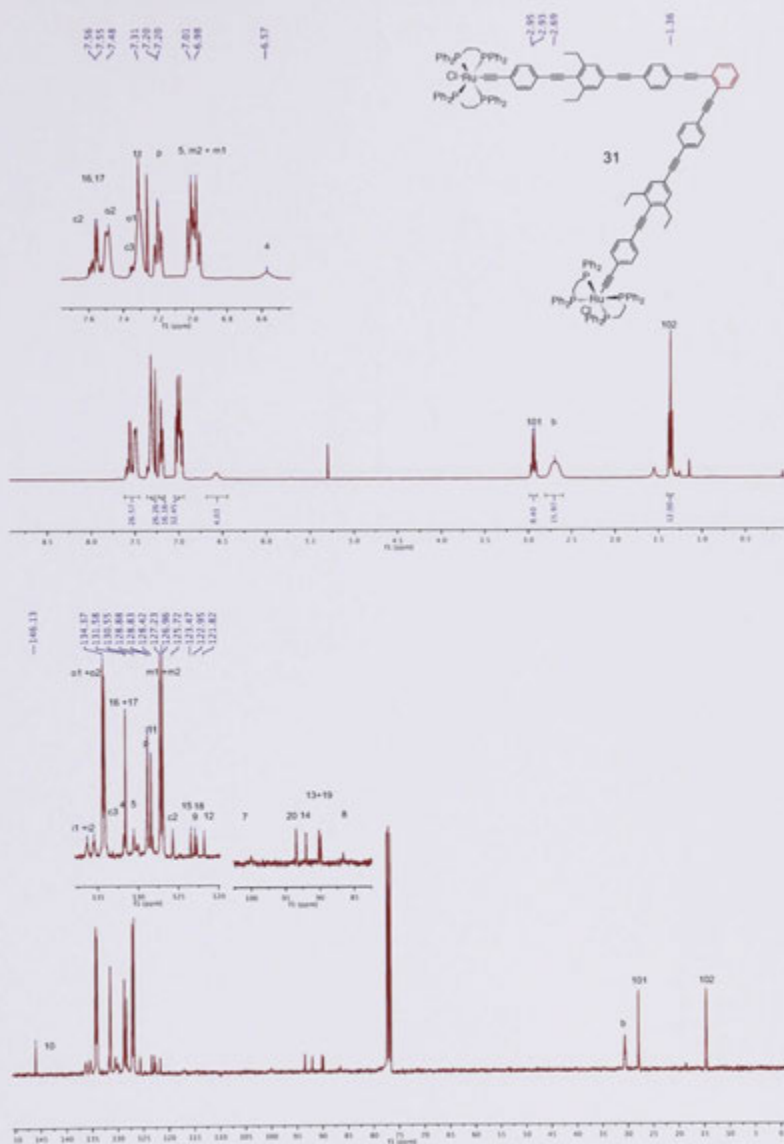


^{31}P NMR spectra for compound 28.

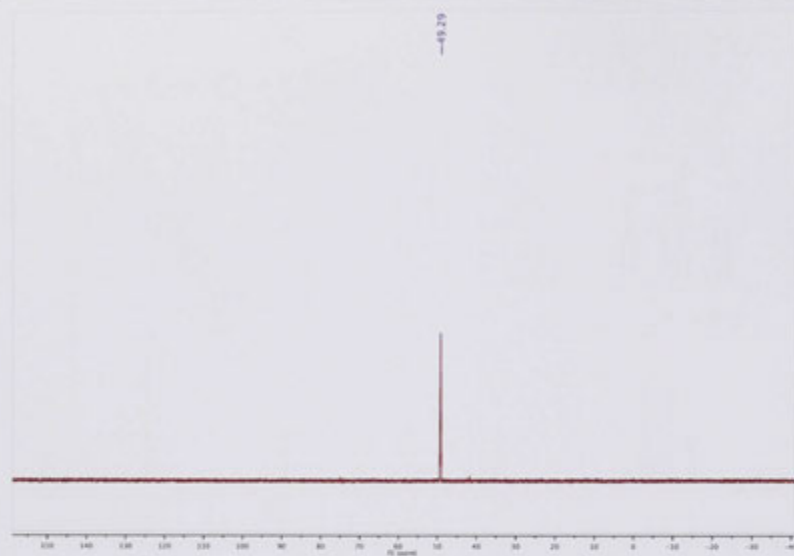


^1H and ^{13}C NMR spectra for compound 29.

¹H and ¹³C NMR spectra for compound 30.



¹H and ¹³C NMR spectra for compound 31.



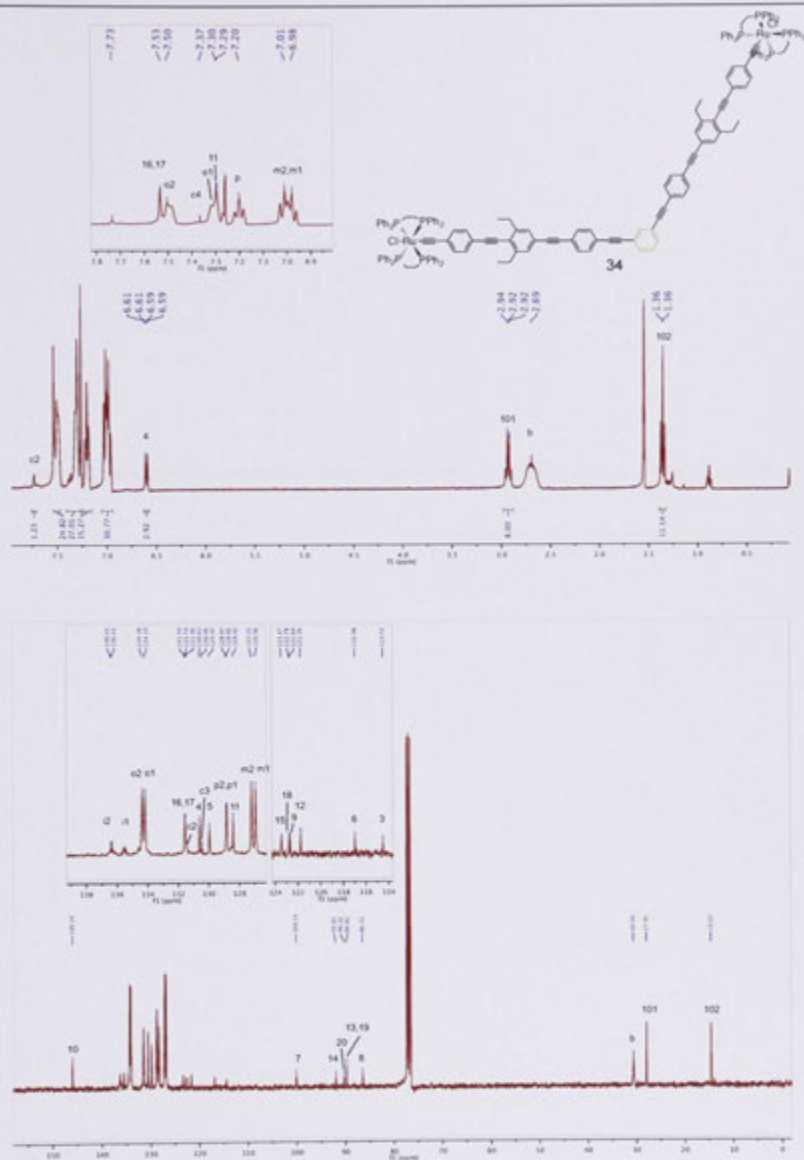
^{31}P NMR spectra for compound 31.



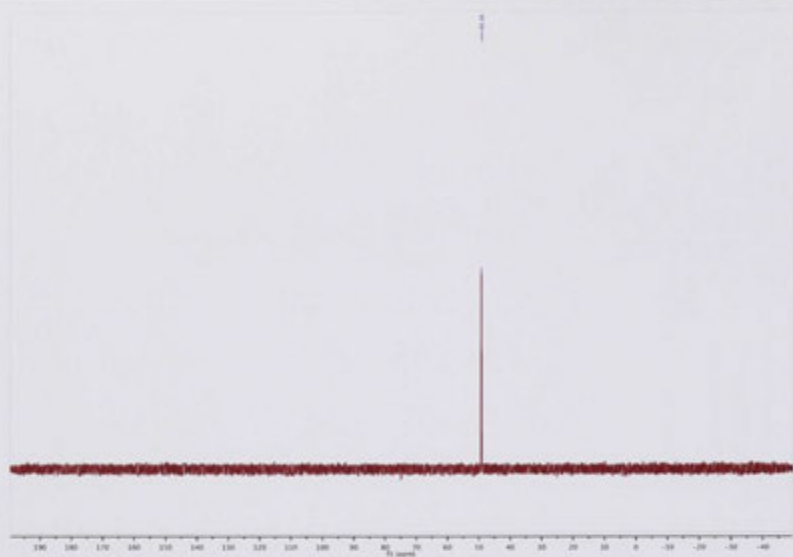
¹H and ¹³C NMR spectra for compound 32.



¹H and ¹³C NMR spectra for compound 33.



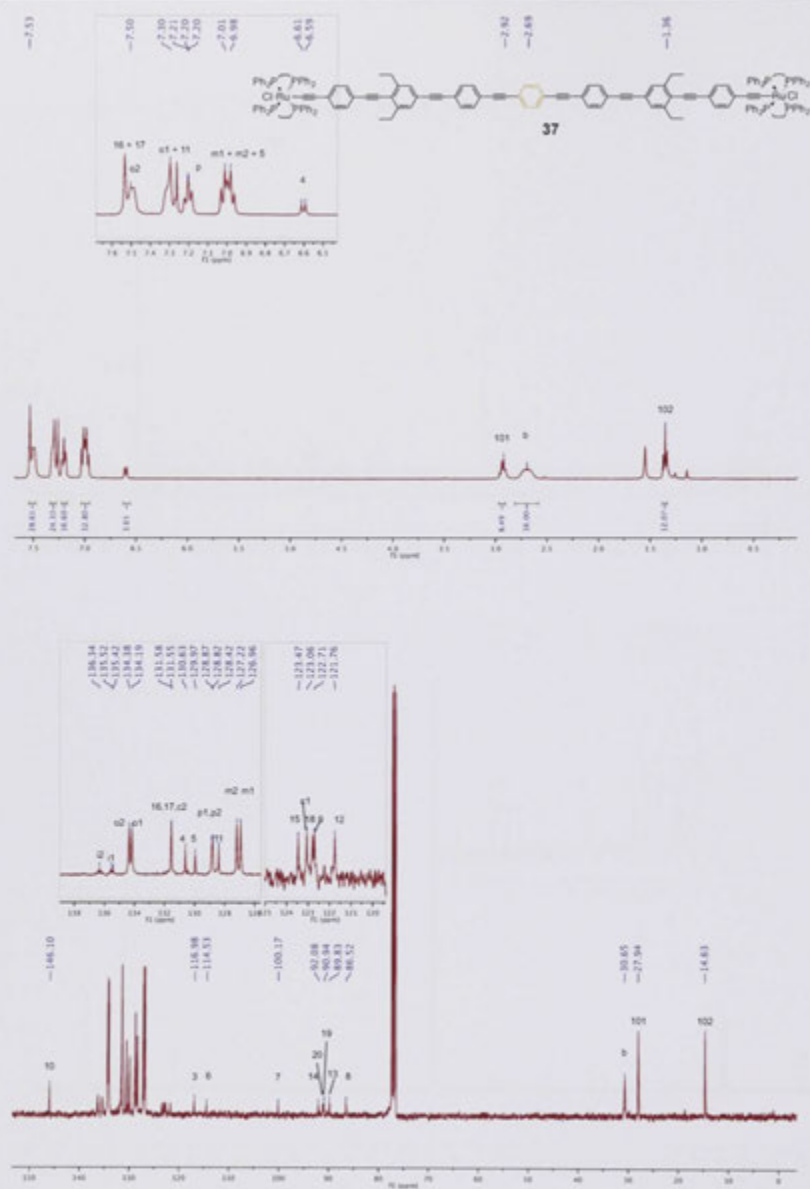
^1H and ^{13}C NMR spectra for compound 34.



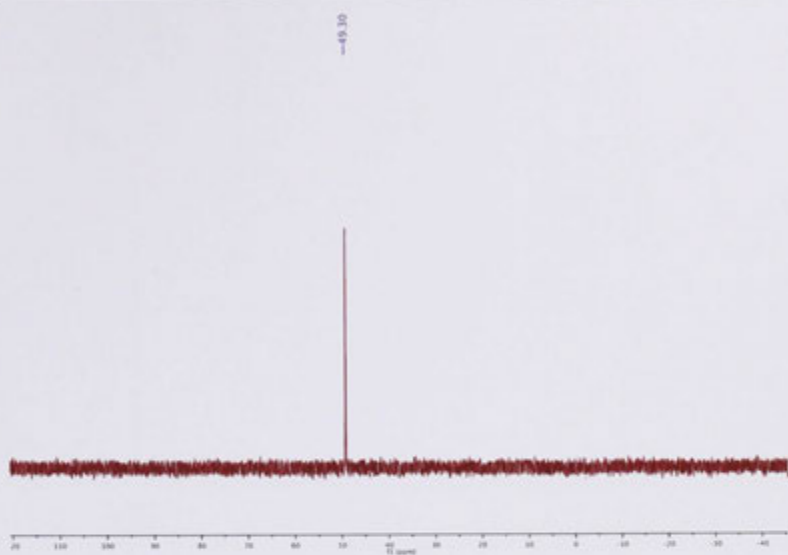
^{31}P NMR spectra for compound **34**.



¹H and ¹³C NMR spectra for compound 35.



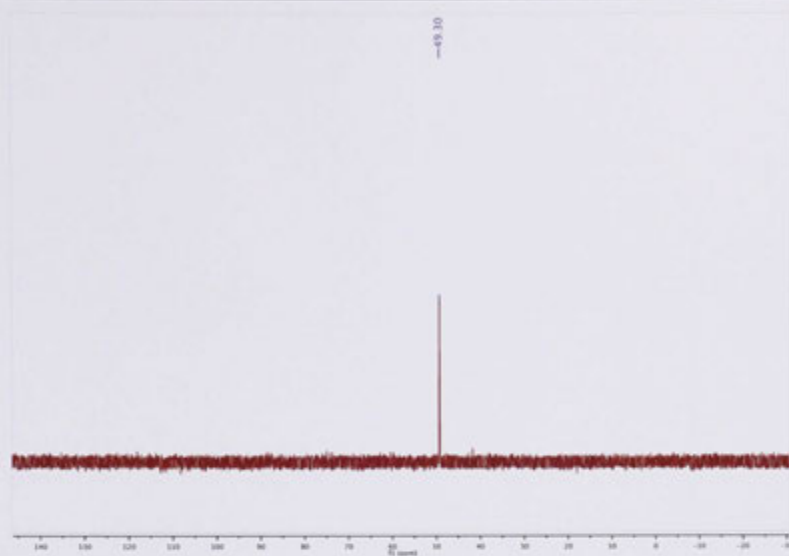
¹H and ¹³C NMR spectra for compound **37**.



^{31}P NMR spectra for compound 37.

¹H and ¹³C NMR spectra for compound **38**.

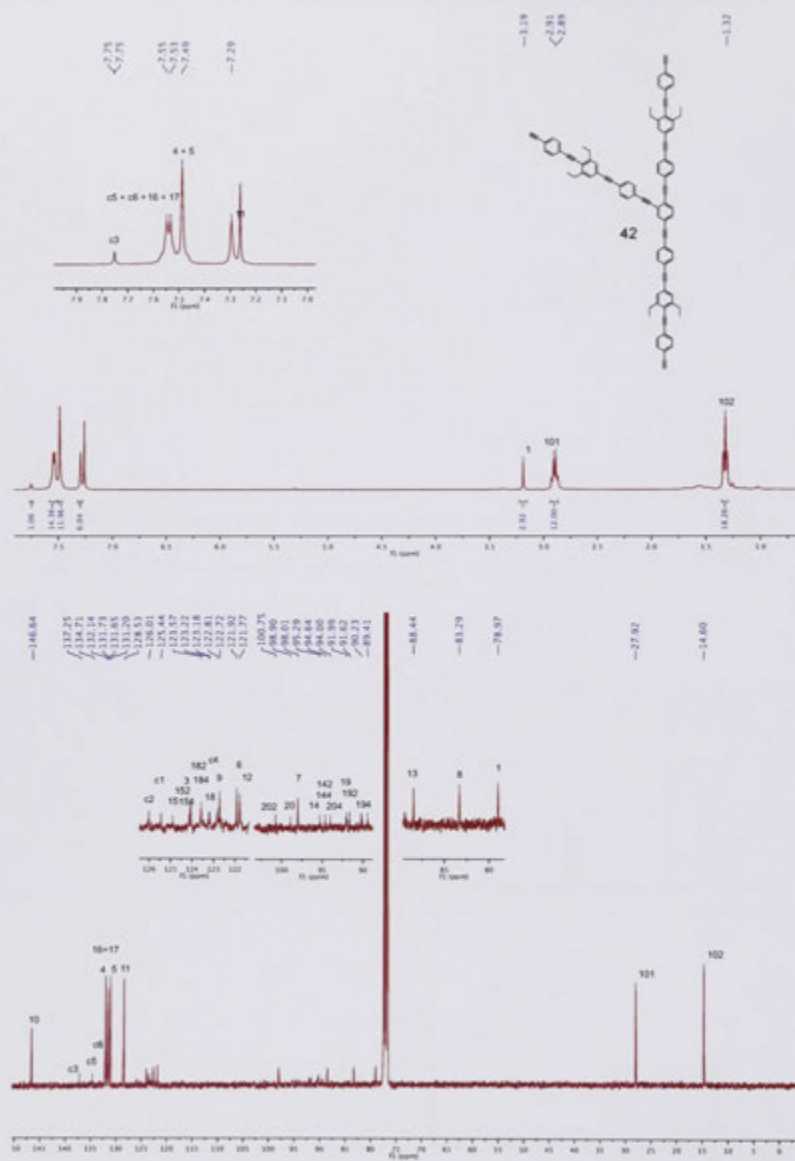
¹H and ¹³C NMR spectra for compound 39.



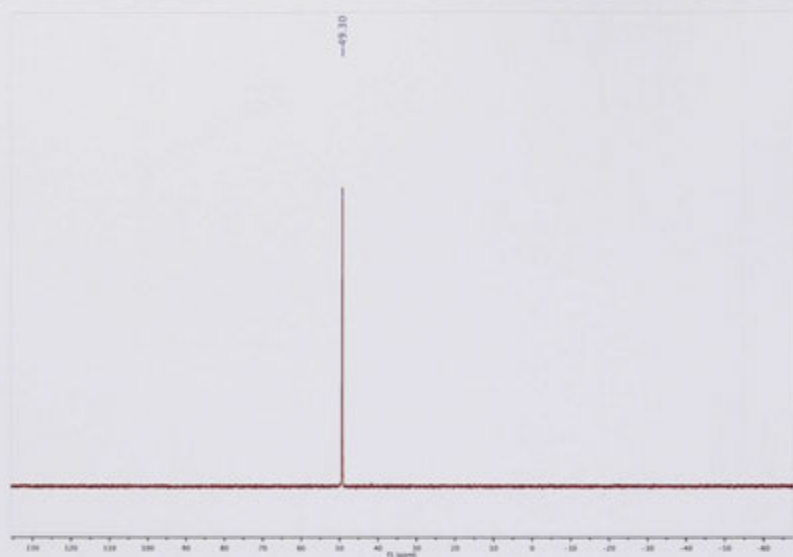
^{31}P NMR spectra for compound 40.



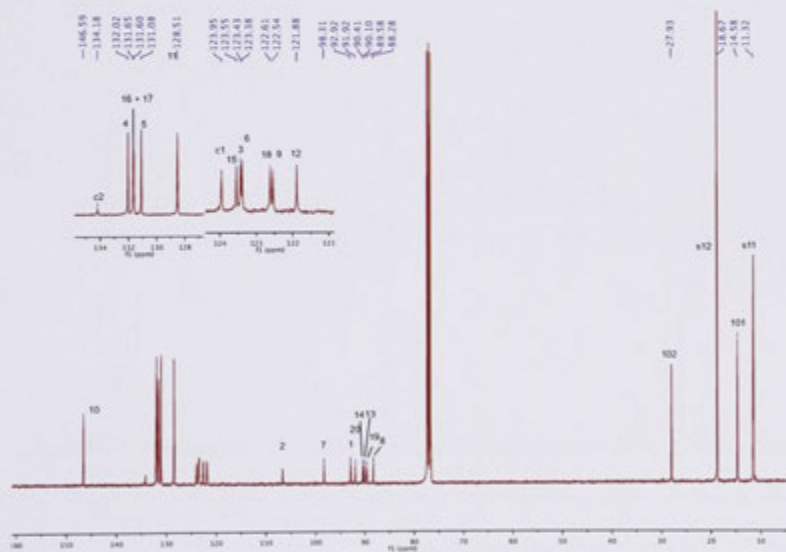
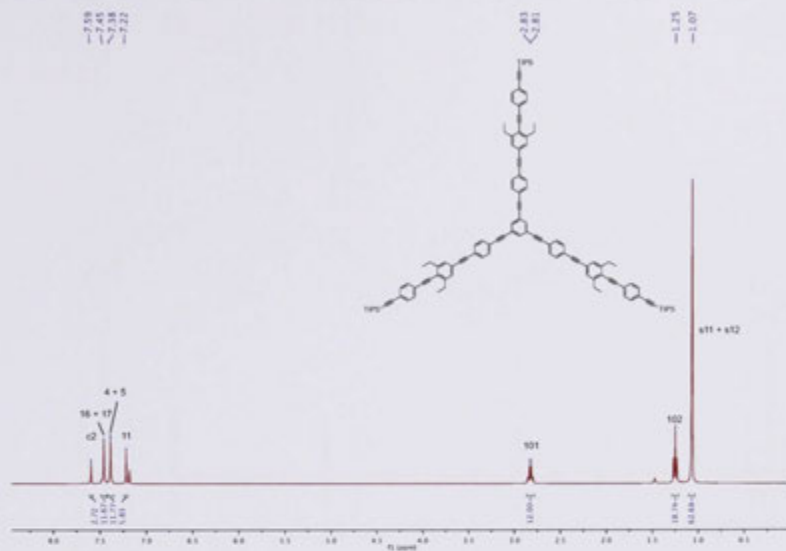
¹H and ¹³C NMR spectra for compound 41.



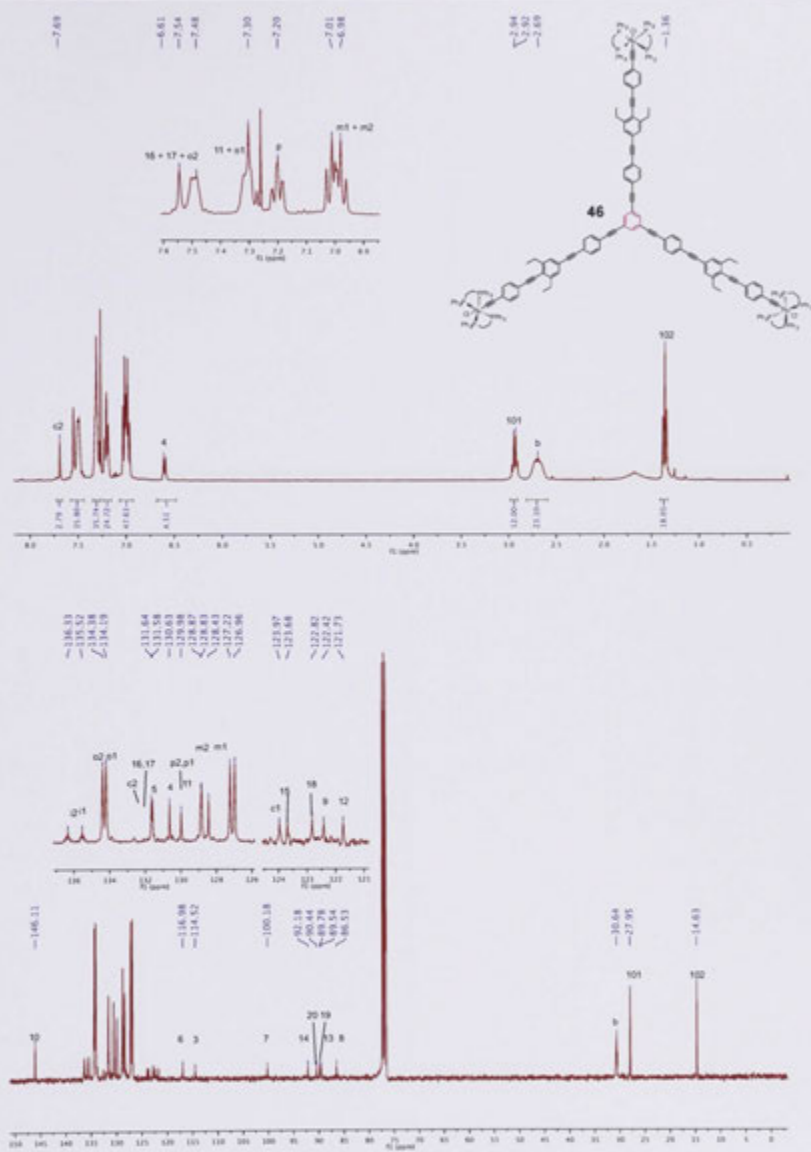
¹H and ¹³C NMR spectra for compound 42.



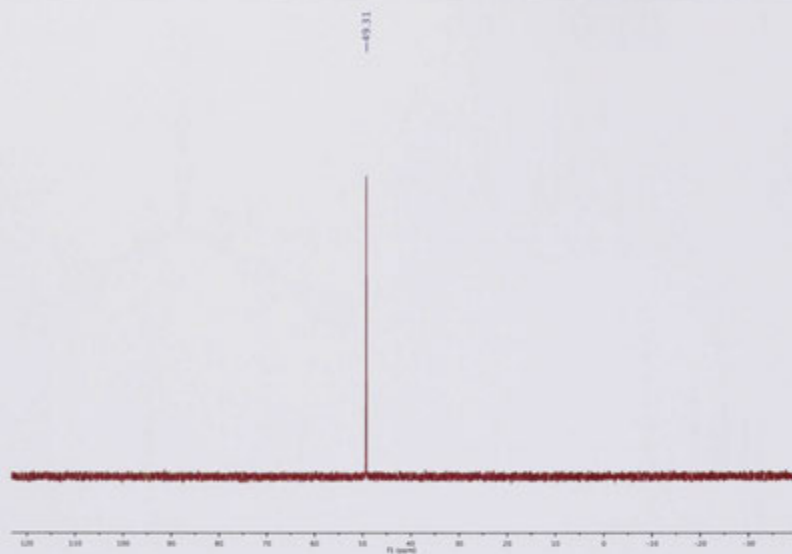
^{31}P NMR spectra for compound 43.

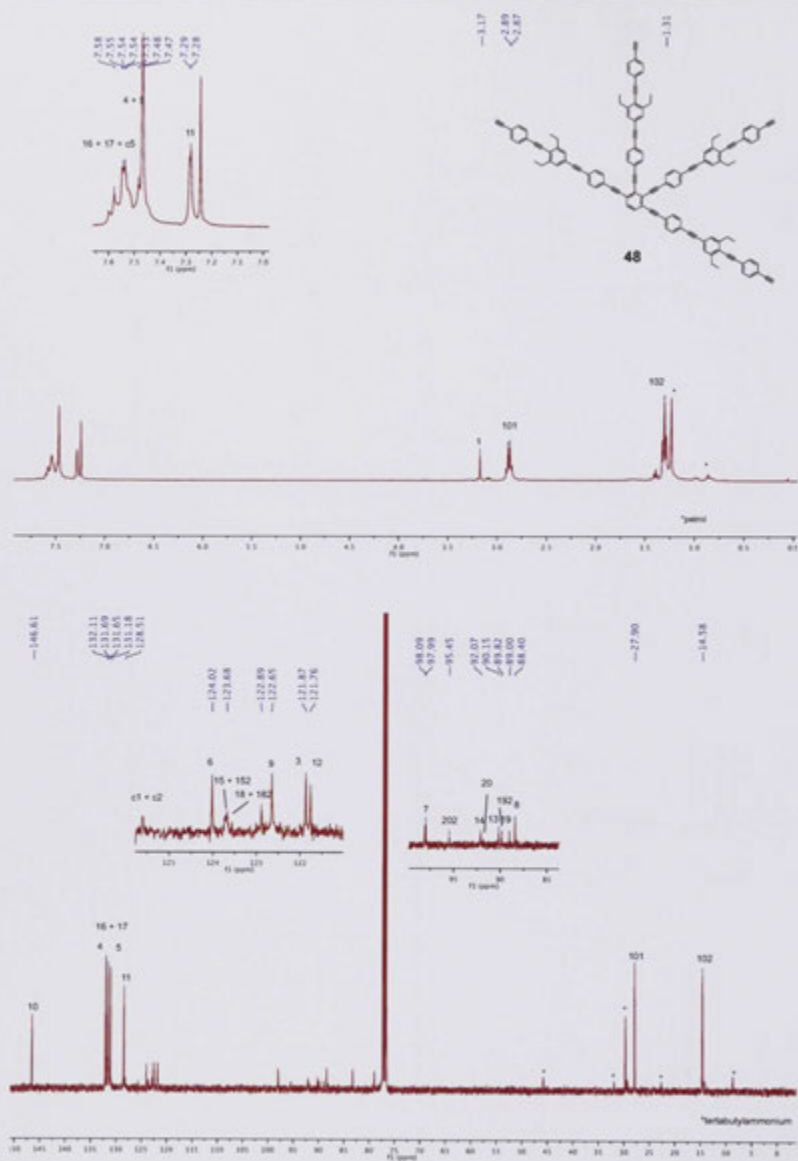


¹H and ¹³C NMR spectra for compound 44.

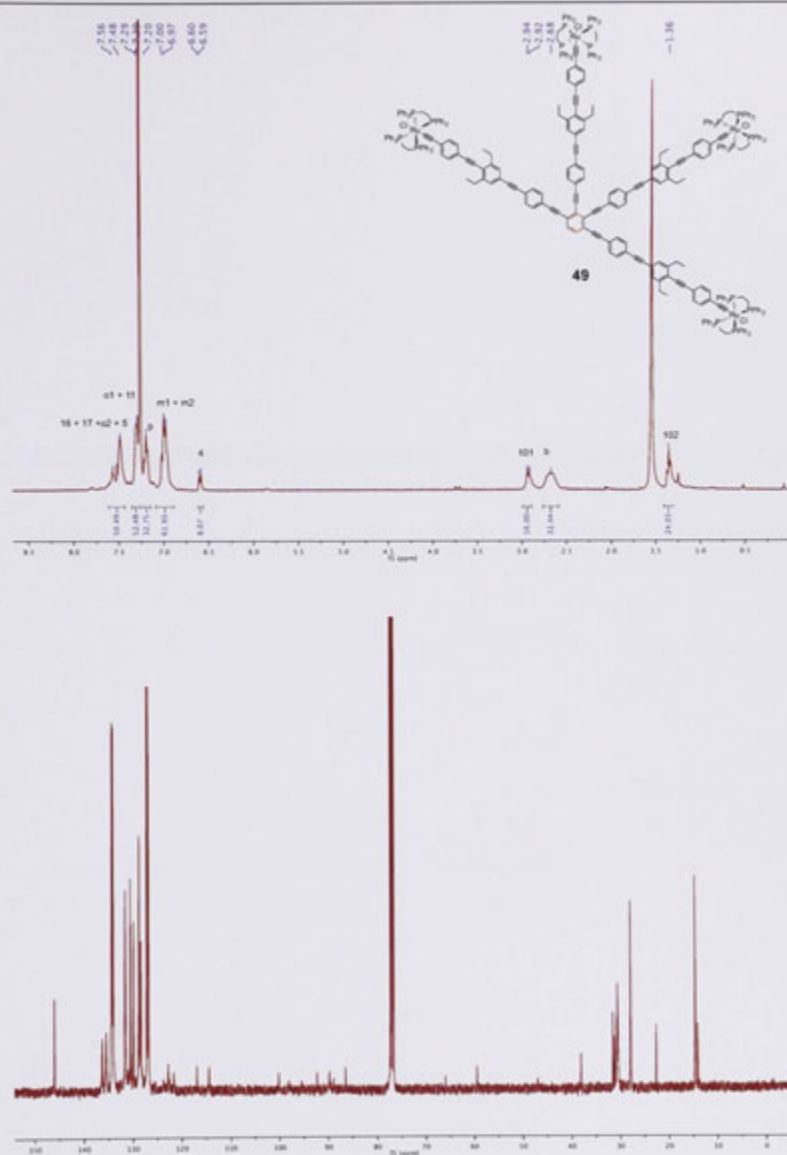


¹H and ¹³C NMR spectra for compound 46.

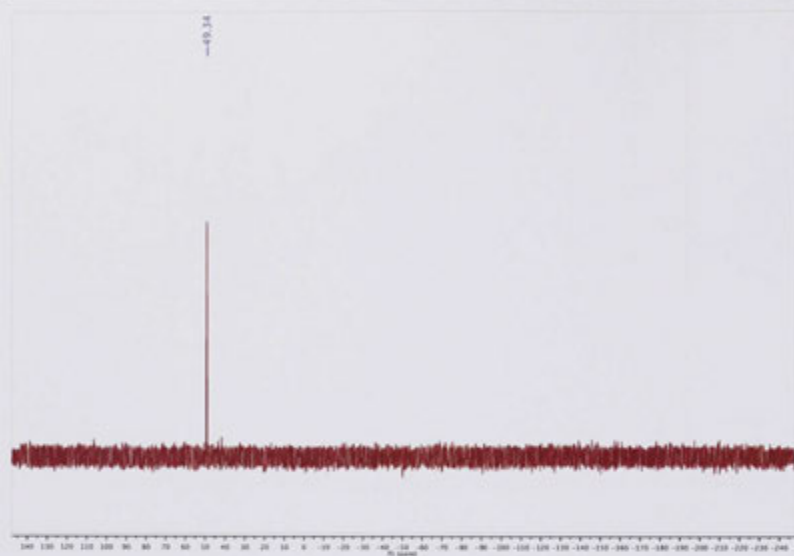
 ^{31}P NMR spectra for compound 46



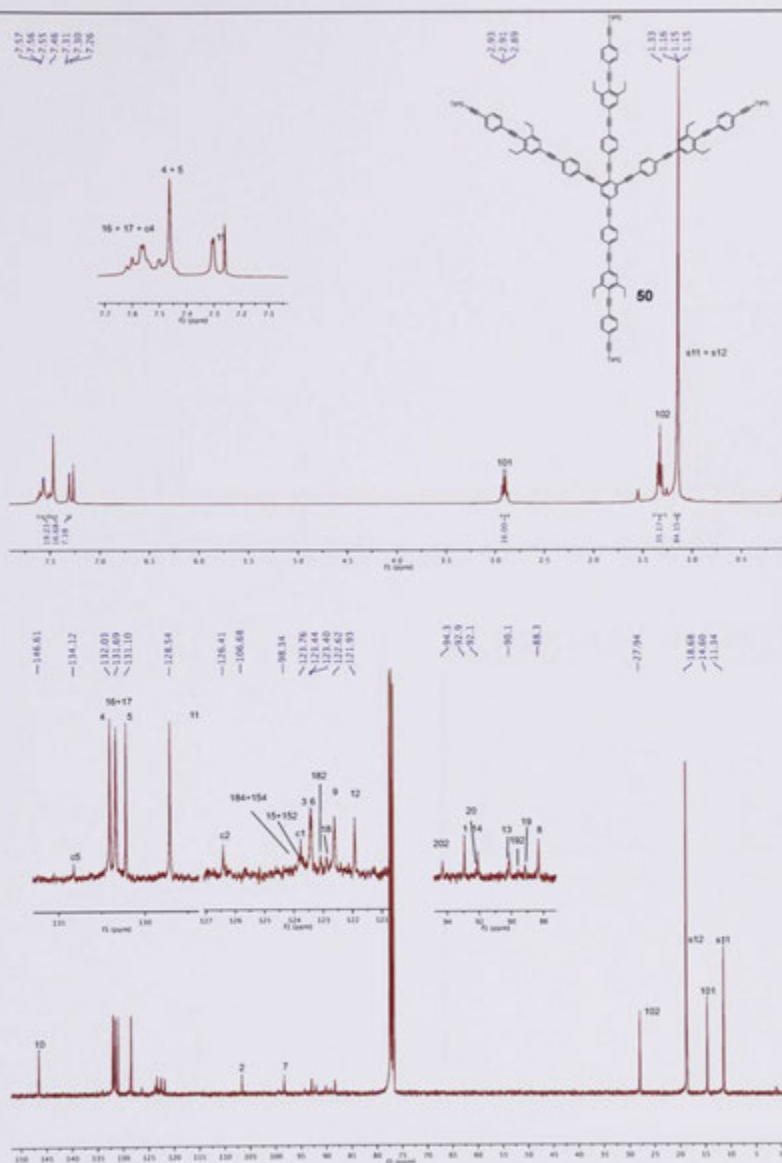
¹H and ¹³C NMR spectra for compound 48.



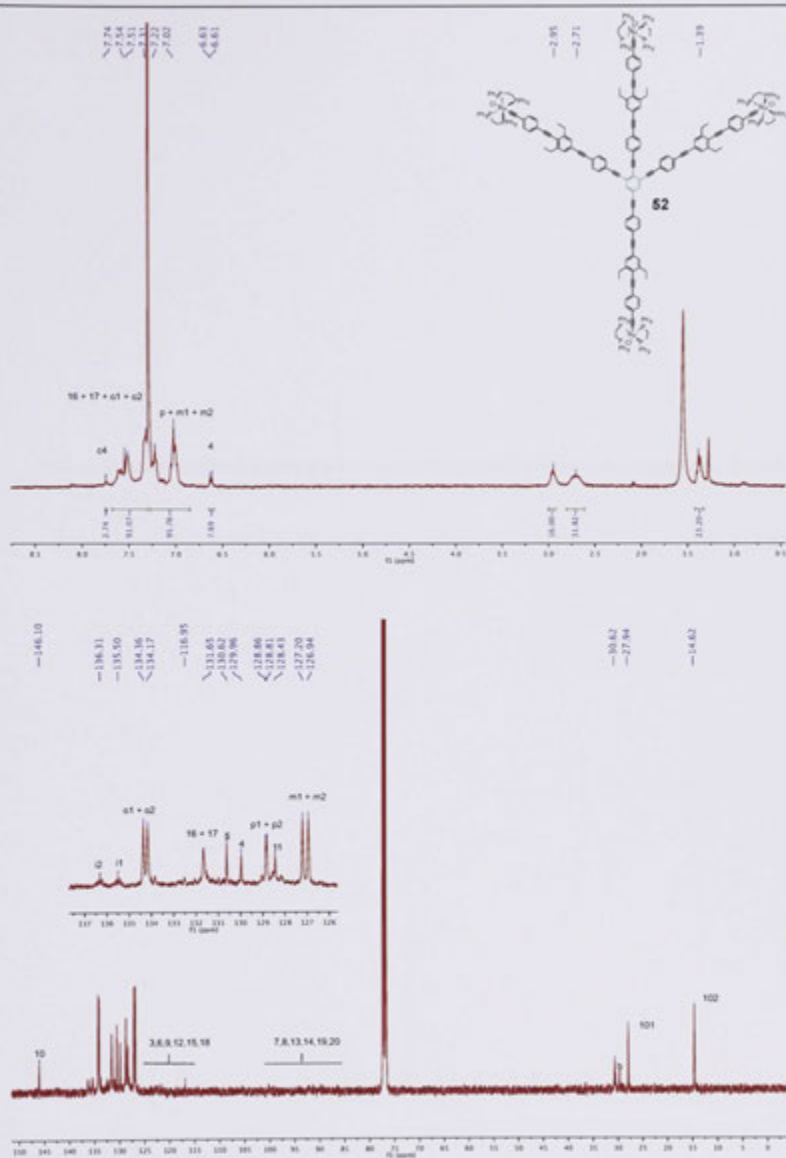
^1H and ^{13}C NMR spectra for compound **49**.



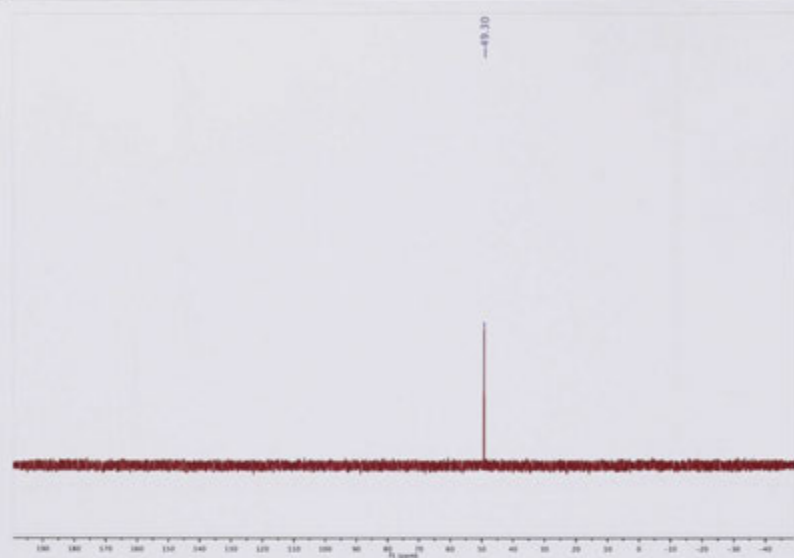
^{31}P NMR spectra for compound **49**.



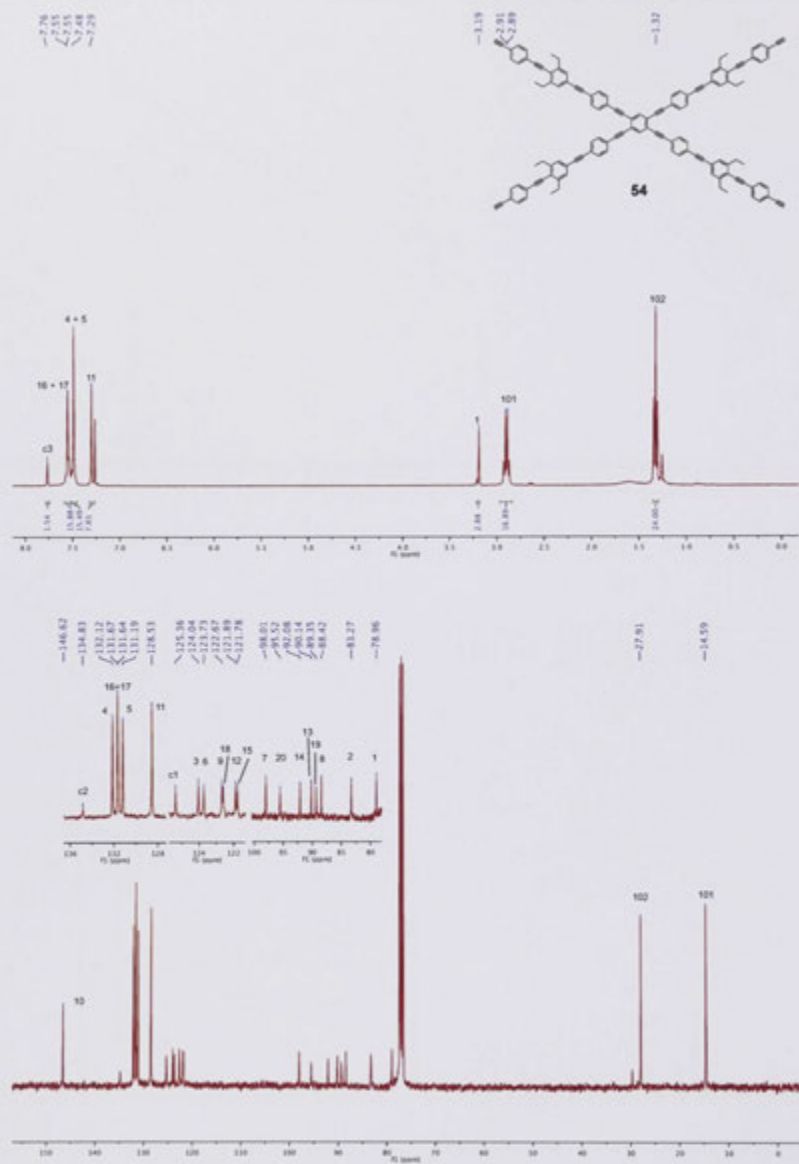
¹H and ¹³C NMR spectra for compound 50.

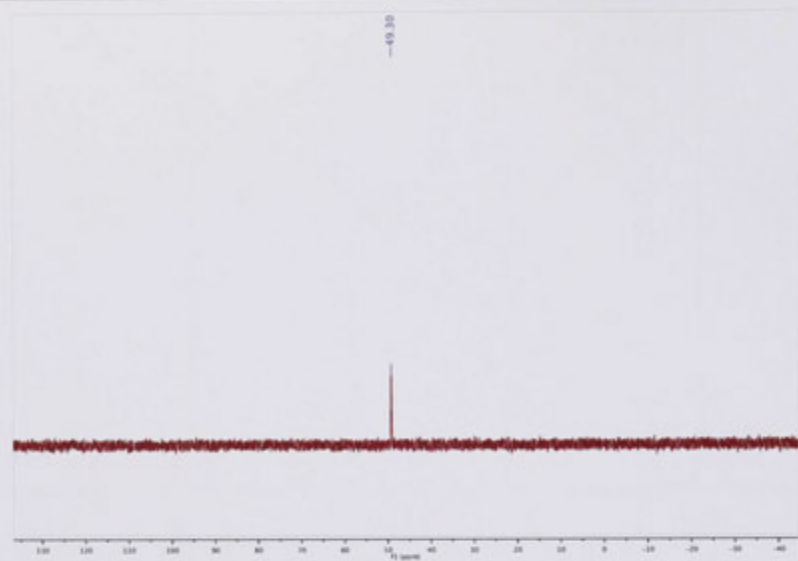


¹H and ¹³C NMR spectra for compound 52.

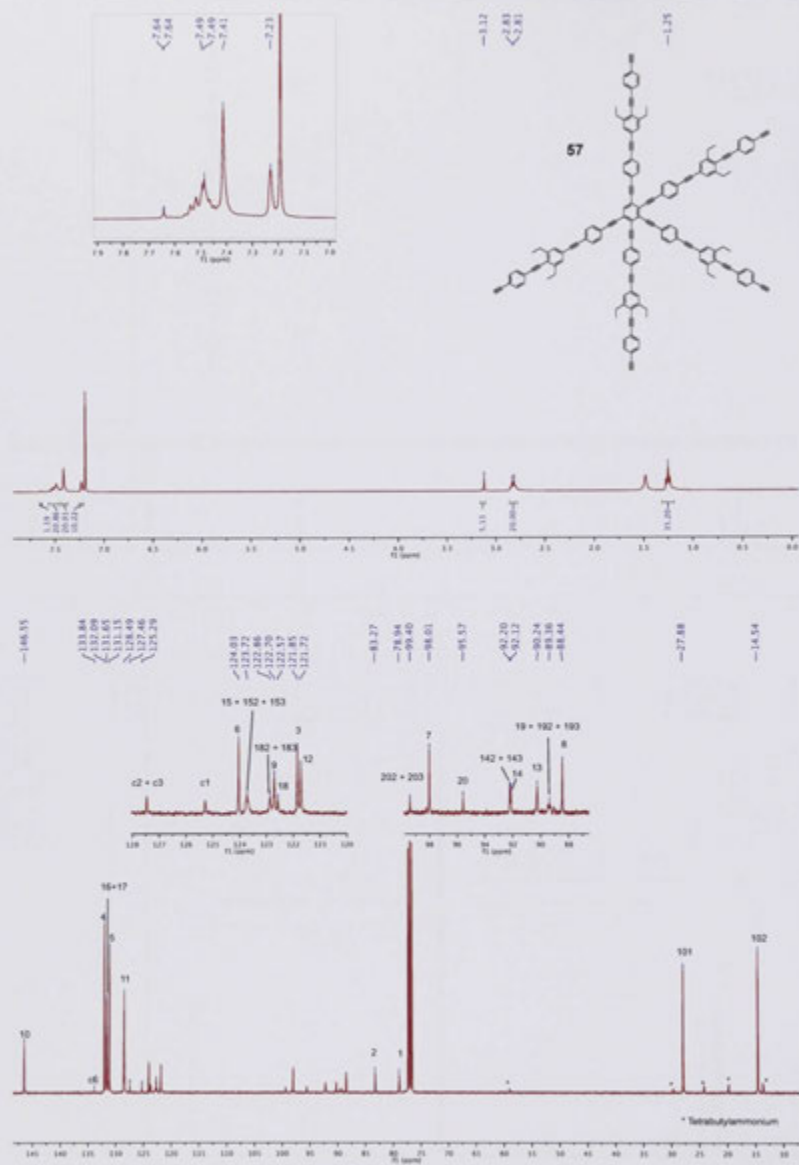


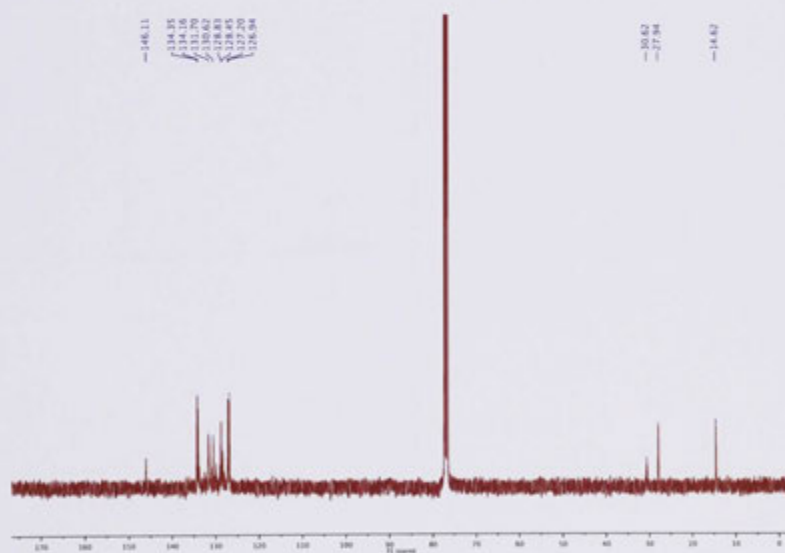
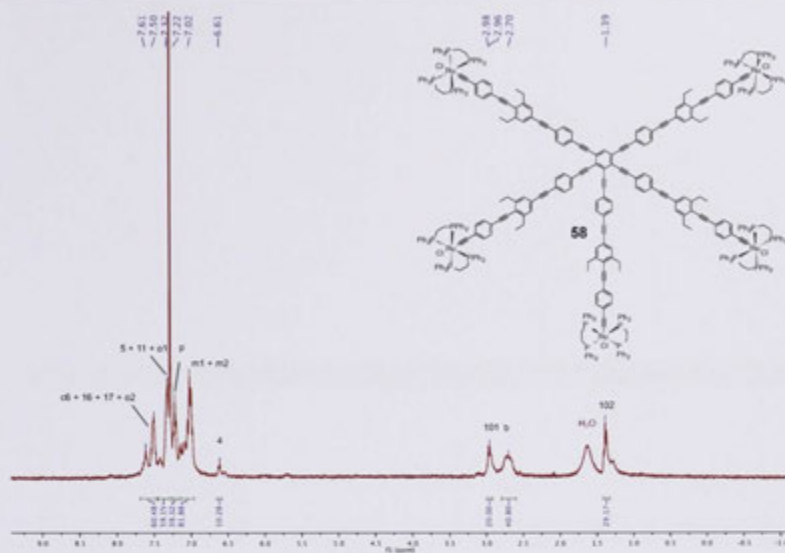
^{31}P NMR spectra for compound 52.

¹H and ¹³C NMR spectra for compound **54**.

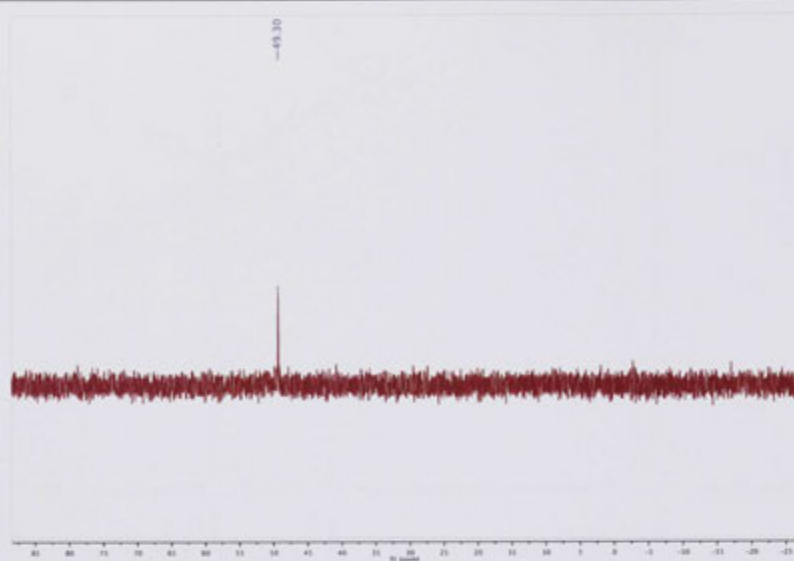


^{31}P NMR spectra for compound 55.

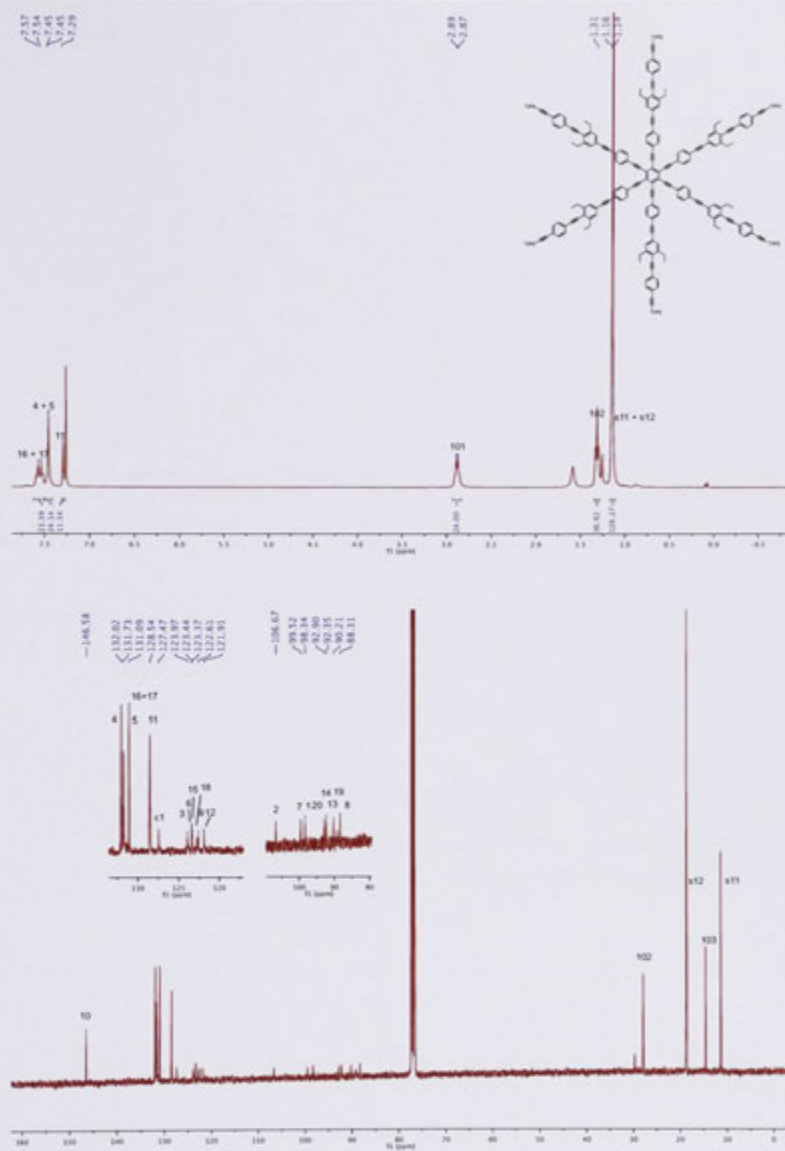




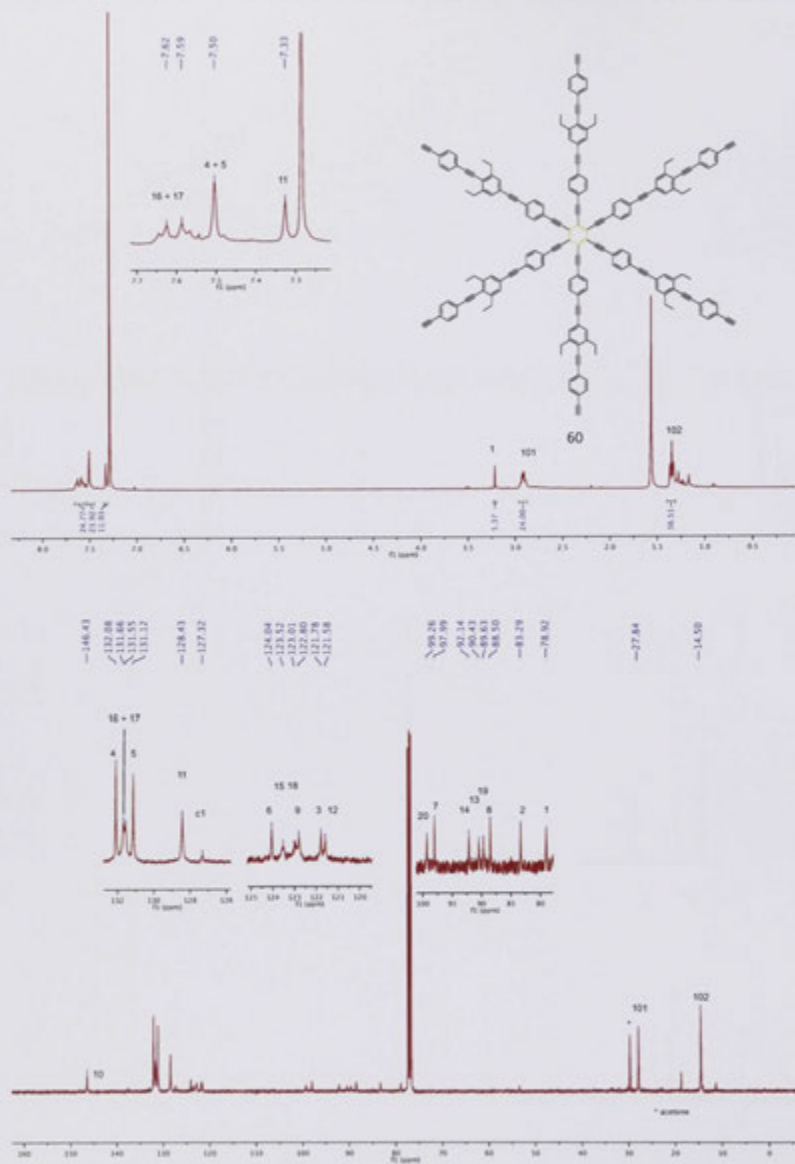
¹H and ¹³C NMR spectra for compound 58.



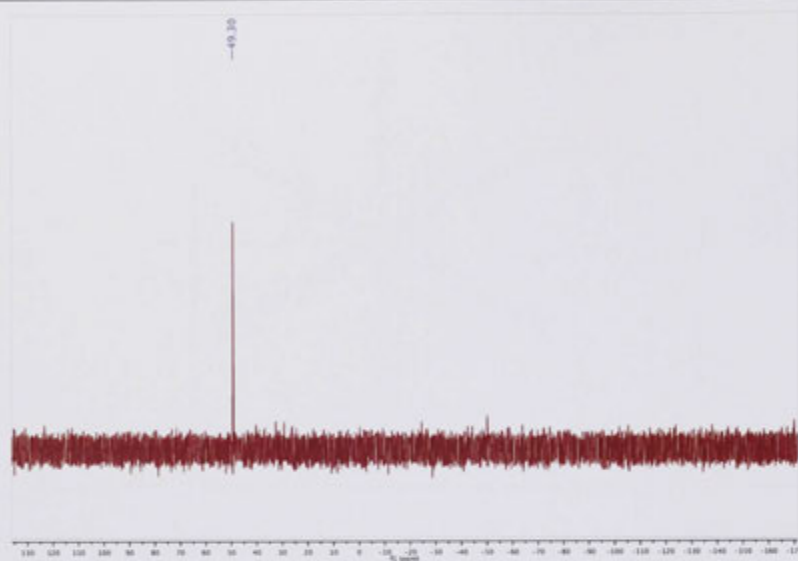
^{31}P NMR spectra for compound 58.



¹H and ¹³C NMR spectra for compound 59.



¹H and ¹³C NMR spectra for compound 60.

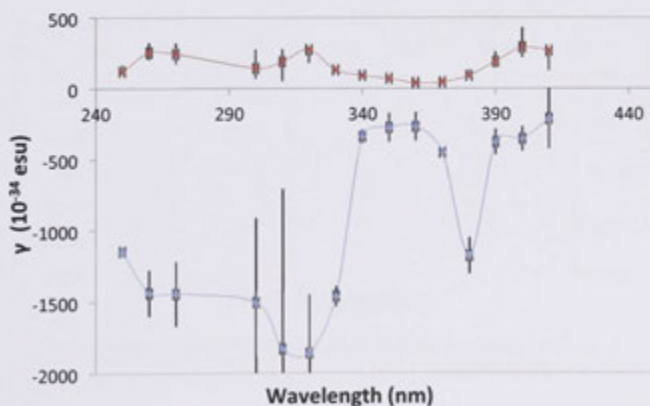
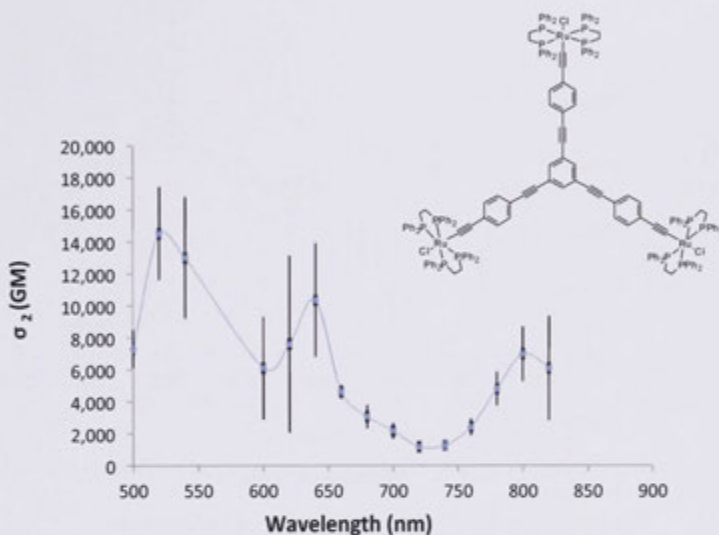


^{31}P NMR spectra for compound **61**.

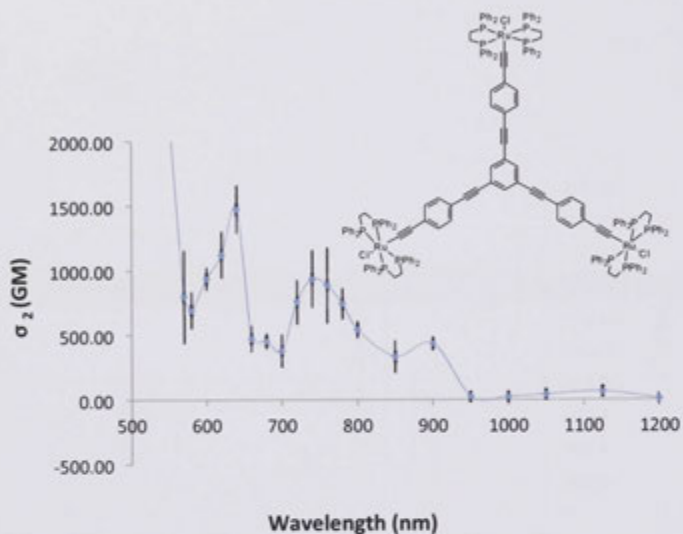
4.2 NLO Data

4.2.1 Chapter 2 NLO data

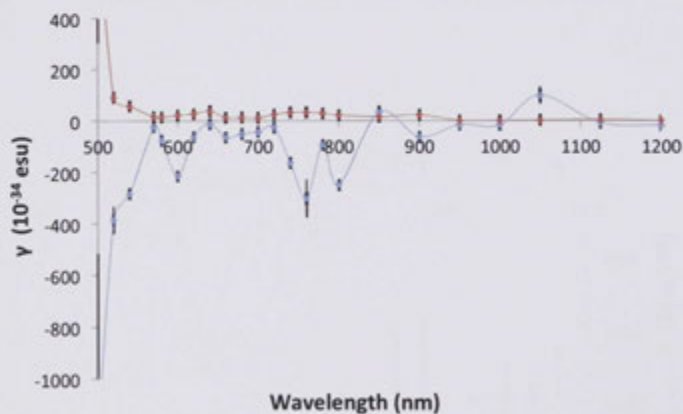
Spectral dependent Z-scan data for **47** (120 mm).



Spectral dependent Z-scan data for **47** (75 mm).

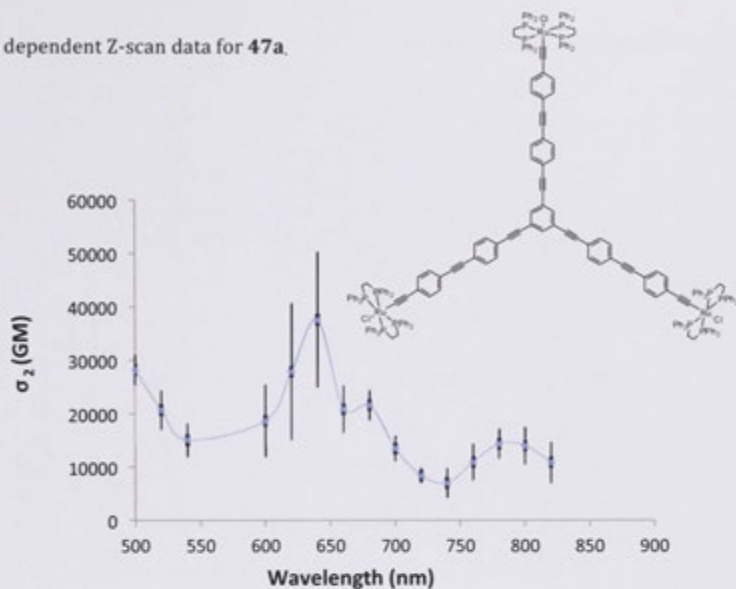


TPA cross-section plot of **47** over a wavelength range of 500-850 nm

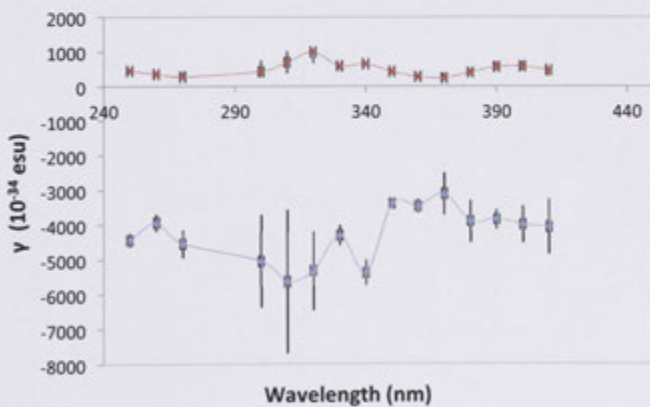


The γ_{real} (blue) and γ_{imag} (red) data of **47**. A trend line has been added to the γ values to aid observation

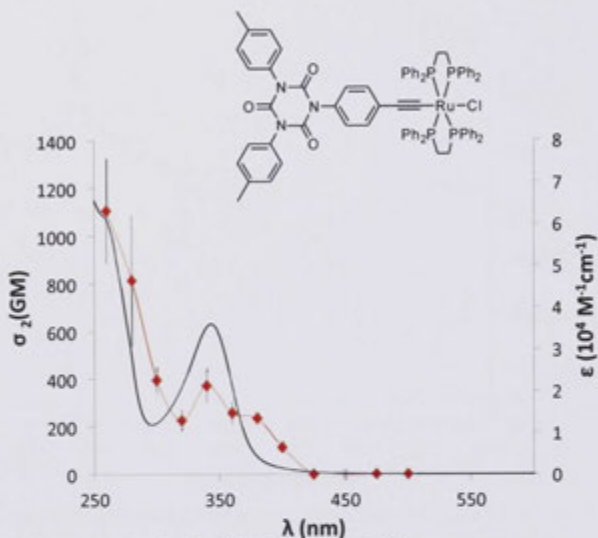
Spectral dependent Z-scan data for **47a**.



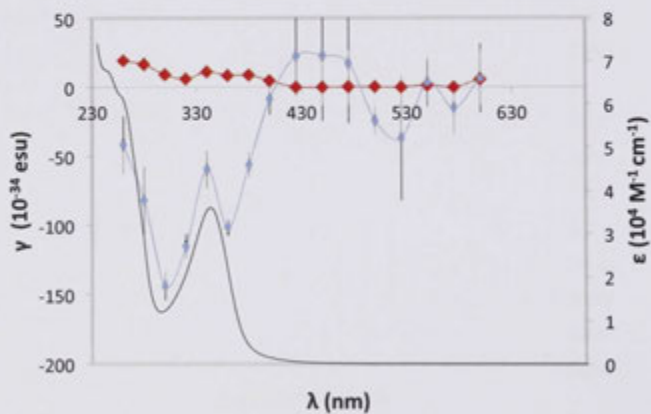
TPA cross-section plot of **47a** over a wavelength range of 500-850 nm



The γ_{real} (blue) and γ_{imag} (red) data of **47a**. A trend line has been added to the γ values to aid observation

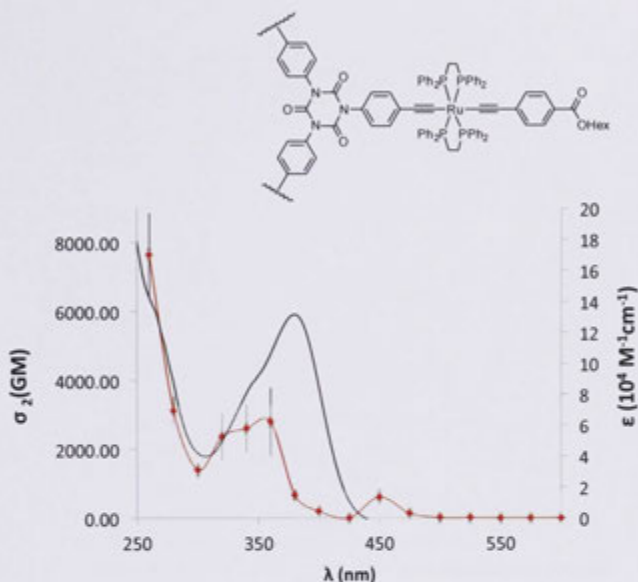
Spectral dependent Z-scan data for **48**.

TPA cross-section plot (red) of **48** plotted at half the measurement wavelength overlaid on the UV-Vis spectrum (black).

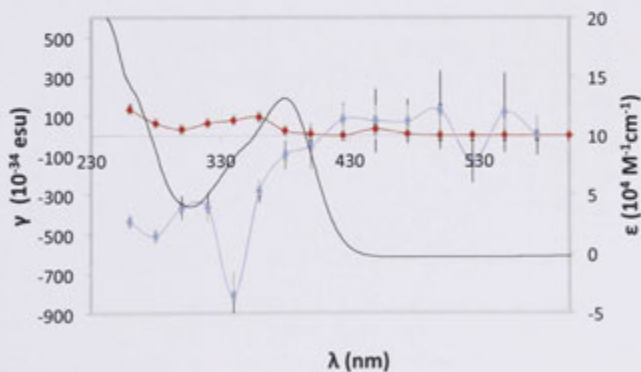


The γ_{real} (blue) and γ_{imag} (red) data of **48** plotted at half the measurement wavelength overlaid on the UV-Vis spectrum. A trend line has been added to the γ values to aid observation

Spectral dependent Z-scan data for **49**.

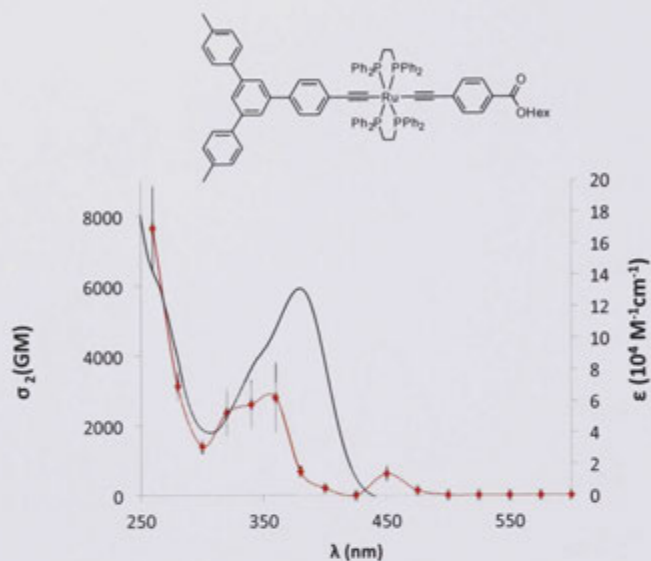


TPA cross-section plot (red) of **49** plotted at half the measurement wavelength overlaid on the UV-Vis spectrum (black).

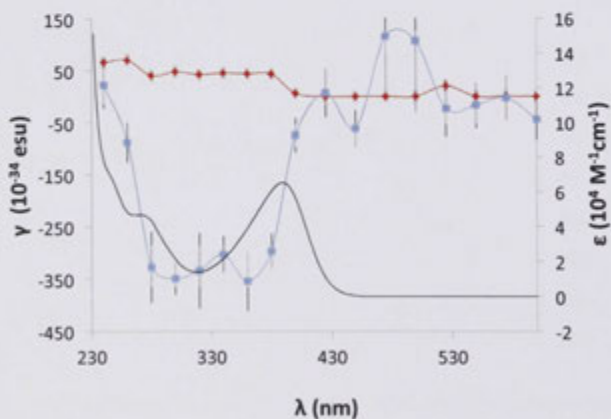


The γ_{real} (blue) and γ_{imag} (red) data of **49** plotted at half the measurement wavelength overlaid on the UV-Vis spectrum. A trend line has been added to the γ values to aid observation

Spectral dependent Z-scan data for **50**.

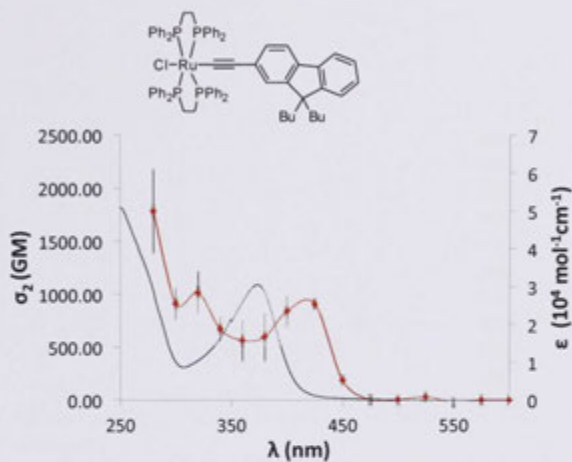


TPA cross-section plot (red) of **50** plotted at half the measurement wavelength overlaid on the UV-Vis spectrum (black).

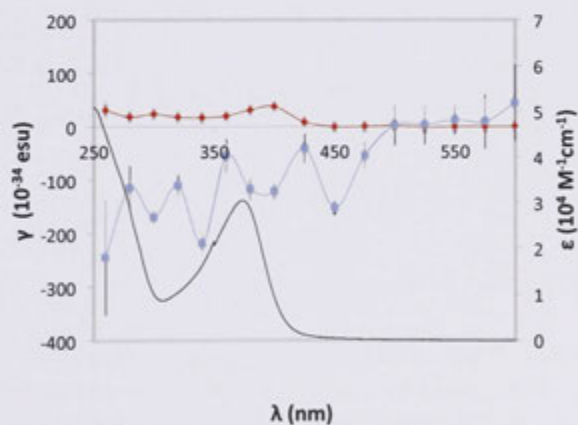


The γ_{real} (blue) and γ_{imag} (red) data of **50** plotted at half the measurement wavelength overlaid on the UV-Vis spectrum. A trend line has been added to the γ values to aid observation

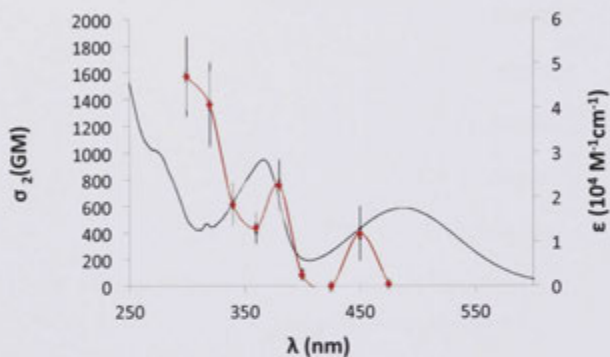
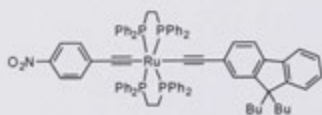
Spectral dependent Z-scan data for **51**.



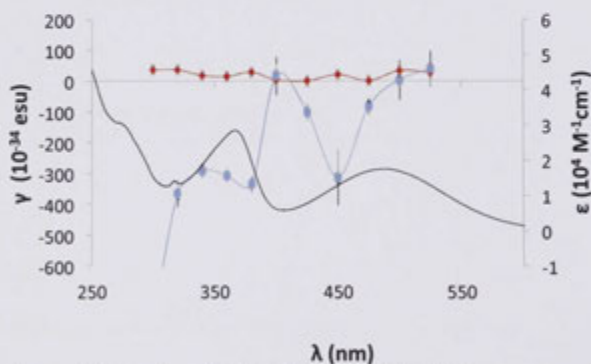
TPA cross-section plot (red) of **51** plotted at half the measurement wavelength overlaid on the UV-Vis spectrum (black).



The γ_{real} (blue) and γ_{imag} (red) data of **51** plotted at half the measurement wavelength overlaid on the UV-Vis spectrum. A trend line has been added to the γ values to aid observation

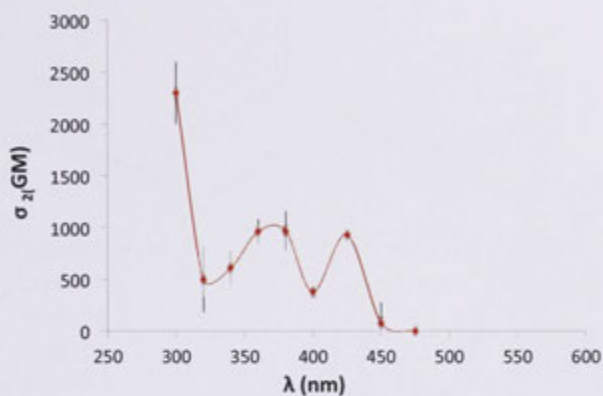
Spectral dependent Z-scan data for **52**.

TPA cross-section plot (red) of **52** plotted at half the measurement wavelength overlaid on the UV-Vis spectrum (black).

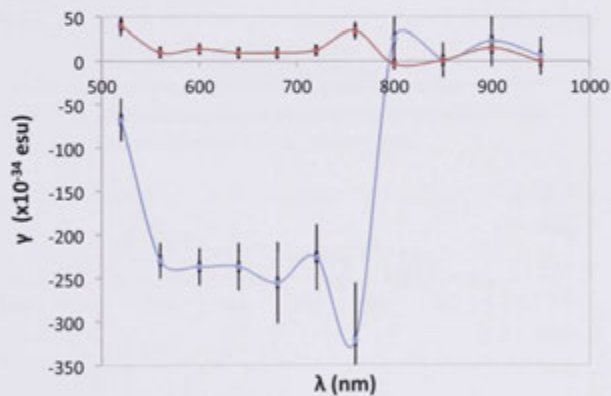


The γ_{real} (blue) and γ_{imag} (red) data of **52** plotted at half the measurement wavelength overlaid on the UV-Vis spectrum. A trend line has been added to the γ values to aid observation

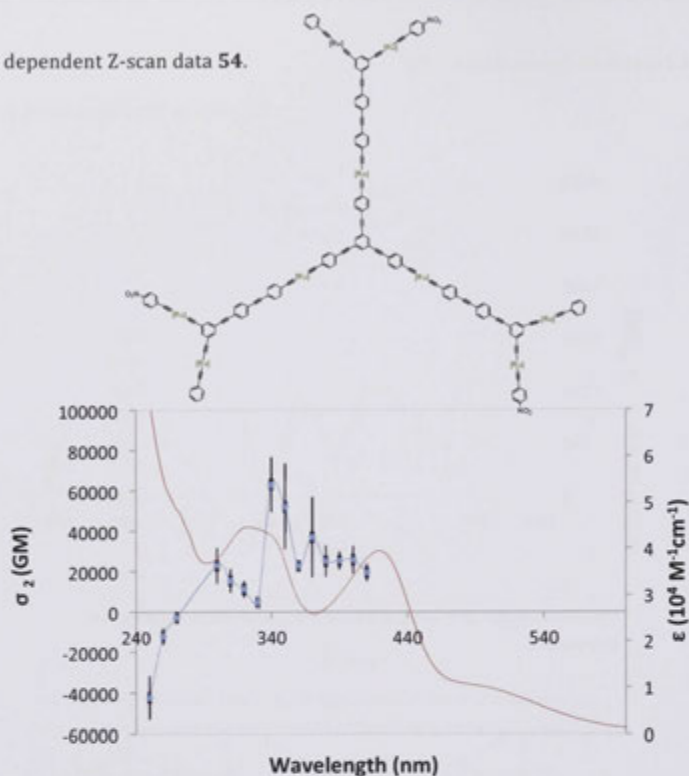
Spectral dependent Z-scan data for **53**.



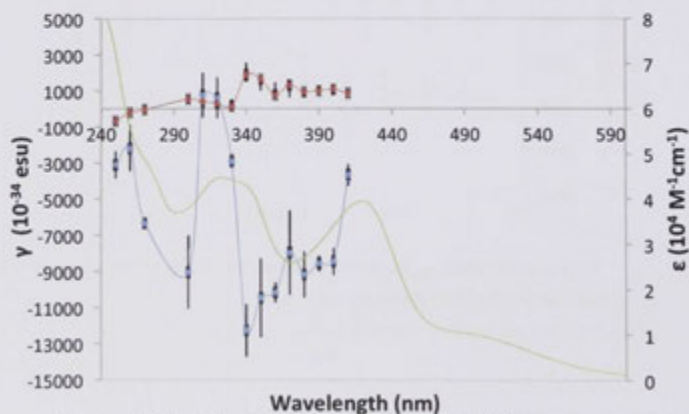
TPA cross-section plot (red) of **53** plotted at half the measurement wavelength.



The γ_{real} (blue) and γ_{imag} (red) data of **53**. A trend line has been added to the γ values to aid observation

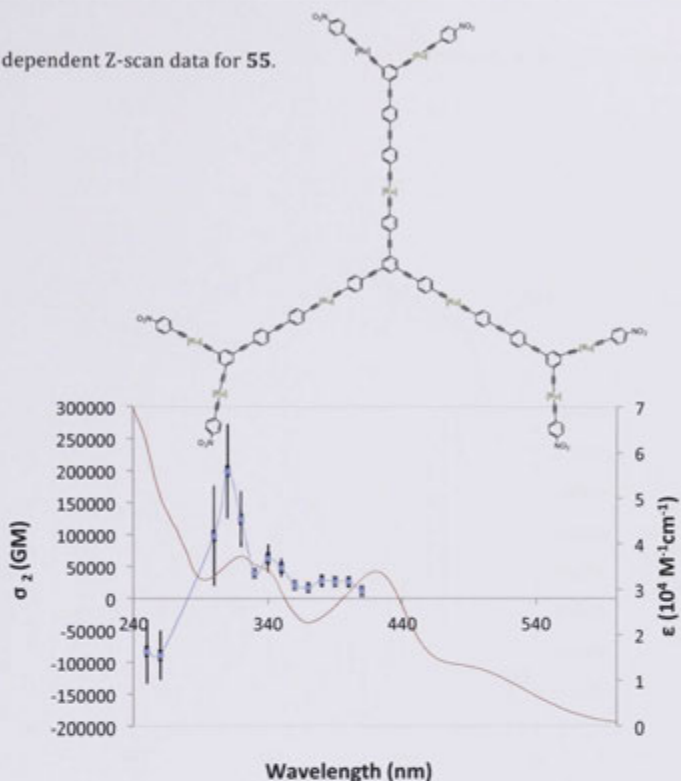
Spectral dependent Z-scan data **54**.

TPA cross-section plot (blue) of **54** plotted at half the measurement wavelength overlaid on the UV-Vis spectrum (red).

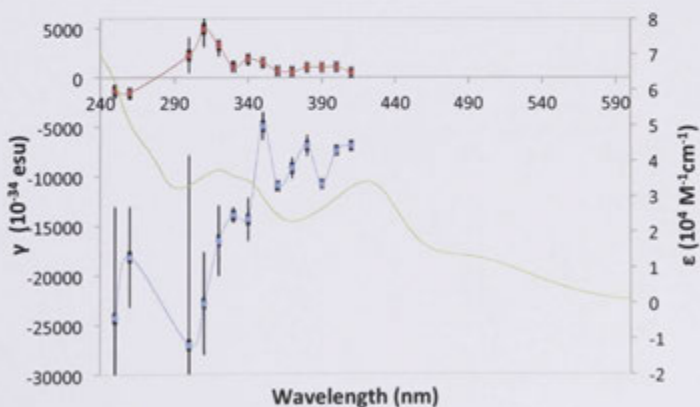


The χ_{real} (blue) and χ_{imag} (red) data of **54** plotted at half the measurement wavelength overlaid on the UV-Vis spectrum (green). A trend line has been added to the χ values to aid observation

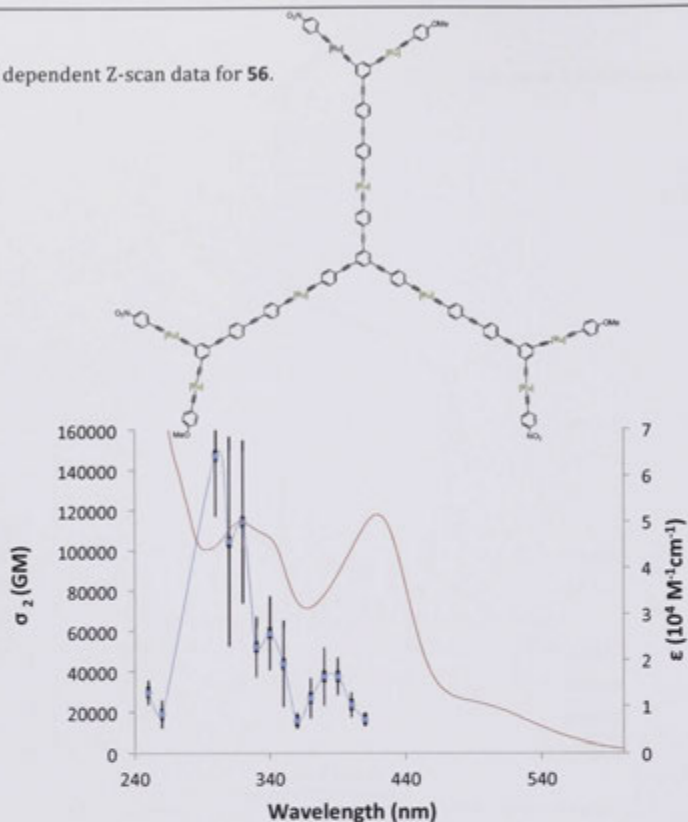
Spectral dependent Z-scan data for **55**.



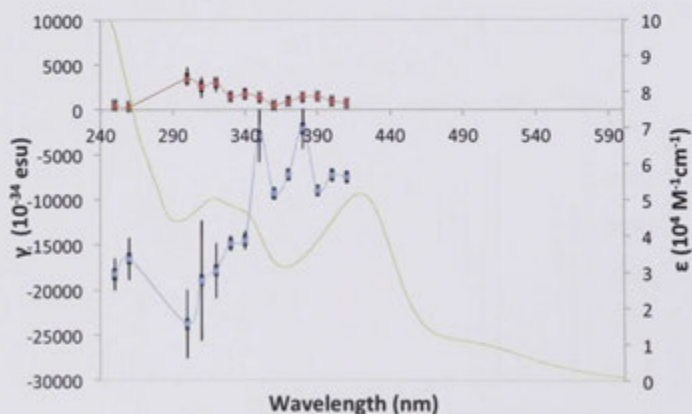
TPA cross-section plot (blue) of **55** plotted at half the measurement wavelength overlaid on the UV-Vis spectrum (red).



The γ_{real} (blue) and γ_{imag} (red) data of **55** plotted at half the measurement wavelength overlaid on the UV-Vis spectrum (green). A trend line has been added to the γ values to aid observation

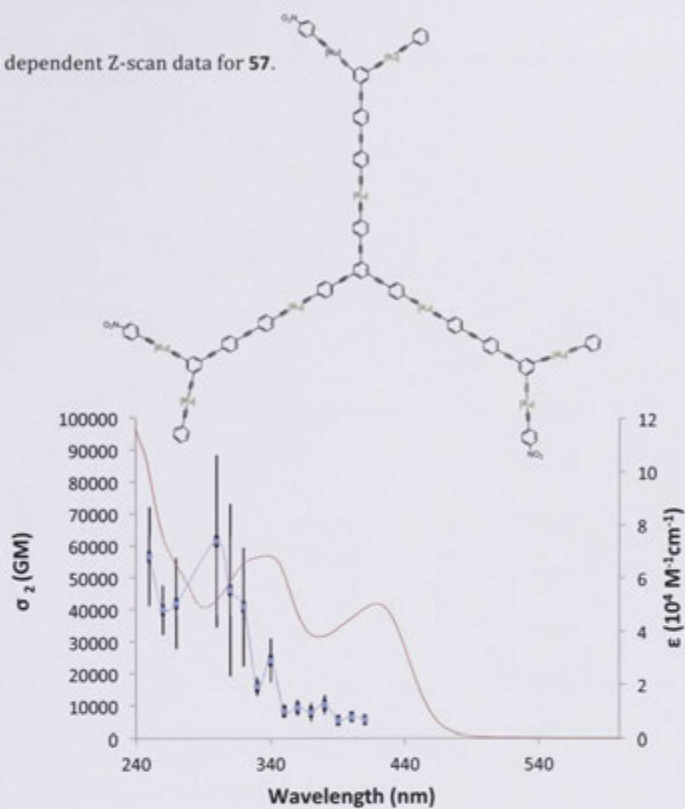
Spectral dependent Z-scan data for **56**.

TPA cross-section plot (blue) of **56** plotted at half the measurement wavelength overlaid on the UV-Vis spectrum (red).

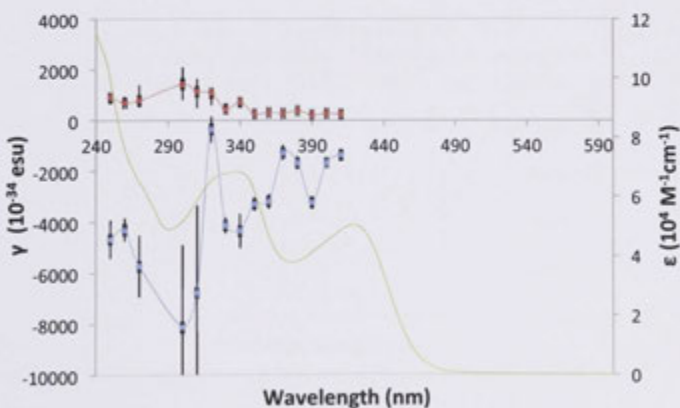


The γ_{real} (blue) and γ_{imag} (red) data of **56** plotted at half the measurement wavelength overlaid on the UV-Vis spectrum (green). A trend line has been added to the γ values to aid observation

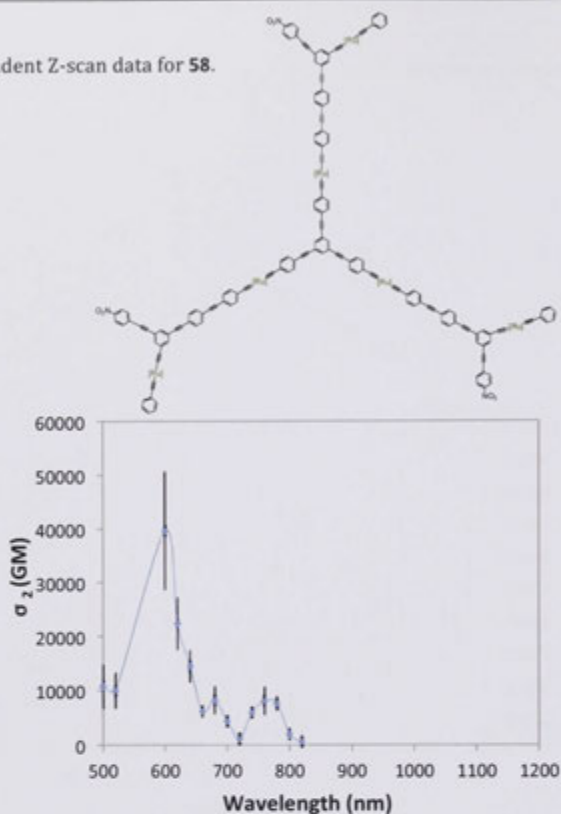
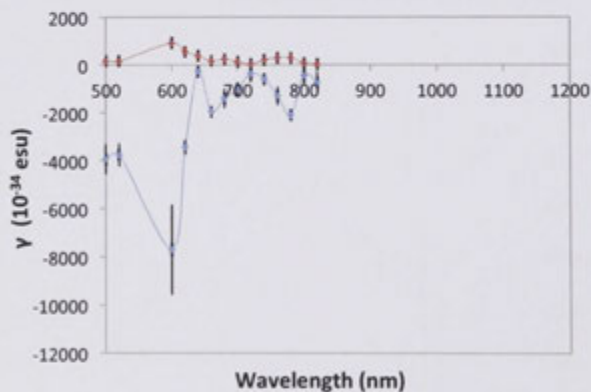
Spectral dependent Z-scan data for **57**.



TPA cross-section plot (blue) of **57** plotted at half the measurement wavelength overlaid on the UV-Vis spectrum (red).

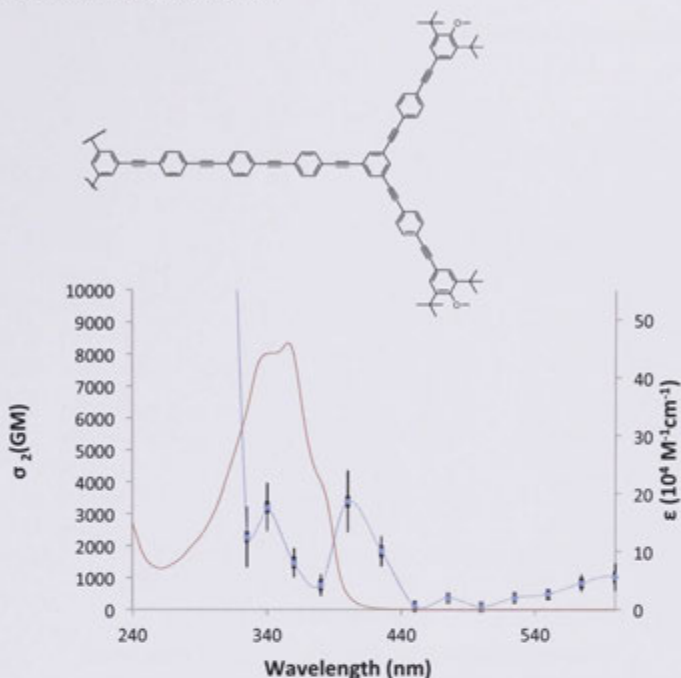


The γ_{real} (blue) and γ_{imag} (red) data of **57** plotted at half the measurement wavelength overlaid on the UV-Vis spectrum (green). A trend line has been added to the γ values to aid observation

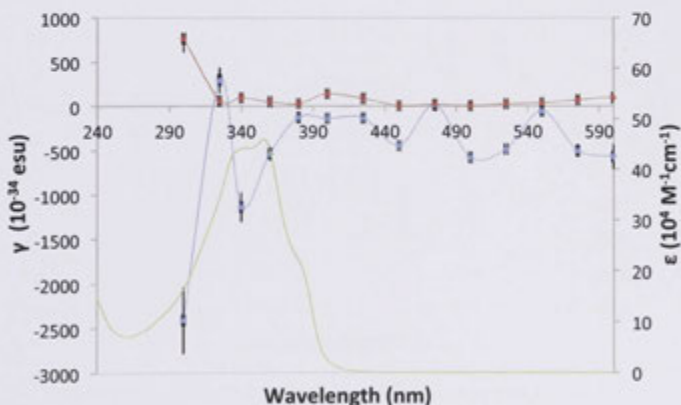
Spectral dependent Z-scan data for **58**.TPA cross-section plot of **58** plotted from 500 - 850 nm.

The γ_{real} (blue) and γ_{imag} (red) data of **58**. A trend line has been added to the γ values to aid observation.

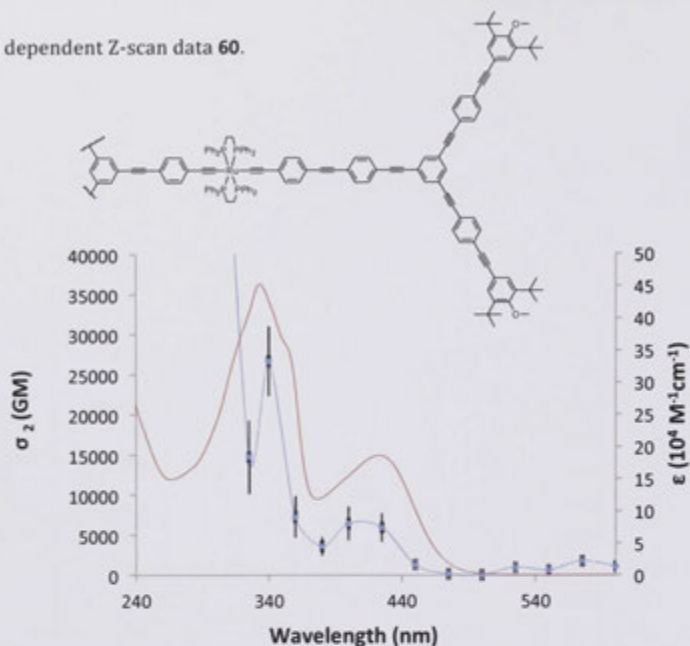
Spectral dependent Z-scan data for **59**.



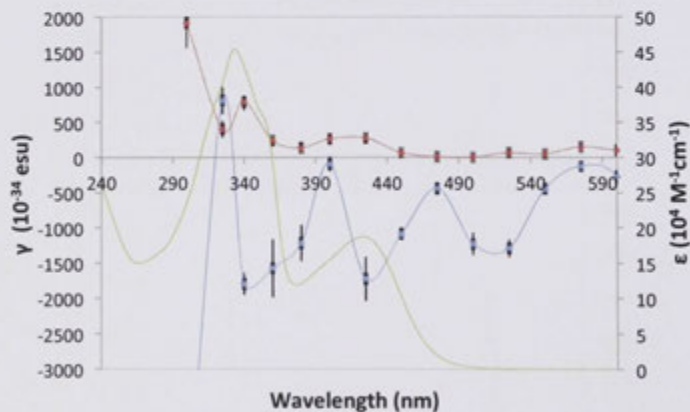
TPA cross-section plot (blue) of **59** plotted at half the measurement wavelength overlaid on the UV-Vis spectrum (red).



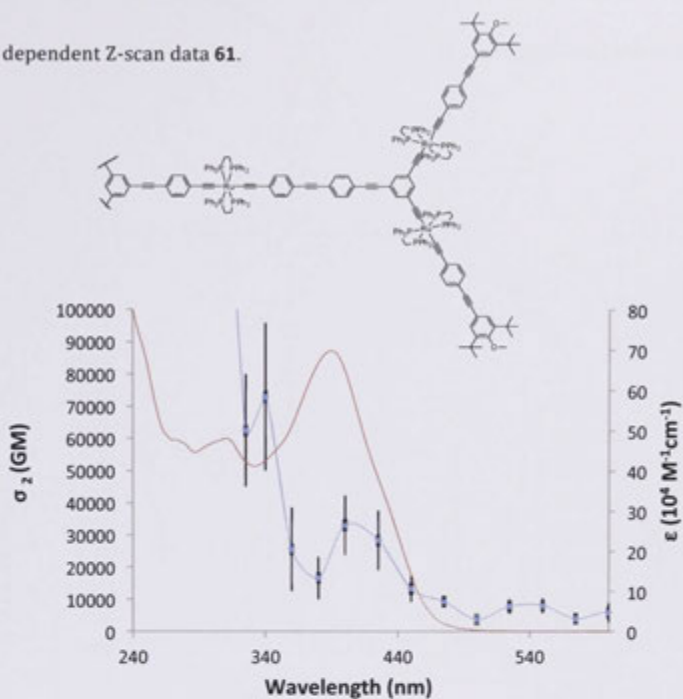
The γ_{real} (blue) and γ_{imag} (red) data of **59** plotted at half the measurement wavelength overlaid on the UV-Vis spectrum (green). A trend line has been added to the γ values to aid observation

Spectral dependent Z-scan data **60**.

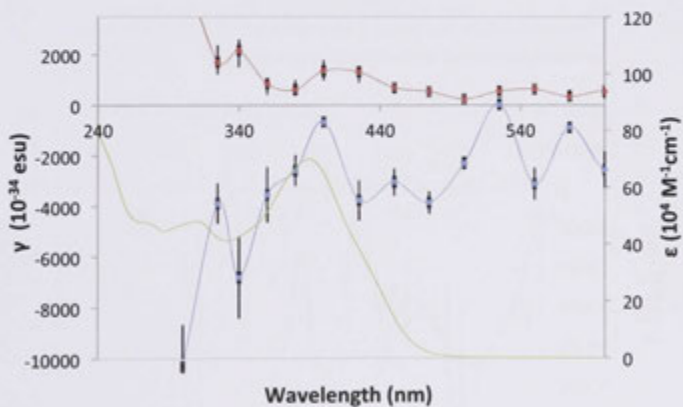
TPA cross-section plot (blue) of **60** plotted at half the measurement wavelength overlaid on the UV-Vis spectrum (red).



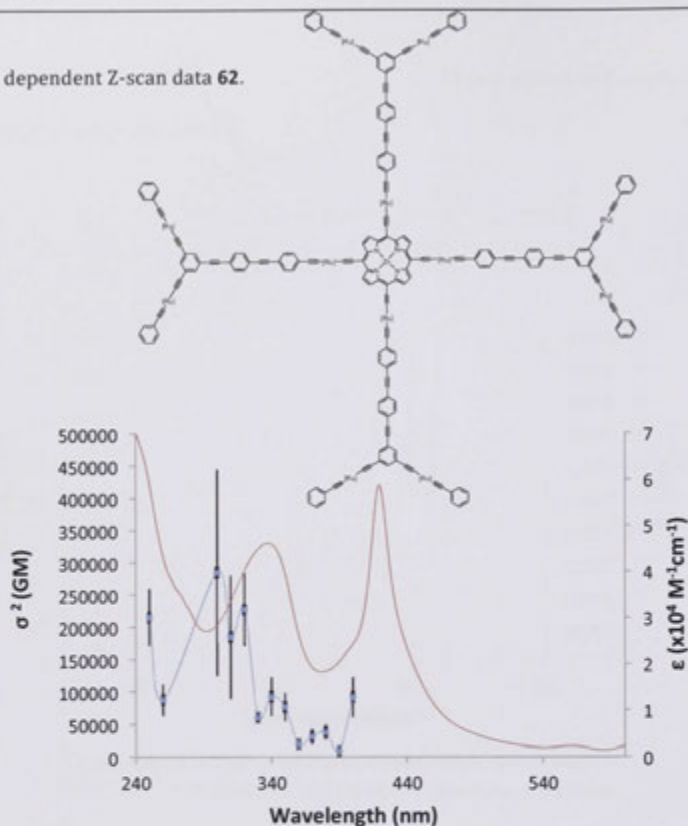
The γ_{real} (blue) and γ_{imag} (red) data of **60** plotted at half the measurement wavelength overlaid on the UV-Vis spectrum (green). A trend line has been added to the γ values to aid observation

Spectral dependent Z-scan data **61**.

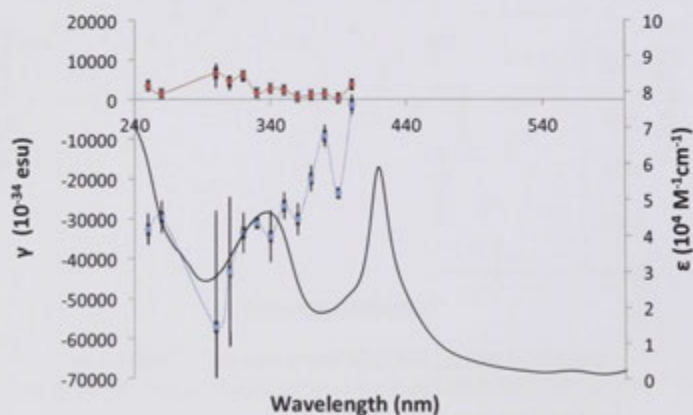
TPA cross-section plot (blue) of **61** plotted at half the measurement wavelength overlaid on the UV-Vis spectrum (red).



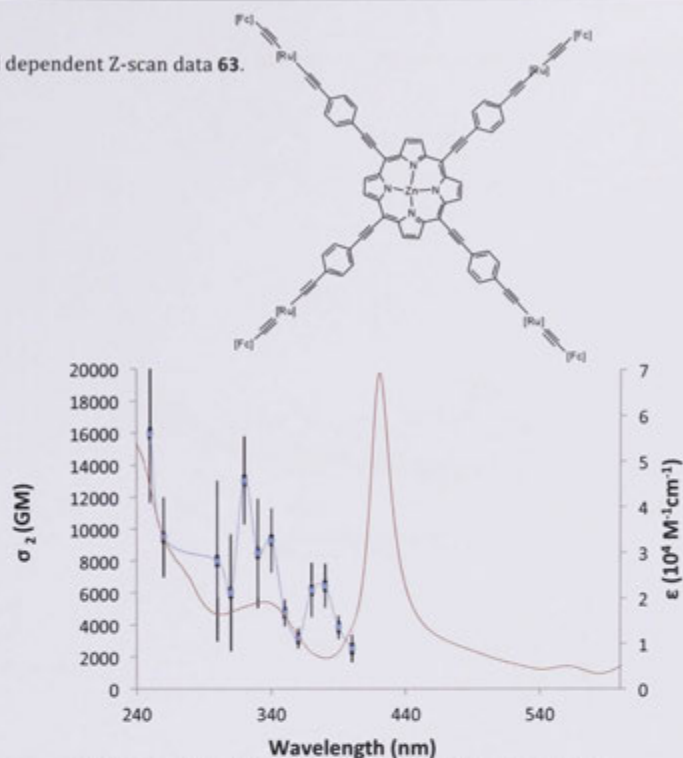
The γ_{real} (blue) and γ_{imag} (red) data of **61** plotted at half the measurement wavelength overlaid on the UV-Vis spectrum (green). A trend line has been added to the γ values to aid observation

Spectral dependent Z-scan data **62**.

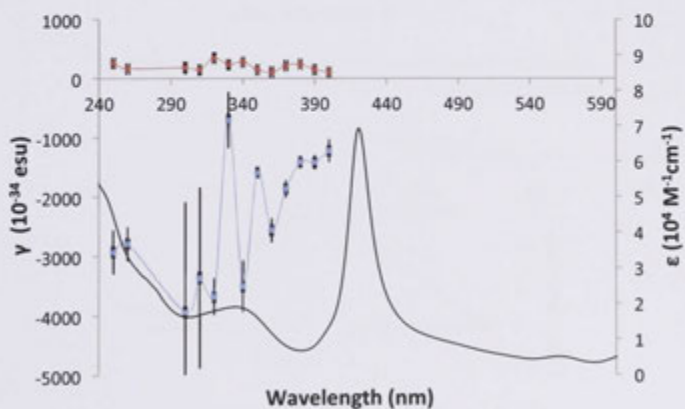
TPA cross-section plot (blue) of **62** plotted at half the measurement wavelength overlaid on the UV-Vis spectrum (red).



The χ_{real} (blue) and χ_{imag} (red) data of **61** plotted at half the measurement wavelength overlaid on the UV-Vis spectrum (green). A trend line has been added to the χ values to aid observation

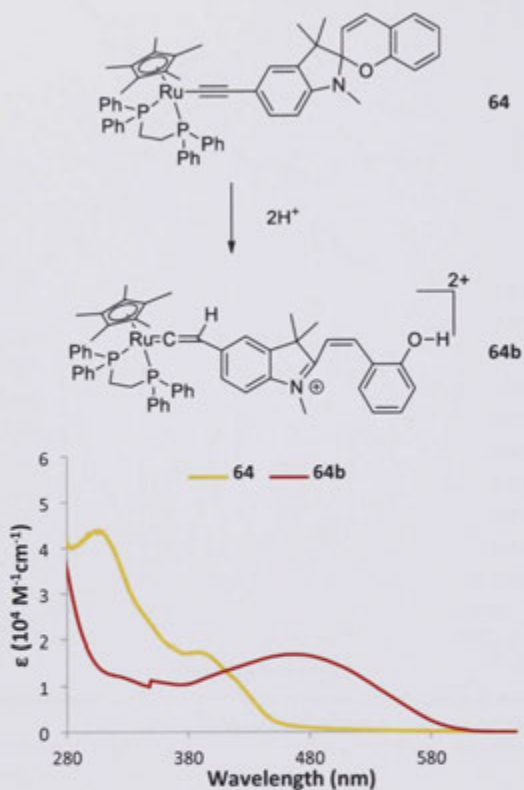
Spectral dependent Z-scan data **63**.

TPA cross-section plot (blue) of **63** plotted at half the measurement wavelength overlaid on the UV-Vis spectrum (red).

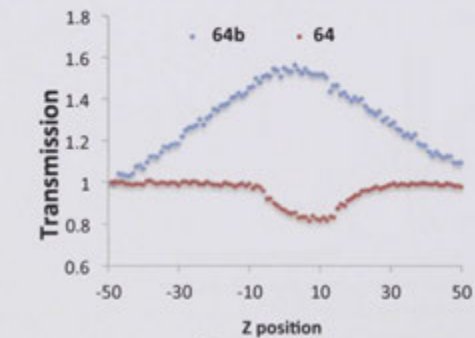


The χ_{real} (blue) and χ_{imag} (red) data of **63** plotted at half the measurement wavelength overlaid on the UV-Vis spectrum (black). A trend line has been added to the χ values to aid observation

UV-VIs and open aperture experiment traces of **64** and **64a**.

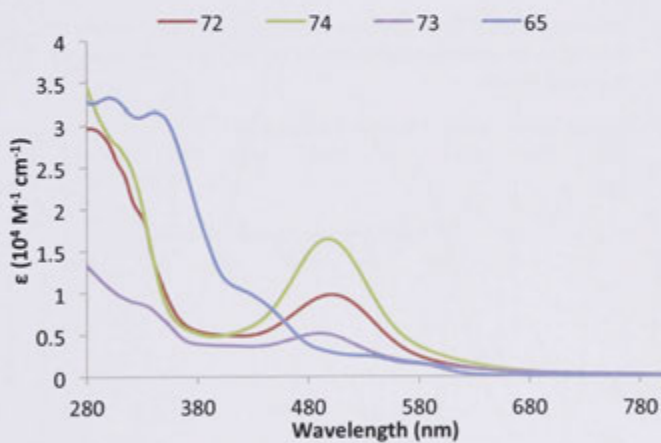
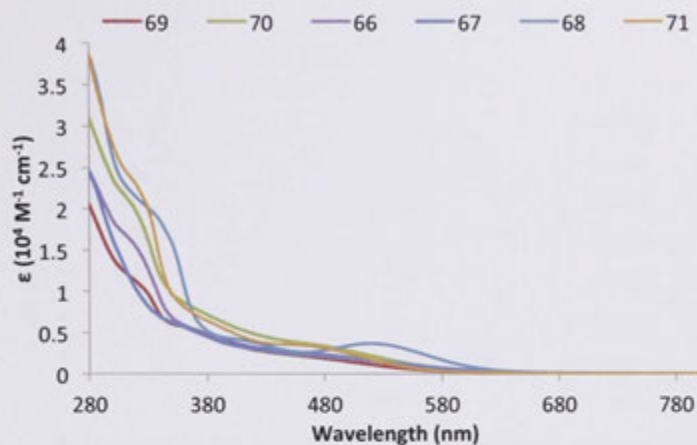


Scheme for the conversion of **64** to **64b** (top) and the UV-VIs of **64** and **64b** (bottom).



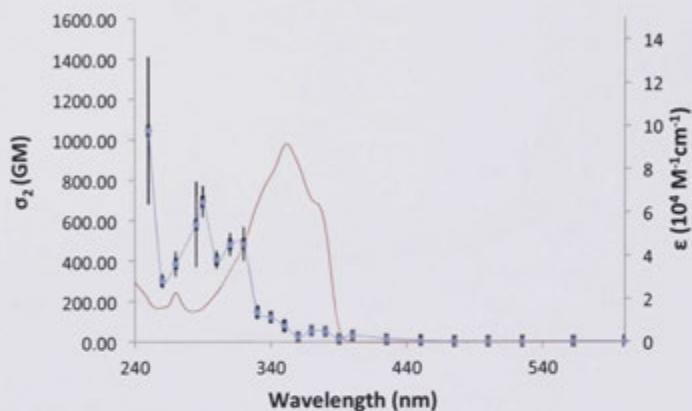
Open aperture traces of **64** and **64b**.

UV-Vis of complexes 65-74

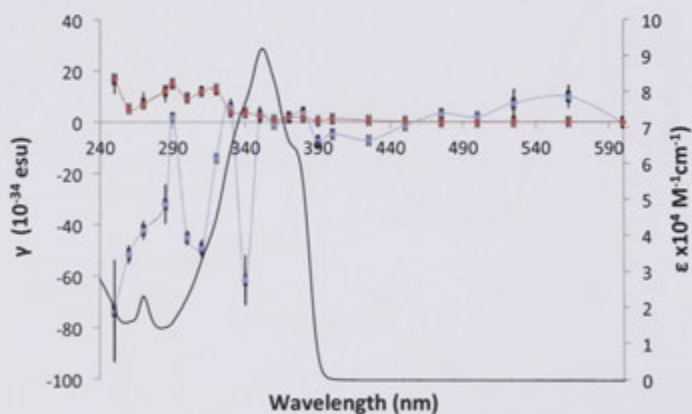


4.2.2 Chapter 3 NLO data

Spectral dependent Z-scan data for **26** (75 mm).

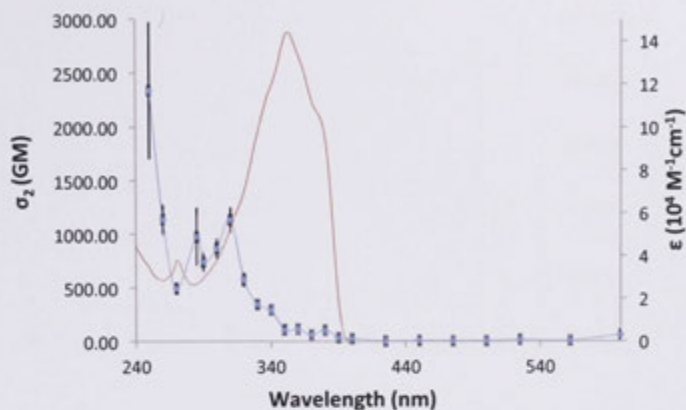


TPA cross section of **26** (blue) plotted at half the measurement wavelength overlaid on UV-vis spectrum (red). A trend line has been added to the TPA as a visual aid only.

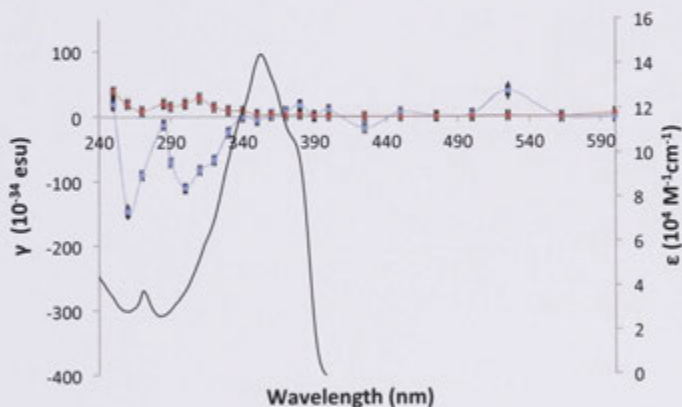


The γ_{real} (blue) and γ_{imag} (red) data of **26** plotted at half the measurement wavelength overlaid on the UV-Vis spectrum (black). A trend line has been added to the γ values to aid observation.

Spectral dependent Z-scan data for **29** (75 mm).

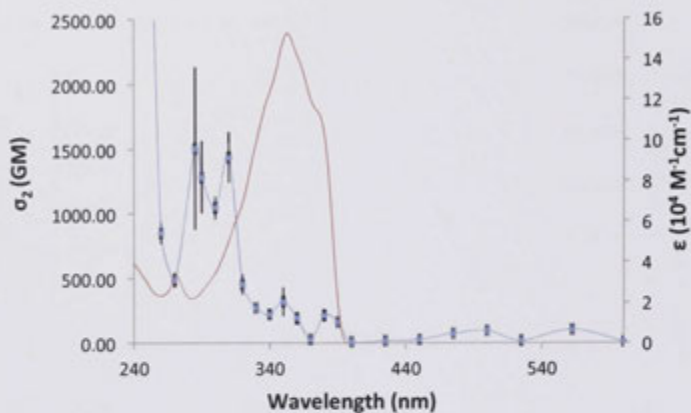


TPA cross section of **29** (blue) plotted at half the measurement wavelength overlaid on UV-vis spectrum (red). A trend line has been added to the TPA as a visual aid only.

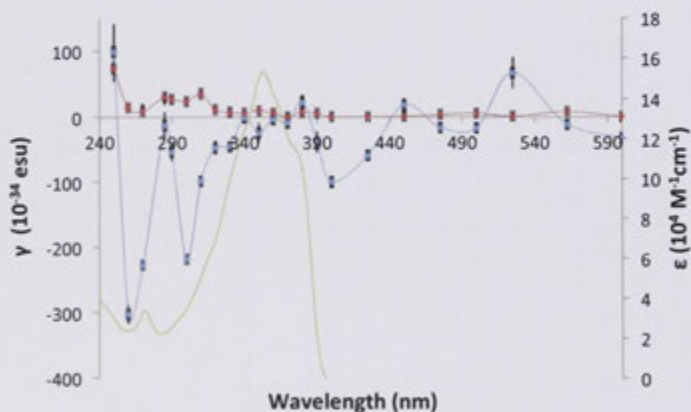


The γ_{real} (blue) and γ_{imag} (red) data of **29** plotted at half the measurement wavelength overlaid on the UV-Vis spectrum (black). A trend line has been added to the γ values to aid observation

Spectral dependent Z-scan data for **32** (75 mm).

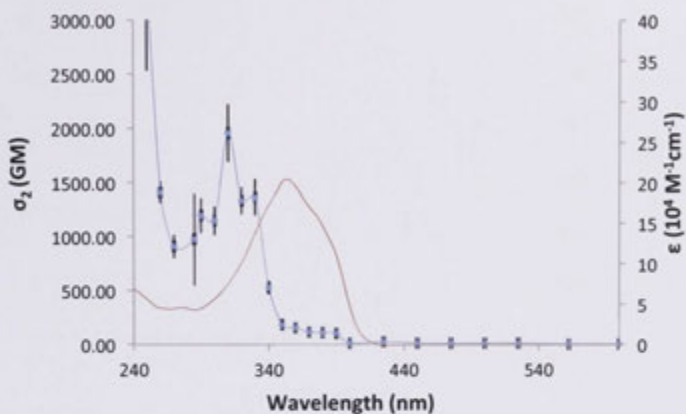


TPA cross section of **32** (blue) plotted at half the measurement wavelength overlaid on UV-vis spectrum (red). A trend line has been added to the TPA as a visual aid only.

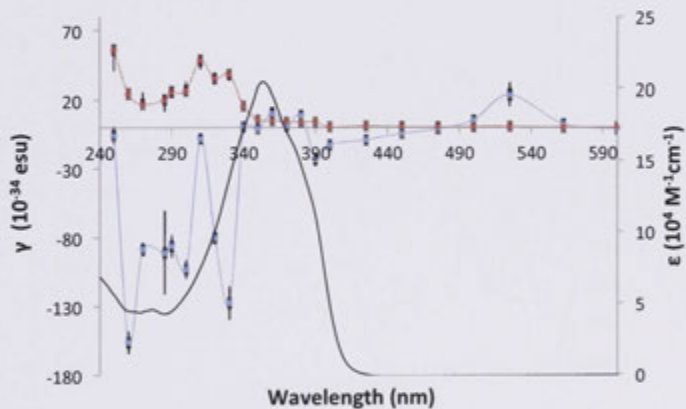


The γ_{real} (blue) and γ_{imag} (red) data of **32** plotted at half the measurement wavelength overlaid on the UV-Vis spectrum (black). A trend line has been added to the γ values to aid observation

Spectral dependent Z-scan data for **38** (75 mm).

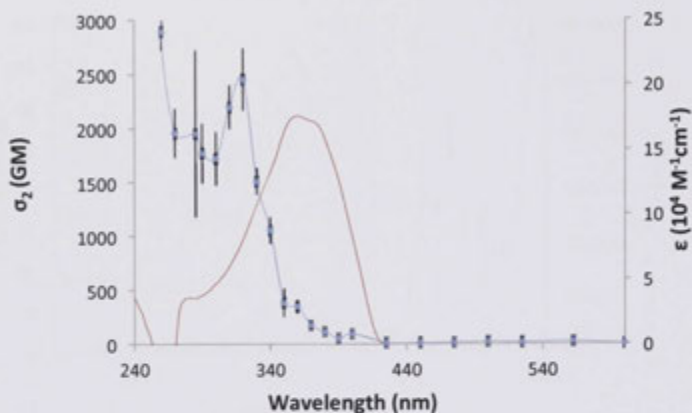


TPA cross section of **38** (blue) plotted at half the measurement wavelength overlaid on UV-vis spectrum (red). A trend line has been added to the TPA as a visual aid only.

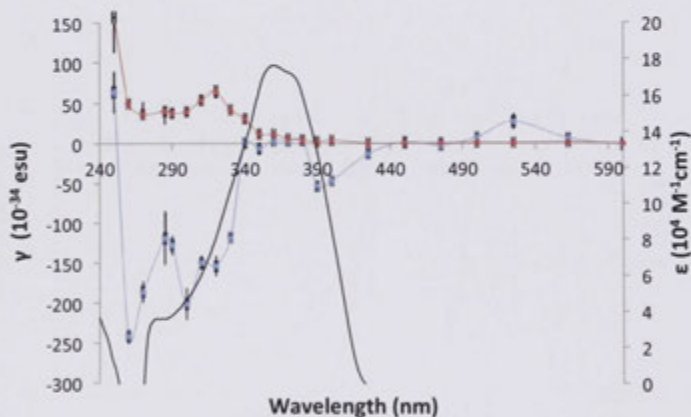


The γ_{real} (blue) and γ_{imag} (red) data of **38** plotted at half the measurement wavelength overlaid on the UV-Vis spectrum (black). A trend line has been added to the γ values to aid observation

Spectral dependent Z-scan data for **41** (75 mm).

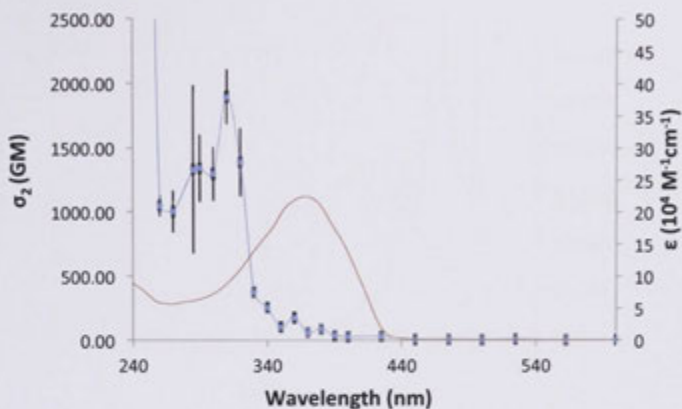


TPA cross section of **41** (blue) plotted at half the measurement wavelength overlaid on UV-vis spectrum (red). A trend line has been added to the TPA as a visual aid only.

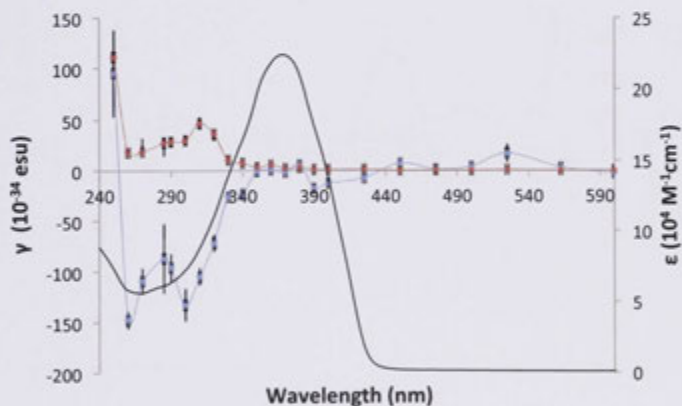


The γ_{real} (blue) and γ_{imag} (red) data of **41** plotted at half the measurement wavelength overlaid on the UV-Vis spectrum (black). A trend line has been added to the γ values to aid observation

Spectral dependent Z-scan data for **44** (75 mm).

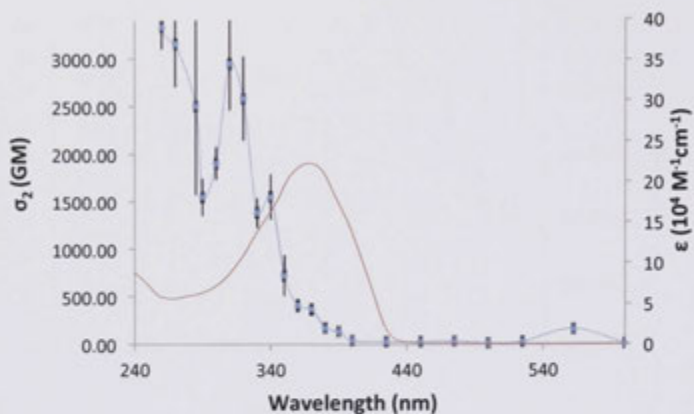


TPA cross section of **44** (blue) plotted at half the measurement wavelength overlaid on UV-vis spectrum (red). A trend line has been added to the TPA as a visual aid only.

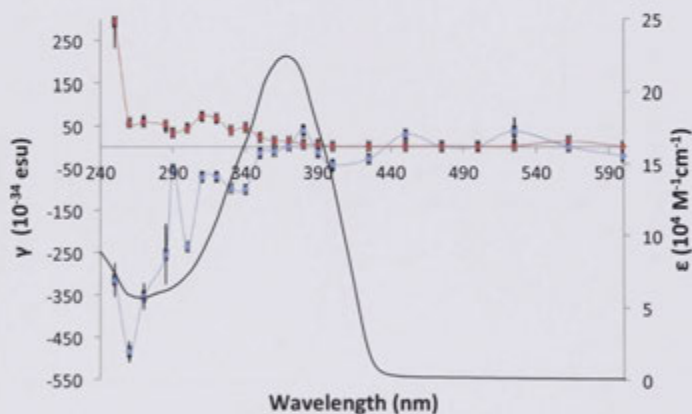


The γ_{real} (blue) and γ_{imag} (red) data of **44** plotted at half the measurement wavelength overlaid on the UV-Vis spectrum (black). A trend line has been added to the γ values to aid observation

Spectral dependent Z-scan data for **47** (75 mm).

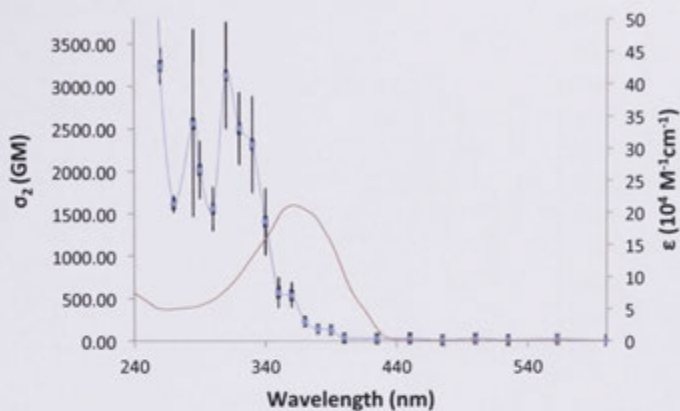


TPA cross section of **47** (blue) plotted at half the measurement wavelength overlaid on UV-vis spectrum (red). A trend line has been added to the TPA as a visual aid only.

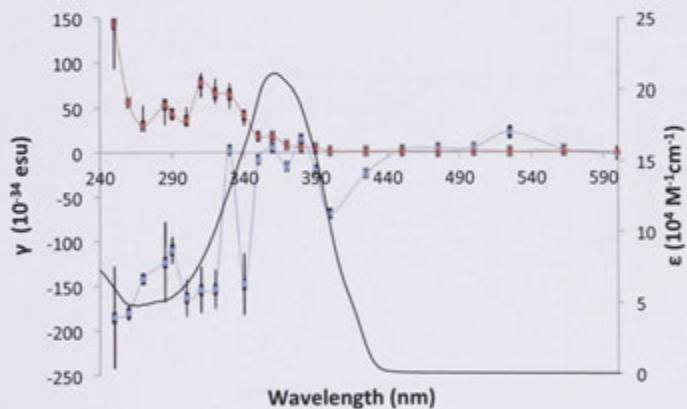


The γ_{real} (blue) and γ_{imag} (red) data of **47** plotted at half the measurement wavelength overlaid on the UV-Vis spectrum (black). A trend line has been added to the γ values to aid observation

Spectral dependent Z-scan data for **50** (75 mm).

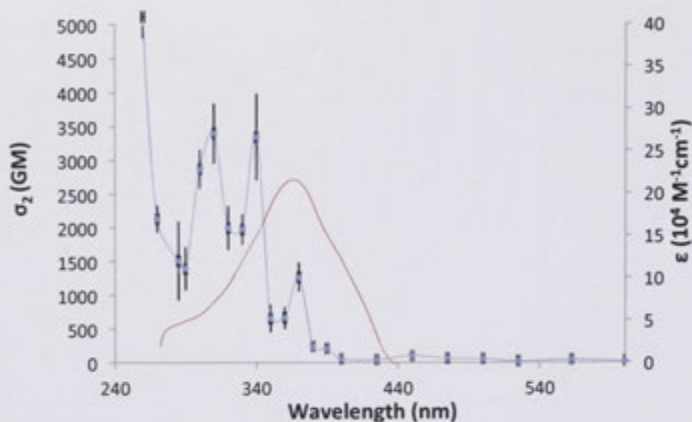


TPA cross section of **50** (blue) plotted at half the measurement wavelength overlaid on UV-vis spectrum (red). A trend line has been added to the TPA as a visual aid only.

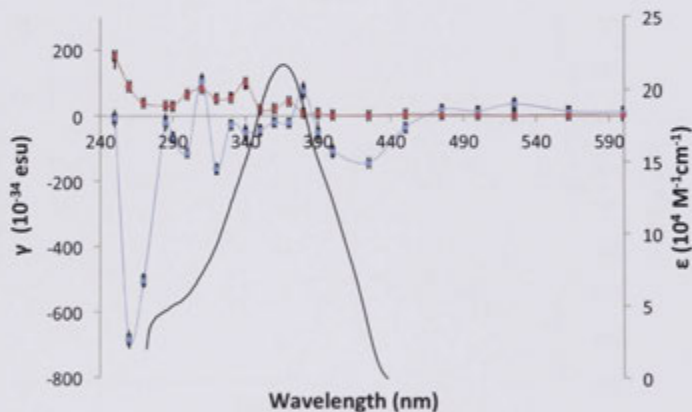


The χ_3^{real} (blue) and χ_3^{imag} (red) data of **50** plotted at half the measurement wavelength overlaid on the UV-Vis spectrum (black). A trend line has been added to the χ values to aid observation

Spectral dependent Z-scan data for **53** (75 mm).

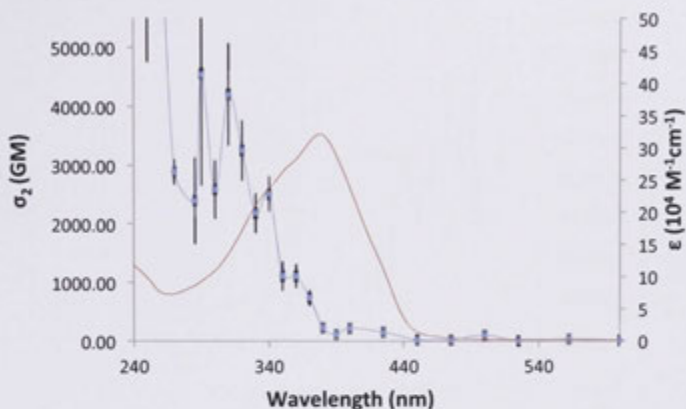


TPA cross section of **53** (blue) plotted at half the measurement wavelength overlaid on UV-vis spectrum (red). A trend line has been added to the TPA as a visual aid only.

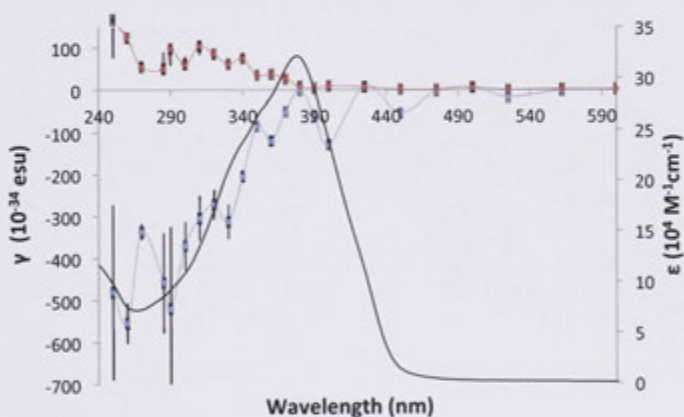


The γ_{real} (blue) and γ_{imag} (red) data of **53** plotted at half the measurement wavelength overlaid on the UV-Vis spectrum (black). A trend line has been added to the γ values to aid observation

Spectral dependent Z-scan data for **56** (75 mm).

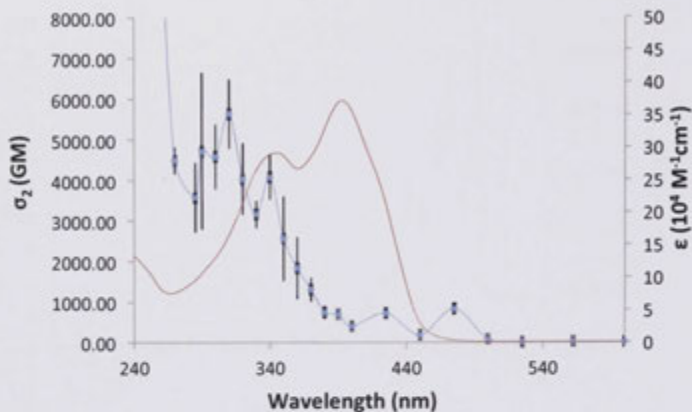


TPA cross section of **56** (blue) plotted at half the measurement wavelength overlaid on UV-vis spectrum (red). A trend line has been added to the TPA as a visual aid only.

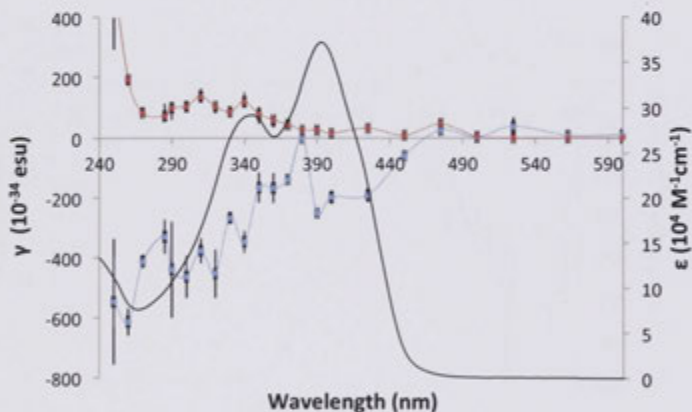


The χ_{real} (blue) and χ_{imag} (red) data of **56** plotted at half the measurement wavelength overlaid on the UV-Vis spectrum (black). A trend line has been added to the χ values to aid observation

Spectral dependent Z-scan data for **59** (75 mm).

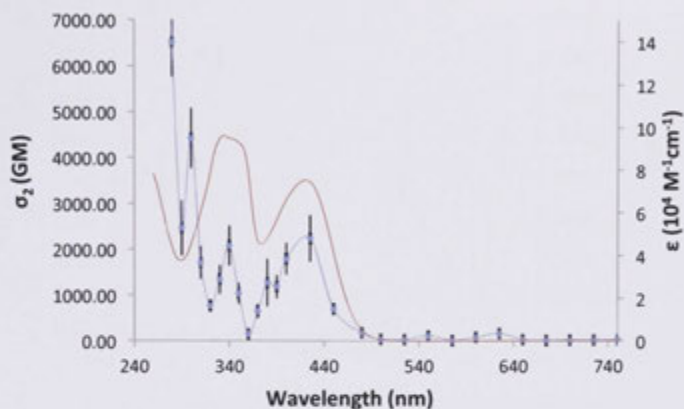


TPA cross section of **59** (blue) plotted at half the measurement wavelength overlaid on UV-vis spectrum (red). A trend line has been added to the TPA as a visual aid only.

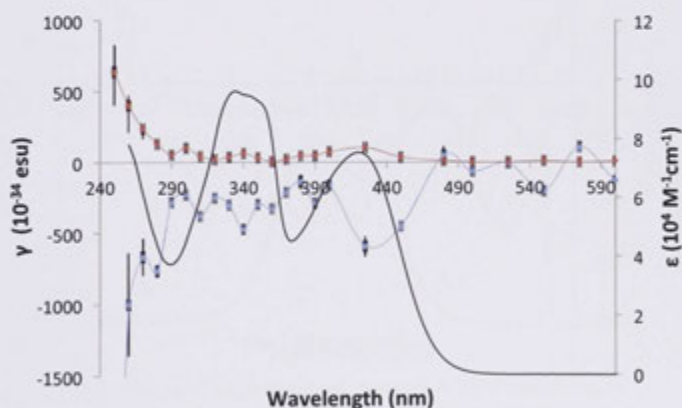


The γ_{real} (blue) and γ_{imag} (red) data of **59** plotted at half the measurement wavelength overlaid on the UV-Vis spectrum (black). A trend line has been added to the γ values to aid observation

Spectral dependent Z-scan data for **28** (120 nm).

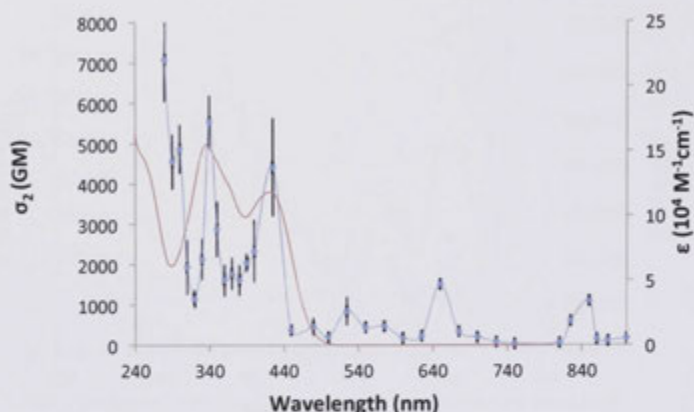


TPA cross section of **28** (blue) plotted at half the measurement wavelength overlaid on UV-vis spectrum (red). A trend line has been added to the TPA as a visual aid only.

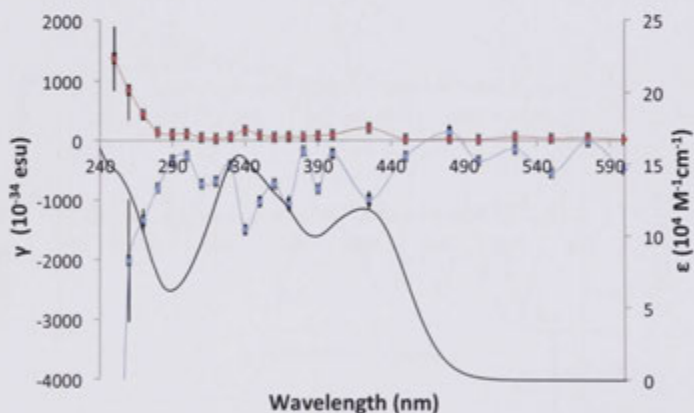


The γ_{real} (blue) and γ_{imag} (red) data of **28** plotted at half the measurement wavelength overlaid on the UV-Vis spectrum (black). A trend line has been added to the γ values to aid observation

Spectral dependent Z-scan data for **31** (120 mm).

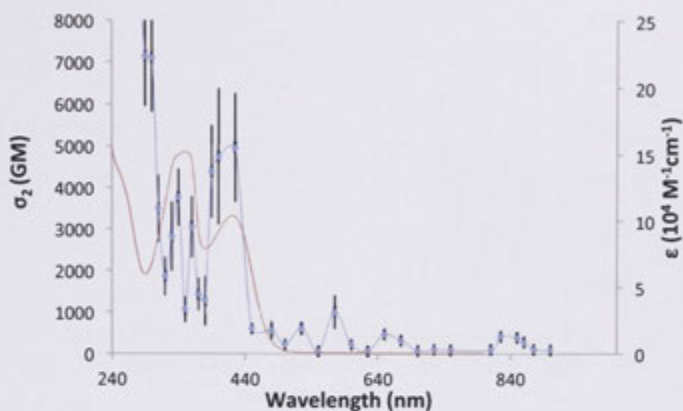


TPA cross section of **31** (blue) plotted at half the measurement wavelength overlaid on UV-vis spectrum (red). A trend line has been added to the TPA as a visual aid only.

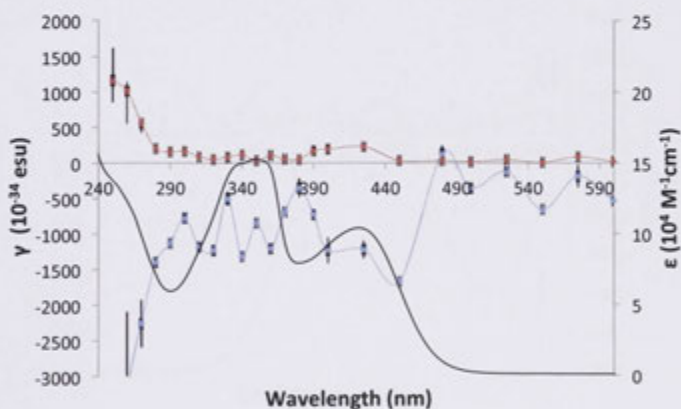


The γ_{real} (blue) and γ_{imag} (red) data of **31** plotted at half the measurement wavelength overlaid on the UV-Vis spectrum (black). A trend line has been added to the γ values to aid observation

Spectral dependent Z-scan data for **34** (120 mm).

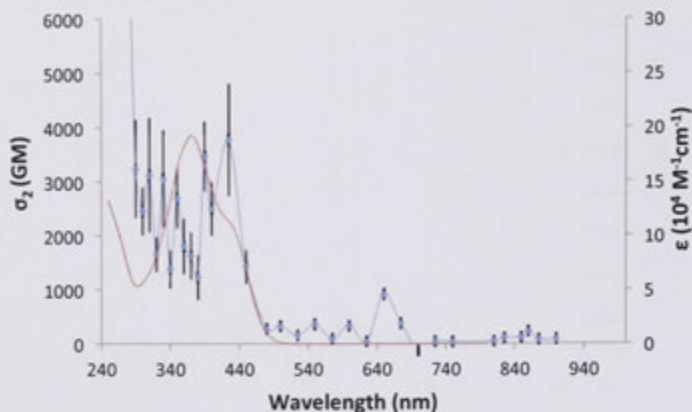


TPA cross section of **34** (blue) plotted at half the measurement wavelength overlaid on UV-vis spectrum (red). A trend line has been added to the TPA as a visual aid only.

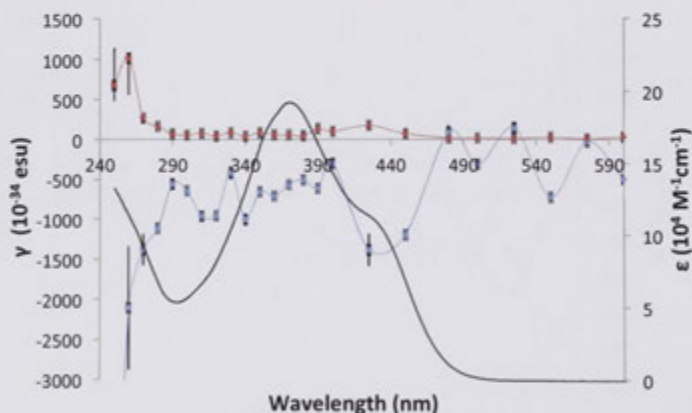


The χ_{real} (blue) and χ_{imag} (red) data of **34** plotted at half the measurement wavelength overlaid on the UV-Vis spectrum (black). A trend line has been added to the χ values to aid observation

Spectral dependent Z-scan data for **37** (120 mm).

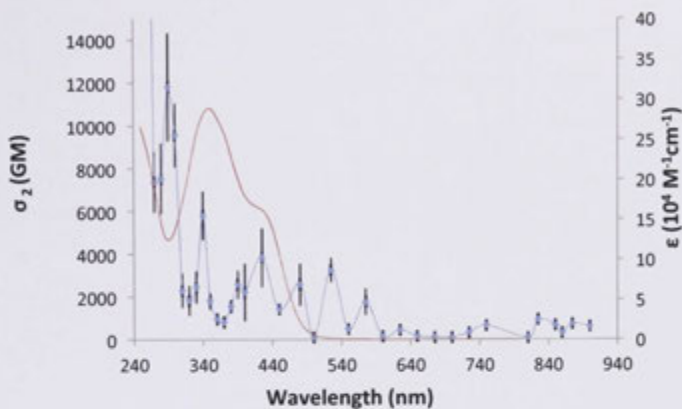


TPA cross section of **37** (blue) plotted at half the measurement wavelength overlaid on UV-vis spectrum (red). A trend line has been added to the TPA as a visual aid only.

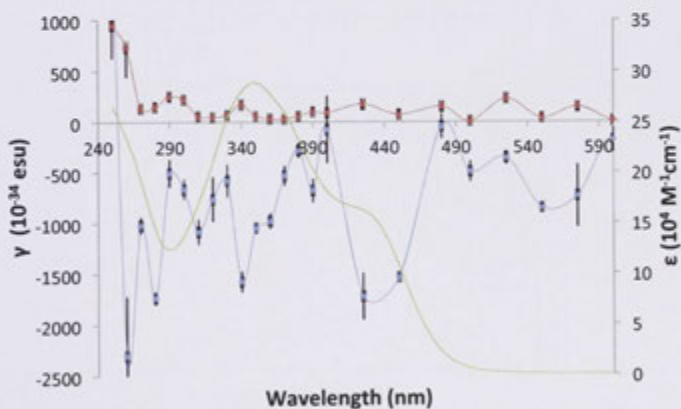


The γ_{real} (blue) and γ_{imag} (red) data of **37** plotted at half the measurement wavelength overlaid on the UV-Vis spectrum (black). A trend line has been added to the γ values to aid observation

Spectral dependent Z-scan data for **40** (120 mm).

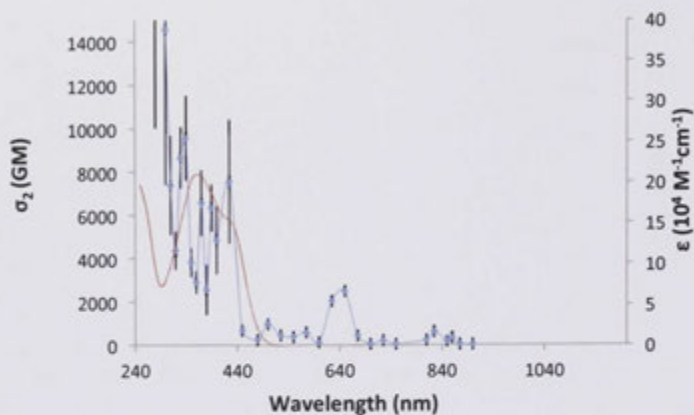


TPA cross section of **40** (blue) plotted at half the measurement wavelength overlaid on UV-vis spectrum (red). A trend line has been added to the TPA as a visual aid only.

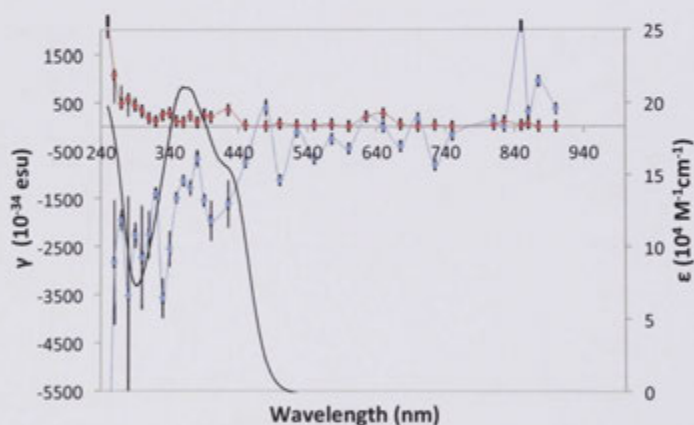


The γ_{real} (blue) and γ_{imag} (red) data of **40** plotted at half the measurement wavelength overlaid on the UV-Vis spectrum (black). A trend line has been added to the γ values to aid observation

Spectral dependent Z-scan data for **43** (120 mm).

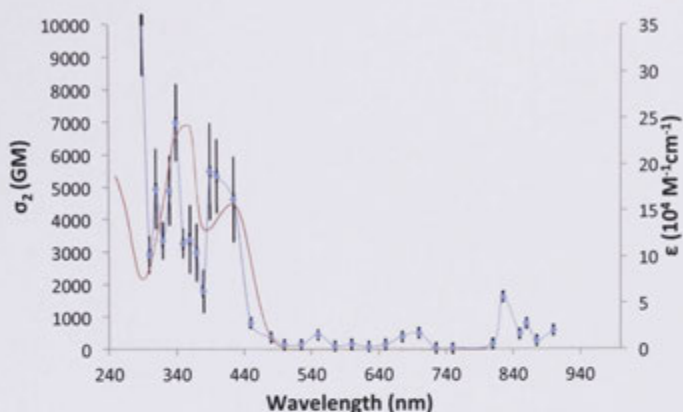


TPA cross section of **43** (blue) plotted at half the measurement wavelength overlaid on UV-vis spectrum (red). A trend line has been added to the TPA as a visual aid only.

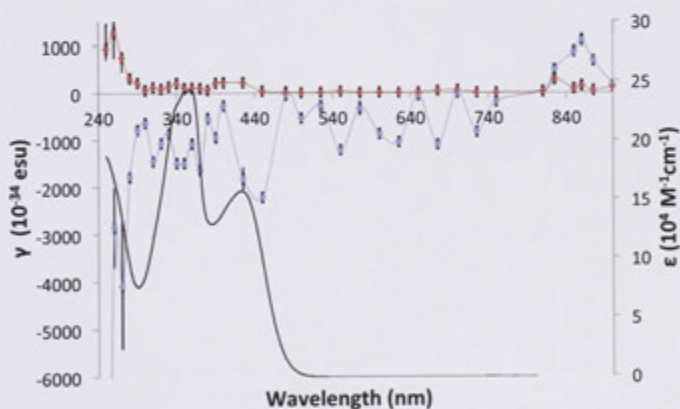


The γ_{real} (blue) and γ_{imag} (red) data of **43** plotted at half the measurement wavelength overlaid on the UV-Vis spectrum (black). A trend line has been added to the γ values to aid observation

Spectral dependent Z-scan data for **46** (120 mm).

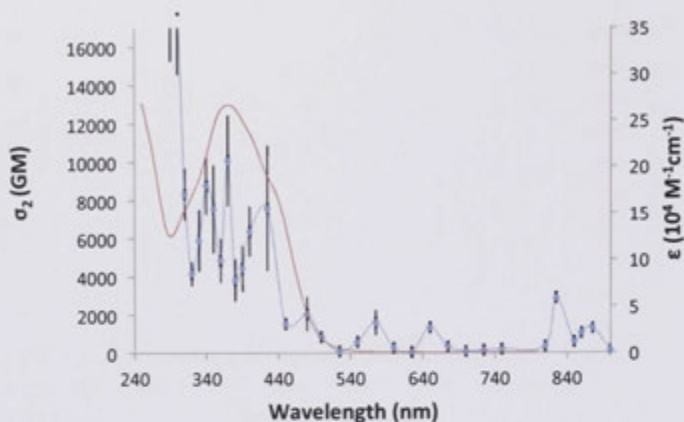


TPA cross section of **46** (blue) plotted at half the measurement wavelength overlaid on UV-vis spectrum (red). A trend line has been added to the TPA as a visual aid only.

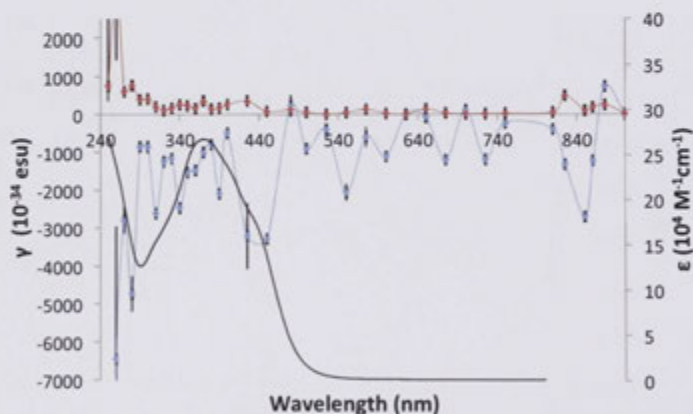


The γ_{real} (blue) and γ_{imag} (red) data of **46** plotted at half the measurement wavelength overlaid on the UV-Vis spectrum (black). A trend line has been added to the γ values to aid observation

Spectral dependent Z-scan data for **49** (120 mm).

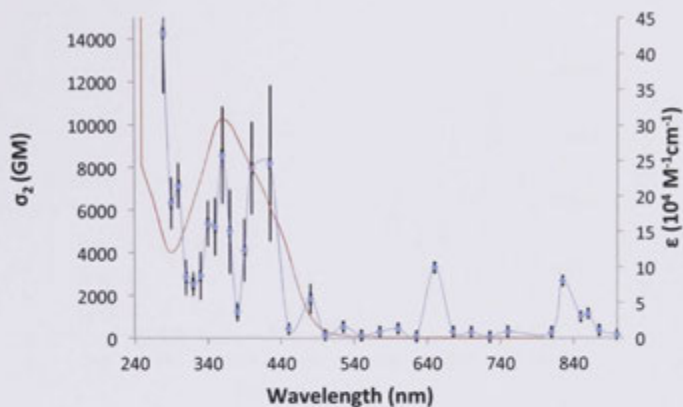


TPA cross section of **49** (blue) plotted at half the measurement wavelength overlaid on UV-vis spectrum (red). A trend line has been added to the TPA as a visual aid only.

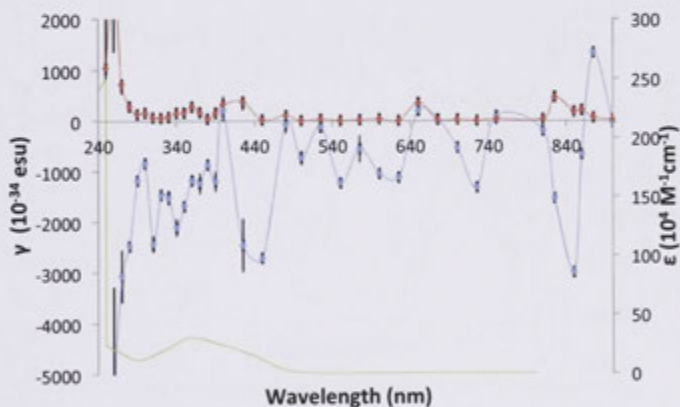


The γ_{real} (blue) and γ_{imag} (red) data of **49** plotted at half the measurement wavelength overlaid on the UV-Vis spectrum (black). A trend line has been added to the γ values to aid observation

Spectral dependent Z-scan data for **52** (120 mm).

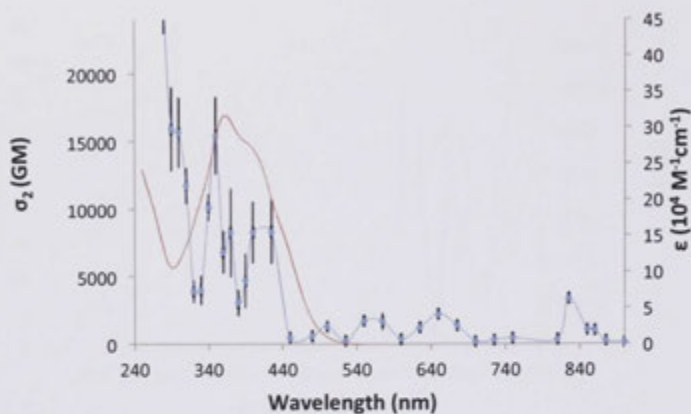


TPA cross section of **52** (blue) plotted at half the measurement wavelength overlaid on UV-vis spectrum (red). A trend line has been added to the TPA as a visual aid only.

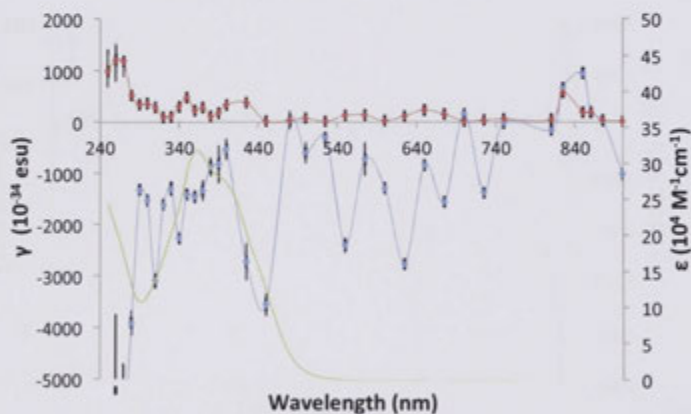


The γ_{real} (blue) and γ_{imag} (red) data of **52** plotted at half the measurement wavelength overlaid on the UV-Vis spectrum (black). A trend line has been added to the γ values to aid observation

Spectral dependent Z-scan data for 55 (120 mm).

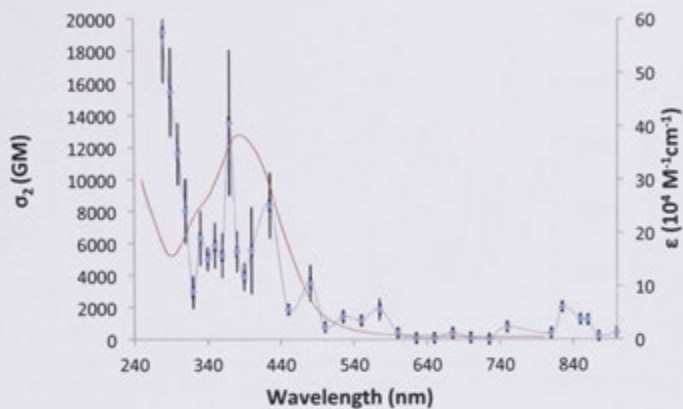


TPA cross section of 55 (blue) plotted at half the measurement wavelength overlaid on UV-vis spectrum (red). A trend line has been added to the TPA as a visual aid only.

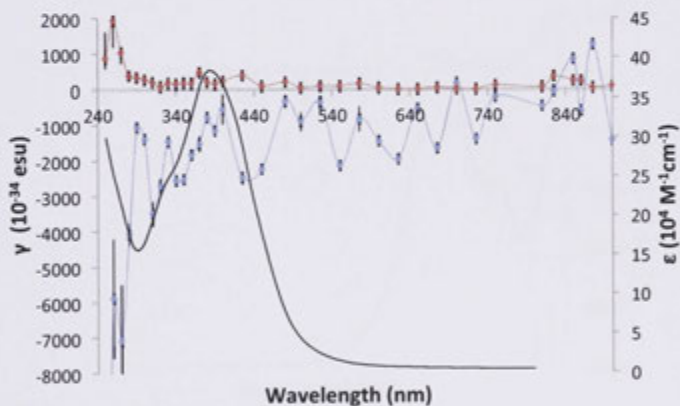


The γ_{real} (blue) and γ_{imag} (red) data of 55 plotted at half the measurement wavelength overlaid on the UV-Vis spectrum (black). A trend line has been added to the γ values to aid observation

Spectral dependent Z-scan data for **58** (120 mm).

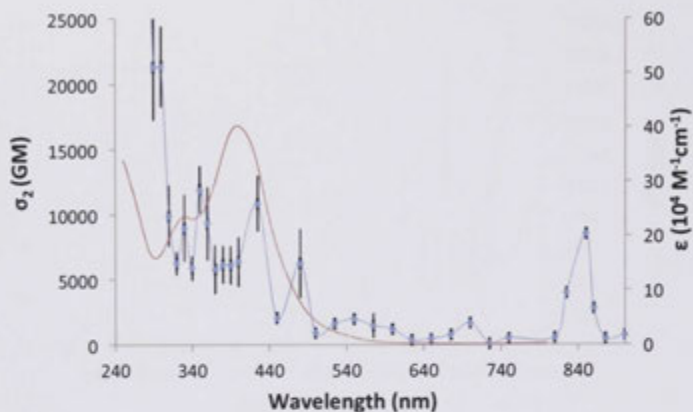


TPA cross section of **58** (blue) plotted at half the measurement wavelength overlaid on UV-vis spectrum (red). A trend line has been added to the TPA as a visual aid only.

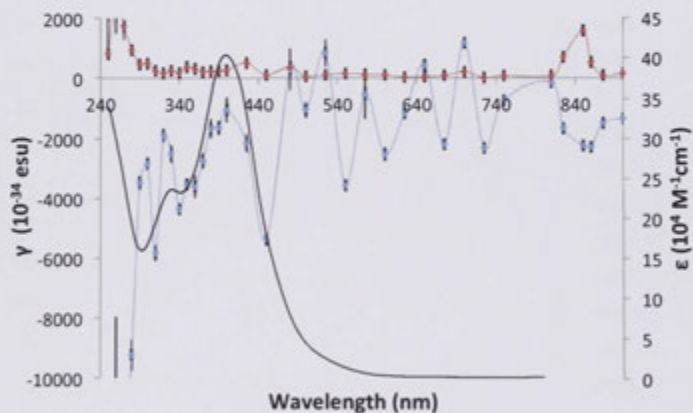


The γ_{real} (blue) and γ_{imag} (red) data of **58** plotted at half the measurement wavelength overlaid on the UV-Vis spectrum (black). A trend line has been added to the γ values to aid observation

Spectral dependent Z-scan data for **61** (120 mm).

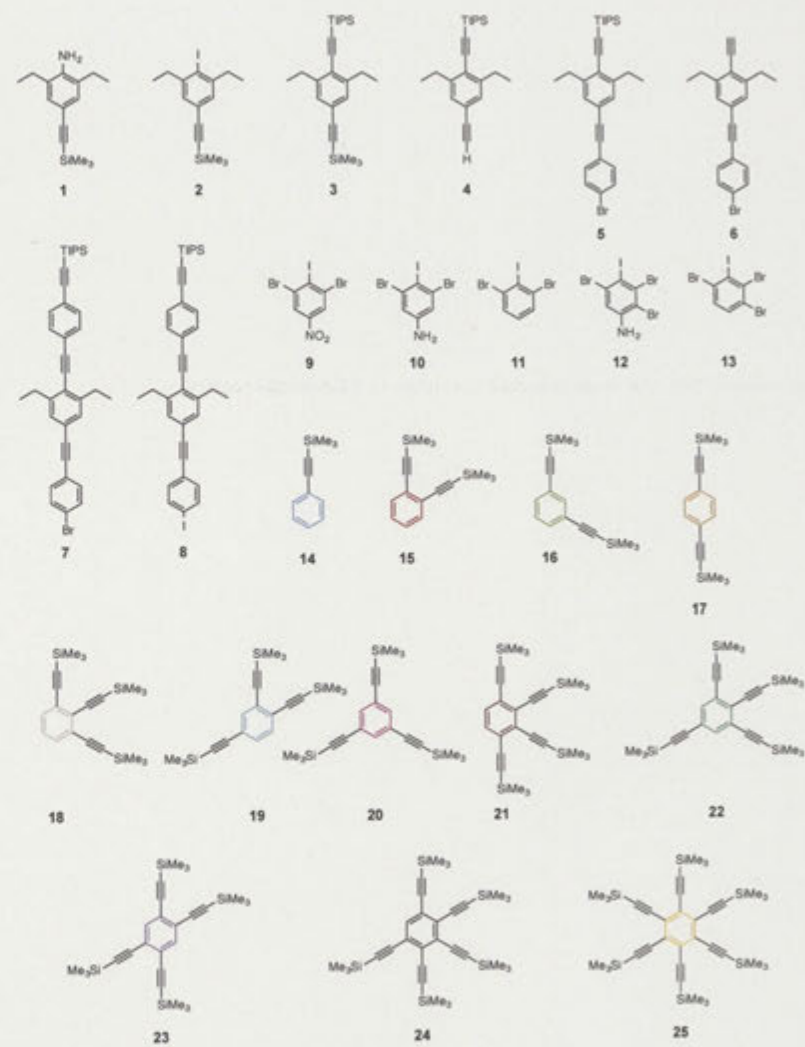


TPA cross section of **61** (blue) plotted at half the measurement wavelength overlaid on UV-vis spectrum (red). A trend line has been added to the TPA as a visual aid only.



The γ_{real} (blue) and γ_{imag} (red) data of **61** plotted at half the measurement wavelength overlaid on the UV-Vis spectrum (black). A trend line has been added to the γ values to aid observation

Foldout Figure 4.3.1 Structures of Compounds in Core Modification Series – Part 1



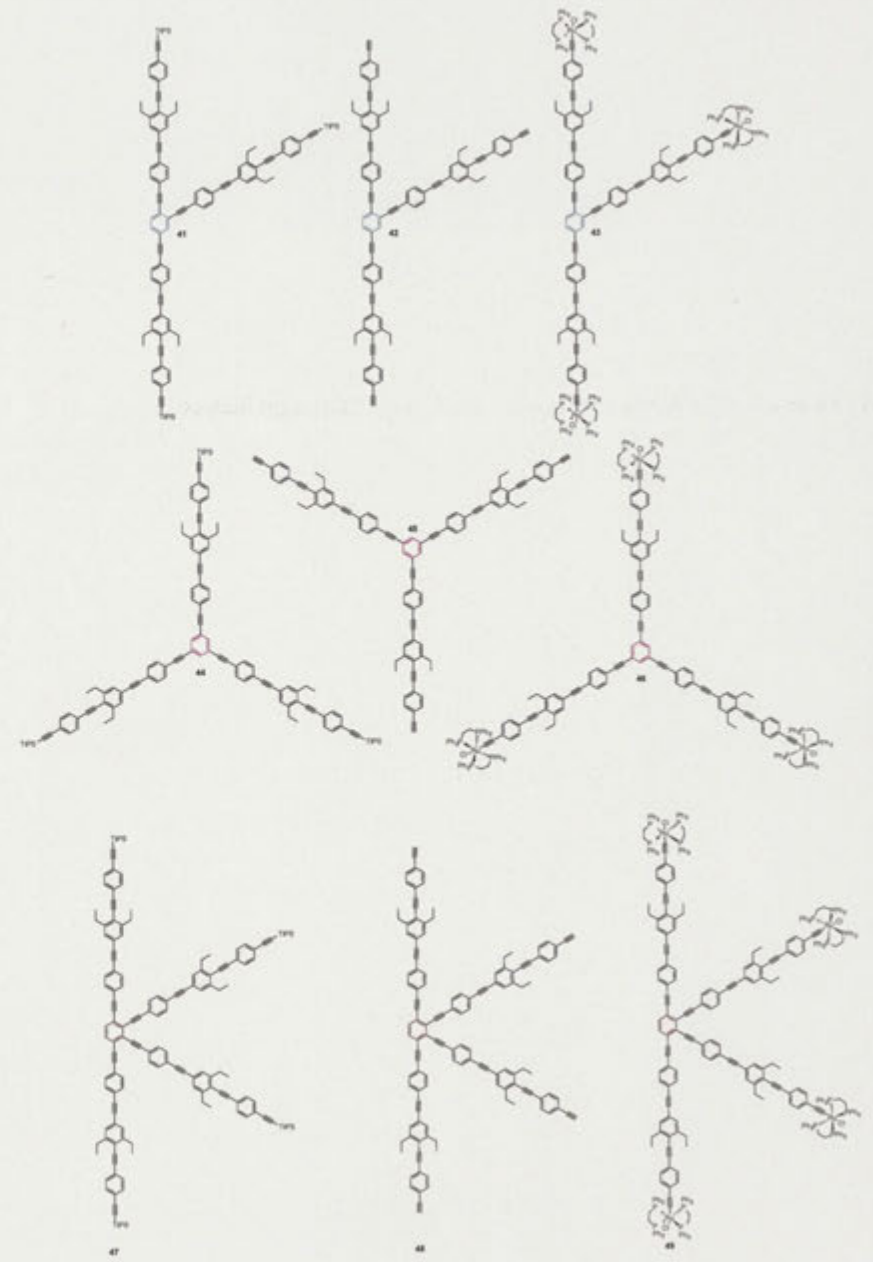
Foldout Figure 4.3.1 Structures of Compounds in Core Modification Series – Part 1

Foldout Figure 4.3.2 Structures of Compounds in Core Modification Series – Part 2



Foldout Figure 4.3.2 Structures of Compounds in Core Modification Series – Part 2

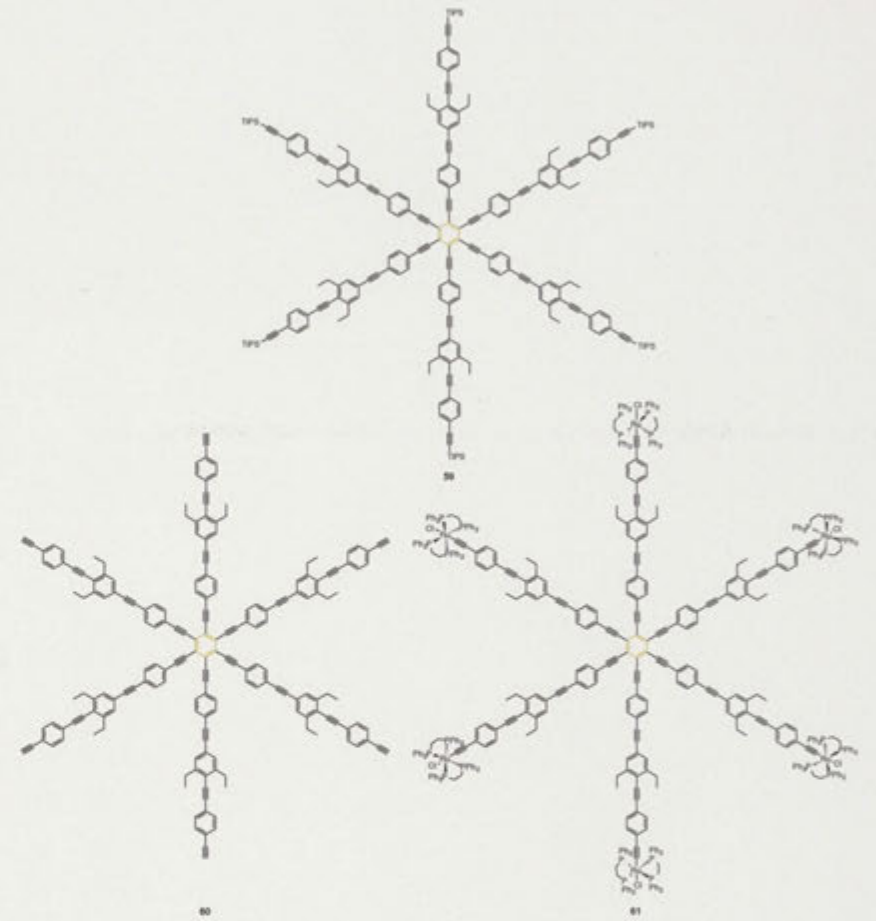
Foldout Figure 4.3.3 Structures of Compounds in Core Modification Series – Part 3



Foldout Figure 4.3.3 Structures of Compounds in Core Modification Series – Part 3

Foldout Figure 4.3.4 Structures of Compounds in Core Modification Series – Part 4

Foldout Figure 4.3.5 Structures of Compounds in Core Modification Series – Part 5



Foldout Figure 4.3.5 Structures of Compounds in Core Modification Series – Part 5

Foldout Figure 4.3.6 NMR atom labeling for compounds 1 - 61.